

**2007 SUMMER RESEARCH PROGRAM FOR HIGH SCHOOL JUNIORS**

**AT THE**

**UNIVERSITY OF ROCHESTER'S**

**LABORATORY FOR LASER ENERGETICS**

**STUDENT RESEARCH REPORTS**

**PROGRAM COORDINATOR**

**Dr. R. Stephen Craxton**

**March 2008**

**Laboratory Report 353**

**2007 SUMMER RESEARCH PROGRAM FOR HIGH SCHOOL JUNIORS**

**AT THE**

**UNIVERSITY OF ROCHESTER'S**

**LABORATORY FOR LASER ENERGETICS**

**STUDENT RESEARCH REPORTS**

**PROGRAM COORDINATOR**

**Dr. R. Stephen Craxton**

**LABORATORY FOR LASER ENERGETICS**

University of Rochester

250 East River Road

Rochester, NY 14623-1299

During the summer of 2007, 14 students from Rochester-area high schools participated in the Laboratory for Laser Energetics' Summer High School Research Program. The goal of this program is to excite a group of high school students about careers in the areas of science and technology by exposing them to research in a state-of-the-art environment. Too often, students are exposed to "research" only through classroom laboratories, which have prescribed procedures and predictable results. In LLE's summer program, the students experience many of the trials, tribulations, and

rewards of scientific research. By participating in research in a real environment, the students often become more excited about careers in science and technology. In addition, LLE gains from the contributions of the many highly talented students who are attracted to the program.

The students spent most of their time working on their individual research projects with members of LLE's scientific staff. The projects were related to current research activities at LLE and covered a broad range of areas of interest including experimental diagnostic development and analysis, computational modeling of implosion hydrodynamics and electron transport, database development, materials science, computational chemistry, and solid-state switch development. The students, their high schools, their LLE supervisors, and their project titles are listed in the table. Their written reports are collected in this volume.

The students attended weekly seminars on technical topics associated with LLE's research. Topics this year included laser physics, fusion, holographic optics, fiber optics, liquid crystals, error analysis, and global warming. The students also received safety training, learned how to give scientific presentations, and were introduced to LLE's resources, especially the computational facilities.

The program culminated on 29 August with the "High School Student Summer Research Symposium," at which the students presented the results of their research to an audience including parents, teachers, and LLE staff. Each student spoke for approximately ten minutes and answered questions. At the symposium it was announced that Mr. Christian Bieg, a physics teacher at Fairport High School, was the recipient of the 11th annual William D. Ryan Inspirational Teacher Award. This award honors a

teacher, nominated by alumni of the LLE program, who has inspired outstanding students in the areas of science, mathematics, and technology. Mr. Bieg was nominated by Rui Wang, a participant in the 2006 Summer Program and a finalist in the 2007 Intel Science Talent Search.

A total of 218 high school students have participated in the program since it began in 1989. The students this year were selected from approximately 50 applicants. Each applicant submitted an essay describing their interests in science and technology, a copy of their transcript, and a letter of recommendation from a science or math teacher.

In the past, several participants of this program have gone on to become semifinalists and finalists in the prestigious, nationwide Intel Science Talent Search. This tradition of success continued this year with the selection of two students (Katherine Manfred and Alan She) as among the 300 semifinalists nationwide in this competition.

LLE plans to continue this program in future years. The program is strictly for students from Rochester-area high schools who have just completed their junior year. Applications are generally mailed out in early February with an application deadline near the end of March. Applications can also be obtained from the LLE website. For more information about the program, please contact Dr. R. Stephen Craxton at LLE.

This program was supported by the U.S. Department of Energy Office of Inertial Confinement Fusion under Cooperative Agreement No. DE-FC52-92SF19460.

<b>High School Students and Projects (Summer 2007)</b>			
<b>Name</b>	<b>High School</b>	<b>Supervisor</b>	<b>Project Title</b>
Joshua Bell	Churchville-Chili	W. R. Donaldson	Development of a GaAs Photoconductive Switch for the Magneto-Inertial Fusion Electrical Discharge System
Margaret Connolly	Mercy	T. C. Sangster, M. McCluskey, S. Roberts	Response of CR-39 to Heat Exposure
Juraj Culak	Brighton	P. B. Radha	Neutron Imaging of Inertial Confinement Fusion Implosions
Daniel Fleischer	Brighton	R. Boni, P. A. Jaanimagi	ROSS Performance Optimization
Jean Gan	Pittsford Sutherland	K. L. Marshall	Patterned Photoresist Spacers and Photo-Induced Alignment Coatings for Liquid Crystal Waveplates and Polarizers
Roy Hanna	Williamsville	J. A. Delettrez	Extension of the Modeling of Collisional Blooming and Straggling of the Electron Beam in the Fast Ignition Scenario
Katherine Manfred	Fairport	R. S. Craxton	Polar Direct-Drive Simulations for a Laser-Driven HYLIFE-II Fusion Reactor
Richard Marron	Allendale Columbia	R. Kidder	Development of an Ontology for the OMEGA EP Laser System
Alan She	Pittsford Mendon	R. S. Craxton	Thermal Conductivity of Cryogenic Deuterium
Benjamin Smith	Webster Schroeder	L. M. Elasky	Expansion of Search Capabilities for the Target Fabrication Database
Alexander Tait	Allendale Columbia	W. A. Bittle	Data Analysis for Electro-Magnetic Pulse (EMP) Measurements
Ernest Wang	Pittsford Mendon	K. L. Marshall	Computational Modeling of Spectral Properties of Azobenzene Derivatives
Eric Welch	Livonia	J. P. Knauer	Design of an X-Ray Photoconductive Device Spectrometer
Andrew Yang	Fairport	R. Epstein	Unfolding X-Ray Spectra from a Multichannel Spectrometer

**Development of a GaAs Photoconductive Switch for the Magneto-Inertial  
Fusion Electrical Discharge System**

**Joshua Bell**

*Development of a GaAs Photoconductive Switch for the Magneto-Inertial Fusion  
Electrical Discharge System*

**Joshua Bell**

Churchville-Chili Senior High School

LLE Advisor: William Donaldson

Introduction

The Magneto-Inertial Fusion Electrical Discharge System (MIFEDS) is an accessory used in the OMEGA Laser System. MIFEDS is used to generate a very strong magnetic field between two coils positioned around an inertial confinement fusion (ICF) target being shot by the OMEGA laser. This magnetic field is used to trap the high energy electrons that are emitted from the target, providing more energy to the fusion process. To generate this magnetic field, a very large increase in electrical current needs to pass through the two coils in a very short period of time. This current is provided by two large capacitors that are discharged into the coils through a rapid closing switch.<sup>1</sup>

At this time, an ionizing switch is employed to deliver the current, energizing the magnetic field. The ionizing switch uses two electrodes in a nitrogen gas atmosphere. The MIFEDS laser sends a focused pulse through a lens in the switch, ionizing the nitrogen gas allowing the current to arc across the electrodes, discharging the capacitors. The nitrogen gas switch has two limitations due to the arcing. The arc itself reduces the maximum current, which reduces the overall magnetic flux, and the electrodes are damaged from the arcing process requiring that the electrodes be replaced occasionally.

The Laboratory for Laser Energetics would like to evaluate alternative switching devices that can handle the high voltages and current while reliably delivering a fast switching time. One possibility could be to use a laser-triggered gallium arsenide (GaAs) solid state switch. The specific goal of this project was to develop an analytical model and a test setup to imitate the MIFEDS system. This allowed preliminary calculations and measurements to be made which characterized two available samples of GaAs. From this initial analysis and testing it will be determined if laser-triggered GaAs switches are viable candidates for use as a switching device in MIFEDS.

To be used on MIFEDS, the size of the GaAs must be optimized to prevent melting as a result of the energy flowing through it. The GaAs also needs to hold off the flow of current stored in the MIFEDS capacitors that discharge current into the coils until it is hit with the triggering laser. It must deliver an energy pulse of about 30 kV and 100 kA to the coils positioned around the ICF target in less than 400 nanoseconds. The lifetime of the GaAs switch is also important. Over time, the GaAs will be damaged from the laser pulses and the current going through it. The GaAs needs to maintain functionality for a long enough life time to be a feasible alternative to the nitrogen gas switch currently being used.

### Analysis and Experimentation

In order to assure that the GaAs would not melt when shot with the laser, a study was done to determine the volume and dimensions of GaAs needed. A spreadsheet analyzing cross-sectional area and length of the GaAs was created. The other variables in the spreadsheet are voltage, load resistance, current, specific heat of GaAs, the power of the laser, and the length of the laser pulse. The cross-sectional areas and lengths of the two GaAs

samples available were put into the model and found to be sufficient with very little expected rise in temperature.

The samples of GaAs were modified by depositing gold electrodes on each end so that they could be integrated into a test setup (see Figure 1). Gold was chosen as the material because of its low resistance and high malleability.<sup>2</sup>



Figure 1 – Two samples of GaAs with gold electrodes. (The 2.25cm x 2.25cm x 0.3cm GaAs switch was used for all results in this report)

A test chamber was built to simulate MIFEDS. The chamber consisted of the square GaAs switch, capacitors equaling 500 pF, a load resistor of 1 M $\Omega$ , a DC power supply, and a 280-nH inductor to simulate the MIFEDS coils (see Figure 2). The test chamber had limitations as to how much voltage it could handle due to the maximum voltage rating on the connectors used. No more than 5000 V could be applied to the test fixture. Voltages approaching the 30 kV required for MIFEDS were therefore not obtainable and not tested at this time.

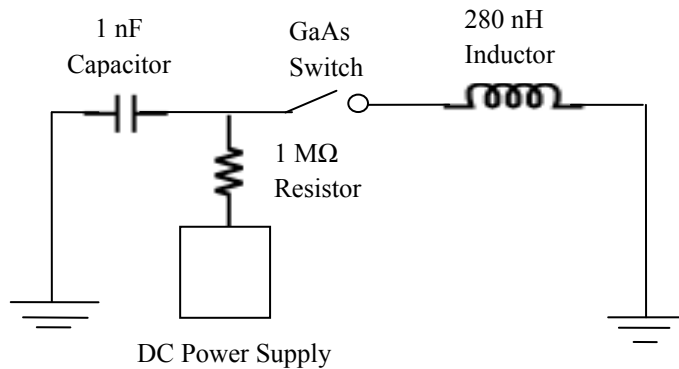


Figure 2 – Schematic of test chamber built to simulate MIFEDS

To get a general feel for how reliable the hold off of the GaAs switch was, the voltage was ramped up slowly until the maximum voltage of 5000 V was achieved. With the capacitors fully charged, the power supply remained set at 5000 V in order to keep the capacitor charge steady. An oscilloscope was placed in the circuit to measure any current increase. At 5000 V, the switch was capable of holding off the flow of current in the capacitors. This proved that GaAs has the potential to work in MIFEDS but still needs to be tested at voltages around 30 kV.

To measure the capability of the GaAs switch to deliver a high energy pulse in less than 400 nanoseconds, the voltage across the inductor and the current of the circuit were recorded using an oscilloscope as the GaAs switch was triggered by the laser. The oscilloscope was triggered when the GaAs switch closed, recording the voltage across the inductor vs. time and the current vs. time. With the power supply set at 5000 V, the GaAs switch was able to deliver 90 amps through the inductor (see Figure 3).

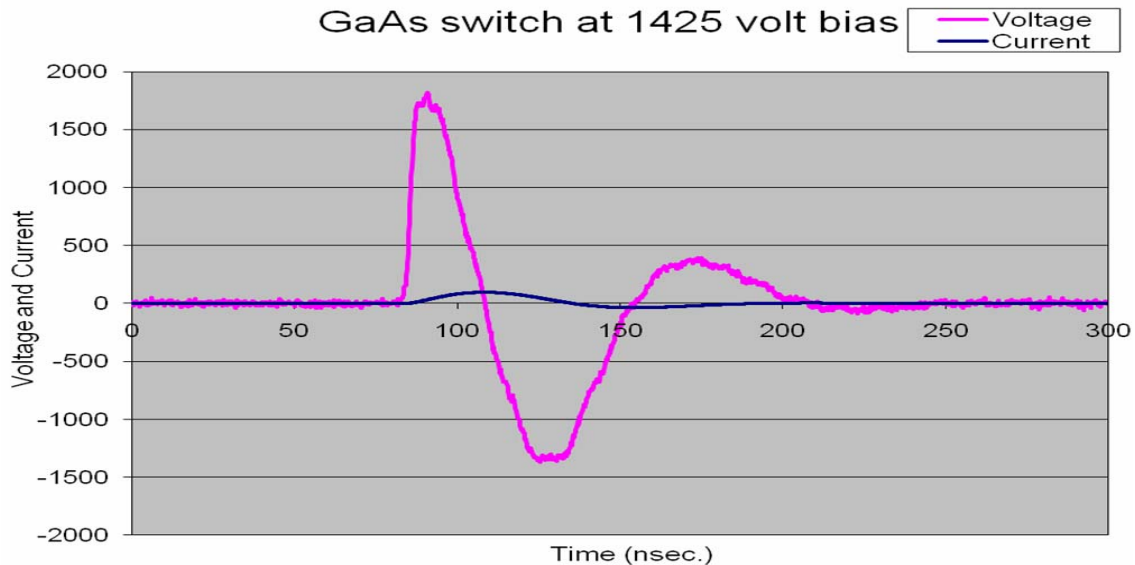


Figure 3 – Current and voltage across a 280 nH inductor produced by a GaAs switch at a bias of 1.5 kV.

The current versus voltage (I/V curve) characteristic of the GaAs (see Figure 4) can be used as a measure of how well the switch is operating and any deterioration in performance due to damage over time. To evaluate the life of the GaAs switch compared to the nitrogen gas switch currently being used on MIFEDS, the GaAs switch was exposed to over 1000 laser shots coupled with the capacitors discharging. The I/V curve was measured both before and after the 1000 shots. Comparing these two curves shows that the leakage current through the GaAs had increased by about 40% but the switch was still functional. There was also visual damage to the switch electrodes. The fact that the switch was still operational after 1000 shots is promising, but additional testing should be done to fully understand what is causing the damage. Also, experimentation should be done to identify the point at which the damage to the switch becomes too severe for operation. An excess of damage to the switch would cause the switch to leak too much current.

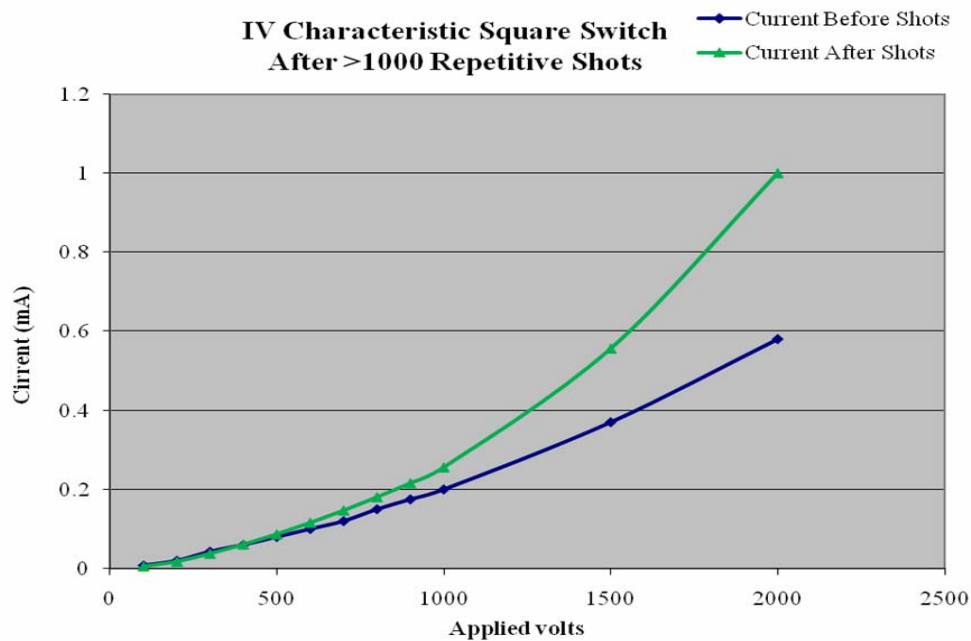


Figure 4 – I/V characteristic of the GaAs switch before and after more than 1000 laser shots.

This leakage current would reduce the energy stored in the capacitor and thus reduce the energy in the pulse used to generate a strong enough magnetic field around the ICF target.

### Conclusion

A new GaAs solid state switch trigger has been investigated for the MIFEDS system used to generate very strong magnetic fields for OMEGA experiments. The new switch shows promise as an alternative to the nitrogen gas switch currently used for MIFEDS.

A test chamber for the switch was designed and built. Voltages ranging from 50 V to 5000 V were applied to the test chamber using a 2.3cm x 2.3cm x 0.3cm square sample of GaAs. Successful switching of the GaAs was demonstrated at all voltage levels. The switch was found to have an excellent hold off for the voltages tested. The GaAs switch also held up to over 1000 repetitive shots without being significantly damaged.

Additional testing needs to be done at higher voltages and currents. Also, the cylindrical shaped GaAs sample needs to be tested to further analyze and optimize the size and shape of the GaAs switch.

### References:

[1] O. V. Gotchev, N. W. Jang, J. P. Knauer, M. D. Barbero, and R. Betti, "Laser-Driven Magnetic Flux Compression for Magneto-Inertial Fusion", in *LLE Review* vol. 110, (2007) 65-73.

[2] W. C. Nunnally and R. B. Hammond, "Optoelectronic Switch for Pulsed Power", in

*Picosecond Optoelectronic Devices*, C.H. Lee, Ed. Academic Press (1984) 373-398.

## Acknowledgements

Advisors:

William Donaldson

Orlin Gotchev

Machining:

Joseph Henderson

Electronics:

Joe Addamo

I would also like to thank Dr. R. S.Craxton for giving me the opportunity to take part in such a wonderful program.

# **Response of CR-39 to Heat Exposure**

**Margaret Connolly**

**Response of CR-39 to Heat Exposure**

Margaret Connolly

Our Lady of Mercy High School  
Rochester, NY 14610

Advisor: Craig Sangster

**Laboratory for Laser Energetics**  
University of Rochester  
Rochester, NY

August 2007

## **Abstract**

As a nuclear track detector, CR-39 (polyallyl diglycol carbonate) is used to reveal the products of fusion reactions. Positioned around the OMEGA target chamber, pieces of CR-39 absorb and are damaged by ejected particles. The plastic is then etched in NaOH solution at 80°C for 6 hours, resulting in the formation of nuclear tracks visible under a digital microscope. The etching process also reveals background noise, speculated in part to be the result of exposure to heat during shipment between suppliers and laboratories. To determine the effects of heat exposure on data analysis, pieces of CR-39 were exposed to high temperatures for various times. Heated pieces were then exposed to protons of known energies using the particle accelerator at SUNY Geneseo. Each exposed piece was etched and compared to a control. Pieces were found to oscillate between a visibly cloudy and clear appearance as a function of time exposed to high temperatures. This property was measured and quantified via reflectance and transmission of light. Furthermore, it was observed that exposure to temperatures above 100°C resulted in inaccurate data collection as etch rate and therefore track size were affected. This combination of results is an indication that current tests of the purity of CR-39 before use on OMEGA may not be sufficient.

## **1. Introduction**

The Laboratory for Laser Energetics (LLE) is currently investigating inertial confinement<sup>1</sup> as a viable means of inducing and sustaining fusion reactions as an alternate source of power. Using the OMEGA 60-beam laser system fuel capsules are imploded, achieving pressures and temperatures high enough to overcome the electrostatic repulsion of nuclei to be fused. Once these extreme conditions are produced, deuterium and tritium atoms are able to undergo a reaction in which a helium atom and a high energy neutron are formed as products.<sup>2</sup>

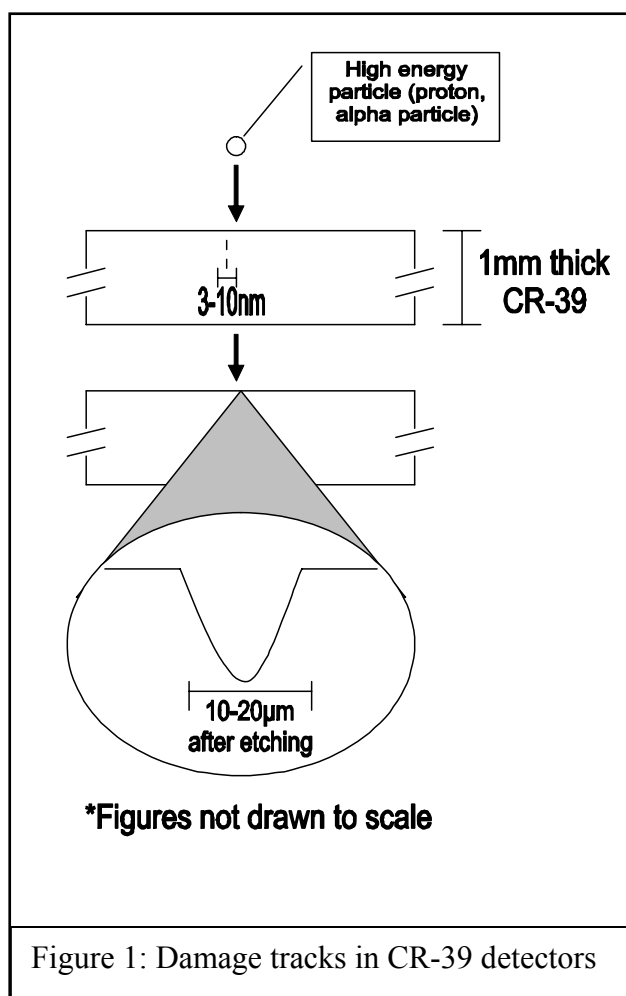
For research to progress it is imperative that an accurate record of the products of these implosion reactions be generated.

The nuclear track detector CR-39 is used to fulfill this purpose. A relatively inexpensive diagnostic, CR-39 is exceptionally sensitive to ejected protons and other larger particles produced during implosion.<sup>3</sup> Through the use of filters, CR-39 can also be prepared to register particles of a broad range of energies. The chemical composition of this plastic is homogenous and isotropic allowing for the creation of an accurate calibration of observed measurements independent of detector orientation.<sup>3</sup>

While particles are produced with constant energies, the energies with which these particles reach detectors vary. Data collected from CR-39 diagnostics can be used to quantify the amount of energy lost between particle production and absorption by the detector. This information can then be used to calculate the fuel areal density<sup>4</sup> as almost all energy loss can be attributed to collisions between ejected particles and particles of the unfused fuel between core and detector as reactions are initiated in vacuum environments, minimizing collisions with unrelated particles. The fuel areal density can further be used to determine how much fuel was successfully fused and how much fuel did not react. Thus CR-39 detectors provide a means by which to quantify the success of individual reactions.

Before the initiation of reactions, pieces of CR-39 are positioned around the periphery of the target chamber. This chamber is then evacuated and a sequence of laser pulses is fired at a target in the center of the chamber. During a burn interval of about 150 ps CR-39 diagnostics are bombarded by the high energy products of implosion reactions.<sup>4</sup> These particles, including protons, alpha particles, and deuterium and tritium atoms, penetrate the surface of detectors, breaking bonds in the plastic along tracks of depths proportional to the initial kinetic energies of

ejected particles. These tracks generally range in diameter from 3 to 10 nm,<sup>3</sup> a size too small to be made visible with a digital microscope.



Detectors are removed from the target chamber after each reaction and for this experiment immersed in six-molar NaOH solution for six hours. This solution is maintained at a constant temperature of 80°C throughout the etching process by resting solution containers in an 80°C water bath. Throughout the six hours of etching, undamaged plastic is removed at a bulk etch rate. The plastic surrounding tracks is removed at a higher rate, the track etch rate, thus forming conical pits with depth and diameter proportional to particle energy.<sup>3</sup> The process by which pits are formed is shown in

Figure 1. These pits, about 10-20 µm in diameter, are visible under a digital microscope. The etched tracks can thus be examined using the Charged Particle Spectroscopy (CPS) program developed by scientists at MIT.

This program first observes eccentricity of pits to eliminate tracks of particles that did not impact the detector normal to its surface. While particles approaching the detector at a 90° angle produce circular tracks, the particles approaching from other angles have tracks of greater eccentricity. Contrast is then evaluated with darker pits being those caused by higher energy

particles and lighter pits resulting from the impact of lower energy particles. Finally, pit diameters are measured, larger pits indicating lower energies and smaller pits indicating higher energies, to determine the energy spectra of particles ejected during implosion. It is important to note, however, that measured pit diameters correlate to different energies depending on the mass of the particle by which such pits were created. A sample image of CR-39 exposed to one type of particle is shown in Figure 2.

With differences in diameter of less than  $1\mu\text{m}$  significantly changing measured energy, small errors can compromise collected data. While CR-39 is ideally stored in a freezer at about  $0^{\circ}\text{C}$ , it can be exposed to temperatures well above  $40^{\circ}\text{C}$  during shipment despite efforts to maintain a low temperature environment including shipping in coolers and with ice.

Thus it became necessary to investigate the effects of heat exposure during transportation from the diagnostic manufacturer: Track Analysis Systems Ltd. (TASL) in England, and between LLE and Massachusetts Institute of Technology (MIT).

## 2. Pit Diameter Change

For this experiment, pieces of CR-39 were stored in a freezer at  $0^{\circ}\text{C}$  prior to use. The frames were etched to reveal any visible impurities. Samples near compromised frame areas were removed.

The remaining samples were exposed to temperatures ranging from  $100^{\circ}\text{C}$  to  $150^{\circ}\text{C} \pm 1^{\circ}\text{C}$  for 2 to 24 hours  $\pm 1$  minute. To accomplish this, each piece was set in a preheated

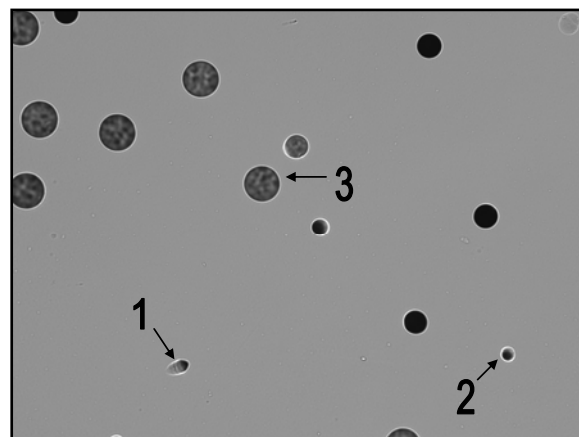


Figure 2: Digital microscope image  
Pit 1 would be eliminated in the CPS system because of its high eccentricity. Pit 2 would be identified as resulting from the impact of a high energy particle while pit 3 would be identified as being created by a low energy particle.

autoclave for the designated time. No time was allowed for gradually warming. Each piece was then taken from the autoclave directly into a room at about 25°C and left to cool for at least 24 hours. The samples were then taken to SUNY Geneseo where each was individually exposed to accelerated protons with energies of 1.000, 1.500, and 3.000 MeV $\pm$ 0.022 MeV.

Because of the high density of the particle beam, it was necessary to scatter particles off a gold foil target instead of directly exposing the CR-39. As the mass of the nucleus of a gold atom is very high in comparison to the mass of a proton, a relatively elastic collision can be assumed to occur between the accelerated proton and gold foil. Samples were exposed in a vacuum environment to avoid energy loss in collisions with other molecules. Thus the measured beam energy can be assumed equal to the energy of particles impacting the CR-39 surface within a small error. Each piece of CR-39 was secured in a spring loaded holder set at a scattering angle of 58° to the gold foil target. The surface of the CR-39, 142.7 mm from the foil target, was protected by a 0.0125 mm thick aluminum filter. A Rutherford backscattering grazing (RBG) detector was set at an angle of -58° to the foil target. This detector was measured to be 63.48 mm from the foil target.

In order to regulate the density of particles hitting the CR-39 detector, ideally 5000 particles/cm<sup>2</sup>, it was necessary to calculate the corresponding number of particles registered in the RBG detector. For this calculation the exposed area of the RBG detector was measured to be 0.07800 cm<sup>2</sup>; the exposed area of the CR-39 detector was measured to be 10.88 cm<sup>2</sup>. From this data the ideal number of particles impacting the CR-39 surface was determined to be 5.440 $\times$ 10<sup>4</sup> particles. The solid angle of each detector was then calculated by dividing the detector's surface area by the square of its distance from the foil target. Finally a proportion was set up in which the number of particles impacting the CR-39 detector divided by the CR-39 solid angle was set equal

to the number of particles impacting the RBG detector divided by the RBG solid angle. This equation was solved giving  $1.971 \times 10^3$  particles as the desired number of particles to be registered in the RBG detector. It was not necessary however to register this exact number of particles as the main purpose of density regulation was to avoid the overlapping of pits after etching.

After being exposed samples were returned to LLE, etched, and scanned using the CPS program. Measured pit diameters for each of the three energies were then compared to expected diameters according to the calibration curve developed at MIT. Pit diameters measured from the control piece were found to fit this calibration. Diameters of pits created by particles of 1.022, 1.522, and 3.021 MeV particles correlated to energies of 0.923, 1.472, and 3.240 MeV respectively with errors of 9.69%, 3.29%, and 6.82%.

Heating for two hours at 100°C prior to exposure introduced large errors. Pit diameters changed drastically such that the diameters of pits created by particles with energies of 1.022 MeV were too large to fall within the range of the calibration curve for CR-39, indicating impact by particles of energies too small to be registered by a CR-39 detector. The measured diameters of pits created by particles of energies 1.522 and 3.021 MeV correlated to energies of 1.056 and 4.743 MeV respectively. Thus heating detectors at 100°C for two hours prior to bombardment with energetic particles introduced errors of 30.6% and 57.0% in the measured diameters of pits created by 1.522 and 3.021 MeV protons.

Heating at higher temperatures prior to exposure also introduced large errors. Data from some particle impacts was lost, with only one peak appearing on a histogram of measured pit diameters (see Figure 3). As all samples were exposed to a consistent number of protons at three controlled energies, each diagram should display peaks similar to those shown in the control

sample graph. However, at temperatures of 100°C the three peaks are shifted to include tracks of larger diameters. Fewer tracks were accepted by the CPS system in these shifted peaks. At higher temperatures, only one peak, excluding that of the background noise, is measured. The central portion of this peak accounts for considerably fewer tracks than those of the control sample. The appearance of only one peak indicates exposure to particles of only one energy despite actual exposure of all samples to particles of three distinct energies.

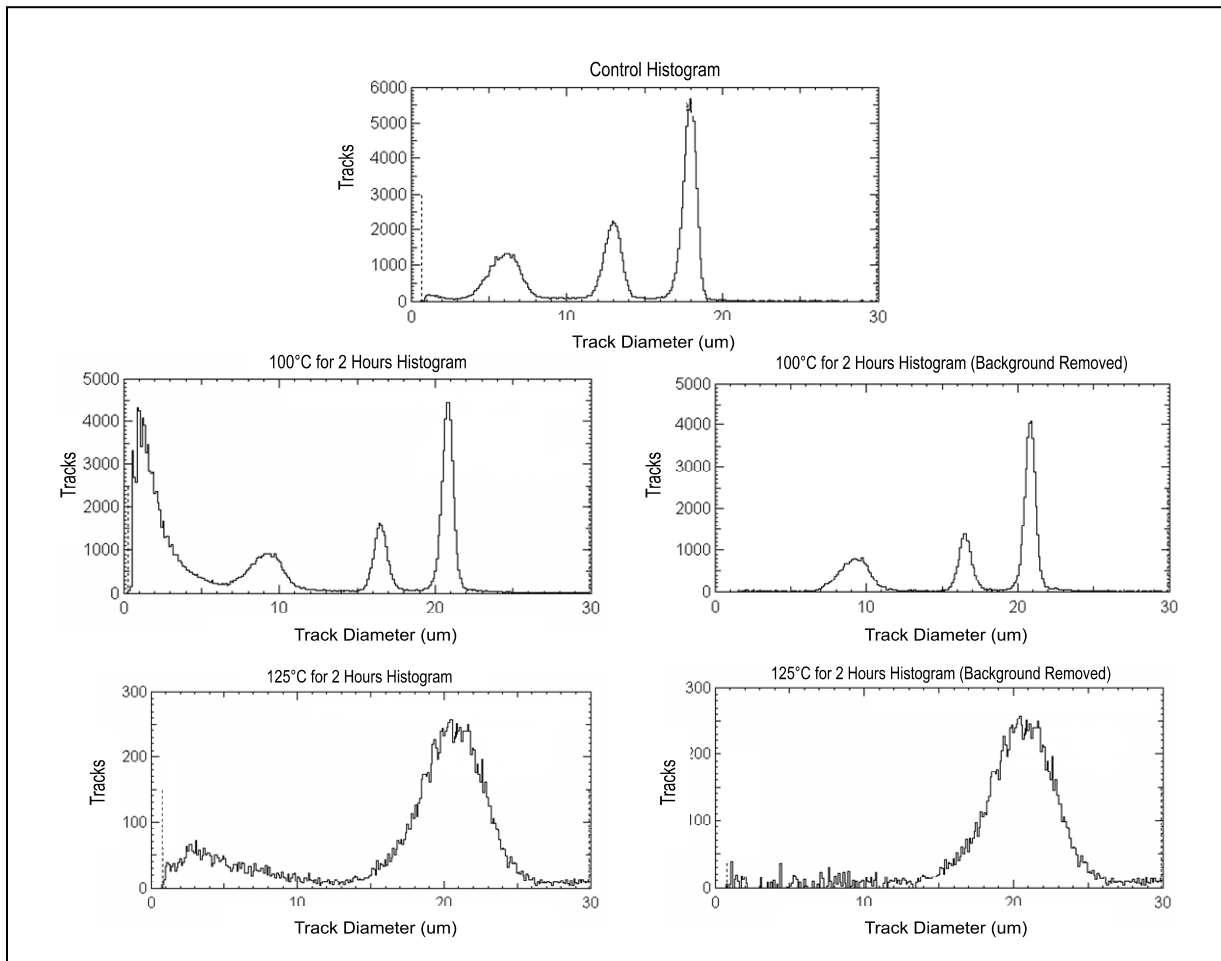


Figure 3: Collected data histograms

The histogram of the control is shown at the top. On the left are histograms including background noise. This noise is seen as a peak at the lower end of the x-axis. Across from these histograms are plots of data from the same CPS scans. Tracks of diameters and depths assumed to be background noise were removed in these histograms.

Diameters at which these peaks occurred were also shifted, correlating to particle energies outside of the range to which samples were exposed. Measured diameters from samples heated at 125°C for two hours prior to exposure identified particles of energies too low to be registered by CR-39 as impacting the detector. Data from samples heated at 150°C for two hours and at 125°C for six hours indicated exposure to particles of only one energy as well, 6.947 and 7.526 MeV respectively. Heating samples for longer periods, including 24 hours at 100°C, resulted in loss of all data. These results are shown in Figure 4.

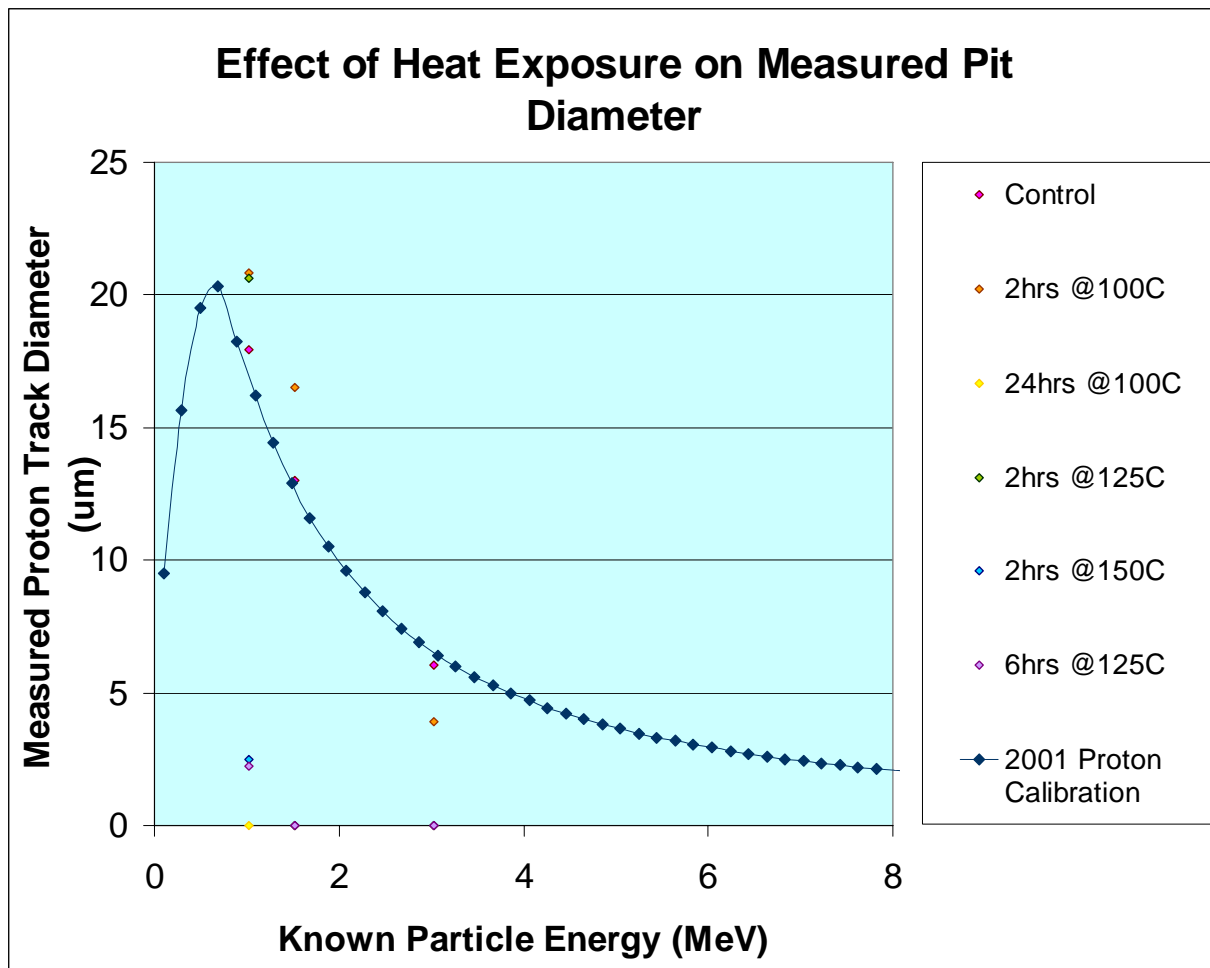


Figure 4: Effect of heat exposure on measured pit diameter

Values on the x-axis represent particle energies as defined by the particle accelerator at SUNY Geneseo. Values on the y-axis represent pit diameters measured using the CPS analysis program developed at MIT. Implied energies can be found by documenting the point at which the “2001 Proton Calibration” curve and a line represented by  $y = \text{measured pit diameter}$  intersect. The x-value given for this point of intersection is the energy with which particles forming measured pits will be assumed to have impacted the detector surface when data is analyzed.

### **3. Background Noise**

In addition to a change in pit diameter, increased background noise was observed in heated samples (see figure 3). This noise can sometimes be difficult to distinguish from legitimate particle tracks. Little background noise was observed in the control sample, while in heated samples the number of background sites accepted by the CPS system was large in proportion to the number of particle tracks accepted.

It was possible to remove some of this background noise. A CPS scan was taken of an unexposed area of each heated sample. Pits of depths and diameters similar to those accepted in the scan of the unexposed area were then removed from the data set. The results of this process can be seen in Figure 3. Though this method proved successful in removing most of the background noise, some legitimate data may also have been rejected.

### **4. Testing for Heat Exposure**

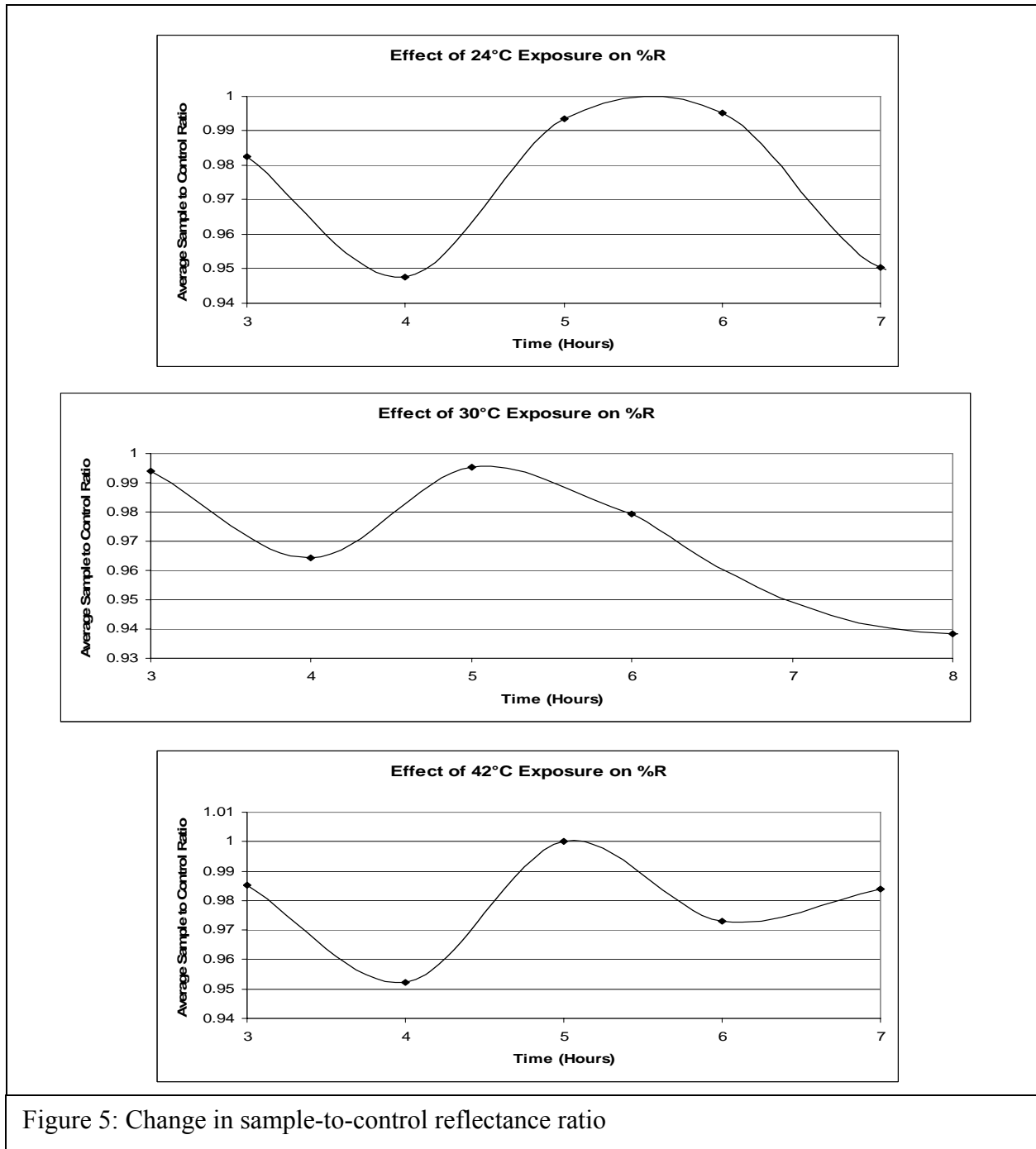
As background noise was observed to increase with heat exposure, it was speculated that surface roughness also increased. All samples were cleaned with ethanol before processing in order to avoid interference from dust particles on the surface of diagnostics. For this part of the experiment, additional detectors were exposed to temperatures ranging from 24°C to 100°C  $\pm 1^\circ\text{C}$  and etched in the same manner as the previously described samples. These pieces of CR-39 were not exposed to accelerated particles. Light transmission and reflectance properties of all samples were measured in order to find a simple test to suggest heat exposure. Such a test could be used to identify compromised diagnostics before using these samples on OMEGA or other laser systems, saving time and resources.

Samples heated at temperatures greater than 100°C could visibly be seen to oscillate between clear and cloudy as a function of time. To quantify this observation, the ability of each

sample to transmit light between wavelengths of 200 and 800 nm was measured by means of a spectrophotometer. Cloudy pieces would absorb more light than clear pieces. Sample transmission measurements were then compared to transmission measurements taken from an etched control. The sample-to-control ratio of percent transmission was seen to consistently oscillate as a function of time exposed. However, this oscillation was of a small magnitude. Consequently, it was necessary to seek another test in which results would demonstrate change much greater than that which could be attributed to measurement error.

The reflection properties of each sample for light of wavelengths of 200 to 800 nm were measured by means of a reflectometer. All samples were again cleaned with ethanol before measurements were taken. Samples were then attached to triangular prisms with a silicone index matching solution. This would limit measured light to only that reflected off the outer surface of each sample, eliminating anomalies caused as light passed through the plastic. By applying index matching solution, light that would normally be reflected upon reaching the plastic-air boundary, coming out of the sample, was made to pass from sample to index matching solution to prism without reflecting and then reflect off the interior prism walls at oblique angles. This light would consequently fail to return to the detector in the reflectometer and would therefore not affect measurements.

The baseline for measurements to be taken from was set with an unheated and unetched detector. The reflectance of each heated sample and of a control was then measured. All heated sample measurements were then compared to control measurements (see Figure 5). Heat was seen to significantly affect the relationship between a control sample's reflectance and that of a heated sample. By etching the frames surrounding detectors during shipment and comparing the reflectance properties of these pieces to the reflectance properties of a control it may be possible



to identify compromised pieces prior to their exposure on the laser system. Those pieces with sample-to-control reflectance ratios deviating greatly from one will be rejected before being used on the OMEGA laser system. However, further research is necessary to create more accurate

curves for comparison and a method of testing for heat exposure in those pieces where the sample-to-control reflectance ratio has oscillated back to a value close to one.

## **5. Conclusions**

Exposure of CR-39 to high temperatures clearly affects the accuracy of data collected from these detectors after exposure on the OMEGA laser system. Background noise resulting from heat exposure may inadvertently be accepted as data and thus considered the track of a particle ejected during an attempted fusion reaction. At the same time the tracks of real ejected particles are lost due to changes in properties of the plastic detectors. Heat exposure also causes measured diameters and depths of tracks to deviate from expected values, resulting in inaccurate identification of ejected particles. One simple test for prior exposure to high temperatures is the comparison of the reflectance properties of unused frames to reflectance properties of a control sample. Such frames are made of the same material as detectors and are exposed to the same conditions as the detectors they surround during shipping.

## **6. Acknowledgements**

I would like to express my gratitude to my advisor Craig Sangster and supervisors Michelle McCluskey, Robert Boni, and Sam Roberts for their patience and enthusiasm. I would also like to thank Stephen Padalino for his persistence and dedication to providing an environment in which to expose my samples. Finally, I would like to thank Stephen Craxton for his efforts in maintaining the Laboratory for Laser Energetics' High School Program.

## **7. References**

- <sup>1</sup> "The Inertial Confinement Fusion Concept." General Atomics: Fusion Energy Research. 15 February 2002. General Atomics. 27 August 2007 <<http://web.gat.com/ift/concept/index.html>>.

<sup>2</sup> “Inertial Confinement.” Laboratory for Laser Energetics. 25 January 2008. <[http://www.lle.rochester.edu/02\\_visitors/02\\_grad\\_inertialconf.html](http://www.lle.rochester.edu/02_visitors/02_grad_inertialconf.html)>.

<sup>3</sup> Hicks, Damien G. Charged Particle Spectroscopy: A New Window on Inertial Confinement Fusion. Ph. D. thesis, Massachusetts Institute of technology (1999).

<sup>4</sup> Séguin, F.H., et al. “Spectrometry of Charged Particles from Inertial-Confinement-Fusion Plasmas.” *Rev. Sci. Instrum.* 74, 975 (2003).

# **Neutron Imaging of Inertial Confinement Fusion Implosions**

**Juraj Culak**

**Neutron Imaging of Inertial Confinement Fusion Implosions**

Juraj Culak

Brighton High School  
Rochester NY

Advisor: Radha Bahukutumbi

Laboratory for Laser Energetics  
University of Rochester  
Rochester NY  
August 2007

**Abstract.**

During an inertial confinement fusion implosion, energy is produced as the kinetic energy of neutrons that are released from the deuterium-tritium (D-T) fusion reaction. Neutron imaging techniques indicate neutron producing and non-producing regions of the compressed target, allowing a spatial map of target conditions. Primary neutrons from the D-T fusion reaction, at 14.1 MeV, leave the target, some hitting a neutron imager producing an image. Others leaving the target enter dense regions, scatter from the unburned fuel, and are ejected from the core with reduced energies. Two-dimensional hydrodynamics simulations of direct-drive implosions have been postprocessed to calculate neutron images. While imaging the primary neutrons does not give much information about the core, imaging the scattered neutrons can be useful in determining core characteristics. These images can provide information about core distortions, and subsequently about the implosion. This will enable a deeper understanding of why certain implosions fail and why others succeed, aiding in the development of more successful implosions at the OMEGA laser facility, and eventually ignition at the National Ignition Facility.

**Introduction.**

Nuclear fusion power is one of the most important alternative energy sources. Nuclear fusion is the process by which lighter atomic nuclei combine to form a heavier nucleus. This process involves the release of energy. The most common form of fusion is the deuterium-tritium fusion, in which a deuteron, an isotope of hydrogen, and a triton, a

heavier isotope of hydrogen, combine to form a helium nucleus and a neutron as defined by the formula:  ${}^2_1\text{H} + {}^3_1\text{H} \rightarrow {}^4_2\text{He} + {}^1_0\text{n}$ <sup>1</sup>.

At the University of Rochester Laboratory for Laser Energetics, inertial confinement fusion is researched as a way to make fusion a viable energy source. In inertial confinement fusion, a pellet of deuterium-tritium fuel is compressed by a laser pulse so that fusion can occur. The pellet needs to be compressed because the particles that are fusing have positive charges and therefore repel each other. The laser pulse compresses the pellet, ideally shrinking it over thirty times and bringing it to a temperature of 100 million degrees Celsius<sup>2</sup>. The outer layer heats up from the laser pulse, and explodes away. As it ablates the equal and opposite force, directed inward, compresses the target. As the target compresses, the nuclear reactions occur in the hot core of the pellet, releasing energy in the form of high-energy neutrons. For the reaction to be as effective as possible the pellet needs to compress evenly; however in most cases it does not and distortions occur in the target. These distortions limit the amount of neutrons, and therefore energy, produced<sup>3</sup>.

For more successful fusion reactions to occur, it is important to study the previous reactions that succeeded, and diagnose those that failed. To do this, imaging techniques are used to make an image of the core of the reaction. Products from the nuclear reactions can be used to study the core region because high energy (multi-MeV) particles produced have the energy to penetrate the core and escape from the center of the reaction<sup>4</sup>. Traditional imaging techniques include x-rays and other light based imaging. However, using neutrons to image would be useful, since neutrons are produced in abundance by the reaction. Also, it is more difficult to image the colder shell around the core of the

reaction because fewer x-rays are produced in colder areas. Neutron imaging provides a way to do this successfully, using downscattered neutrons.

In the center of the reaction, there is a hot low density core where the majority of the neutrons are produced. This occurs because in this higher temperature region, at about 10 keV, the reactant particles, the deuterons and tritons, have enough energy to react and fuse when they collide. Surrounding this core, there is a cold high density shell, with temperatures closer to 1 keV, and densities up to 400 g/cc.

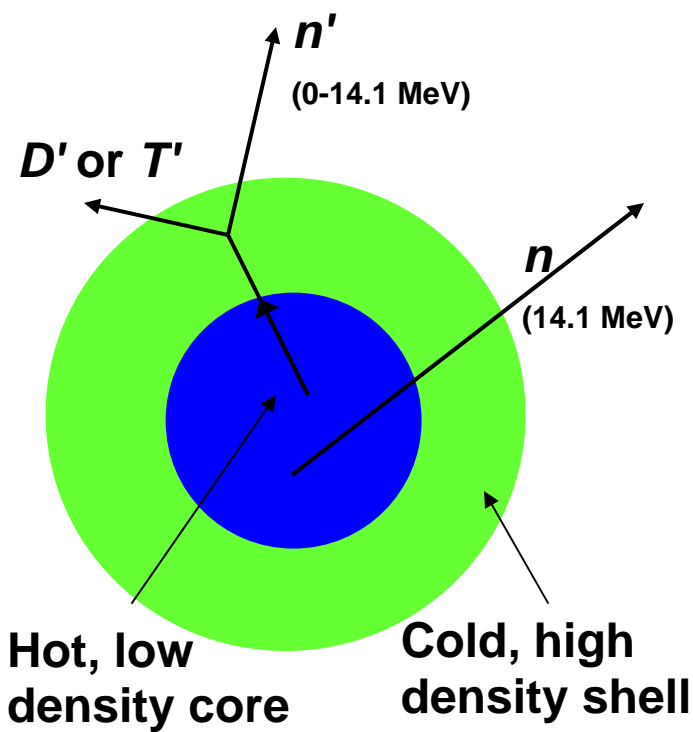


**Fig 1.** Schematic of a core during fusion reactions.

Primary and downscattered neutrons emerge from the compressed core of a pellet during a fusion reaction (Figure 1). The neutrons generated by the fusion reaction have an energy of 14.1 MeV. These then fly out of the target. While leaving the target, these neutrons travel through the

cold shell, and some are downscattered. Downscattered, or secondary, neutrons strike an unburned triton or deuteron and are scattered off in a new direction with a reduced velocity and energy because of conservation of momentum. Since the primary neutrons come from the core they can be used to image it. The downscattered neutrons have a new apparent origin: where they were scattered from. Since the neutrons are most often

scattered from regions of high density, the cold shell, they can be used to image it.

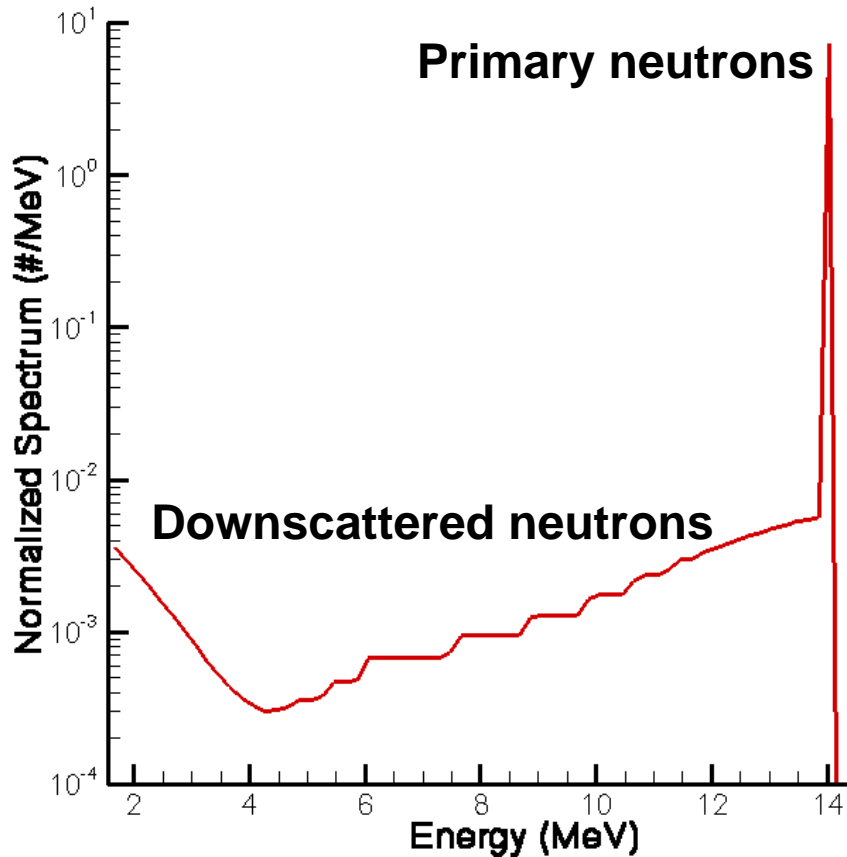


**Fig 2.** Relative proportions of primary and downscattered neutrons produced

However, neutrons are not downscattered in abundance (Figure 2). Images formed using downscattered neutrons are about two to three orders of magnitude less intense than those formed using primary neutrons<sup>5</sup>. It is thus important to study whether they will be of use as an imaging tool.

### Imaging.

Spherically symmetric and distorted profiles were imaged. The spherically symmetric model was used to test the code. It consisted of two regions, an inner core of higher temperature and lower density, and a shell of higher density and lower temperature, both symmetric spheres (Figure 3). This would be characteristic of a ‘perfect’ implosion, where the pellet would collapse evenly insuring the best reaction. Unfortunately this is not feasible. For a more realistic analysis of the situation, a snapshot of a DRACO simulation of a PDD (polar direct drive)<sup>6</sup> implosion (Figure 4) was used to give a more realistic scenario to test. DRACO<sup>7</sup> is hydrodynamics computer code used to

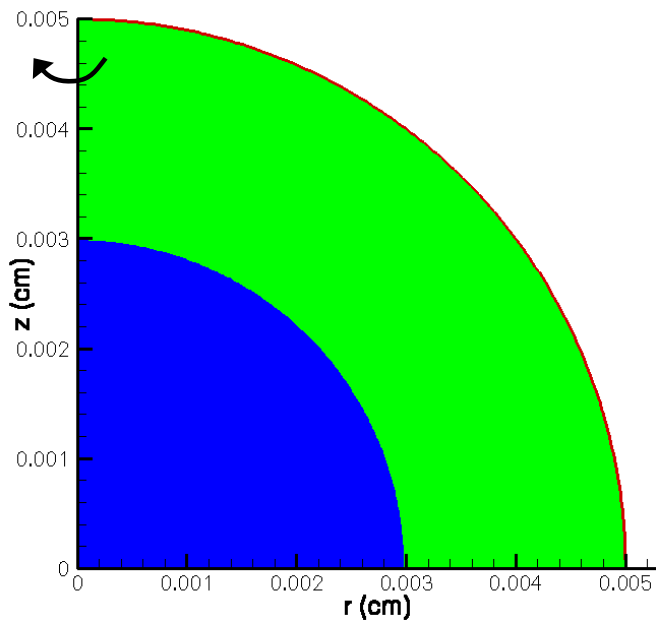


**Fig 3.** Schematic of a spherically symmetric implosion. The blue area is the hot inner core, and the green area is the cold dense shell.

simulate inertial confinement fusion implosions. PDD is one implosion method planned to be used at the National Ignition Facility (NIF). With PDD, the laser beams are not pointed straight at the target center but at angles offset from the center, to compensate for the NIF beams not being arranged evenly around the target chamber. PDD ensures the most

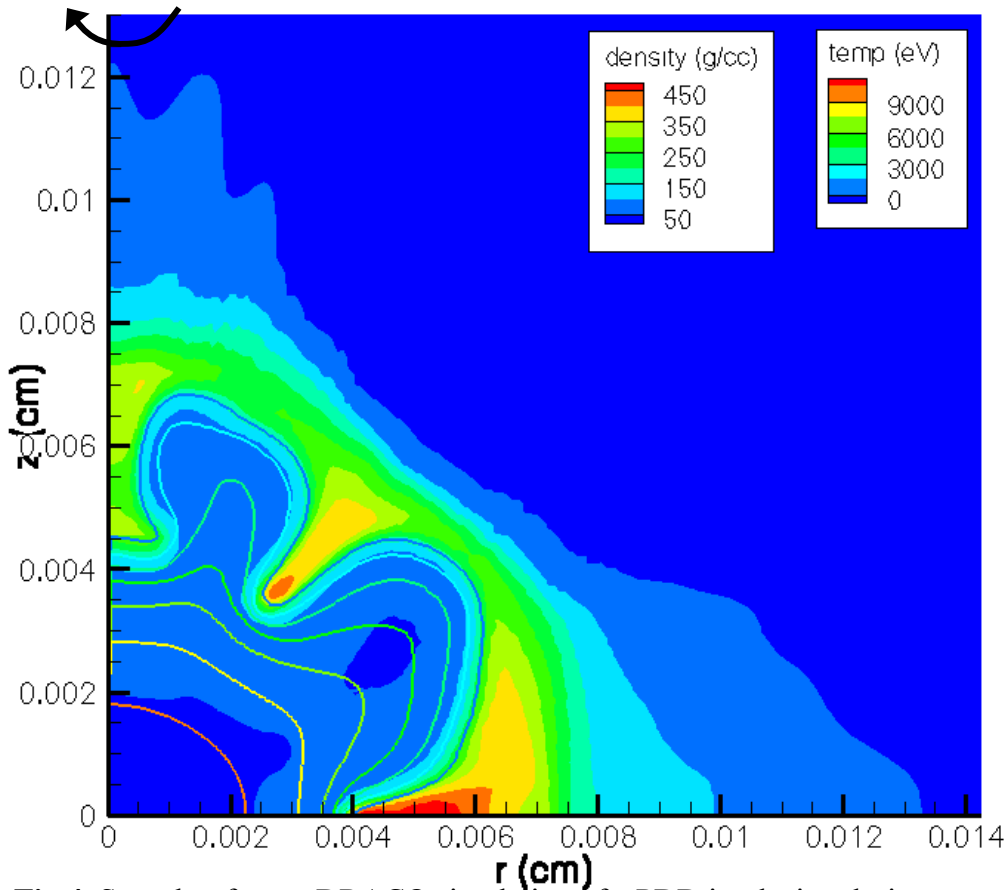


**Fig 4.** Snapshot from a DRACO simulation of a PDD implosion during peak neutron production. The shaded areas indicate density and the contour lines temperature.

unif  
orm  
com  
pres  
sion  
of  
the  
targe  
t.

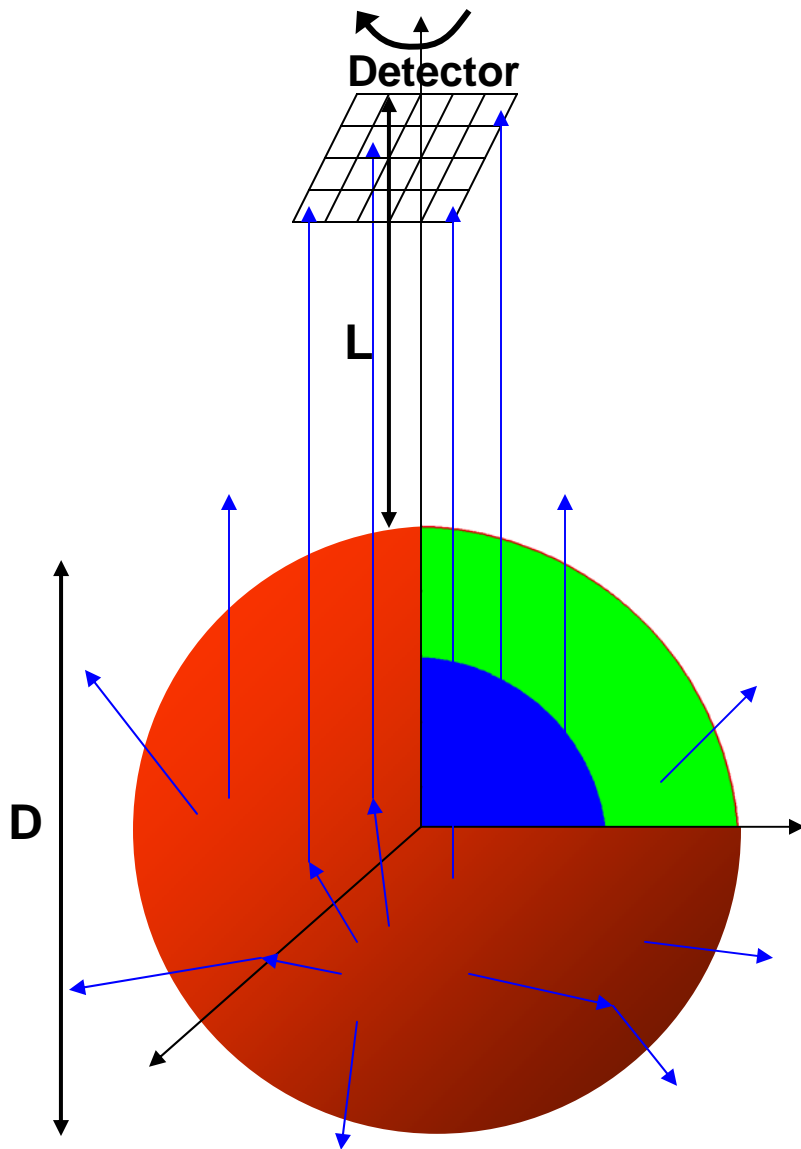


**Fig 5.** A conceptual schematic of the operation of the IRIS code.

The two dimensional profiles were rotated about the z axis to form a three dimensional profile. Using this profile, three dimensional straight line transport was used to image cores from an IRIS simulation. IRIS<sup>8</sup> is a Monte Carlo code that tracks neutrons and their interactions. In essence it randomly generates a large, statistically significant number of neutrons which it proceeds to monitor and interact with other particles that would be found in a typical implosion scenario. The

two dimensional profiles and fundamental variables describing the pellet and core constants were loaded into the IRIS simulation. The simulation then tracked the motion and interactions of the neutrons as they left the target.

IRIS was modified to image the neutrons. It now takes the neutrons that are produced in the ignition scenario and transports them to a detector (Figure 5). The detector is located far away from the target; the distance from the detector to the target is several orders of magnitude greater than the diameter of the compressed target. The

detector was an ideal detector: 20 pixels by 20 pixels, each 5  $\mu\text{m}$  in size. IRIS analyzed the movement of the neutrons and recorded their positions when they struck the detector. This data was used to calculate the image of the core as recorded by the neutron detector.

## **Results.**

Imaging primary neutrons provided useful information about the hot core. This makes sense because this is where the neutrons are produced. When the fusion reactions take place the primary neutrons directly leave the core and are not downscattered; thus their position on the detector reveals where they came from in the core. The images of the primary neutrons (Figs. 6 and 7 for the spherically symmetric and PDD models, respectively) show the defined spheres of neutron production. The size of the image is equal to that of its respective hot core in the profiles (see Figs. 3 and 4) and is a little bigger for the distorted profile. Ignoring the higher prevalence of neutrons on the axes of the images, an artifact of the imaging process, the image from the spherically symmetric model (Figure 6) is more uniform, as would be expected. It is not perfectly uniform because of statistics associated with the finite number of neutrons transported. The image of the distorted profile (Figure 7) is less even, and shows neutrons preferentially emitted from a well defined ring.

The images from the downscattered neutrons (Figures 8 and 9) provide useful information about the shell. Downscattered neutrons from within the energy range 6-8 MeV were imaged. In both images the region of the cold dense shell is well defined. In the spherically symmetric case (Figure 8) the region shown on the image is better defined. This is caused by the fact that the spherically symmetric case is unrealistic. The cold shell region is much larger than it would be in an actual implosion, thus the region

imaged is much larger. In the more realistic DRACO snapshot, the density of the cold region drops significantly outside of the dense shell, while the shell in the spherically symmetric case extends to the edge of the profile. The image for the downscattered neutrons of the distorted profile (Figure 9) from the DRACO polar direct drive implosion simulation reveals more about the viability of neutron imaging. The most evident feature of the image is the fact that the definition of the shell region is much lower. This is caused because the shell region is much smaller and more distorted. Also, there were poorer statistics for the distorted case. Since there were differences between the two profiles affecting neutron production, the distorted simulation produced less neutrons to be imaged than the symmetric case for the same running time.

## **Conclusion.**

Neutron imaging is a useful tool for diagnosing the compressed shell during an inertial confinement fusion implosion. Traditional imaging techniques, primarily x rays, have a difficult time imaging the cold higher density shell of an ICF implosion because fewer x rays are produced there due to the colder temperatures. Primary deuterium-tritium neutrons at 14.1 MeV and downscattered neutrons (0 to 14.1 MeV) have been studied as an imaging tool. While primary neutrons can image the hot core well, x rays already do this well. Downscattered neutrons, on the other hand, can be used to image the cold shell, because this is where they are scattered from the most easily, and thus their apparent origin is there. While the neutron yield on the OMEGA laser system may not be enough to produce high quality neutron images, the NIF laser system should create a significant yield to allow neutron imaging to be a valuable diagnostic tool.

Images From Primary Neutrons.

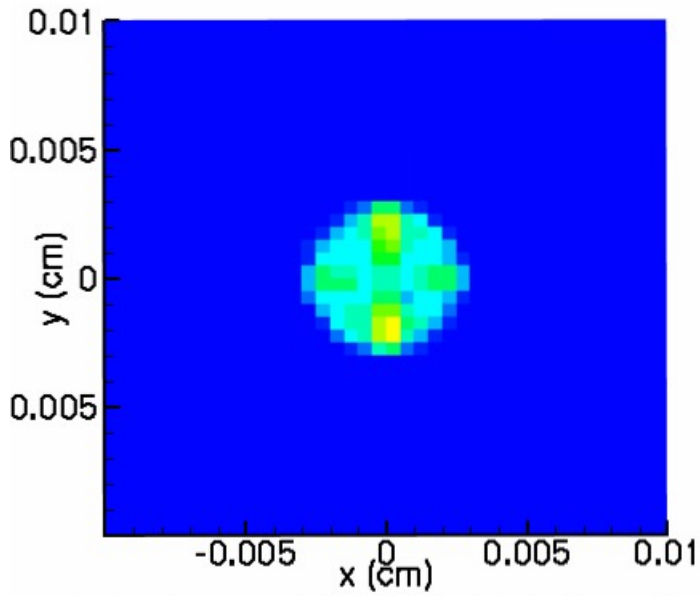


**Fig 6.** Spherically Symmetric Profile

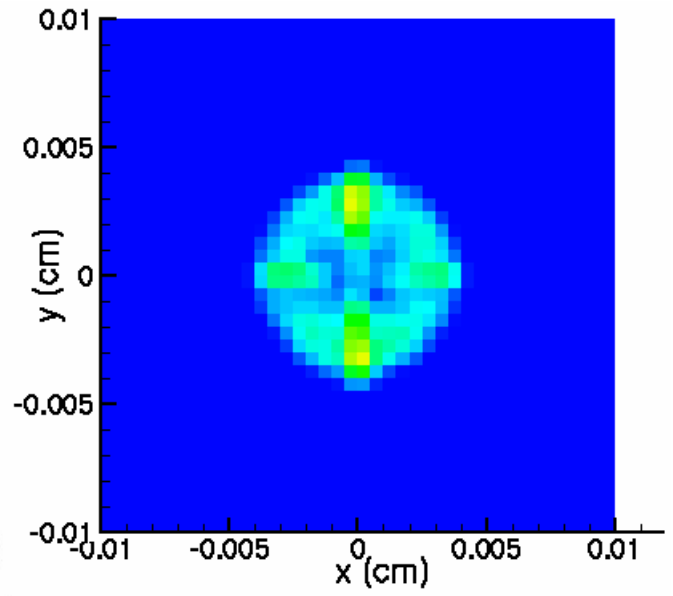


**Fig 7.** Distorted Profile

Images from Downscattered Neutrons

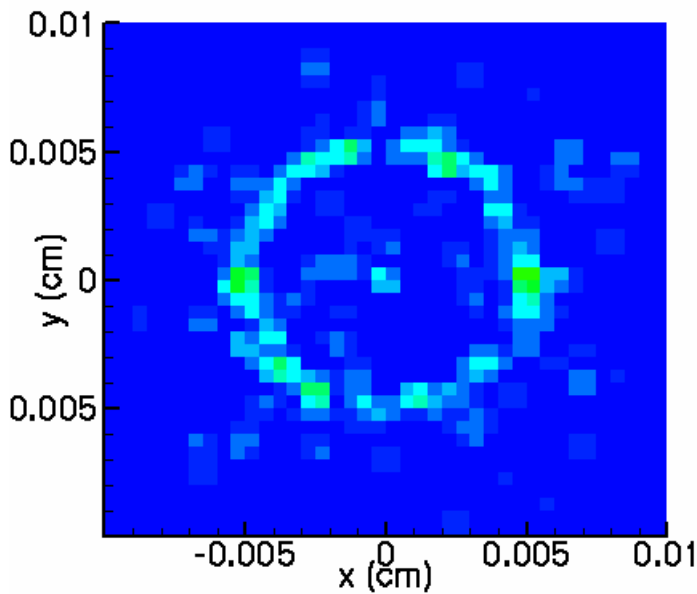


**Fig 8.** Spherically Symmetric Profile

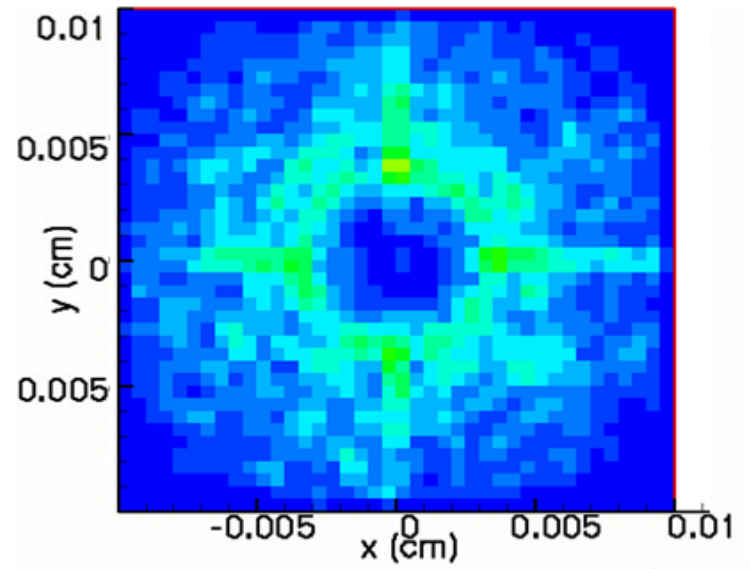


**Fig 9.** Distorted Profile

**Future Work.**

Other steps can be taken to expand the significance of this investigation into neutron imaging. The number of neutrons simulated needs to be increased to get better results. Better statistics are needed to determine whether core distortions can be imaged using neutrons. To improve statistics within the imaging simulation, its features, such as axisymmetry can be exploited to increase the statistical return of IRIS. More realistic images would give more information about the full viability of neutron imaging. As of now, the images are snapshots; time-integrating the images would lead to more realistic images. In addition, the appropriate scintillators and detectors have not yet been created for proper neutron imaging. However the expected detector response can be folded in to the simulation and imaging process. Other energy ranges and views of the target should be investigated to determine which are the most effective for imaging the core distortions<sup>9</sup>. Assuming that distortions can be imaged to some degree of success, correlating failure modes with images would be an important step for using neutron imaging as a successful diagnostic tool.

**Acknowledgements.**

I would like to thank my advisor, Dr. Radha Bahukutumbi, for all the advice and guidance I received this summer. I would like Dr. Tim Collins for his advice on my presentation. I would like to thank the tech support for their unending help. I would like to thank Dr. Stephen Craxton for setting up and directing the excellent LLE summer internship program.

## References.

1. Craxton, R. S., R. L. McCrory, and J. M. Soures, *Progress in Laser Fusion*, Scientific American, Vol. 255, 68-79. August 1986.
2. Emmett, J., J. Nuckolls, and L. Wood, *Fusion Power by Laser Implosion*, Scientific American, 24-37, June 1974.
3. Lindl, J., R. L. McCrory, E. M. Campbell, *Progress Toward Ignition and Burn Propagation in Inertial Confinement Fusion*, Physics Today, 32- 40, September 1992.
4. Cable, M., *Nuclear measurements of ICF implosions*, Laser Plasma Interactions 5: Inertial Confinement Fusion, 191- 197, (1995).
5. Moran, M., S. Haan, S. Hatchett, J. Koch, C. Barrera, and E. Morse, *Downscattered Neutron Imaging*, The 15<sup>th</sup> Topical Conference on High-Temperature Plasma Diagnostics, April 22, 2004.
6. Skupsky S., J. A. Marozas, R. S. Craxton, R. Betti, T. J. B. Collins, J. A. Delettrez, V. N. Goncharov, P. W. McKenty, P. B. Radha, T. R. Boehly, J. P. Knauer, F. J. Marshall, D. R. Harding, J. D. Kilkenny, D. D. Meyerhofer, T. C. Sangster, and R. L. McCrory., *Polar Direct Drive on the National Ignition Facility*, Physics of Plasmas, Vol. 11, No. 5, 2763-2770, May 2004.
7. Radha, P. B., V. N. Goncharov, T. J. B. Collins, J. A. Delettrez, Y. Elbaz, V. Yu. Glebov, R. L. Keck, D. E. Keller, J. P. Knauer, J. A. Marozas, F. J. Marshall, P. W. McKenty, D. D. Meyerhofer, S. P. Regan, T. C. Sangster, D. Shvarts, S. Skupsky, Y. Srebro, R. P. J. Town, and C. Stoeckl, *Two-Dimensional Simulations of Plastic-Shell, Direct-Drive Implosions on OMEGA*, Phys. Plasmas **12**, 032702 (Feb 2005).
8. Radha P. B., S. Skupsky, R. D. Petrasso, and J. M. Soures, *A Novel Charged-Particle Diagnostic for Compression in Inertial Confinement Fusion Targets*, Phys. Plasmas **7**, No. 5, 1531-1538 (May 2000).
9. Moran, M., S. W. Haan, S. P. Hatchett, N. Izumi, J. A. Koch, R. A. Lerche, and T. W. Phillips, *Energy-resolved neutron imaging for inertial confinement fusion*, Review of Scientific Instruments, Vol. 74, No. 3, 1701-1704, March 2003.

# **ROSS Performance Optimization**

**Daniel Fleischer**

# ROSS Performance Optimization

Daniel Fleischer  
Brighton High School  
Advisors: R. Boni, P.A. Jaanimagi

# ROSS Performance Optimization

Daniel Fleischer  
Advisors: R. Boni, P.A. Jaanimagi

*Summer High School Academic Research Program, July-August 2007  
University of Rochester  
Laboratory for Laser Energetics (LLE)*

## **I. Abstract**

An inertial confinement fusion implosion driven by the OMEGA laser takes place over a span of approximately one nanosecond. To study the physics of the implosion on OMEGA, a streak camera with subnanosecond time resolution, good spatial resolution, and high dynamic range is necessary. The Rochester Optical Streak System (ROSS) is able to make measurements with 1% accuracy using its Optical Calibration Module (OCM). Software scripts have been written to optimize the alignment and focus of the camera using the OCM. Because the P510 streak tube has a slot accelerator and a single electrostatic lens, it will have optimal temporal and spatial foci at different focus voltages. A common mode voltage (CMV) added to the deflection plate voltage allows the plates to act as an additional electrostatic lens, while still retaining deflection capabilities. This technique focuses a P510 tube simultaneously in both the temporal and spatial dimensions. A script has been written to determine the optimal CMV and resulting focus voltage for the ROSS with a P510 tube. Additionally, the performance of low voltage photocathode extraction fields has been measured and agrees with electron optics code predictions. The low field power supply doubles the usable photocathode

area and will be used in photon-starved experiments.

## II. Background

The ROSS<sup>1</sup> is a streak system capable of being calibrated to within 1% accuracy.<sup>2</sup> The ROSS achieves this calibration via its OCM which is a self-contained calibration unit. The OCM contains fiber optic inputs, a fiber optic head, a flat field illumination head, a patterned reticle, a flip-in mirror to switch between calibration and input, an Offner mirror that images the input or calibration onto the streak tube window, and controlling electronics. For this project, the flat field illuminator, the patterned reticle, and the free space input (as shown in Fig. 1) were utilized to create a calibrated image. The goals of this project were to use program scripts to simultaneously focus the camera in the temporal and spatial directions using a P510 streak tube<sup>3</sup>, and to test the effects of a

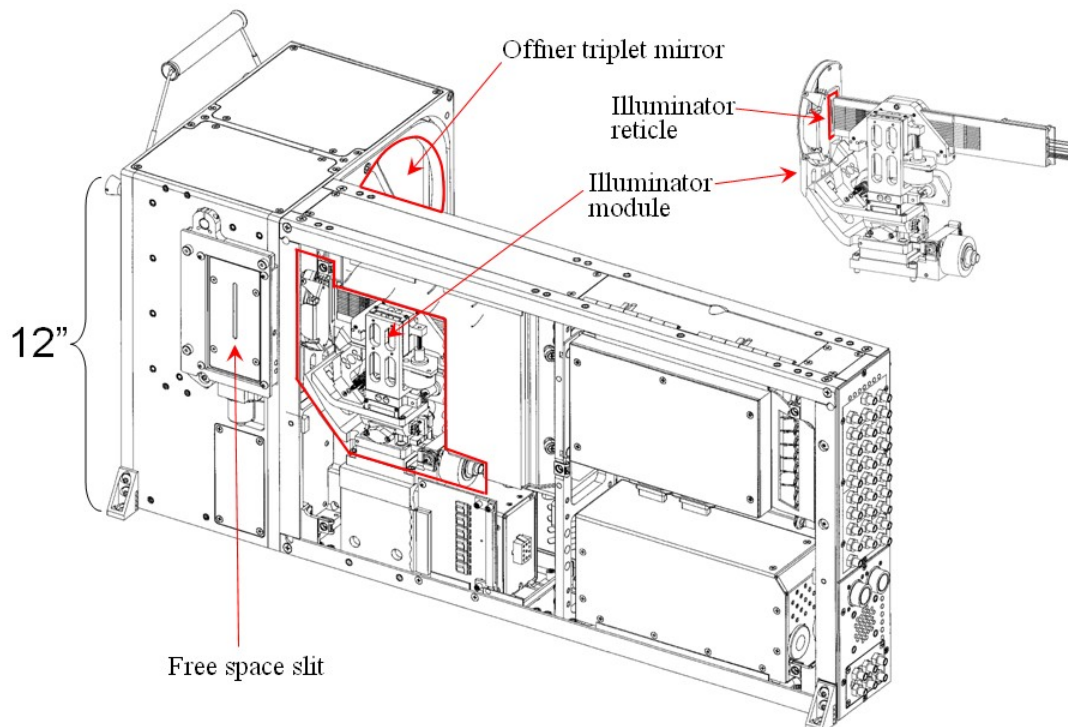


*Fig. 1: The ROSS OCM and illumination module. The OCM is used to calibrate the streak camera to within 1% accuracy. The flat field illumination and fiber optic module has been separated for clarity.*

low-field power supply (LFPS) on the light capturing abilities of the ROSS. The focusing program would help capture more accurate images with the P510 tube, and the LFPS would allow minute amounts of light to be measured for photon-starved experiments.

### III. Problem

#### 1. Focus Voltage Optimization

The problem with P510 streak tubes is that they contain a single tubular electrostatic lens. This lens will thus only focus the image in the time and space direction equally. This would not be a problem if the electrons did not need to be accelerated by an electric field. The P510 tube uses a slot accelerating plate (shown in Fig. 2) to speed up the electrons, typically with 2500 Volts between the cathode and the slot plate. Figure 2 illustrates how the fringing effects of the slot cause the electric field to bend in the time direction causing the virtual focus to be behind the cathode. Because the virtual focus is on the cathode in the space direction, the P510 tube focuses best in the time direction at a

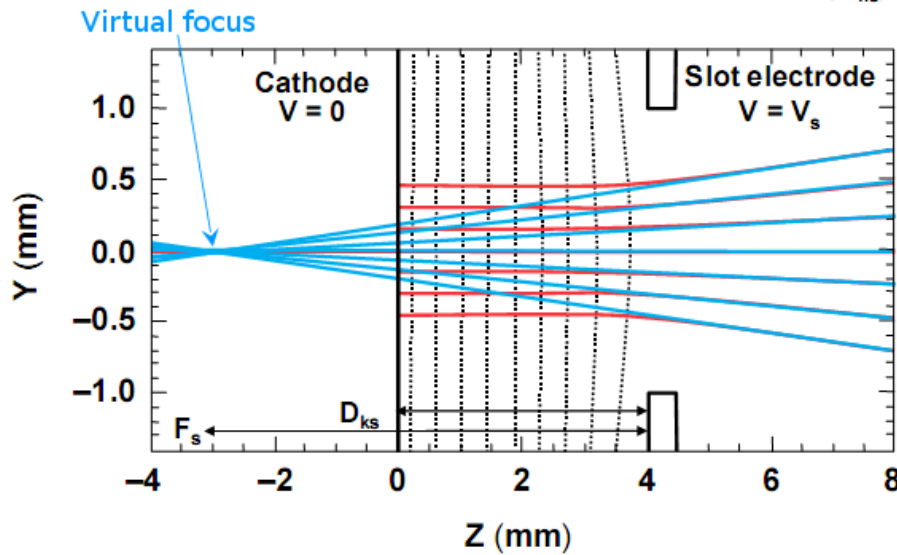


Fig. 2: Electron optics ray trace of slot accelerator. The virtual focus is behind the cathode a distance  $F_s$  due to fringing effects that result from using a slot accelerator.

different focus voltage than it focuses in the space direction.

Without any other corrections to fix this problem, the streak camera will have the smallest full-width at half maximum (FWHM) at one focus voltage and the best spatial contrast at another focus voltage. Scientists utilizing the P510 streak tube for past experiments have picked which was better for the experiment (spatial or temporal focus) or just decided that between the two voltages was “good enough.” This project succeeded in creating a program that uses a CMV to focus the P510 streak tube simultaneously in the spatial and temporal directions.

## 2. Power Supply Comparison

The other objective of this project was to test the effect of using a low-field power supply (LFPS) that would provide 1/5 of the 2500 V normally used between the cathode and the slot with a high-field power supply (HFPS). The reason for using this lower voltage is to allow more of the light to reach the CCD from the cathode. Figure 3 shows a trace of the LFPS on the left and the HFPS on the right. Expression 1 shows the electron optic equivalent of the index of refraction, which is calculated with respect to voltage.

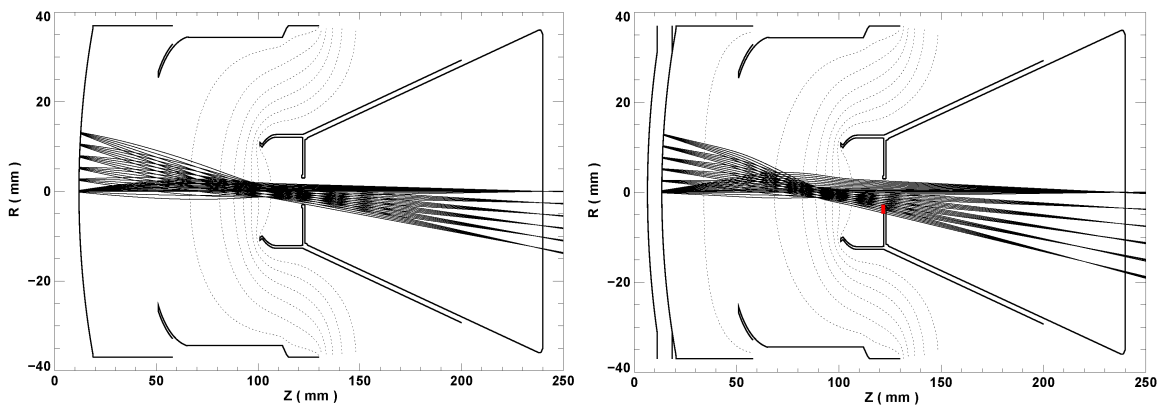


*Fig. 3: Ray traces for low field ( $V_{ks}=500\text{ V}$ ) and high field ( $V_{ks}=2500\text{ V}$ ) power supplies, respectively. More light reaches the cathode with an LFPS because more light is allowed through the anode aperture. The red line shows the part of the anode that blocks rays as a result of using the HFPS.*

$$\sqrt{V(1 + \frac{eV}{2mc^2})} \quad (1)$$

This expression includes  $[eV/2mc^2]^{1/2}$  which corrects for relativistic effects if the electrons are traveling close to the speed of light. Because the electrons in the P510 are not close to relativistic speeds, we can ignore this term. Thus the expression just becomes  $\sqrt{V}$ . This means that if you decrease voltage, the light is refracted less by the electrostatic lens and more light passes through the anode aperture. The the lower accelerating voltage provided by the LFPS decreases the index of refraction of the slot accelerator and lowers the magnification of the image, allowing more light to pass through the anode aperture. The HFPS causes some of the light to be blocked by the anode aperture. Photon starved experiments need the extra light that gets through the anode aperture.

#### **IV. Methods**

##### 1. Focus Voltage Optimization

To optimize the focus voltage, a program was written that added a CMV on to the deflection plates. For this calibration, a flat field illumination from the OCM was used to create a pattern with 5 or 10 line pairs per millimeter (LP/mm) vertically. The program adds a certain negative CMV to the deflection plates in order to repel the electrons and focus them in the time direction independent of the spatial direction. The program then scans across a range of focus voltages while measuring FWHM and contrast, as shown in Figure 4. It fits a Gaussian to the contrast curve to find the maximum and a parabola to the FWHM curve to find the minimum. These points indicate the best spatial and temporal focus, respectively. The program measures the difference between the two focus

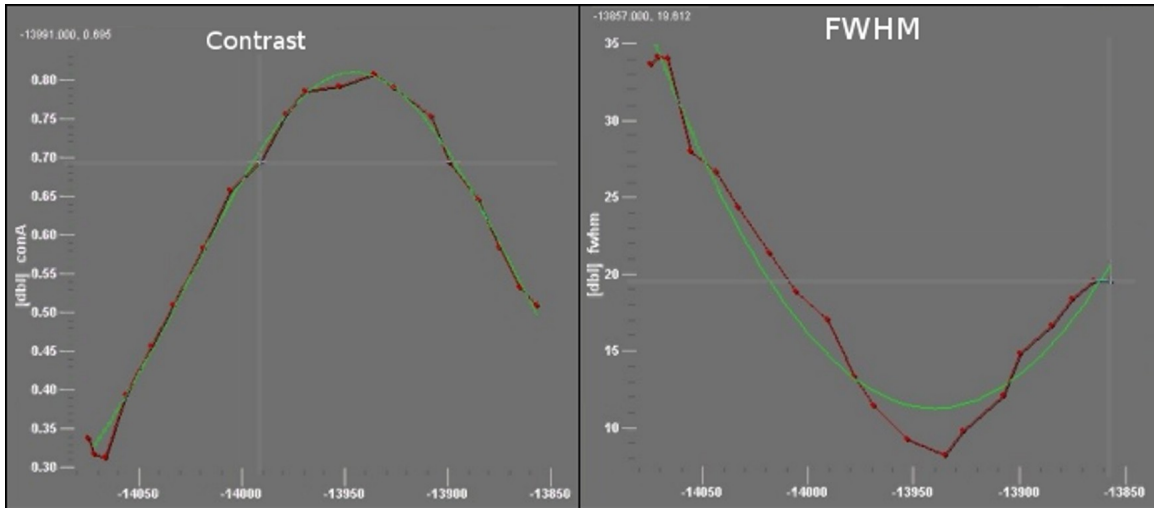


Fig. 4: Contrast vs. Focus Voltage and FWHM vs. Focus Voltage. The program fits a Gaussian and a parabola to the contrast and FWHM data, respectively.

voltages and plots that to another graph. Every cycle of the program adds more negative charge to the deflection plates and should bring the difference in focus voltage through zero. The final plot (CMV vs. distance between spatial and temporal focus optimums) is fit with a line regression and the x-intercept is calculated as the CMV that will bring simultaneous temporal and spatial focus. The program then rescans for the optimum focus voltage by setting the CMV at the calculated optimum and reports the results to the user.

## 2. Power Supply Comparison

To compare the effects of low and high acceleration field power supplies, the camera was first run through a series of tests using the existing HFPS and later, this was swapped out for the LFPS. The spatial magnification and sweet spot width (the width of the usable cathode), were measured. Line spread functions (optimal temporal focus), spatial focus (paraxial and off-axis), and dual focus with a CMV were optimized.

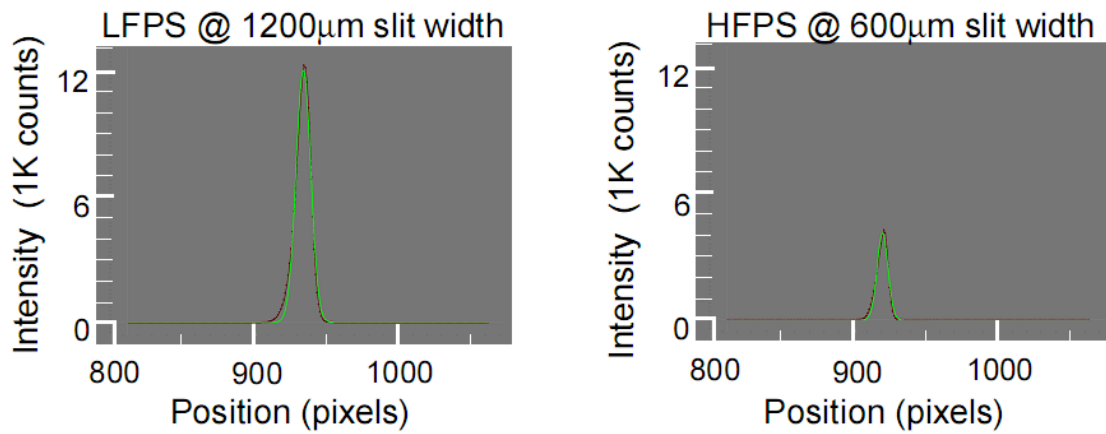


Fig. 5: Comparison of LFPS and HFPS photoelectron throughput. The photoelectron throughput is the FWHM (in  $\mu\text{m}$ ) times the intensity of the image.

## V. Results

The focus optimization program successfully optimized the temporal and spatial focus using a CMV. The contrast was raised and the FWHM lowered by using a CMV. This method gets better image results than just taking halfway between the optimal spatial and temporal focus voltages. For the 5 LP/mm slits, the contrast stayed around 93% with FWHM only increasing about  $6.35 \mu\text{m}$  when focused optimally using a CMV. For the 10 LP/mm slits, the contrast remained close to 78% with FWHM similarly close. These changes are from optimizing solely based upon either contrast or FWHM. The use of a CMV effectively optimized the focus voltage to optimize both temporal and spatial resolution.

Additionally, many tests were run to see the effect of using an LFPS with the ROSS camera. These tests demonstrated many of the expected differences between using HF and LF power supplies. For example, the sweet spot width for the LFPS was  $1,193 \mu\text{m}$ , compared to only  $603 \mu\text{m}$  for the HFPS. The reduction of the acceleration voltage from 2500 V to 500 V should have theoretically allowed for 2.236 times the sweet spot

width due to reduced index of refraction, and the actual ratio is about 1.978. Also, the photoelectron throughput (Intensity times FWHM) was about 4.34 times greater for the LFPS than for the HFPS, as shown in figure 5. However, the LFPS showed drawbacks that result from increased light throughput, mainly reduced temporal and spatial resolution. While the HFPS does offer superior spatial and temporal resolution, running the ROSS with an LFPS allows more than four times the photoelectron throughput to reach the cathode. This increased throughput is necessary for photon-starved experiments.

## **VI. Future Work**

There is the possibility for future work to continue improving the program, to help improve the programming interface, and to help implement the program for use in scientific experiments. Currently, the program for optimizing CMV has to scan through a range of focus voltages and take around 20 exposures to find the distance between the two optimum voltages. It has to do a cycle of 20 exposures for at least five possible CMVs to create the linear regression to optimize the CMV. Finally, it has to find the optimal focus voltage that corresponds to the optimal CMV. This whole process is very time consuming if done fully. The program can be sped up by limiting the cycles or exposures, or increasing the bin size for the images captured, but these speed compensations hurt the accuracy of the results. Future work could be done to find the best compromise between program speed and program accuracy.

Additionally, the programming interface for the ROSS is fairly limited. The interface could be made more user friendly for scientists. Also, the interface limited this

project from doing an inverted Gaussian fit of the FWHM. This feature would increase the program's accuracy. Finally, both the CMV program and the LFPS need to be implemented for experiments. Additional work would make the ROSS more easily usable by experimenters and more flexible.

## **VII. Conclusion**

The aim of this project was to write software scripts which would automatically focus the ROSS with a P510 streak tube in both temporal and spatial directions, and to test the ability of a low field power supply to increase sensitivity of the camera for photon starved experiments. The software scripts effectively were able to focus the ROSS in both the temporal and spatial directions using a single focus voltage together with a single common mode voltage on the deflection plates. The LFPS was able to increase photoelectron throughput and usable photocathode width. Future work may help improve and implement these programs for use in scientific experiments. These programs will increase the utility and usability of ROSS camera systems by calibrating simultaneous temporal and spatial focus and by increasing the sensitivity of the ROSS for photon starved experiments.

## VIII. Acknowledgments

I would like to thank Robert Boni, Dr. Paul Jaanimagi, and Matt Millecchia for the time that they invested in my project. I know that this experience helped me to gain valuable knowledge and skills that will help me excel in the future, and that I could not have completed this project without their help and guidance. Also, I would like to thank Dr. Stephen Craxton for admitting me to this program. I learned more about working in a real world research environment, and I gained experience presenting and writing for a technical or non-technical audience.

## IX. References

1. P.A. Jaanimagi, R. Boni, D. Butler, S. Ghosh, W.R. Donaldson, and R.L. Keck, "The Streak Camera Development Program at LLE." in *26<sup>th</sup> International Congress on High-Speed Photography and Photonics*, edited by D.L. Paisley, S. Kleinfelder, D.R. Snyder, and B.J. Thompson (SPIE, Bellingham, WA, 2005), Vol. 5580, p. 408.
2. R. Boni and P. Jaanimagi, "System for Photometric Calibration of Optoelectronic Imaging Devices Especially Streak Cameras," U.S. Patent No. 6,642,499 (19 July 1999).
3. PHOTONIS, 19106 Brive, France.

**Patterned Photoresist Spacers and Photo-Induced Alignment Coatings  
for Liquid Crystal Waveplates and Polarizers**

**Jean Gan**

**Patterned photoresist spacers and photo-induced alignment coatings  
for liquid crystal waveplates and polarizers**

Jean Gan  
Pittsford Sutherland High School

Advisor: Kenneth L. Marshall

University of Rochester  
Laboratory for Laser Energetics  
Summer High School Research Program 2007

## **ABSTRACT**

The OMEGA laser system uses waveplates and polarizers to alter the polarization of the laser light. Both devices are formed using two glass substrates that contain alignment layers and are separated by vacuum-deposited thin-film spacers and filled with liquid crystals (LCs). Vacuum deposition of thin-film spacers is time-consuming and requires the use of expensive equipment. In this study, spacers were formed by photopatterning of a negative photoresist material using standard photolithographic techniques. These photoresist spacers are comparable to thin-film spacers in quality and are much easier to produce. A new non-contacting method for generating uniform LC alignment by irradiation of a linearly photopolymerizable polymer (ROLIC ROP-203/2CP) with polarized UV light was also investigated as an alternative to the current mechanical buffing process, which leaves particles and static charges on the substrate. This “photobuffing” process is easily scalable to large apertures. Because the application of photoresist spacers does not impact the laser damage threshold of the optics and the ROLIC photoalignment material has high laser induced damage resistance, both materials are feasible for use in the laser system.

## 1. INTRODUCTION

### 1.1 Vacuum deposition of thin-film spacers

The current process for manufacturing liquid crystal waveplates (LCWs) involves vacuum depositing thin-film spacers onto the inner surface of each glass substrate.<sup>1</sup> When the LC cell is assembled, the spacers create a gap between the two substrates, which is then filled with LC material. These spacers are formed by depositing a spacer coating in even layers on the surface of the substrates until the desired spacer thickness is attained. A spacer coating run may take four to six hours to produce the specified thickness of  $6.5 \pm 0.23 \mu\text{m}$  for an LCW.<sup>2</sup> Several coating runs may be necessary to ensure the spacer thickness is correct. This process takes a fair amount of coater time in set-up and operation. Thus, vacuum deposition of thin-film spacers is time-consuming and requires the use of expensive equipment, including large vacuum chambers.

### 1.2 Mechanical buffing of alignment layers

Liquid crystal waveplates are filled with LCs, which alter the polarization of light when all the LC molecules are properly aligned along the same axis of polarization, facing the same direction. To align the LC molecules, the inner surface of each glass substrate is spin-deposited with a nylon coating and then mechanically buffed in a single direction to create microscopic grooves in the surface of the coating.<sup>2</sup> After the cell is constructed and filled, the LC molecules will orient themselves along the grooves, resulting in uniform alignment. However, this “rubbing” technique that is used to align the LCs leaves unwanted particles and static charges on the substrate.<sup>3</sup> The

mechanical buffing procedure also utilizes costly equipment that requires set-up and must be maintained (Fig. 1).

## **2. EXPERIMENT**

### **2.1 Substrate preparation**

In order for the spacer and alignment coatings to adhere to the substrates, the surfaces of each substrate must be properly cleaned and prepared. In this study, substrates were first wetted and scrubbed using 0.22  $\mu\text{m}$  filtered water and 0.05  $\mu\text{m}$  deagglomerated alumina polish until the water broke on the surfaces of the substrates. The substrates were then thoroughly rinsed and cleansed in an ultrasonic bath for 60 minutes (Fig. 2). After cleansing, substrates were rinsed with deionized water, dried using a nitrogen air gun, and baked at 90°C on a covered hotplate for 60 minutes.

### **2.2 Patterned photoresist spacers**

In this study, spacers were formed by photopatterning of a negative photoresist material using standard photolithographic techniques<sup>4</sup> (Fig. 3). To obtain maximum process reliability, the substrates were baked at 200°C on a covered hotplate for 5 minutes, thereby ensuring that the surfaces were clean and dehydrated. Next, the surfaces of the substrates were covered with Microchem SU-8 2010. SU-8 is a negative photoresist, which, after exposure to a UV light source, becomes insoluble when developed. The coated substrates were then spun under cover at 2500 rpm for 60 seconds to produce a 12  $\mu\text{m}$  step height for the spacers. After spin-coating, substrates were pre-baked at 65°C on a covered hotplate for 1 minute, then softbaked at 95°C for 2 minutes. Before UV illumination, a metal photoresist spacer mask was positioned and secured over the coated side of

each substrate. The mask contained small holes that would allow some areas of the coating to be exposed to the light source, resulting in four uniformly sized spacers on the surface of the substrate. The substrates were then illuminated under a UVP mercury vapor lamp, coated sides facing upward, for 18 seconds (Fig. 4). Following exposure, substrates were post-exposure baked on a covered hotplate at 65°C for 1 minute, and at 95°C for 2 minutes. Then, substrates were allowed to stand for 10 minutes before developing.

The SU-8 photoresist was developed using an immersion develop process. Substrates were completely submerged with the coated sides facing upward, in SU-8 Developer fluid for 3 minutes (Fig. 5). Strong agitation was applied while developing to ensure maximum resist removal. Afterwards, substrates were rinsed using isopropanol for 5-10 seconds, and then rinsed briefly using deionized water. Substrates were then dried using a nitrogen air gun and hard baked at 150°C on a covered hotplate for 10 minutes. Overall, the process for photopatterning resist spacers takes about 30-40 minutes.

### **2.3 Photo-induced alignment coatings**

As an alternative to mechanical buffing, the process of “photobuffing” was investigated as a cleaner, non-contacting method for generating uniform LC alignment across the surface of a substrate. First, substrates were rinsed using deionized water and dried using a nitrogen air gun. Substrates were not wiped dry to prevent damage of the photoresist spacers. Next, substrates were heated at 110°C on a covered hotplate for 60 minutes to remove any remaining moisture before being spin-coated. Once dry, substrates were coated with filtered cyclohexanone using a 0.45  $\mu\text{m}$  PTFE 4 mm hydrophobic-

filtered syringe. The spin-coater was covered using a glass dish for 2 minutes before spin-coating, in order to fill the ambient with cyclohexanone, providing for a more even alignment coating. The cyclohexanone was then spun off for 15-20 seconds (Fig. 6).

About 1/3 mL (or enough to cover the surface of the substrate) of 1-25% diluted ROLIC ROP-203/2CP was uniformly distributed onto the surface of each substrate using a 0.25  $\mu\text{m}$  filtered syringe. ROLIC is a linearly photopolymerizable polymer (LPP), which, when irradiated using a polarized UV light, will polymerize along the direction of polarization of the light source. Once a device is assembled and filled with LCs, the LC molecules will orient themselves along the polymer chains in the LPP, producing alignment without leaving any residue, unlike the mechanical buffing process.<sup>5</sup>

After dispensing the ROLIC material onto the substrates, the spin-coater was covered to decrease evaporation of the coating material while substrates were allowed to stand for 30 seconds. Next, substrates were spun under cover at 3000 rpm for 60 seconds, and then placed on a covered hotplate at 130°C for 10 minutes. Substrates were removed from the hotplate and left to cool for 60 minutes in a clean area. Finally, the substrates were set in a metal holding chamber and exposed to polarized 365-nm light from a xenon source at 65 watts for 10 minutes each. The substrates were positioned behind a Schott UG-11 light filter and a “pile-of-plates” silica polarizer set at Brewster’s angle, resulting in linear polarization of the ROLIC-coated surfaces (Fig. 7).

## **2.4 Cell assembly**

Following the application of photoresist spacers and photoalignment material, substrates were assembled together to create a cell. Only one substrate in each cell contained spacers (structured substrate). To assemble a cell, a very small amount of UV epoxy was applied to each spacer of a structured substrate. The coated surface of the structured substrate was then carefully aligned with the coated surface of a non-structured substrate, and gentle pressure was applied to ensure good contact. The substrates were aligned with antiparallel polarizations, so that the cell should act as a waveplate when viewed under crossed polarizers. The cell was then exposed under a UVP mercury vapor lamp for 1 minute with a weight placed on top to maintain constant pressure on the epoxy. Once the epoxy was cured, a vertical fill technique was used to fill the cell with the nematic liquid crystal E7 by Merck. The empty cell was held vertically and slowly filled by dispensing drops of LC across the top edge of the cell using a filtered syringe (Fig. 8). A vertical fill technique was used because it is generally more successful than a horizontal fill in creating uniform fills. The filled cell was then observed under crossed polarizers to assess the quality of alignment. The device was sealed around the edge using 5-Minute Epoxy. After allowing the epoxy to fully harden for 15-20 minutes, the finished device was cleaned using acetone.

### **3. RESULTS**

#### **3.1 Liquid crystal cell results**

The goal of this research was to study the feasibility of using patterned photoresist and photo-induced alignment coatings to replace thin-film spacers and buffed nylon coatings, respectively, for use in LCWs. The LC cells that were made had non-uniform polarization, which resulted in light and dark patches of LCs when viewed under crossed polarizers. The xenon light source that was used to polarize the alignment coatings was observed to have imperfect polarization. This resulted in the poor polarization of the ROLIC coatings. The “pile-of-plates” polarizer in the set-up was adjusted to  $56.1^\circ$  to create better alignment.

Despite readjustment of the UV light set-up, the LC cells that were made still lacked uniform alignment. The ROLIC coating on the substrates proved to be too thick and unevenly distributed, producing microscopic ridges that diffracted the light hitting the surface, thereby disrupting polarization. In addition, the inner surface of the irradiation set-up was not completely black, which caused the UV light to scatter and become depolarized. To resolve this, the inside of the set-up and metal holding chamber were resealed using black tape. Overall, high quality alignment of the ROLIC material was achieved over a 1” by 1” area of the coated surface.

#### **3.2 Photoresist and ROLIC material damage test data**

Damage tests demonstrated that both the SU-8 photoresist and the ROLIC photoalignment materials are viable for use in the OMEGA/EP laser systems. Substrates with photoresist spacers were

cleansed repeatedly in an ultrasonic bath to determine the durability of the spacers. After multiple washes, the photoresist spacers proved to be highly wash-resistant, and no visible damage was recorded. The spacer step height is reproducible, and can be easily altered by adjusting the speed and/or time of spin-coating the resist. The ideal step height for this experiment was 12.0  $\mu\text{m}$ , and the spacers produced averaged about 11.7  $\mu\text{m}$  when spun at 2500 rpm for 60 seconds (Fig. 9). Damage testing of substrates with SU-8 resist spacers showed no residue on the clear aperture in the center of the substrates. This demonstrates that cells made using photoresist spacers will be high quality, and will not encounter any interference from excess resist material left in the clear aperture.

High quality samples of the ROLIC photoalignment material were prepared on DTO substrates in order to test the near IR laser damage resistance of the alignment coating. Damage tests were conducted on both samples that had been exposed to low intensity, continuous wave (CW) polarized UV light and samples that were not exposed to any UV to determine whether there was any reduction in the laser damage threshold as a result of the CW irradiation with polarized UV. Damage tests were conducted using a 0.5 mm spot size and a 1 ns pulse at 1054 nm. The 1-on-1 near IR laser damage thresholds of ROLIC samples that had been exposed to low energy, CW polarized UV light for 10 minutes was  $27.4 \pm 4.6 \text{ J/cm}^2$  for defect-containing test sites, and  $57.3 \pm 1.5 \text{ J/cm}^2$  for defect-free sites. The near IR laser damage threshold for an N-on-1 test was  $30.0 \pm 7.7 \text{ J/cm}^2$  for sites with defects. For an unexposed ROLIC sample, the 1-on-1 and N-on-1 damage thresholds were  $45.8 \pm 5.0 \text{ J/cm}^2$  and  $> 43.0 \text{ J/cm}^2$ , respectively. Surprisingly, the laser induced damage resistance of the ROLIC material exceeded that of nylon (14.15-15.81  $\text{J/cm}^2$ ), and was equivalent to that of bare fused silica (30-50  $\text{J/cm}^2$ ).<sup>6</sup>

## **4. CONCLUSIONS**

### **4.1 Application of patterned photoresist spacers**

Photoresist spacers have proven to be much easier than thin-film spacers to develop and apply. The time it takes to make spacers can be reduced from 4-6 hours to 30-40 minutes by photopatterning of an SU-8 resist in a single coating run, as opposed to multiple coating deposits. An additional benefit of the photoresist process is the lack of expensive coating equipment to set-up and maintain. Photoresist spacers are comparable to thin-film spacers in quality, but more research needs to be done to determine the thickness error between spacers on a single substrate.<sup>1</sup> The uniformity of the spacers on each substrate is critical to the quality of the finished device (Fig. 10).

### **4.2 Application of ROLIC photoalignment material**

The high near IR laser damage thresholds of the ROLIC ROP-203/2CP material show that it is feasible for use in the laser system. The alignment coating can be applied using a spin-coating method, with which the coating thickness can be easily adjusted as needed. Following this study, it is worth developing and testing other photoalignment materials in future studies.<sup>6</sup>

### **4.3 Continued development of the photobuffing process**

Photobuffing has the potential to become more convenient and efficient than the current process of mechanical buffing. Non-contact photobuffing of the photoalignment material eliminates residue and is easily scalable to large areas. This study was unable to produce high quality alignment over a large area due either to irradiation non-uniformities or mechanical damage to the alignment coatings

during device assembly. Once uniform alignment is achieved over a greater area, the photobuffing process can be used in combination with a photoresist mask to create cells with patterned directional alignment in multiple, separate alignment domains. Further studies can be done to reduce regions of reverse twist and boundary disclinations, and to reduce surface and coating flaws.<sup>3</sup>

#### **4.4 Future studies**

The next logical step in developing the processes of photobuffing and patterned photoresist spacers would be to make an actual filled LC device for damage testing. The device could be measured for performance as a half-waveplate, taking into account the uniformity and quality of the results.<sup>1</sup> Photobuffing opens scientific avenues to photopatterning through the use of a mask, and its potential application in making modulators, switchable devices, and diffraction gratings.

## **ACKNOWLEDGEMENTS**

I would like to thank Dr. R. Stephen Craxton for giving me the opportunity to pursue this project. I also wish to thank my advisor, Mr. Kenneth L. Marshall, for his instruction and supervision throughout this research. Additionally, I am grateful to Dr. Tanya Z. Kosc, Graham Myhre, Gary Mitchell, and Amy Rigatti for their mentoring and support.

## REFERENCES

- [1] Rigatti, Amy. Private communication (2007).
- [2] *Manufacturing Procedure, Liquid Crystal Optics*, F-FJ-P-01 Rev. A OMEGA Upgrade, p. 17-33, Laboratory for Laser Energetics, Rochester: University of Rochester, 18 Jan. 1993.
- [3] A. R. White. *Photopatterning of Liquid Crystal Alignment Cells*. Laboratory for Laser Energetics, Rochester: University of Rochester, 25 Aug. 2004.
- [4] Microchem. *NANO<sup>TM</sup>SU-8 Negative Tone Photoresist Formulations 2-25*. Newton: Feb. 2002.
- [5] Myhre, Graham. "Updated SU-8 2010/Staralign Process." Laboratory for Laser Energetics, Rochester: University of Rochester, 25 May 2005.
- [6] Marshall, Kenneth L. Private communication (2007).

## FIGURES



Figure 1. Set-up of a mechanical buffer.



Figure 2. Cleaning of substrates in an ultrasonic bath.

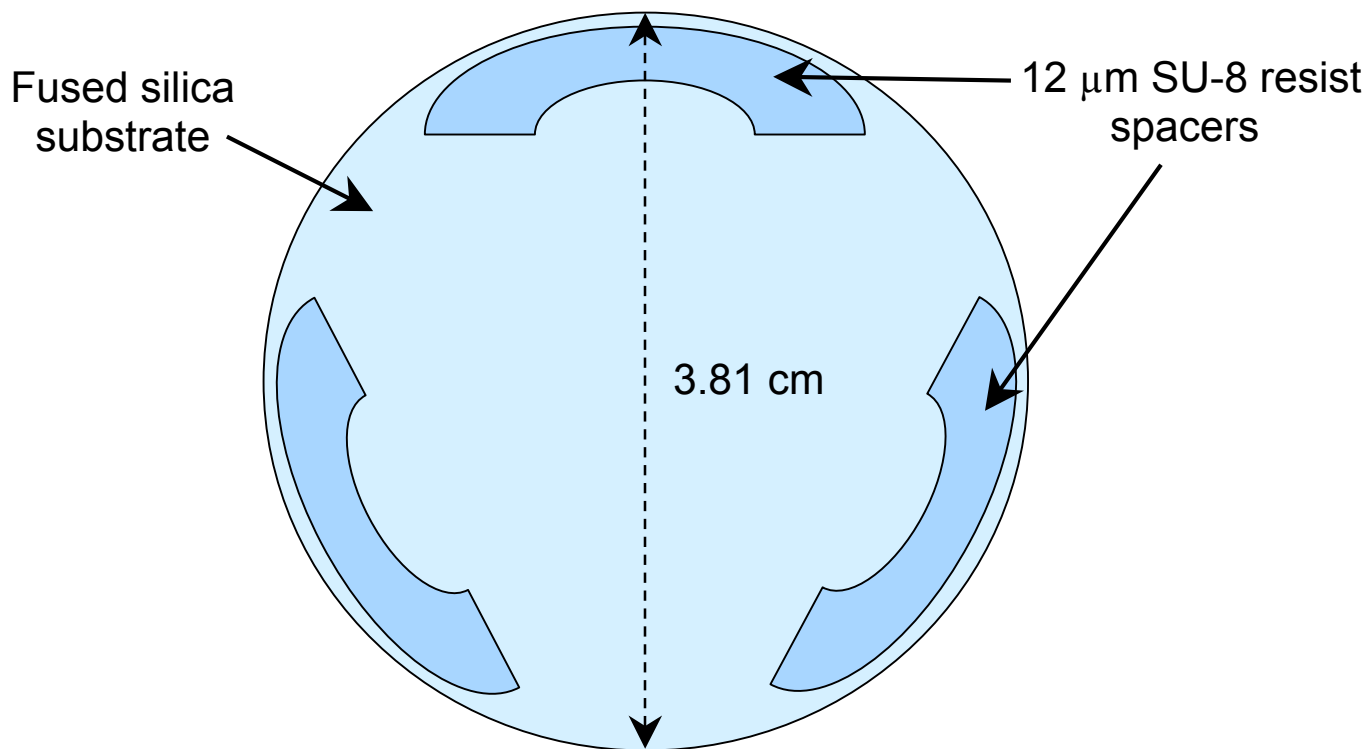


Figure 3. Diagram of spacer arrangement on a fused silica substrate.

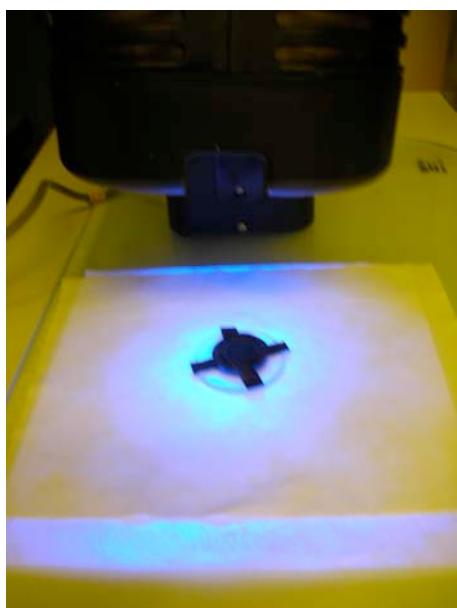


Figure 4. Illumination of substrate under a mercury vapor lamp, showing mask with designated areas where spacers will be exposed.



Figure 5. Immersion development process using SU-8 Developer to remove unexposed resist.



Figure 6. Spin-deposition of ROLIC photoalignment coating. The spin coater is covered with a glass dome to prevent rapid evaporation of the solvent during the deposition process.

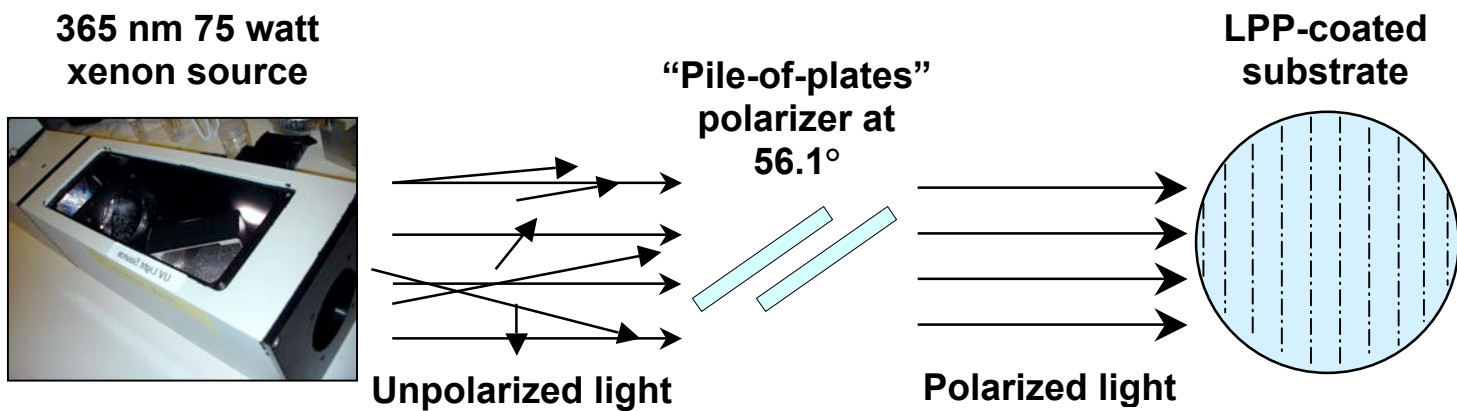


Figure 7. Schematic diagram of contact-free photobuffing process.



Figure 8. A vertical fill technique used to fill a cell with liquid crystals.

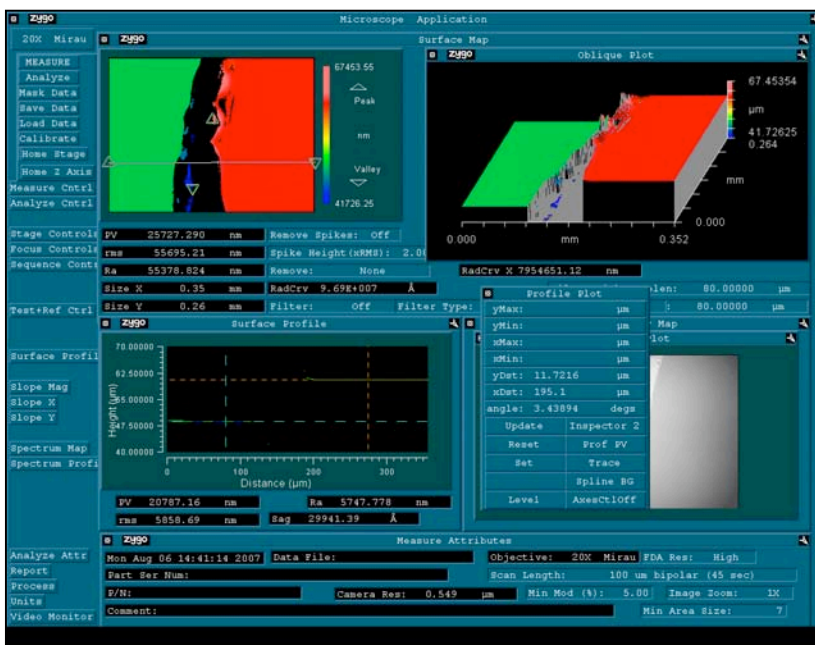


Figure 9. Zygo NewView microinterferometer data for a patterned photoresist spacer (step height: 11.7 μm).

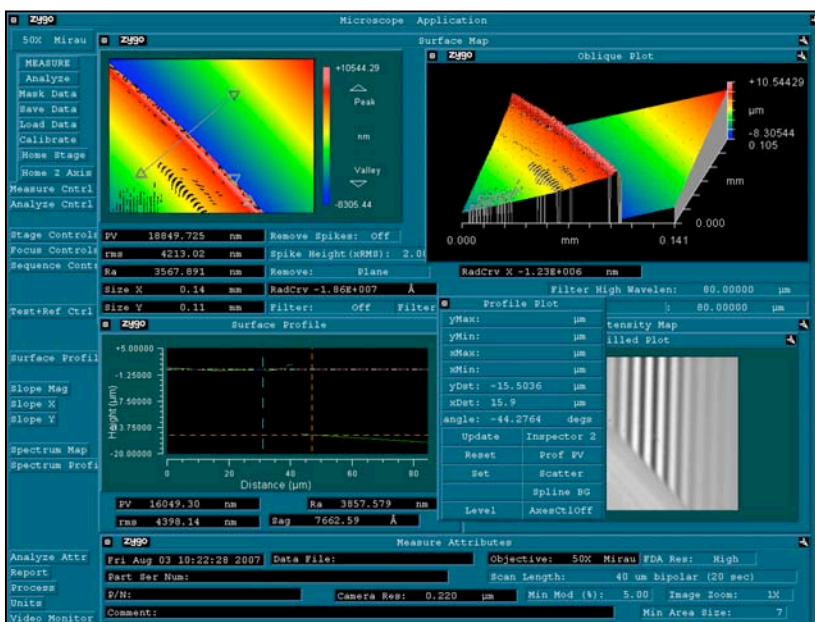


Figure 10. Zygo NewView microinterferometer data for a patterned photoresist spacer (step height: 15.5 μm).

**Extension of the Modeling of Collisional Blooming and Straggling  
of the Electron Beam in the Fast Ignition Scenario**

**Roy Hanna**

Extension of the Modeling of Collisional Blooming and Stragglings of the Electron Beam  
in the Fast Ignition Scenario

Roy Hanna  
Williamsville South High School  
Advisor: Jacques Delettrez

Laboratory for Laser Energetics  
University of Rochester  
Summer High School Research Program  
2007

## **Abstract**

When an electron beam is fired into an imploding target in order to initiate a fast-ignition-type propagating burn, spreading of the electrons occurs within the beam. The spread in the direction of motion (straggling) and the spread perpendicular to the direction of motion (blooming), as well as the energy lost as a result of these phenomena, can be defined by three equations. Previously, a program was written that added the effects of blooming, straggling, and energy deposition to an existing straight-line model. This model functioned by initially creating a single electron which was then split into several simulated electrons of different directions and energies as the probability of spreading increased. However, this method resulted in a too-large number of simulated electrons, consuming large amounts of computer memory. The program was amended by the addition of a protocol to combine simulated electrons that are in close proximity, effectively treating them as one entity and allowing for greater efficiency. This algorithm has been successful in shortening runtime and decreasing memory requirements and was tested for realistic implosion conditions in which the plasma density is nonuniform.

## **Introduction**

Ignition in conventional inertial confinement fusion occurs when fusion products created in the central hot-spot enter surrounding high-density low-temperature fuel, initiating a propagating burn. An alternative method for achieving a propagating burn has been proposed. This entails firing a relativistic beam of electrons into the high-density cold fuel, initiating the propagating burn. The path of these beams moving through plasma must be modeled in order to understand the physics behind fast ignition.

Current simulations provide for straight-line electron movement in which electrons have no deviation from uniform, horizontal travel. Electrons undergo straggling (uneven penetration depths) and blooming (spreading of the electron beam) in reality due to collisions with plasma in the environment.<sup>1,2</sup> A model was recently developed to include the effects of blooming and straggling.<sup>3</sup> This report describes how this previously created model was improved to increase efficiency and accuracy as well as to allow for simulation of electron beams in sloped plasma fields.

### Previously existing model

In this report a method for accounting for blooming and straggling is described, along with how that method was improved. As the electron beam travels through the plasma in the target, collisions occur between electrons and the plasma, causing changes in electron energy (due to energy deposition) and velocity. This is described by the following expression, which is used in the existing model:

$$\frac{dE}{ds} = -\frac{2\pi r_0^2 m_0 c^3 n_i Z}{\beta^2} \left[ \ln \left( \frac{(\gamma - 1) \lambda_D}{2\sqrt{2}\gamma r_0} \right)^2 + 1 + \frac{1}{8} \left( \frac{\gamma - 1}{\gamma} \right)^2 - \left( \frac{2\gamma - 1}{\gamma} \right) \ln 2 + \ln \left( \frac{1.123\beta}{\sqrt{2kT_e/m_0 c^2}} \right)^2 \right], \quad (1)$$

where  $r_0$  is the classical electron radius,  $m_0$  the electron mass,  $c$  the speed of light,  $n_i$  the background ion density,  $Z$  the background average ion charge,  $T_e$  the background electron temperature,  $k$  the Boltzmann constant,  $\gamma$  the relativistic energy divided by  $m_0 c^2$ ,  $\beta$  the relativistic velocity and  $\lambda_D$  is the Debye length. This equation determines the amount of energy lost per distance the electron traveled ( $dE/ds$ ). Previously, blooming

and straggling were added to the initial model. Blooming is defined as the deviation perpendicular to the direction of movement and is described by the equation:

$$\langle y^2 \rangle = \frac{2}{3} \int_{E_0}^E \langle P_1(\cos \theta) \rangle \left( \frac{dE'}{ds} \right)^{-1} \left( \int_{E_0}^{E'} \frac{1 + 2 \langle P_2(\cos \theta) \rangle}{\langle P_1(\cos \theta) \rangle} \left( \frac{dE''}{ds} \right)^{-1} dE'' \right) dE'. \quad (2)$$

where  $P_1(\cos \theta)$  and  $P_2(\cos \theta)$  are Legendre polynomials,  $dE/ds$  is the amount of energy lost per distance the electron traveled, and  $E$  is the energy of the electron.

Straggling is defined as the deviation parallel to the direction of movement (slowing down) and is given by the equation:

$$\langle x^2 \rangle = \frac{2}{3} \int_{E_0}^E \langle P_1(\cos \theta) \rangle \left( \frac{dE'}{ds} \right)^{-1} \left( \int_{E_0}^{E'} \frac{1 - \langle P_2(\cos \theta) \rangle}{\langle P_1(\cos \theta) \rangle} \left( \frac{dE''}{ds} \right)^{-1} dE'' \right) dE', \quad (3)$$

where  $P_1(\cos \theta)$  and  $P_2(\cos \theta)$  are Legendre polynomials,  $dE/ds$  is the amount of energy lost per distance the electron traveled, and  $E$  is the energy of the electron.

This model functioned by initiating a simulation with one electron, representing the entire electron beam. As the electron moved through the plasma field, the calculated probability that it had deviated (through either blooming or straggling) increased, until it reached such a level that the simulation split the electron into slightly offset three daughter electrons, which were each run separately (see Fig. 1). The program continued to function until all electrons had reached negligible energy levels. Splitting would occur millions of times before program completion, especially in more complex plasma densities, so memory consumption became a problem using this model. Also, the

existing model did not easily allow variable-density plasma fields to be simulated. Both of these problems had to be rectified to allow this model to effectively simulate realistic plasma conditions.

## Procedure

A combining algorithm was added to the existing model in order to decrease memory consumption. The medium of movement had previously been divided into grids in order to facilitate movement procedures and to allow for varying plasma densities, so a subroutine was introduced to the program to combine electrons that shared a single grid square (Fig. 2). The model functioned by creating a queue of electrons, and running the simulation of each one individually until it split or ran out of energy; daughter electrons were added to the end of the queue, the current electron was deleted and the next began running. This created problems because only the current electron could be referenced or modified while the program was running – no nearby electrons could even be detected. It was therefore difficult to combine electrons. A modification was put in place to create a loop structure within the program procedure: instead of creating daughter electrons immediately, the data associated with them was saved in the grid squares where they were created. When the queue of electrons to simulate was exhausted, the program then processed each grid square, combining each electron contained therein and then creating a new electron from the new data, which was then placed in the queue. A rule was put in place so that sister electrons (those spawned from the same parent) could not combine (which would undo the effects of blooming and straggling). After being combined, electrons would continue to bloom and straggle until all energy was exhausted.

The original simulation had not been optimized or tested for use with variable-density-plasma environments. Sloped plasma fields could be put in place, but only through the use of equations to determine conditions in each grid square (so that experimental data could not be used to define each square; rather, conditions were limited to configurations that could be expressed using polynomials). The ability to simulate more realistic conditions was necessary. The initial environment generation subroutine was modified to allow data input, and another separate program was written to convert polar coordinate data about imploding targets to a format the simulation program could recognize (essentially a conversion to Cartesian coordinates). The program was tested with a variable-density-plasma field using data from a target implosion (Fig. 3).

## **Results**

Through the use of the combining algorithm, runtime memory use was significantly decreased. The number of electrons stored in memory increased exponentially and without limit in the original program, but the number of electrons was capped at 2143 (a number found to balance accuracy and efficiency) in the new program. Figure 4 compares the number of electrons simulated in the two programs as a function of loops completed (a new loop was considered to have begun when the daughter electrons that were created by the initial electron of the previous loop, had begun running). It is obvious from this graph and accompanying data table that memory consumption in the new model was significantly lower than that of the old model; the program runs much more quickly. There is a loss in accuracy, but it is small enough that it can be discounted – depending on the exact settings used, the results are within a few percent of those from the original model.

Figure 5 depicts the output of the program in graphical form for a simulation of an electron beam moving through the variable-density plasma profile shown in Figure 3. The electron beam enters from the left side of the figure, and the deposition of energy on the grid is shown through the use of different colors. In the first 0.005 cm, there is little spread (because plasma density is low, resulting in little blooming and straggling), but high levels of energy deposition (because large numbers of electrons travel through that region). A sharp increase in the width of the energy deposition region (depicted in brighter colors) is evident at approximately 0.005 cm; this is the point where the electron beam encounters a quick increase in plasma density. This is in keeping with the precept that deviation is caused by collisions with plasma particles. However, there isn't a similar increase in spread evident at 0.0105 cm. This could be because there is so little energy left in the beam at that point that not much deviation occurs, but it could also result from a decrease in data integrity from continual recombining. The figure also shows a "corner structure" at the first deposition region. This may be due to the large distances between blooming/straggling events. There is also a focusing-type structure after 0.013 cm, which occurs because, as distance traveled increases, electrons slowly lose energy and stop. The outermost electrons, with the least energy, stop first, leaving the core. There is little spreading of the electron beam after 0.005 cm because the electrons continue moving parallel with the original beam after blooming. In realistic conditions, they would begin to move at an angle to the original beam. This must be rectified in order to create more realistic simulations.

## **Future Work**

Adding parallelism to decrease runtime of the program is a possibility. Each electron being run is simulated completely independently, so, using the current combination parameters, up to 2143 independent threads could be used to simulate electrons. This would create a much faster simulation. Additionally, because memory consumption is now less of a concern, the parameters for simulation of blooming and straggling could be set to allow more frequent adjustment with less significant changes in order to increase the accuracy of the simulation. This would mitigate problems such as the corner structure found in Figure 5. There is one major shortcoming in the current simulation: after blooming occurs within electron beams, they continue moving in parallel with the original beam. Realistically, they should move at an angle for the rest of the simulation. This must be changed in order to ensure more accurate simulations.

## **Conclusion**

A method for combining electrons in order to decrease memory consumption and runtime has been added to an existing model which simulates the progression of electrons within the fast-ignition approach to inertial confinement fusion. This method functions by combining electrons in close spatial proximity, and only suffers from a small loss of accuracy. Additionally, the program was refined to allow for variable-density-plasma environments to be simulated.

## **References**

1. C. K. Li and R. D. Petrasso, Phys. Rev. E 73, 016402 (2006).
2. C. K. Li and R. D. Petrasso, Phys. Rev. E 70, 067401 (2004).

3. E Dobson, "Modeling Collisional Blooming and Straggling of the Electron Beam in the Fast Ignition Scenario", LLE High School Program Project Report (2006).

### Acknowledgements

I would like to thank my advisor, Dr. Jacques Delettrez, for his guidance, support, and advice throughout this project. I would also like to thank Dr. Christian Stoeckl for his assistance in the final stages of the project and in the creation of the symposium presentation. Many thanks also to Dr. Stephen Craxton for his time and energy in directing the High School Summer Research Program at the Laboratory.

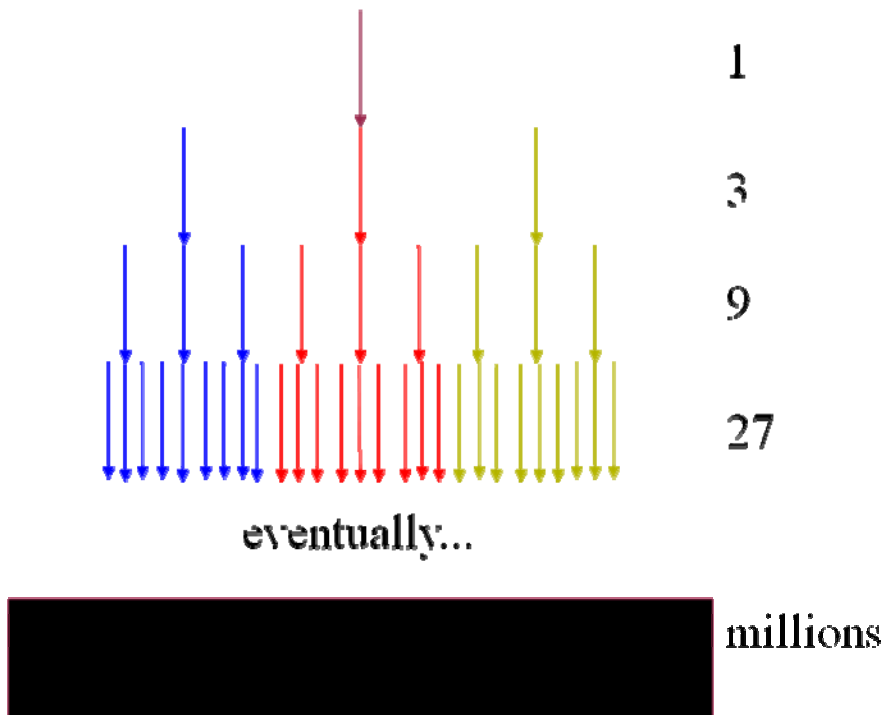


Figure 1: Spreading of electrons, as conducted in the original program

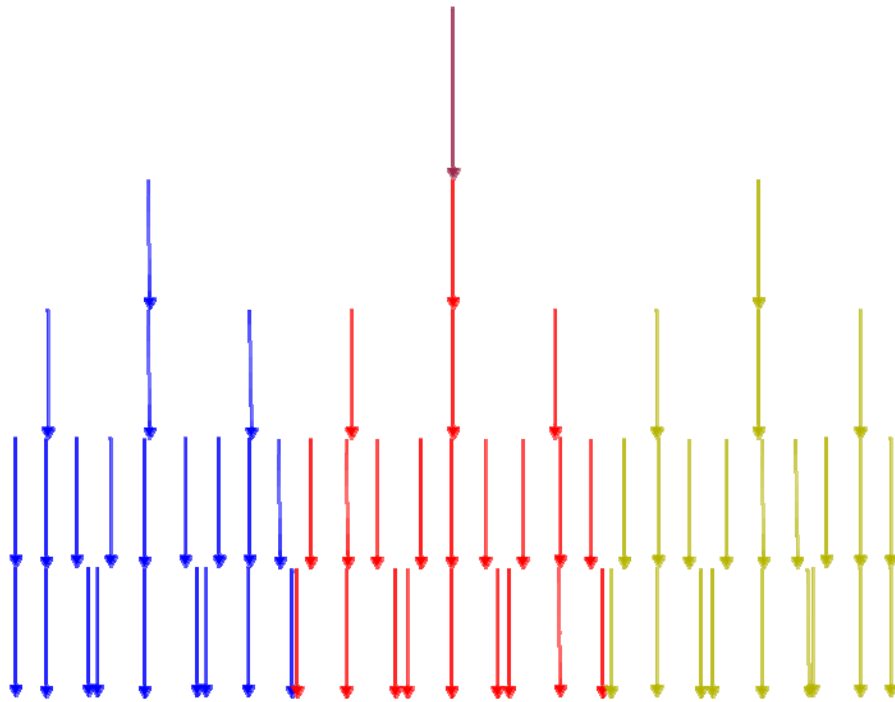


Figure 2: Recombination of electrons using new combining algorithm. The bottom row of arrows depicts pairs of electrons that have been combined, reducing memory consumption. As the simulation presently occurs, horizontal movement does not enter into calculations after initial blooming – all electrons remain parallel in movement.

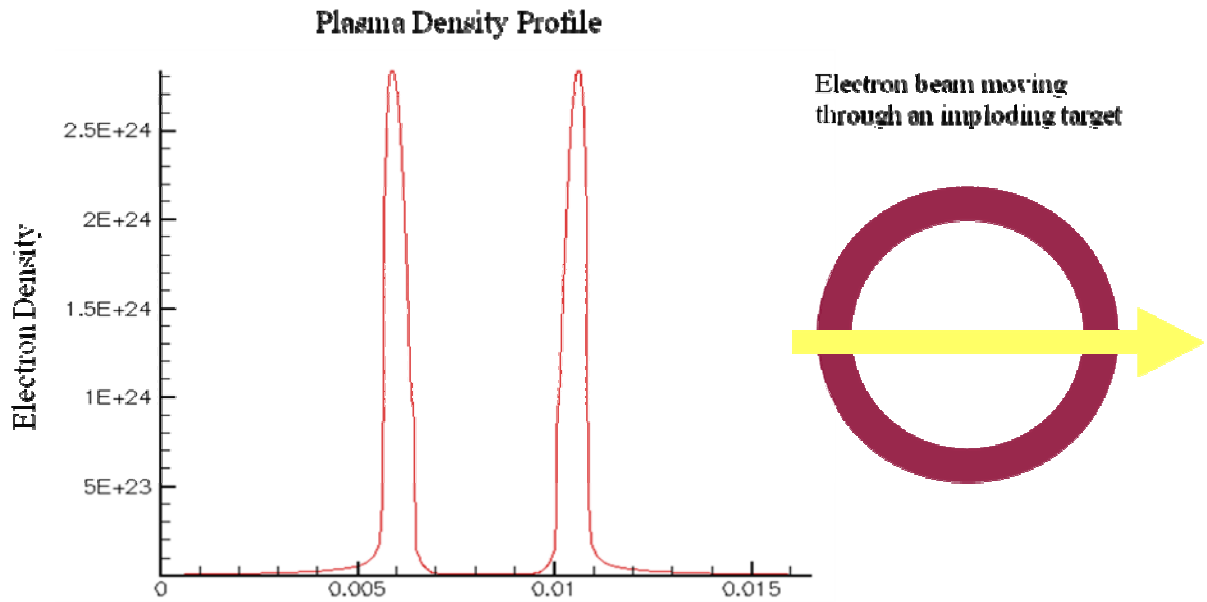


Figure 3: The new variable-density-plasma profile used in the simulation. The graph on the left and diagram on the right are two perspectives on the same thing – the red ring represents the increase in density which appears in cross-section in the graph.

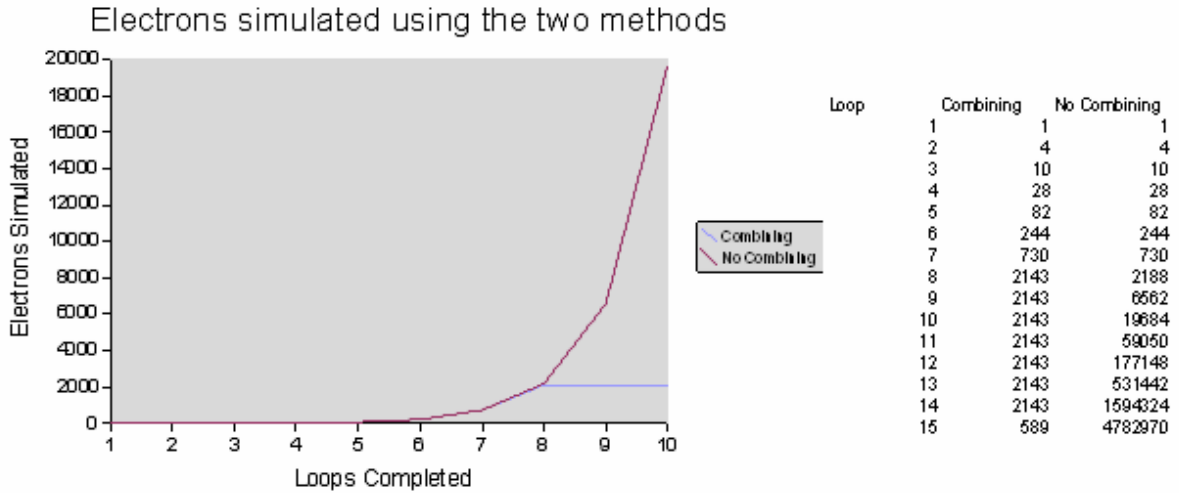


Figure 4: Graph of the number of electrons simulated using the two methods. The number of electrons simulated in the combining method is capped at 2143 (the optimal number). A “loop” is considered to have been completed when the daughter electrons of the electron that initiated the previous loop are processed.

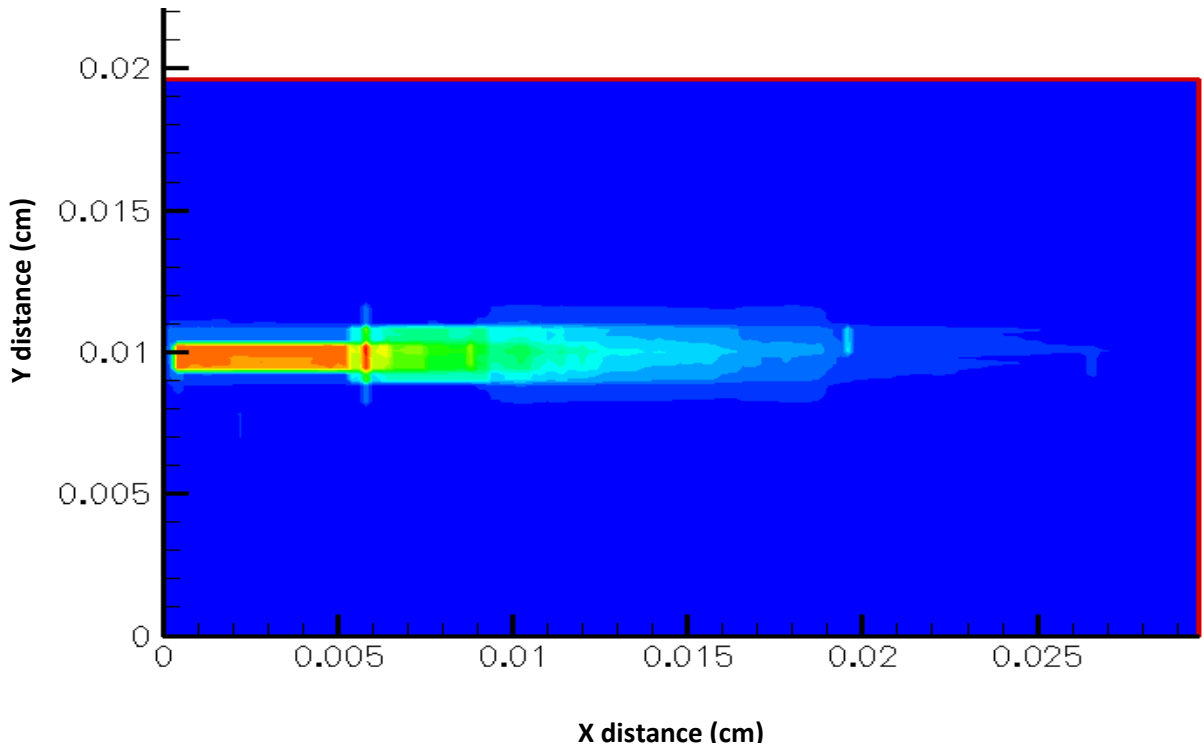


Figure 5: Graph of energy deposition of the electron beam as calculated by the model. The electron beam enters from the left of the figure, and moves through the profile shown in Fig. 3. High levels of energy deposition are shown with bright colors (red, yellow, and green), while low levels are shown with darker colors (shades of blue).

**Polar Direct-Drive Simulations for a Laser-Driven  
HYLIFE-II Fusion Reactor**

**Katherine Manfred**

**Polar Direct-Drive Simulations for a Laser-Driven  
HYLIFE-II Fusion Reactor**

Katherine M. Manfred

**Fairport High School**  
Fairport, New York

Advisor: Dr. R. S. Craxton

**Laboratory for Laser Energetics**  
University of Rochester  
Rochester, New York

November 2007

## Abstract

This report explores the possibility of using laser-driven fusion on the HYLIFE-II fusion reactor, which was originally designed for ion beam fusion. The reactor design surrounds the imploding hydrogen-containing target with a fluid waterfall, which limits any laser beams irradiating the target to  $20^\circ$  or less from a central axis. Difficulties in irradiating the equator of the target with oblique rays are overcome by concentrating beams on the equator and adjusting beam variables, such as focal spot shape and beam pointing shifts, during the laser pulse. Simulations performed using the hydrodynamics code SAGE show that it is possible, using a 2.1 MJ KrF laser, to achieve an implosion in a HYLIFE-II reactor similar to that of a design for the 1.5 MJ laser at the National Ignition Facility (NIF). This result demonstrates that laser-driven fusion may be viable on the HYLIFE-II reactor.

## 1. Introduction

Nuclear fusion has the potential to become a major source of energy in the future. Fusion involves the combination of two nuclei to release energy. In inertial confinement fusion, a driving force deposits a large amount of energy on the surface of a target, typically a thin shell surrounding the fusion fuel, causing the shell to expand rapidly. The reaction force of this rapid expansion compresses the fuel in the center of the target to very high densities and temperatures. These conditions allow the atomic nuclei to overcome electrostatic repulsion and fuse. Deuterium and tritium, two isotopes of hydrogen, are commonly used as fuel and react according to the equation  $D + T \rightarrow {}^4\text{He} (3.5 \text{ MeV}) + n (14.1 \text{ MeV})$ . The kinetic energy of the neutron is the main output energy. If there is a sufficient amount of fuel at a high density, the helium nucleus deposits its energy in the fuel, providing energy for more fusion reactions. This state of sustained

reactions is known as ignition. For fusion energy to be usable as a source of energy, the fuel must ignite in order to generate a larger amount of energy than is required to initiate the reaction.

Three approaches to inertial confinement fusion are shown in figure 1.1. They involve two broad categories of driving forces: heavy ion beams<sup>1</sup> and lasers<sup>2</sup>. In ion-beam fusion [see figure 1.1(a)], ions are accelerated and compressed in time to form short pulses that pass through the wall of the hohlraum, a gold cylinder surrounding a target. The ions deposit their energy in a thick metal plate, which emits x rays that irradiate the target within the hohlraum. In direct-drive laser fusion [see figure 1.1(b)] the shell of the target absorbs energy from an array of laser beams focused on the target from many sides. Indirect-drive laser fusion [see figure 1.1(c)] involves using laser beams pointed at the inner walls of a hohlraum. The hohlraum absorbs the energy and emits x rays, which irradiate the target.

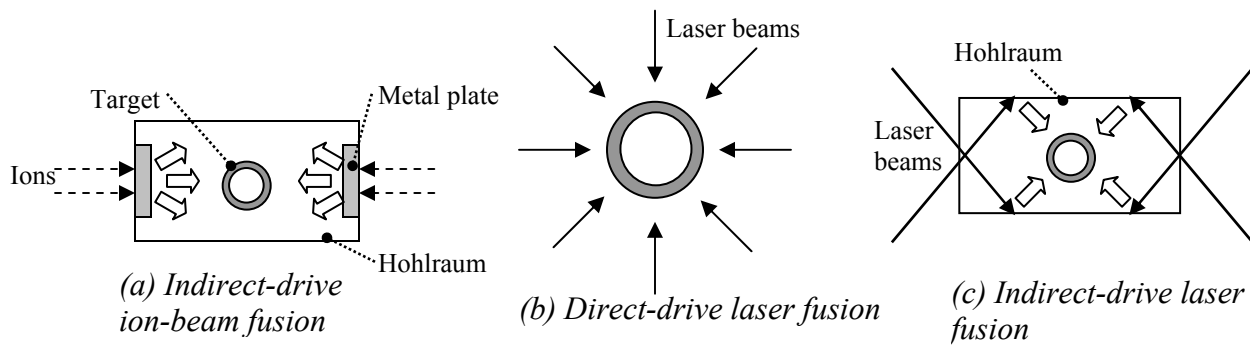


*Figure 1.1: Three approaches to inertial confinement fusion: (a) Ion beam energy is absorbed by a thick metal plate, causing it to emit x rays (block arrows) that are confined within the hohlraum and irradiate the target. (b) Laser beams are directly incident on the surface of the target. (c) Laser energy is incident upon the inner wall of the hohlraum to produce x rays that irradiate the target.*

The High-Yield Lithium-Injection Fusion-Energy (HYLIFE)-II<sup>3,4</sup> fusion reactor design [Figure 1.2(a)] presents an innovative method for harnessing the energy of nuclear fusion reactions. In conventional fusion reactor designs, the wall of the chamber must withstand repeated bombardments by neutrons, x rays, and debris from the reaction. These walls would

have to be replaced quite often to maintain the integrity of the chamber. The HYLIFE-II chamber design, however, features a liquid lithium salt ( $\text{Li}_2\text{BeF}_4$ ) cascade, which protects the structure wall from x ray damage and debris. This liquid flows down from oscillating jets to form pockets around each imploding target. High-velocity neutrons emitted by the fusion reactions are absorbed by the fluid as it flows around the target. The heat gained from this absorption is then used to turn turbines and produce usable power. The neutrons react with lithium to produce tritium atoms according to the equation  ${}^7\text{Li} + n \rightarrow {}^4\text{He} + \text{T} + n$ . The tritium bred in the liquid lithium is an important source for the fuel since naturally occurring tritium is rare. The HYLIFE-II reactor was initially designed for heavy ion beam fusion. The ion beams would be pointed

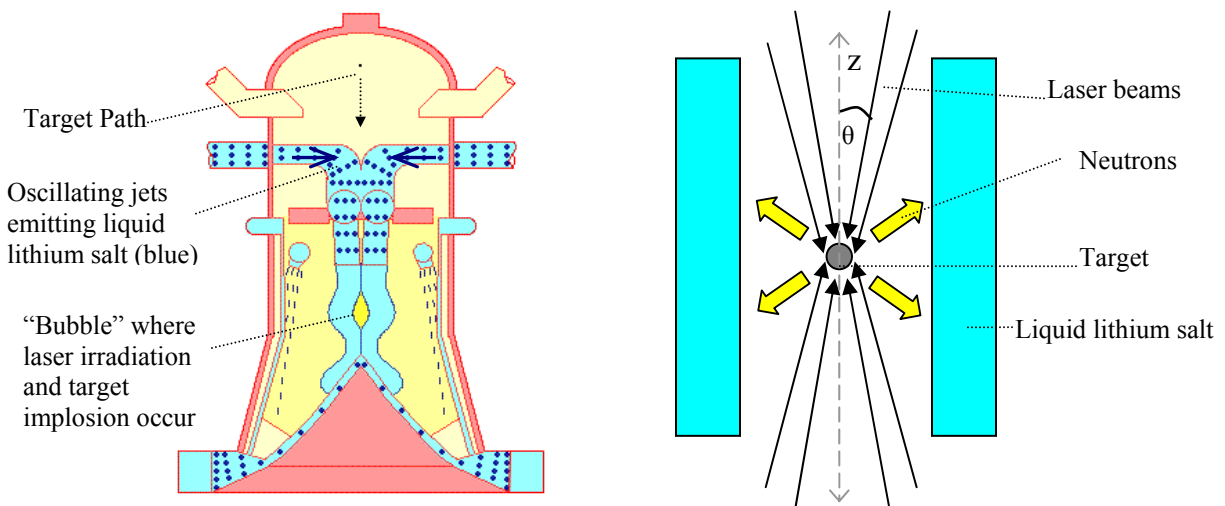


Figure 1.2: (a) Front view of HYLIFE-II reactor design. The target is injected from the top of the chamber and imploded while surrounded by the liquid. (from Ref. 5)

(b) Overhead view of the target while enclosed in lithium salt [perpendicular to Figure 1.2 (a)] Laser beams must enter with  $\theta \leq 20^\circ$ .

at the hohlraum that surrounds the target through a single, narrow aperture in the fluid. Since a narrow break in the fluid is needed for the ion beams to irradiate the hohlraum, only a small portion of the chamber would be unprotected by the liquid cascade.

Laser systems have been used extensively in fusion experiments, a significant advantage

over ion beam drivers. The use of lasers with the HYLIFE-II reactor has previously been considered impossible because the laser beam arrangement is restricted by the liquid lithium flow in the chamber. In order for the liquid to absorb at least 90% of the emitted neutrons, the laser beams must enter the pocket perpendicular to the direction of flow at angles of  $20^\circ$  or less from the central axis [figure 1.2 (b)]. Indirect-drive cannot be adapted to these requirements since current designs require laser beam angles of  $23^\circ$  to  $50^\circ$  to irradiate the interior walls of the hohlraum. This work explores the possibility of using direct-drive laser fusion on the HYLIFE-II reactor. The results show that this method has the potential to be very successful.

## 2. Polar Direct-Drive

The method of using direct drive from two opposing sides of the target, termed polar direct-drive (PDD), has been previously developed<sup>6-9</sup> for the National Ignition Facility (NIF). The NIF, set to be fully operational in 2010, is a 1.8 MJ neodymium-doped glass laser with four

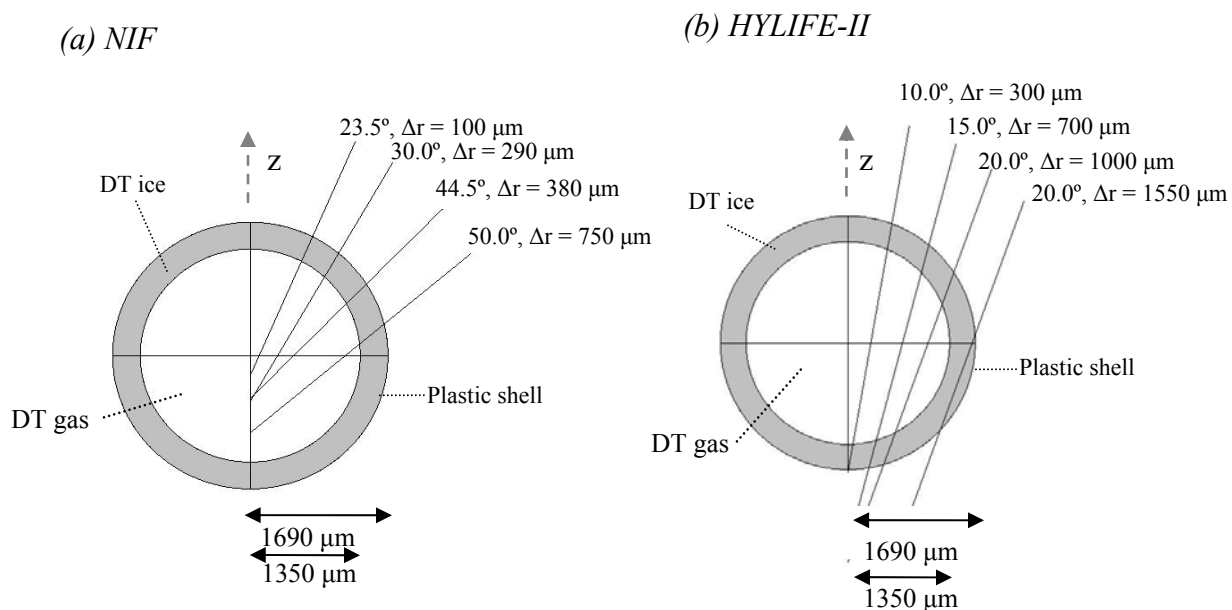


Figure 2.1 (a) Beam pointing arrangement for a direct-drive NIF design. (b) Initial beam pointing proposed for the HYLIFE-II design. Both designs use the same cryogenic DT target.

rings of laser beams that enter from the top of the target chamber and four rings symmetrically aligned on the bottom. The rings are arranged at angles of  $23.5^\circ$ ,  $30.0^\circ$ ,  $44.5^\circ$ , and  $50.0^\circ$  from the vertical [see Figure 2.1(a)] with relative energies of 4:4:8:8, respectively. This arrangement was constructed specifically for indirect-drive experiments, but a PDD design was developed to use the NIF for direct-drive implosions. In this design, beams are shifted away from the center of the target by amounts  $\Delta r$ , measured perpendicular to the laser path. This shift allows laser energy to be deposited evenly across the surface of the target, including the equatorial plane.

In contrast, it is difficult to balance the energy absorbed across the surface using the shallow laser beam angles required for the HYLIFE-II reactor. To explore this, a HYLIFE-II design [see figure 2.1(b)] was developed using the same target used on the NIF; thus the design can be compared to the PDD design for the NIF in order to analyze uniformity and implosion velocity. The target<sup>10</sup> used in these designs is comprised of a plastic (CH) shell surrounding a thick ( $340\ \mu\text{m}$ ) layer of deuterium-tritium (DT) ice and DT gas with a total diameter of  $3380\ \mu\text{m}$ . Targets are produced and maintained at cryogenic temperatures until injected into the reactor.

### **3. Design for HYLIFE-II Reactor**

The proposed design assumes a krypton fluoride (KrF) laser<sup>11</sup> power source. The KrF laser has the ability to allow multiple changes to beam shifting and focal spot shape during the pulse, a flexibility not currently available with glass lasers such as the NIF. Separate laser pulses are passed sequentially through apodizers, which shift the pointing and establish the spatial profile of each pulse. The shorter wavelength of the KrF laser also allows it to penetrate further into the imploding target than traditional glass lasers, thus increasing absorption.

The proposed laser arrangement features two symmetrical clusters of four laser beam

rings with angles of  $10^\circ$ ,  $15^\circ$ ,  $20^\circ$ , and  $20^\circ$ , respectively [see figure 2.1(b)] The intensity ratio for the four rings is 1.5:6:8:20. This design uses a 2.1 MJ KrF laser to achieve very similar results to the PDD design for the NIF, which uses 1.5 MJ of energy. The additional KrF energy is necessary to overcome the decreased absorption due to the oblique angle of some of the laser beams. These beams deposit energy in lower density plasma surrounding the target and the target is not able to absorb the laser energy effectively. Figure 3.1 shows the incident and absorbed power over time. The HYLIFE-II design only absorbs about 44% of the entire energy incident upon the target compared to the  $\sim 60\%$  absorption of the NIF design. Thus, more energy is required to ensure that the implosion takes place at the same rate. Changes to the beam shifting and focal spot shape are made at the times indicated in the figure to provide the maximum absorption and uniformity over short time intervals.

In PDD designs, laser beam pointing is shifted away from the center of the target in order to irradiate the shell uniformly, as shown in figure 2.1. The shifts are made by adjusting the locations of the apodizers at the front end of the laser system. Since the HYLIFE-II design

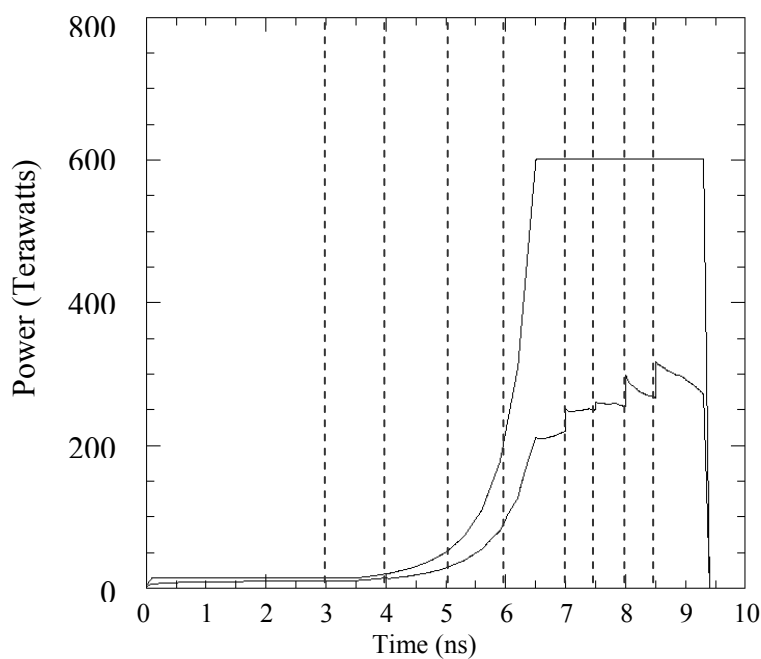


*Figure 3.1: Laser power incident on the target (top curve) and absorbed (bottom curve) over the course of the laser pulse. The dashed vertical lines represent times during the laser pulse when adjustments are made to beam pointing and focal spot shape.*

requires much shallower angles than the NIF design, the challenges of irradiating the target surface evenly are increased. It is necessary to alter the shifts many times during the laser pulse. Figure 3.2 illustrates the shifts made to the outer ring of laser beams. This ring moves in as the target implodes to ensure that the equator absorbs an effective amount of energy. If the original beam pointing were maintained, much of the outer laser beam energy would not irradiate the target shell but merely pass by the target at a later time, as shown by the dashed green line in figure 3.2 (b).

The intensity is assumed to be a generalized Gaussian proportional to  $\exp(-(r/r_0)^n)$  at radius  $r$  with  $n = 2.5$  (see figure 3.3). The  $r_0$  value affects the radius of the beam and is only altered in the outermost ring of beams from 1000  $\mu\text{m}$  to 900  $\mu\text{m}$ . Narrower beams, with lower  $r_0$  values, can be used when small portions of the target need to be driven in more. Wider beams, with larger  $r_0$  values, ensure an effective overlap of beams in the azimuthal ( $\phi$ ) direction. The ellipticity of the focal spot can also be adjusted, and is the primary means of reducing the size of the beams. The focal spot is compressed along the  $z$  axis to form varying degrees of ellipticity without affecting the radius in the  $\phi$  direction. As with the other variables, this is adjusted by the

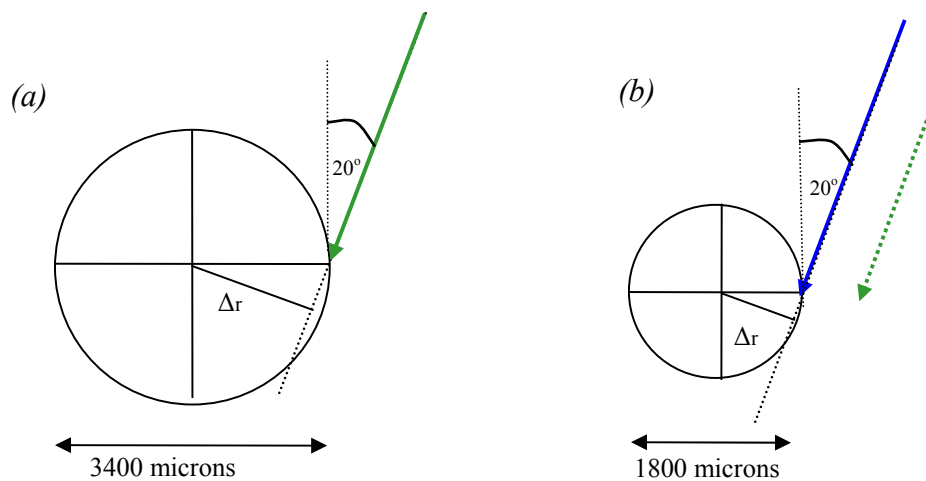
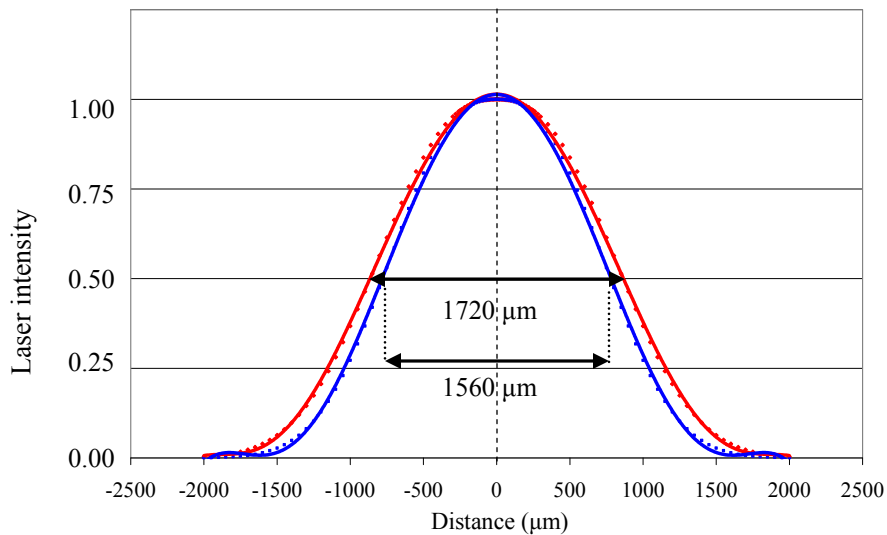


Figure 3.2 (a) Initial target and initial pointing of the outer laser beams. (b) Imploded target about 9 ns into the simulation with the new beam pointing (blue) and the original beam pointing (green).



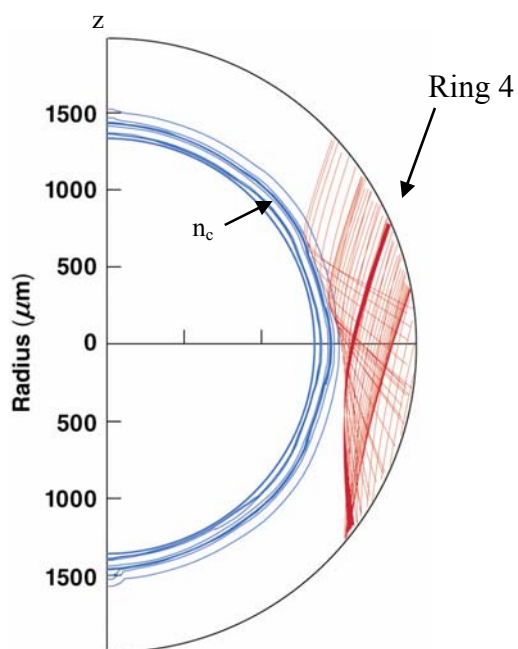
*Figure 3.3: Intensity of laser beam as a function of the distance from the center of the focal spot. The wider beam (red) has an  $r_o$  value of  $1000\ \mu\text{m}$  and the narrower beam (blue) has an  $r_o$  value of  $900\ \mu\text{m}$ .*

apodizers near the laser source. The laser beam specifications are found in the Appendix.

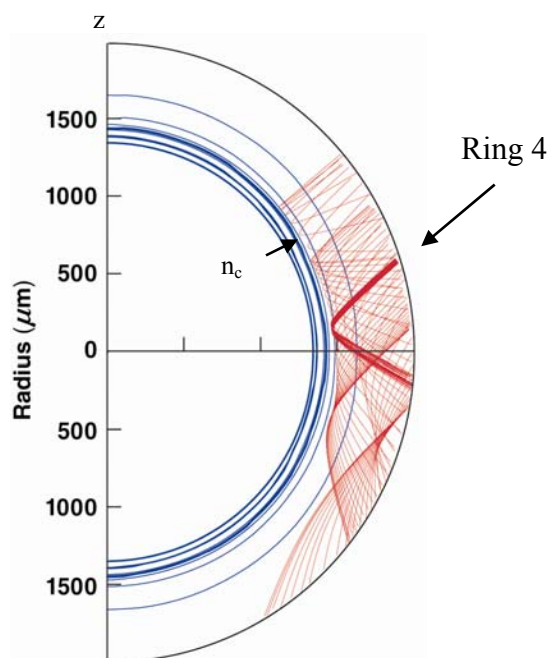
Figure 3.4 (a) shows density contours of the HYLIFE-II design at 5.8 ns. Laser rays from the outermost ring are also shown. The less oblique laser rays penetrate close to the critical density, the maximum density at which the laser beam can deposit energy. The more oblique rays deposit energy in the hot plasma surrounding the target. This energy cannot effectively drive the implosion of the target shell. There is an obvious weakness at the equator of the HYLIFE-II design due to this ineffective absorption of oblique rays. At about  $70^\circ$  from the pole, there is a region of the shell that experiences a higher velocity. This area absorbs energy effectively from the outer parts of laser beams pointed at the equator because these rays hit the surface more directly. Over time, this irregularity exacerbates the weakness at the equator. As the regions around the equator implode faster, mass is pushed toward the equator. The amount of energy deposited on the equator therefore needs to be increased over the course of the implosion to compensate for this increased mass.

Figure 3.4 (b) shows density contours at the same time for the NIF design. The outer ring hits the target at a much higher angle to the vertical axis ( $50^\circ$ ) and the equator implodes at a

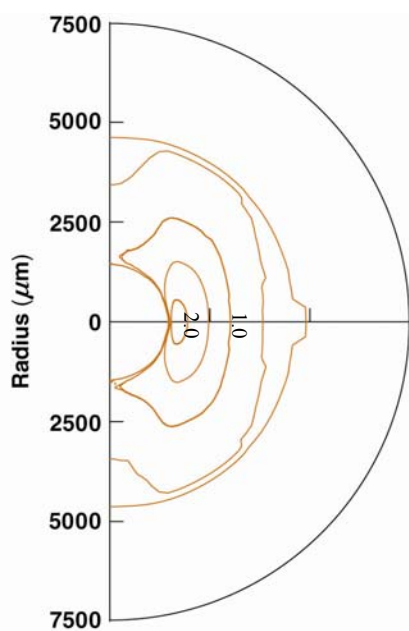
(a) HYLIFE-II: Density Contours (5.8 ns)



(b) NIF: Density Contours (5.8 ns)



(c) HYLIFE-II: Temperature Contours



(d) NIF: Temperature Contours

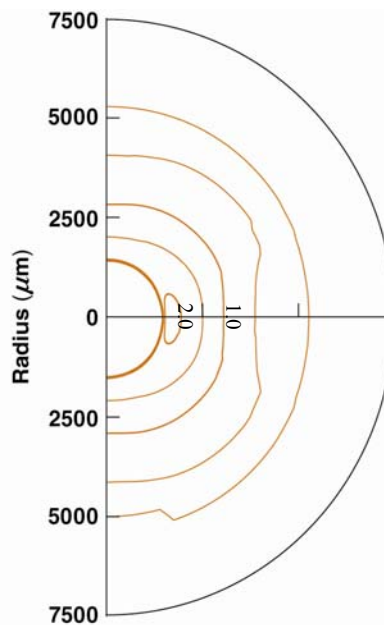
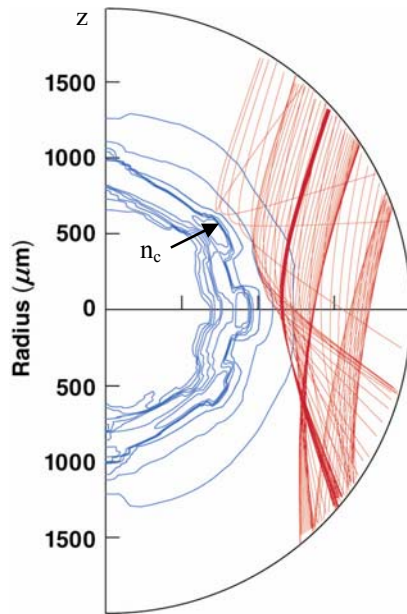


Figure 3.4: (a) Density contours of the HYLIFE-II target at 5.8 ns with rays from an outer laser beam. The critical density ( $n_c$ ), or the maximum electron density to which the laser can penetrate, is also shown. (b) Density contours of the NIF design at the same time. In these plots azimuthal symmetry about the  $z$  axis is assumed. (c) Temperature contour plot (keV) of the HYLIFE-II design at 5.8 ns. The maximum temperature is 2.5 keV. (d) Temperature contours of the NIF design with a maximum temperature of 2.1 keV.

(a) HYLIFE-II: Density Contours (9 ns)



(b) NIF: Density Contours (9 ns)

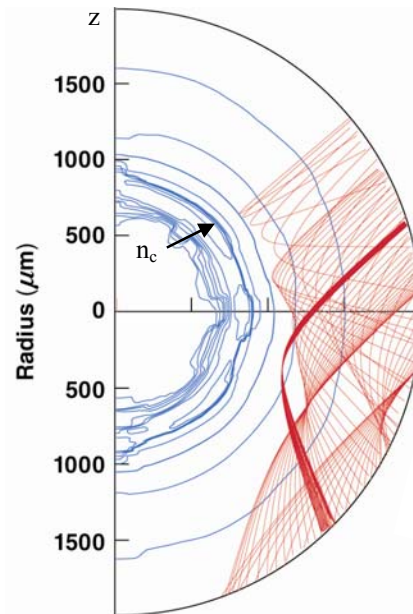


Figure 3.5: (a) Density contours of the HYLIFE-II design at 9 ns showing rays of the outer laser beam ring. Azimuthal symmetry is assumed about the  $z$  axis. (b) Same for the NIF design at 9 ns.

higher velocity at this point in the simulation. The overall uniformity is better than that of the HYLIFE-II design at this time.

The temperature contours [see figure 3.4 (c) and (d)] of the two designs are very similar; however, the HYLIFE-II design experiences a higher maximum temperature near the equator: 2.5 keV versus 2.1 keV for the NIF design. Both maxima occur very near the equator of the target; however, the HYLIFE-II design experiences a greater temperature difference between the poles and equator. Since hot plasma absorbs laser energy less efficiently, this high temperature further intensifies the nonuniformity at the equator on the HYLIFE-II design.

Density contours of the designs at 9 ns are shown in figure 3.5. The HYLIFE-II design maintains an approximately spherical shape as it implodes. There are three weak points in the

target where the mass has imploded slower than in adjacent regions, which mirror similar regions of nonuniformity in the NIF design [see figure 3.5 (b)]. In both designs, the target has imploded to about half its original size by this time.

Figure 3.6 shows the center of mass radius of the imploding shell as a function of angle  $\theta$  measured from the vertical pole ( $z$  axis) for the HYLIFE-II design at three times and the NIF design at 9 ns. The root-mean-square (rms) deviation of the radius is calculated by averaging the radius over the surface of the target. The deviation of the radius increases from  $7.1 \mu\text{m}$  at 5.8 ns to  $32 \mu\text{m}$  at 9 ns. Though the deviation at 9 ns is considerably higher than the NIF deviation of  $12.0 \mu\text{m}$ , it is small compared with the  $900 \mu\text{m}$  decrease in target radius. Both designs share similar weak points, specifically around the equator and at  $\theta \sim 60^\circ$  from the poles. These irregularities appear even at very early times and only intensify during the implosion.

Figure 3.7 shows the inward velocity of the target as a function of angle  $\theta$  for the HYLIFE-II and NIF designs, at the same times as figure 3.6. Consistent velocity across the

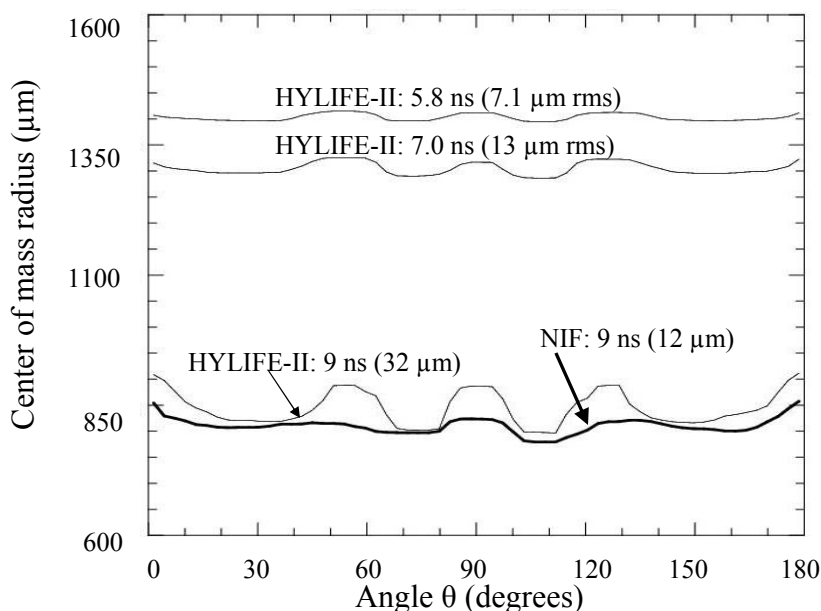


*Figure 3.6: The center of mass radius versus angle from the vertical pole. The average center of mass radius at 9 ns for the HYLIFE-II design is very similar to the NIF design at 9 ns (bold line).*

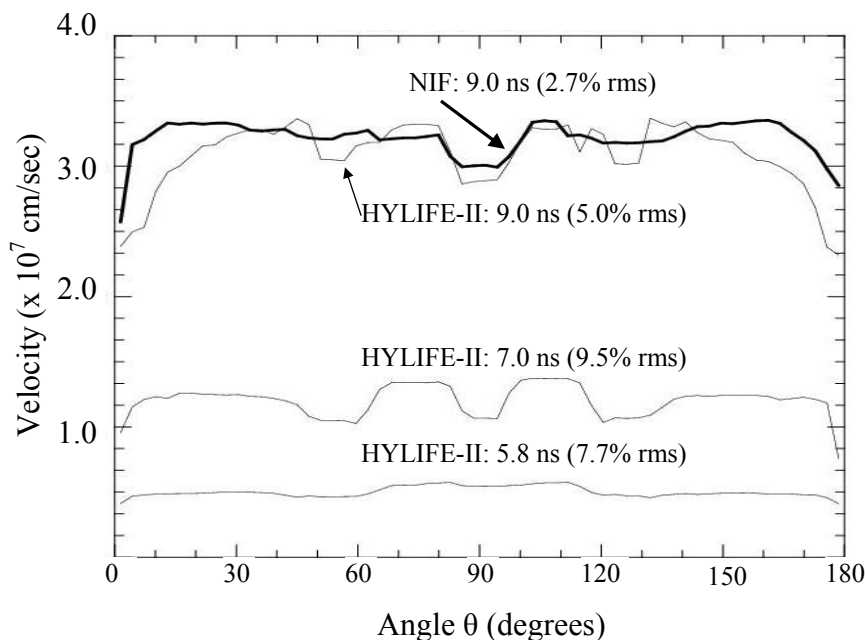


Figure 3.7: The average inward velocity of the imploding target versus angle  $\theta$  from the pole at the same times as figure 3.6. Velocity uniformity remains fairly good throughout the implosion and is comparable to that of the NIF design at 9 ns.

surface of the target demonstrates a balanced distribution of driving energy across the target shell. The average velocities of the two target designs near the end of the laser pulse are quite similar:  $3.1 \times 10^7$  cm/sec for the HYLIFE-II design and  $3.2 \times 10^7$  cm/sec for the NIF design at 9 ns. Though the 5.0% velocity rms for the HYLIFE-II design is higher than the 2.7% rms of the NIF design, some of this nonuniformity is due to slower implosion at the poles. With a few minor refinements to the design, this deficiency can probably be eliminated.

#### 4. Optimization

Over a thousand simulations were conducted using the hydrodynamics code SAGE<sup>12</sup> to develop this design for the HYLIFE-II reactor. The design was developed by optimizing each time interval successively by analyzing graphs such as Figures 3.6 and 3.7. Beam specifications for each interval would often produce good uniformity early in the interval that would deteriorate as time progressed, leading to the need to create the next interval. The optimized design requires nine time intervals. Fewer than nine intervals were found to lead to a sharp increase in shell

irregularities. Figure 4.1 shows a comparison between the uniformity at 5.8 ns of the optimized design and a similar design with one less time interval. The unoptimized design, produced by delaying a large move of the third ring of laser beams for a nanosecond, yielded a very nonuniform implosion.

Figure 4.2 shows the degree to which beam shifting and focal spot shape are changed on two different beams. The pointing shift of the outermost ring is shown in figure 4.2 (a). As the target implodes and the core compresses, the outer ring of laser beams shifts often to maintain its focus on the equator. This ring moves from an initial position of 1550  $\mu\text{m}$  from the center of the target to 900  $\mu\text{m}$  at 9 ns. Larger changes are made at later times in the pulse when the target is imploding at a higher velocity and becomes more sensitive to pointing changes.

Figure 4.2 (b) shows the increasing ellipticity of the laser beams in the third ring. Circular focal spot shapes are used at early times so that the overlapping of multiple beams can

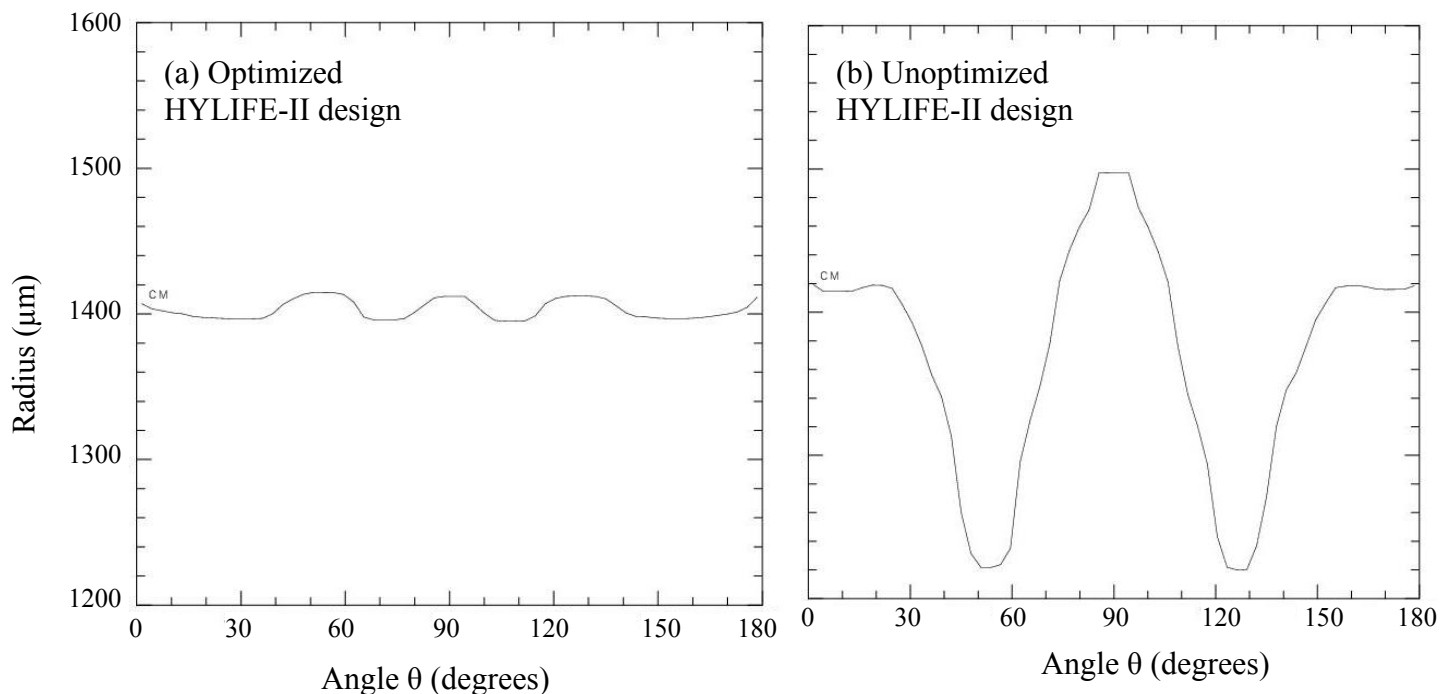


Figure 4.1: (a) Center of mass radius as a function of  $\theta$  at 5.8 ns for the HYLIFE-II design. (b) Center of mass radius for the same time using one less time interval.

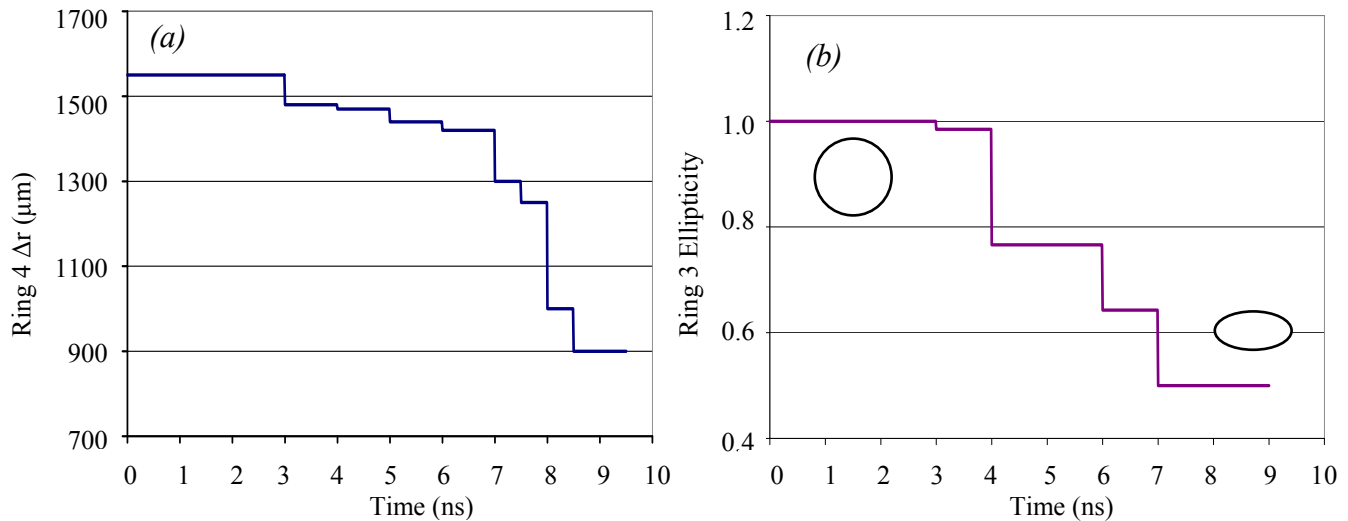


Figure 4.2: (a) Beam shifts of the outermost laser beam ring over the course of the laser pulse. (b) Ellipticity (b:a ratio) of the focal spots of ring 3 beams as a function of time. The insets show visual representations of the initial shape (circular) and final shape (elliptical).

smooth out the energy deposition across the surface of the target. At later times, however, beam shapes flattened in the z direction are required. Beams in the second and third ring require the most adjustment to the focal spot shape as the target implodes. The outermost laser beam ring maintains a very elliptical spot in order to concentrate energy on a narrow band around the equator, while inner beams, in general, have a more circular spot shape.

## 5. Conclusions

A laser-driven target design suitable for the HYLIFE-II reactor was developed using hydrodynamic simulations. The level of flexibility offered by a KrF laser allows adjustments to beam shifting and focal spot shape over several intervals throughout the course of the laser pulse. By adjusting these parameters, a design was developed in which the target implodes to half its original radius with a velocity root-mean-square nonuniformity of 5.0%.

Further explorations are required to develop an ideal configuration. Many possible variables were not explored extensively, such as different laser beam angles within the 20° limitation, the number of laser beam rings, and the n parameter affecting the focal spot shape. Simulations can be conducted with different beam shapes, such as crescent-shaped focal spots. By adjusting the width and curvature of these shapes, the laser beam can wrap around the equator for more effective irradiation and absorption. A ring-shaped beam with the ring diameter approximately equal to the target diameter would also be a possible solution. This shape would provide very uniform irradiation in the  $\phi$  direction around the equator. This beam could be pointed directly along the axis of the target, thus falling well within the constraints of the reactor geometry.

Although nonuniformities in the imploding shell were not eliminated, this work shows the viability of using lasers to drive fusion reactions in the HYLIFE-II reactor. Previously, it was not considered plausible to consider a laser-driven design because the reactor requires laser beam angles of 20° and less. The initial design shows great promise for laser-driven fusion on HYLIFE-II, and it will serve as the foundation for future such designs for this reactor.

## **6. Appendix**

Specifications of the three key parameters of the HYLIFE-II design are presented in Table 6.1 with the time at which each group of variables is initiated. Each ring of beams maintains a specific angle to the central axis (z) of the target throughout the irradiation. Beam shifts, denoted by  $\Delta r$ , are measured from the center of the target perpendicular to the trajectory of the rays. The focal spot intensity is assumed to be proportional to  $\exp(-(r/r_0)^n)$  where  $n = 2.5$ . The  $r_0$  value affects the width of the focal spot, and is maintained at a moderately large value to

ensure adequate overlapping of focal spots in the azimuthal direction around the target shell.

The ellipticity ( $\varepsilon$ ) is the b:a ratio of the focal spot, with b indicating the height of the focal spot produced by compressing the spot vertically.

*Table 6.1: Specification of the HYLIFE-II design presented in this report. Each change in parameter settings occurs at the time listed and is maintained until the next indicated change. ( $r_o$  = beam radius,  $\varepsilon$  = ellipticity,  $\Delta r$  = beam shift.) All distances are in  $\mu\text{m}$ .*

Time (ns)	Beam 1: $10^\circ$ ( $r_o = 1000 \mu\text{m}$ )		Beam 2: $15^\circ$ ( $r_o = 1000 \mu\text{m}$ )		Beam 3: $20^\circ$ ( $r_o = 1000 \mu\text{m}$ )		Beam 4: $20^\circ$ ( $\varepsilon = 0.42$ )	
	$\Delta r$	$\varepsilon$	$\Delta r$	$\varepsilon$	$\Delta r$	$\varepsilon$	$\Delta r$	$r_o$
0.0	-300	1.00	-700	1.00	-1000	1.00	-1550	1000
3.0	-300	1.00	-600	1.00	-800	0.98	-1480	1000
4.0*	-300	1.00	-750	0.98	-1460	0.77	-1470	1000
5.0	-300	1.00	-750	0.87	-1450	0.77	-1440	1000
6.0	-200	0.99	-750	0.97	-1410	0.64	-1420	1000
7.0	-200	0.94	-720	0.77	-1310	0.50	-1300	1000
7.5	-200	0.94	-720	0.77	-1270	0.50	-1250	1000
8.0	-650	0.87	-1060	0.77	-1020	0.50	-1000	1000
8.5	-50	1.00	-650	0.87	-900	0.50	-900	900

\* This time interval was eliminated for the unoptimized HYLIFE-II design used for figure 4.1 (b).

There are noticeable discontinuities in some of the parameters, especially the shifting of the second ring of laser beams in the interval starting at 8 ns. While the parameters in Table 6.1 provided reasonable uniformity, a more continuous alternative could probably be found.

## 7. Acknowledgements

I would like to thank my advisor Dr. R. Stephen Craxton for generously sharing his time, expertise, and enthusiasm, as well as Alexandra Cok for her valuable guidance and encouragement. I would also like to thank Dr. Craxton and the entire Laboratory for Laser Energetics for providing this wonderful research opportunity.

## 8. References

1. D. Callahan, *et al.*, “Advances in Target Design for Heavy Ion Fusion.” *Plasma Phys. Control. Fusion* **47**, B379 (2005).
2. J. Nuckolls, *et al.*, “Laser Compression of Matter to Super-High Densities: Thermonuclear (CTR) Applications,” *Nature* **239**, 139 (1972).
3. R.W. Moir, “HYLIFE-II Inertial Fusion Energy Power Plant Design,” *Fusion Technology* **25**, 1475 (1992).
4. R.W. Moir, *et al.*, “HYLIFE-II: A Molten-Salt Inertial Fusion Energy Power Plant Design – Final Report,” *Fusion Technology* **25**, 5 (2004).
5. F. Peterson, “Target Chambers for Inertial Confinement Fusion”, (University of California Berkeley Department of Nuclear Engineering, Berkeley, CA, 1998), <http://www.nuc.berkeley.edu/thyd/icf/>
6. S. Skupsky, *et al.*, “Polar Direct Drive on the National Ignition Facility,” *Phys. Plasmas* **11**, 2763 (2004).
7. R.S. Craxton, *et al.*, “Polar Direct Drive: Proof-of-Principle Experiments on OMEGA and Prospects for Ignition on the National Ignition Facility,” *Phys. Plasmas* **12**, 056304 (2005).
8. R.S. Craxton and D.J. Jacobs-Perkins, “The Saturn Target for Polar Direct Drive on the National Ignition Facility,” *Phys. Review Letters* **94**, 095002 (2005).
9. J.A. Marozas, *et al.*, “Polar-Direct-Drive Simulations and Experiments,” *Phys. Plasmas* **13**, 0563311 (2006).
10. P.W. McKenty *et al.*, “Analysis of a Direct-Drive Ignition Capsule for the National Ignition Facility,” *Phys. Plasmas* **8**, 2315 (2001).

11. J.D. Sethian, *et al.*, “Electron Beam Pumped KrF Lasers for Fusion Energy,” *Phys. Plasmas* **10**, 2142 (2003).
12. R.S. Craxton and R.L. McCrory, “Hydrodynamics of Thermal Self-focusing in Laser Plasmas,” *Journal Appl. Phys.* **56**, 108 (1984).

# **Development of an Ontology for the OMEGA EP Laser System**

**Richard Marron**

*Development of an Ontology for the OMEGA EP Laser System*

**Richard C. Marron**

Allendale Columbia School

Rochester, New York

Advisor: Richard Kidder

**Laboratory for Laser Energetics**

University of Rochester

Rochester, New York

February 2006

## **Abstract**

An ontology is a working model of objects and relationships in a particular domain of knowledge. It can allow a computer to infer relationships between separate objects. There are several different types of relationships: transitive, symmetrical, inverse and functional. The use of these relationships together allows a complex ontology to be created, an ontology that a computer can infer knowledge from. Using these relationships an ontology could understand that if all Chardonnay comes from France, and a particular wine is a Chardonnay, then this wine must be from France.

The base for a laser system ontology was created to allow a computer to understand that if the beam passes through one object in the beam path it will then pass through the next object. These relationships are the building blocks for the ultimate goal of a semantic web. This semantic web will allow a user to ask a question about the laser systems, and the service will be able to answer this question. This will eliminate the tedious search process through documents to find small hidden facts.

## **I. Introduction**

The ultimate goal of an ontology is to create a system for storing and searching data, a single uniform repository for all data used at the Laboratory for Laser Energetics (LLE). LLE currently has an extensive database system with vast amounts of information. This data is stored in many complex repositories in many different formats ranging from Word documents to schematics to

spreadsheets. These repositories are difficult to navigate without previous experience in the particular database. The current databases are the Project Data Management (PDM) database and the Oracle Database. The PDM system can be navigated in three ways: a hierarchy of links, specifying the range of the documents viewed, a Google search bar, or a serial code. The document can then be viewed in PDF format. The Oracle Database is simply a series of tables with information relevant to shot operations [1]. The ontology would unify these databases into one.

This system would not only contain the information represented by the text documents, the spreadsheets, and the images, but also the information coded for in the ontology itself, and this information coded into the ontology would not only be information but would be knowledge. The key difference between information and knowledge is that knowledge contains relationships defining how the elements combine and work together. Knowledge can allow new information to be inferred creating a dynamic wealth of data, while information alone can only be understood as it is.

Once one has created an ontology, and therefore a knowledge base, the possibilities are endless. Some possible applications relevant to LLE are question-answering systems that produce "knowledgeable" answers, applications to determine the current path of a beam line and provide information relevant to the beam line, and applications to display shot data in a more efficient manner.

## **2. Process**

### **2.1. Know the Application**

The future functions of the ontology determine the necessary structure. In order to determine the information and the relationships that must be put into the ontology the final applications must be known and carefully analyzed [3]. There is too much information relevant to LLE for all of it to be coded into the ontology, and therefore, it must be reduced to information relevant to the application at hand. If one were creating an ontology solely for the purpose of determining the beam path, information regarding the requirements of the UV calorimeter would be irrelevant. However if one were creating an application for question answering regarding the diagnostic tables this information would be relevant and should be included in the ontology. While it is the relationships between the information that makes an ontology special, the base of information defines the applications that it can be used for.

Knowing the future applications before starting the ontology is also necessary in determining the proper relationships to include. Relationships between components of the laser system such as `beamGoesTo`, which defines where the beam goes immediately after leaving a component, can be used in the application determining beam path. However, a relationship between components such as `hasDiagnostic`, which determines which diagnostics are branched off a component, would not be relevant to simply determining the beam path [3].

## **2.2. Individuals**

Once the applications are determined, the creator of the ontology must determine which objects to include. The objects will be known as individuals. They are anything that can be seen or touched; in essence, anything that exists[4]. The Short Pulse Highly Reflective Mirror 2 is considered an individual; however, a short pulse mirror in general is not considered an individual but rather a class. Once all of the individuals that will be included in the ontology have been determined, choosing the proper class structure for the ontology is the next step.

## **2.3. Classes**

Classes can be anything conceptual, anything that cannot be felt [4]. A good way of determining whether an object would be a class or an individual is if one would refer to the object using the article “a” or the article “the.” When the article “a” is used to describe the object it is normally a general term, known as a class, under which an individual would fall. When the article “the” is used it is normally a specific object that exists and therefore an individual. The class system is important as it is used to determine the basic hierarchy of the ontology. An ontology is based off a tree of “is a” relationships. These relationships are crucial to the function of the ontology as they provide a map for the ontology, a static structure that allows specific objects to be located. Figure 1 displays a portion of the class hierarchy for the ontology that was created for the EP laser system.



Figure 1. A portion of the class structure for LLE's Ontology, each line representing an "is a" relationship.

Inside each class are a series of individuals that are a part of the class. For example, the sixth short pulse highly reflective mirror would be located in the class "short pulse highly reflective mirrors."

## 2.4. Properties

After both the individuals and the classes have been determined and essentially the basic structure of the ontology is complete, the properties of the objects must be determined. These properties are what change the ontology from information to knowledge. They represent the relationships that each object has with each other. There are four separate types of relationships between objects; they are inverse, transitive, symmetrical, and functional [4]. Depending on the type of relationship, it will behave differently.

### 2.4.1. Inverse Relationships

If a property is an inverse property, it will have a corresponding property that is its inverse [4]. A common example of an inverse relationship is a father-son relationship. If John is Billy's father, and the computer knows that father and son are both corresponding inverse relationships, then it can infer that Billy is John's son. This type of a relationship would apply to LLE in the situation of the beamGoesTo and beamComesFrom

relationships. If the computer knows that after the Third Infrared Highly Reflective Mirror the beam goes to the First Tile Grating Assembly through the use of the beamGoesTo relationship, then the computer can infer that the beam came from the Third Infrared Highly Reflective Mirror before hitting the First Tile Grating Assembly (Fig. 2).

This inference can be made based on the inverse

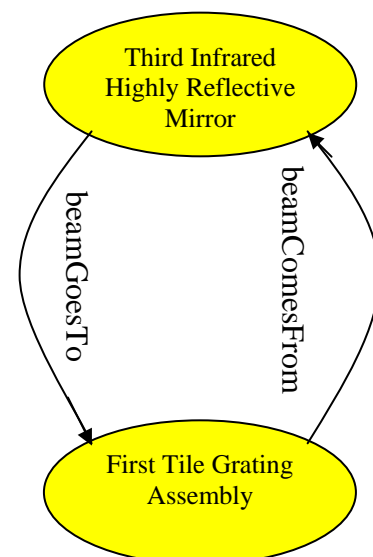


Figure 2. Diagram of an inverse relationship

description of the beamGoesTo and beamComesFrom relationships.

#### 2.4.2. Transitive Relationships

If property P is transitive, and property P is applied between object a and object b and property P is applied between object b and object c, then it can be inferred that property P also relates object a to object c [4]. A common example of a transitive property is the property relatedTo. If Joan is related to Paul and Paul is related to Joe, then it can be inferred that Joan is related to Joe. This can be used in the ontology for LLE with the relationship

beamGoesTo. If the beam comes from the OPCPA output spatial filter and then goes to the short pulse apodizer and then goes to the apodizer output spatial filter, the computer can infer that after the beam goes through the OPCPA output spatial filter it will later go to the apodizer output spatial filter (Fig. 3).

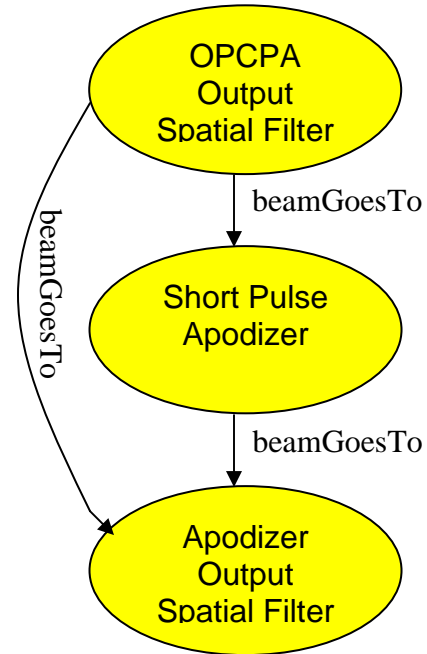


Figure 3. A diagram representing a transitive relationship. The computer inferred the relationship on the far left.

#### 2.4.3. Symmetrical Relationship

If property P is symmetrical, and property P relates object a to object b, then property P also relates object b to object a [4]. A common example of a symmetrical property is the sibling relationship. If Andy is Dale's brother, then Dale must be Andy's brother. This can be used in the ontology for LLE with

the relationship isNextTo. If the Discrete Zoom Spatial Filter is next to the Periscope to the Laser Bay, and the isNextTo relationship is symmetrical, then it can be inferred that the Periscope to the Laser Bay is next to the Discrete Zoom Spatial Filter (Fig. 4).

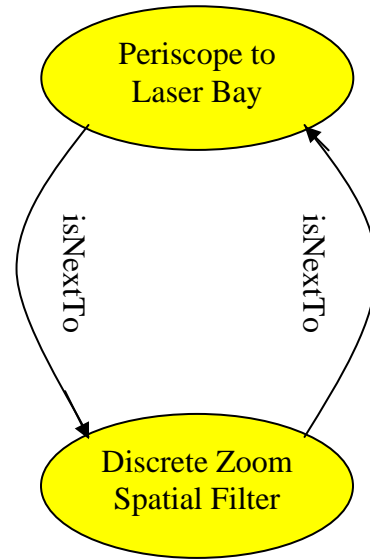


Figure 4. Diagram of a symmetrical relationship

**2.4.4. Functional Relationship**

If property P is functional, and property P relates object a to object b, then object a is related to no other object besides object b by property P [4]. A common example of a functional relationship is the birth mother relationship. If Jane is Dan’s birth mother, it can be inferred that all other individuals are not Dan’s birth

mother. However, if Janine is also described as Dan’s birth mother then it can be inferred that Jane and Janine are the

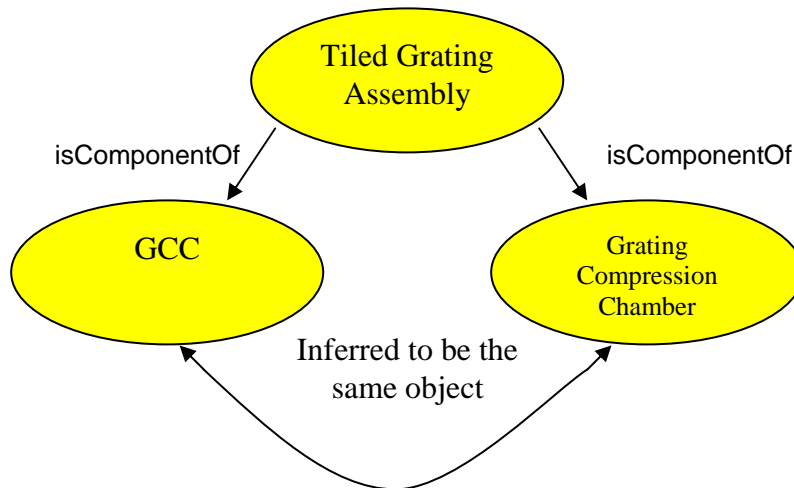


Figure 5. Diagram of a functional property and how it can help the computer infer relationships.

same person. A Functional relationship can be implemented in LLE's ontology in the relationship `isComponentOf`. If the tiled grating assembly is a component of the grating compression chamber and the GCC, it can be inferred that the grating compression chamber and the GCC are the same (Fig. 5).

## 2.5. Domain and Range of Relationships

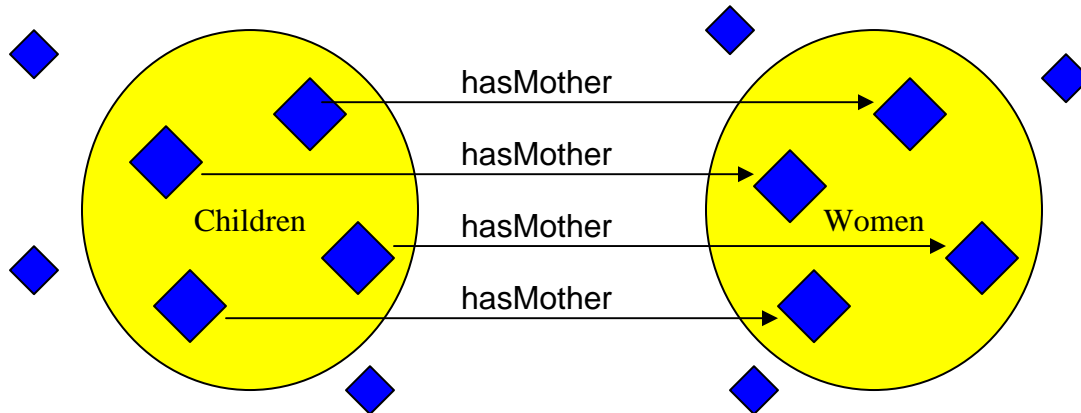


Figure 6. Illustration of the property `hasMother` with the domain children and the range women. The property can only be applied between objects in the domain and range.

The domain and ranges of a relationship must also be determined. This will stop the computer from making incorrect inferences. A property links an object from the domain to an object in the range [4]. A common example of this practice can be seen in the relationship `hasMother` (Fig. 6). If the domain of the relationship `hasMother` is all children and the range of the relationship `hasMother` is all women, then the computer will know not to infer that Dan has Bill as a mother.

While these properties are quite basic, they allow the computer to make these important inferences that are necessary to change the data represented from information to knowledge that can be understood by a computer. A computer is thus allowed to infer its own information.

## 2.6. Restrictions

After the applications, individuals, classes, and relationships for the ontology have been determined, the next step in the creation of the ontology is determining the proper restrictions on the classes. Restrictions restrict which individuals can be forced or inferred into the class. They have three basic components: the restriction type, the property and the filler. There are three basic categories of restriction types: quantifier restrictions, cardinality restrictions, and hasValue restrictions.

### 2.6.1. Quantifier Restrictions

Quantifier restrictions regulate what must be inside a class. There are two types of quantifier restrictions: an existential quantifier and a universal quantifier [4]. The existential quantifier can be thought of as an “at least one” restriction [4]. For example, if the existential quantifier is applied to a class with the property beamGoesTo and the filler short pulse highly reflective mirror, then for an object to be part of the particular class it must send the beam to at least one short pulse highly reflective mirror.

The universal quantifier is very similar. However, it is an “all” restriction [4]. If the universal quantifier is applied to a class with the property beamGoesTo and the filler short pulse highly reflective mirror, then for an object to be a part of the particular class it must send the beam to only short pulse highly reflective mirrors.

### 2.6.2. Cardinality Restrictions

Cardinality Restrictions regulate how many objects can satisfy a certain property. A minimum cardinality restriction sets a minimum number of times that an object must satisfy a property to be considered a part of the class [4]. An example of this would be in the class beam splitter. There is a minimum cardinality restriction stating that an object must go to two or more other objects to be considered a beam splitter.

A maximum cardinality restriction sets a maximum number of times that an object can satisfy a property and still be considered a member of the specific class [4]. An example of this would be in a class such as a nonBeamSplitter in which a maximum cardinality restriction of one would be placed on the beamGoesTo property with the filler as the class component. This makes sure that the beam does not split after leaving the object.

An exact cardinality restriction sets an exact number of times that an object can satisfy a property and still be considered a member of the specific class [4]. An example of this would be in the class beamTerminator in which an exact cardinality restriction of zero would be placed on the beamGoesTo property with the filler as the class component. This restriction would state that in order for a component to be in the class beamTerminator it must not reflect the beam to another component.

### 2.6.3. HasValue Restrictions

HasValue restrictions are very similar to quantifier restrictions. However, instead of having the filler be a class the filler is an individual [4]. An example of

this occurs in the class OMEGA backlighter OAP. The hasValue restriction allows us to state that if the object is a member of the class OMEGA backlighter OAP then it must come from the sixth short pulse highly reflective mirror.

These restrictions all display a necessary condition that an object must comply with in order to be a member of the class. There is another type of restriction that can be placed on these classes and that is a necessary and sufficient condition. These conditions state that if an individual satisfies the condition then it will be inferred into the class and treated as if it were a forced member of the class [4].

## **2.7. Programs**

After the applications, individuals, classes, relationships, and restrictions have all been determined, the next step is to code for the ontology. An open source program exists that provides a convenient interface, eliminating the need for actually coding the ontology. This program is Protégé. It is very well documented and has a useful support forum for any questions. This program encodes the ontology in a Web Ontology Language (OWL). OWL is an extension of the language RDF [1].

With this program one can apply the planned ontology and connect the individuals through the relationships. This is a very tedious task and the computer will infer some of the relationships. However there are still many relationships that the computer cannot infer such as the beamGoesTo relationship, which must be manually applied.

## **2.8. Applications**

The next step is creating the applications previously determined. This can be accomplished using Java and the Jena Library. [2] The Jena Library provides many very useful classes and methods that allow one to navigate the ontology, extract information, and manipulate the ontology. All of these actions are necessary to create an application that fully uses the powers of an ontology.

## **3. Discussion**

Currently the applications of the ontology are limited by technology. The logic proof and trust layers of the semantic web are all under research. Once these layers are completed the applications of an ontology are endless. Applications such as natural language question answering will then be in reach. However, all of the future implementations are dependent on having an extensive ontology ready when the technology catches up.

One problem that is posed is if we do not understand the future applications of the ontology how can we create a good ontology at the moment? The answer to this question is that we can not be sure that we are creating a suitable ontology for future applications; however, if we create an ontology for current applications, there is a very good chance that there will be overlap and portions of the already created ontology will be useful in future applications.

Currently the use of the ontology could be supplemented by other technologies such as an Oracle database. However, the benefit to using an ontology over an Oracle database is not what it can do now, but rather it is what the ontology will be able to do in the future.

#### 4. Acknowledgements

I would like to thank Richard Kidder, Daniel Gresh, Adam Kalb, Collin Kingsley, and Thang Nyugen for helping me with my questions regarding the laser system and ontologies. I would also like to thank Stephen Craxton for giving me this wonderful opportunity to work at the Laser Lab this past summer.

#### 5. References

1. D. Gresh. "Implementing a Knowledge Database for Scientific Control Systems." 2006. <[http://www.lle.rochester.edu/pub/HS\\_reports/2006/Gresh\\_Dan.pdf](http://www.lle.rochester.edu/pub/HS_reports/2006/Gresh_Dan.pdf)>
2. D. Gresh, private communication.
3. H. Chen. "My Experience in Building Ontology-driven Applications." eBiquity Group Meeting. PowerPoint. February 9, 2004 <[ebiquity.umbc.edu/get/a/resource/15.ppt](http://ebiquity.umbc.edu/get/a/resource/15.ppt)>.
4. M. Horridge et al. "A Practical Guide To Building OWL Ontologies Using The Protégé-OWL Plugin and CO-ODE Tools Edition 1.0." The University Of Manchester, August 27, 2004. <<http://www.coode.org/resources/tutorials/ProtegeOWLTutorial.pdf>>

# **Thermal Conductivity of Cryogenic Deuterium**

**Alan She**

# *Thermal Conductivity of Cryogenic Deuterium*

Alan She

Pittsford Mendon High School  
Pittsford, NY

Advisor: Dr. R. S. Craxton

Laboratory for Laser Energetics  
University of Rochester  
Rochester, NY

November 2007

## Abstract

Accurate values of the thermal conductivity and specific heat of deuterium are necessary to make high quality cryogenic laser fusion targets. Due to the difficulty of measuring these values at cryogenic temperatures, the “3 $\omega$ ” method is used. This involves passing an oscillating current through a platinum wire embedded in deuterium and measuring the third-harmonic voltage that results from the temperature dependence of the resistance. A two dimensional model has been built that calculates heat flow in both the axial and radial directions (i.e., along and perpendicular to the wire) including the frequency-dependent skin depth. The model has been fit to four sets of experimental data (the wire in a vacuum and in gaseous, liquid, and solid deuterium) by adjusting the parameters of thermal conductivity and specific heat. Generally, the model and data agree well. The model has enabled the thermal conductivity to be accurately determined at cryogenic temperatures for gaseous, liquid, and solid deuterium.

## 1. Introduction

The thermal conductivity of deuterium is used in the modeling of cryogenic laser fusion targets. In this process, a small fuel pellet, consisting of a mixture of deuterium and tritium, is heated and compressed by high-energy laser beams. This creates conditions similar to those of the Sun, allowing the nuclear fusion of deuterium and tritium to occur through the reaction



Energy is released in the form of the kinetic energy of the resulting neutron. The fuel pellet is initially kept at cryogenic temperatures to maximize the amount of fuel in the small volume.

Knowledge of the thermal conductivity of deuterium is necessary for modeling the heat flow within the target.<sup>1</sup> Knowing the conductivity to better precision improves target quality. The conductivity is also used in modeling the behavior of the target when exposed to the environment.

Initially, the target is covered by a “shroud” to protect it from the environment. Immediately before the laser shot, the shroud is quickly removed. It is of interest to model what happens in the interval between the removal of the shroud and the shot, such as the rate of increase of pressure in the center of the target due to the conduction of heat resulting from external radiation.

In 1954, early measurements of the thermal conductivity of deuterium were made by Powers.<sup>2</sup> The setup was of the parallel plate type, where heat was deposited at a known rate at one end of a cylinder containing deuterium and exited through a heat bath at the other end. The temperature gradient across the cylinder was measured by a multiple-junction-difference thermocouple. The experiment was prone to errors including heat flow into the walls (requiring correction), convection due to the geometry of the setup, and lack of symmetry from the intrusion of measurement devices.

First introduced by Cahill<sup>3</sup> in 1986 and subsequently used by various authors,<sup>4,8</sup> the  $3\omega$  method measures thermal conductivity in a geometry where the avenues of heat flow are simpler to accommodate than in previous methods. There is also less susceptibility to convection. The method uses a wire or thin film as both a heater and a thermometer to produce and measure temperature oscillations in a chosen medium.

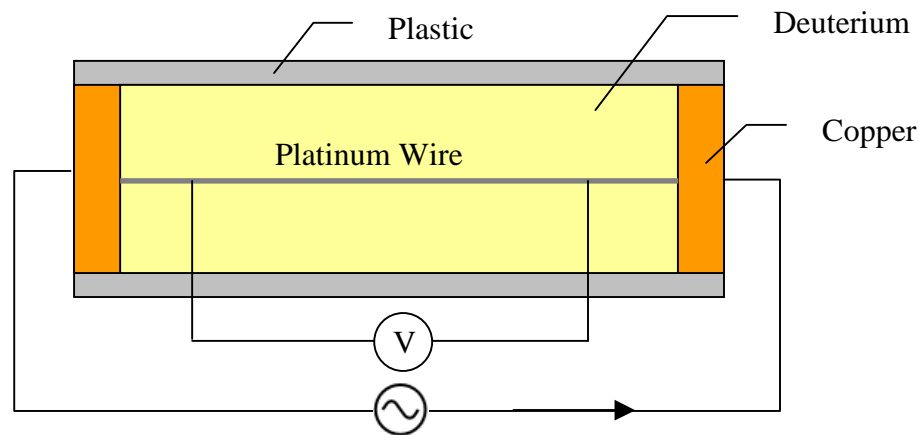


*Figure 1.1* Diagram of the experiment. An oscillating current is passed through the wire, and the voltage across a portion of the wire is measured. The plastic and copper are heat baths.

In recent experiments,<sup>9</sup> the  $3\omega$  method was used to determine the thermal conductivity of cryogenic deuterium. As indicated in Figure 1.1, a platinum wire is embedded in deuterium. A sinusoidal current through the wire deposits heat into the system. Heat exits the system by the heat baths, which are set at the desired temperature. The time-averaged thermal equilibrium of the system (“steady state”) is established after a brief interval, after which the voltage across a portion of the wire is measured. The temperature dependence of the resistance of the wire results in a small third-harmonic voltage, which has both in-phase and out-of-phase components with respect to the phase of the power. It is possible to determine the oscillatory temperature from this voltage. The temperature is out of phase with the oscillating power at high drive frequencies and in phase in the limit as the frequency approaches zero.

A computer program was built to model this experiment. The model accounts for the two-dimensional (2D) geometry of the experiment (there is thermal conduction parallel and perpendicular to the wire). It has been used to determine the significance of the 2D effects and to provide improved accuracy over the one-dimensional (1D) numerical solutions, which ignore heat flow along the wire, that were previously used to model experiments.<sup>10</sup> By matching the predicted temperature amplitudes of the program to the experimental data, the thermal conductivities of solid, liquid, and gaseous deuterium have been determined.

## 2. Analysis of the $3\omega$ Method

This section shows how the amplitude of the temperature oscillations in the wire can be determined from the experimentally obtained voltages.

The resistance of the wire changes with the temperature  $T$ :

$$R = R_0 + \alpha(T - T_0), \quad (2-1)$$

where  $R_0$  is the resistance at temperature  $T_0$  and  $\alpha$  is a constant ( $\alpha = dR/dT$ ).

The sinusoidal current applied to the wire can be expressed in complex form:

$$I(t) = I_{0s} \sin(\omega t) + I_{0c} \cos(\omega t) = \frac{1}{2} [\tilde{I} e^{i\omega t} + \tilde{I}^* e^{-i\omega t}], \quad (2-2)$$

where  $\tilde{I}$  is complex and  $\tilde{I}^*$  indicates its complex conjugate. Generally,  $I_{0s} = 0$  and  $\tilde{I}$  is real. The temperature has a steady time-averaged component,  $T_1(t)$ , and real and imaginary components that are in phase and out of phase with the power, respectively:

$$T(t) = T_1(t) + \frac{1}{2} [\tilde{T} e^{2i\omega t} + \tilde{T}^* e^{-2i\omega t}]. \quad (2-3)$$

The temperature oscillates at the second harmonic, since the power,  $P = I^2 R$ , brings in  $e^{2i\omega t}$  terms from (2-2). Using (2-1) to (2-3), the voltage across the wire is

$$V(t) = I(t)R(t) = \frac{1}{2} [\tilde{I} e^{i\omega t} + \tilde{I}^* e^{-i\omega t}] \left\{ R_0 + \alpha \left[ T_1(t) + \frac{1}{2} [\tilde{T} e^{2i\omega t} + \tilde{T}^* e^{-2i\omega t}] - T_0 \right] \right\}, \quad (2-4)$$

which can be written as

$$V(t) = \frac{1}{2} [\tilde{V}_\omega e^{i\omega t} + \tilde{V}_\omega^* e^{-i\omega t} + \tilde{V}_{3\omega} e^{3i\omega t} + \tilde{V}_{3\omega}^* e^{-3i\omega t}], \quad (2-5)$$

where

$$\tilde{V}_\omega \approx \tilde{I} R_0 \quad \text{and} \quad \tilde{V}_{3\omega} = \frac{1}{2} \alpha \tilde{T} \tilde{I}. \quad (2-6)$$

The amplitude of the first harmonic voltage is the product of the current and the time-averaged resistance, and the amplitude of the third harmonic voltage is proportional to the product of the first harmonic current and the second harmonic temperature.

Dividing the two parts of (2-6) to eliminate the current shows that the amplitude of the temperature oscillation can be determined from the ratio of the third harmonic voltage to the first harmonic voltage:<sup>10,11</sup>

$$\tilde{T} = 2 \frac{\tilde{V}_{3\omega} R_0}{\tilde{V}_\omega \alpha}. \quad (2-7)$$

### 3. 2D Computer Model

A 2D computer model was built to model the experiment. It was constructed in (R, Z) geometry: perpendicular and parallel to the wire, respectively (see Figure 2.1). The model includes the platinum wire, deuterium, and the surrounding heat baths.

The radius of the wire (7.5  $\mu\text{m}$ ) is small when compared to the radial width of the deuterium medium (1 to 3 mm), and hence a variable-size grid was implemented in the deuterium, wherein the radial widths of the cells increase geometrically with their distance from the wire. The cell widths in Z are kept uniform for all media. The average of the platinum and deuterium conductivities is used as the conductivity at the platinum-deuterium boundary. There is no heat flux across the lower boundary of the platinum wire (the Z axis).

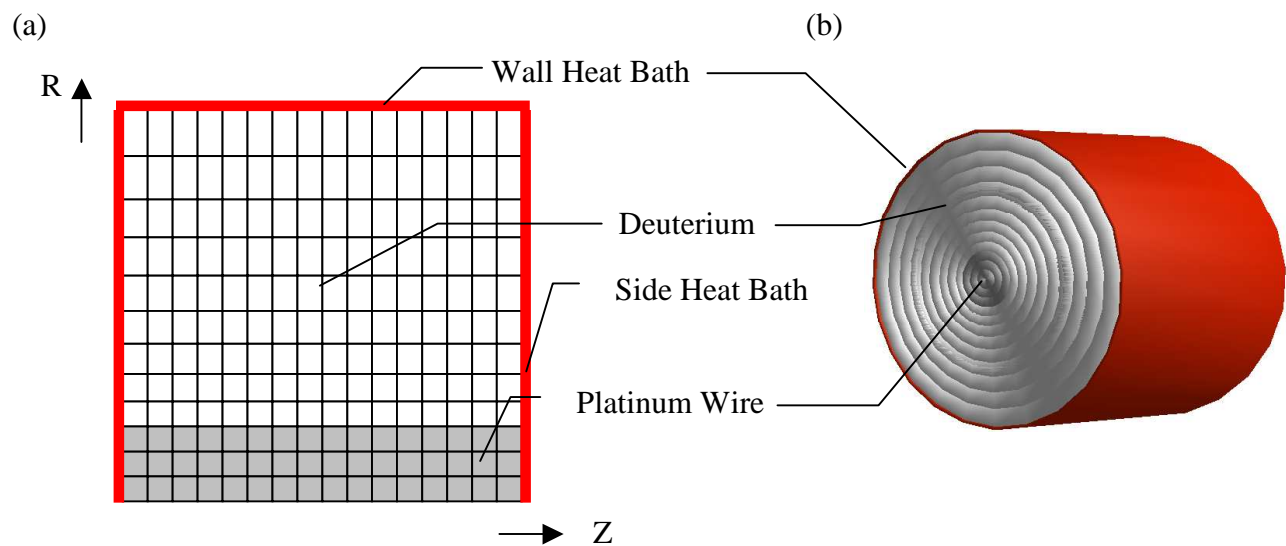


Figure 2.1 (a) A depiction of the computer model including the cells used to solve the heat flow equation. Side heat baths and the wall heat bath are named differently for identification but function identically. (b) A 3D depiction of the model, where each cell is a ring.

The equation solved for each cell is

$$C \frac{\partial T}{\partial t} + \nabla \cdot Q = W, \quad (3-1)$$

where the heat flux  $Q$  is given by

$$Q = -\kappa \nabla T. \quad (3-2)$$

Here  $C$  is the specific heat of the cell,  $T$  is the temperature,  $\kappa$  is the thermal conductivity and  $W$  is the heat deposited per unit volume. This can be solved as an initial value problem to give the full solution of the form (2-3), or it can be solved for the complex  $\tilde{T}$  in the “steady state,” in which case  $\partial T / \partial t$  is replaced with  $\frac{1}{2}(2i\omega)[\tilde{T}e^{2i\omega t} - \tilde{T}^*e^{-2i\omega t}]$ .

The initial value solution is given by

$$C \frac{T' - T}{\Delta t} - [\theta \nabla \cdot \kappa \nabla T' + (1 - \theta) \nabla \cdot \kappa \nabla T] = W, \tag{3-3}$$

where  $\Delta t$  is the time step,  $T'$  is the temperature after the time step, and  $\theta$  is a numerical parameter between 0 and 1. When  $\theta = 0$ ,  $T'$  at each cell is given explicitly in terms of known quantities. However, the small  $\Delta t$  necessary for stability<sup>12</sup> requires many time steps to reach the “steady state”. For  $\theta \geq 0.5$ , stability is achieved however large  $\Delta t$  is.<sup>12</sup> The choice  $\theta = 1$  is typically made. This gives a backward difference equation in which the  $\nabla T'$  terms couple the unknown  $T'$  at each cell center to the  $T'$  at the four adjacent cells.

Whether the initial value solution ( $T'$ ) with  $\theta > 0$  or the “steady state” solution ( $\tilde{T}$ ) is required, a set of simultaneous equations result that can be solved via matrix inversion (see Appendix). The program constructs a quindagonal coefficient matrix that corresponds to a grid of cells as illustrated in the simplified grid of Figure 3.1.

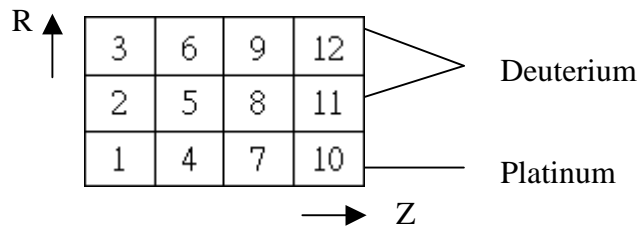


Figure 3.1 A simplified 3x4 grid.

For this grid, with the bottom row as the platinum wire and the top two rows as the deuterium, there is a corresponding 12x12 quindagonal matrix equation:



Figure 4.1 shows the temperature at the center of the wire as a function of time. It takes about 30 ms to reach the “steady state”, which is when the measurements are taken in the experiment. Also, it can be seen that the temperature oscillations are out of phase with the power.

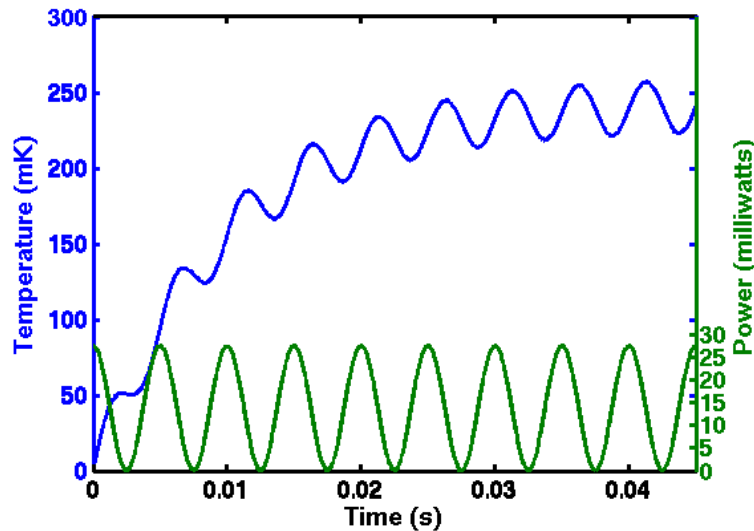


Figure 4.1 Graphs of the temperature in the center of the wire and the power against time for a platinum wire in vacuum with the current oscillating at 100 Hz.

The spatial dependence of the 1D steady-state solutions along  $Z$  is shown in Figure 4.2 for four frequencies from 1 Hz to 1000 Hz. The temperature amplitude is zero at each end due to the side heat baths. At different frequencies the temperature amplitudes along  $Z$  have distinctive shapes, which can be understood in terms of the “penetration depth”<sup>10</sup> ( $d$ ) of the temperature amplitudes. The penetration depth is a measure of how far the temperature oscillations penetrate before falloff and is a function of frequency, thermal conductivity, and specific heat:<sup>2</sup>

$$d = \sqrt{\frac{\kappa}{2\omega \cdot C}}. \quad (4-1)$$

The penetration depth shortens as the frequency increases because there is insufficient time for the changes in temperature to be thoroughly transmitted.

At low frequencies of 10 Hz and less, the temperature profiles (Figures 4.2a and 4.2b) maintain the arch shape, showing the relatively complete penetration of the temperature changes. The quadratic shape results from the maximum temperature being at the middle of the wire.

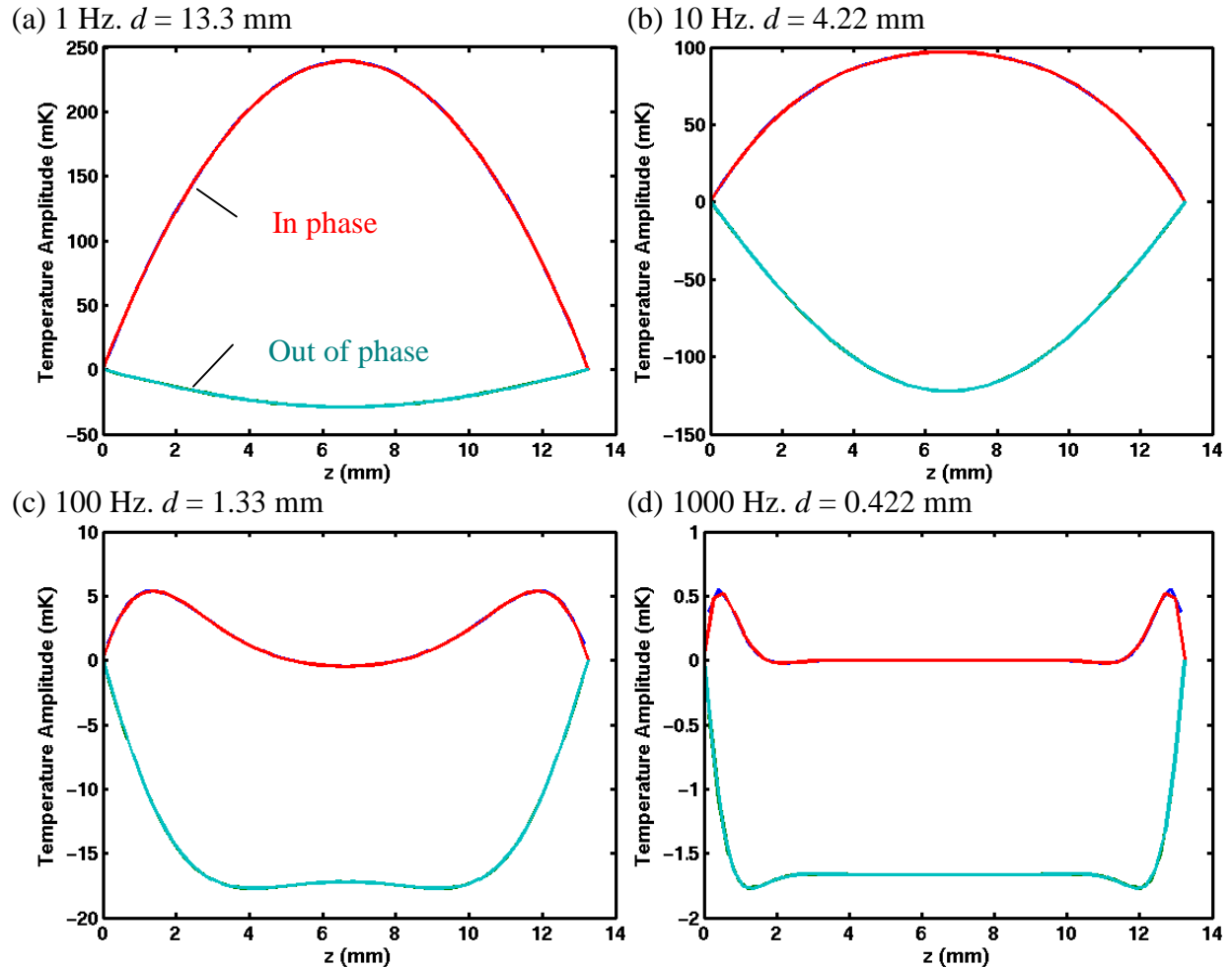


Figure 4.2 Graph of in-phase and out-of-phase temperature amplitudes against distance ( $z$ ) along the platinum wire at (a) 1 Hz, (b) 10 Hz, (c) 100 Hz, and (d) 1000 Hz. The penetration depths “ $d$ ” are also given.

At 1 Hz, the power is oscillating at a sufficiently low frequency that there is enough time for the temperature to change in phase with the power and the in-phase component dominates.

At the upper frequency range (100 Hz and greater), there is insufficient time for the temperature gradient beginning at the heat baths to extend far into the center of the wire. This is illustrated by the relative peaks in temperature amplitude near the heat baths at higher frequencies (Figures 4.2c and 4.2d). Similar behavior was found in Ref. 8. It is also at these frequencies that the imaginary component dominates the real component, and thus the temperature becomes out of phase with the power as seen in Figure 4.1.

Similar steady-state solutions were obtained over a broad range of frequencies, and the

average temperature amplitude at each frequency was obtained by averaging over the platinum cells between the voltage leads (see Figure 1.1). The results are plotted in Figure 4.3 with the conductivity and specific heat chosen to best match the experimental data.

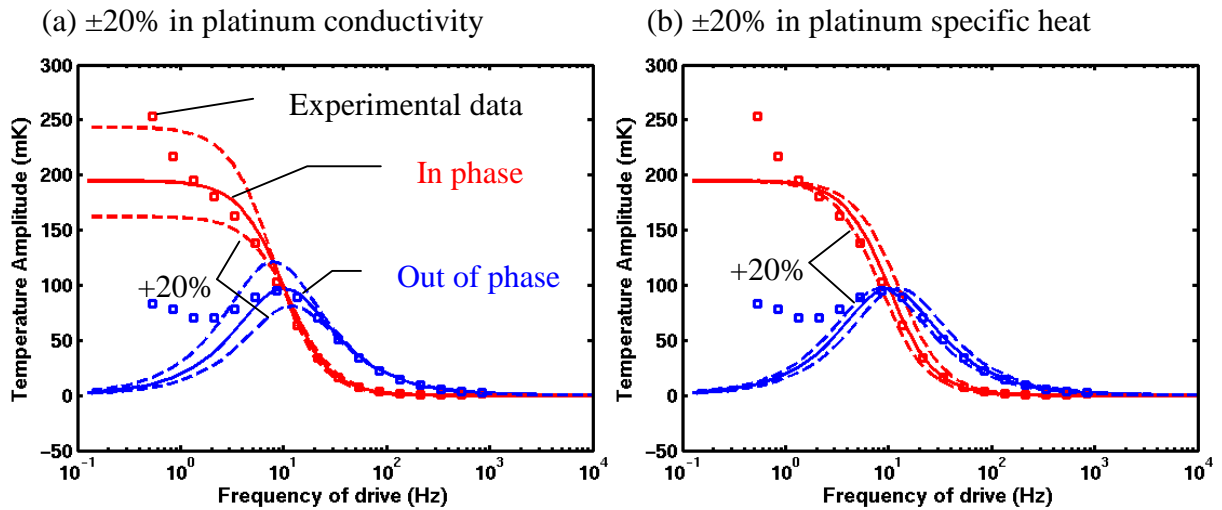


Figure 4.3 The in-phase and out-of-phase temperature amplitudes as a function of frequency. The model predictions are shown by the solid curves. The dashed curves show  $\pm 20\%$  variations in (a) the conductivity and (b) the specific heat of the platinum.

In the low frequency limit, the calculated temperature amplitudes are dominated by the in-phase component, while the out-of-phase component falls to zero. In the high frequency limit, the out-of-phase component dominates, and the in-phase component falls to zero. The data is evidently flawed at less than 10 Hz, since the in-phase component should approach a constant and the out-of-phase component should fall to zero. The distinctive shapes of the real and imaginary curves and the close agreement between simulation and experiment above 10 Hz allowed for the simultaneous determination of both thermal conductivity and specific heat. The thermal conductivity and specific heat of the platinum wire, assumed to be  $7.5 \mu\text{m}$  in radius, were determined to be  $530 \text{ W/m}\cdot\text{K}$  and  $2.8 \times 10^5 \text{ J/m}^3\cdot\text{K}$ , respectively, with an uncertainty of about  $\pm 10\%$  since the curves in Figure 4.3 with  $\pm 20\%$  variations provide poorer fits. These values differ from the literature values of  $430 \text{ W/m}\cdot\text{K}$  and  $1.92 \times 10^5 \text{ J/m}^3\cdot\text{K}$ .<sup>14</sup>

Changes of  $\pm 20\%$  in the platinum conductivity (Figure 4.3a) shift the temperature

amplitude curves both vertically and horizontally. Increasing the conductivity allows heat to be more easily conducted out to the heat baths, shifting the curves down. The results do not depend on conductivity in the high frequency limit. Changes of  $\pm 20\%$  in the specific heat (Figure 4.3b) shift the curves horizontally. Increases in the specific heat shift the curves to the left. The high and low frequency limits remain unaffected. The results do not depend on specific heat in the low frequency limit.

There is, however, another uncertainty in these values due to the uncertainty of the wire radius, which was measured by a light microscope as  $7.5 \mu\text{m}$ . Errors associated with diffraction at the wire's edge are on the order of the wavelength of the light, which is approximately  $1 \mu\text{m}$  and significant in comparison to the radius. An identical fit can be obtained using the standard values of thermal conductivity and specific heat if the radius is adjusted from  $7.5 \mu\text{m}$  to  $8.4 \mu\text{m}$  (a 12% increase). In the rest of this work, the literature values will be used for platinum under the assumption that the wire radius was  $8.4 \mu\text{m}$ .

## 4.2 Gaseous Deuterium

The 2D model is essential when deuterium is included, since heat can now flow in the R direction. The 2D effects are illustrated in Figure 4.4, which shows significant nonuniformity along the wire at 10 Hz. The wire can barely be seen, as it is just the inner  $8.4 \mu\text{m}$ .

The effects on the temperature amplitude due to the side heat baths in the 2D model are qualitatively similar to those found from the 1D model. The temperature amplitudes along Z have the arch shape as in the 10 Hz case of Figure 4.2b. The maximum [in-phase, out-of-phase] temperature amplitudes have been reduced from [100 mK, 130 mK] to [52 mK, 19 mK], because the heat deposited in the platinum wire is conducted into the gas.

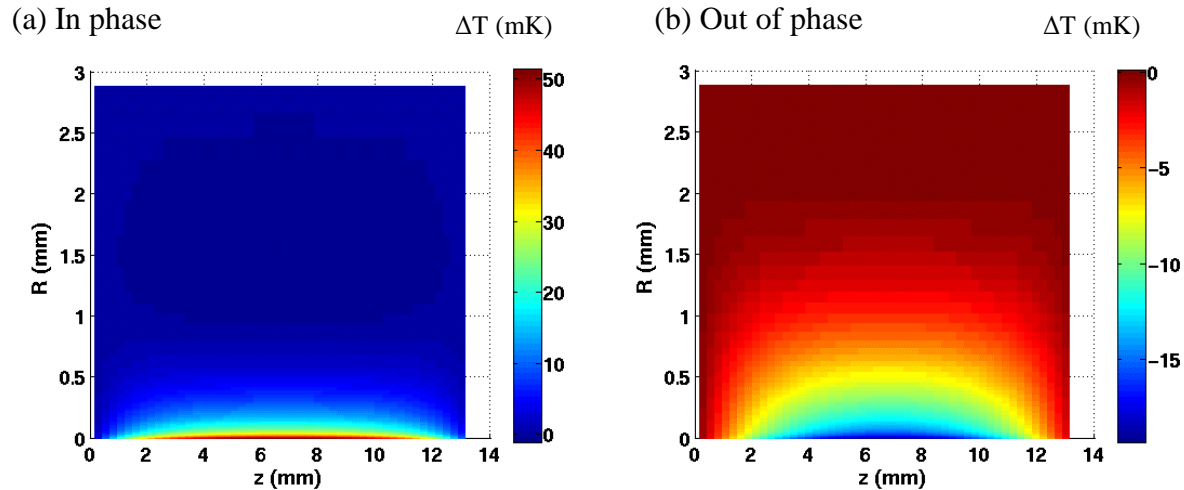


Figure 4.4 Temperature amplitudes for a platinum wire in gaseous deuterium at 10 Hz split into (a) in-phase and (b) out-of-phase components.

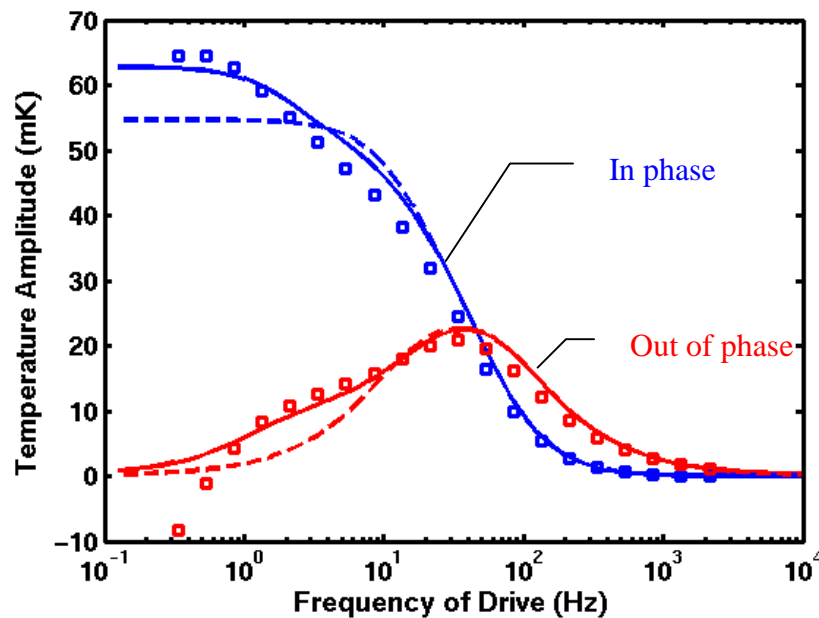
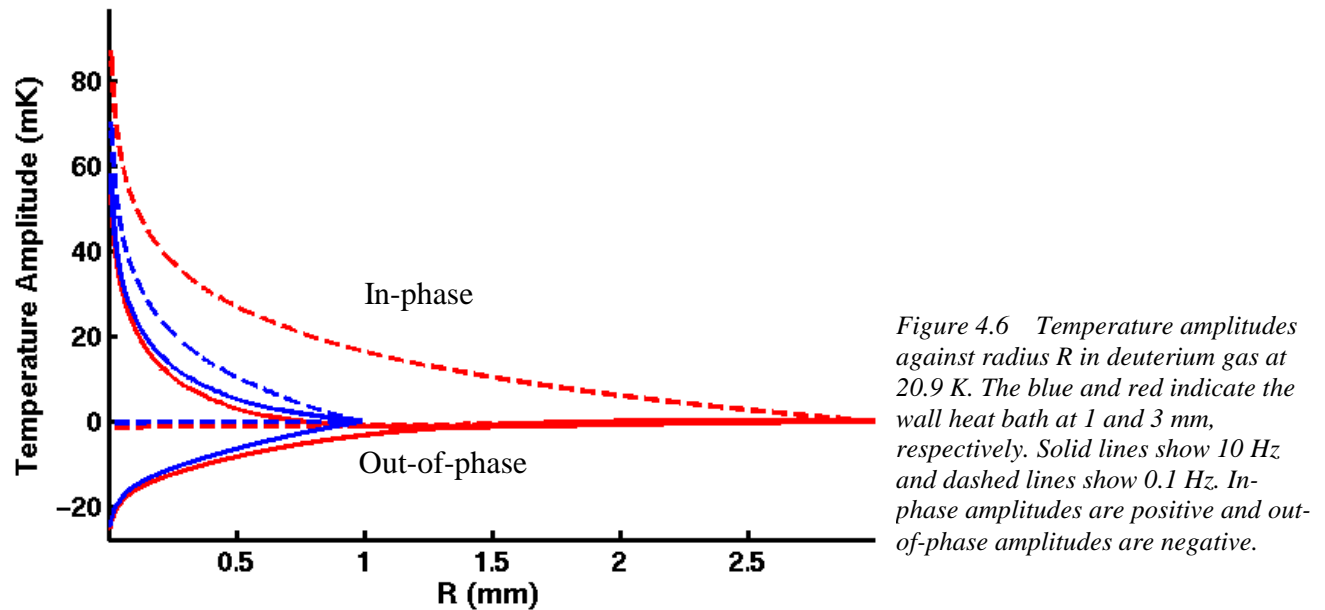


Figure 4.5 In-phase and out-of-phase temperature amplitudes as a function of drive frequency for a platinum wire in 21.0 torr of deuterium gas at 20.9 K. The solid line indicates that the wall heat bath is at 3 mm and the dashed line indicates 1 mm.

From Figure 4.5 (similar to Figure 4.3 but for deuterium gas), the thermal conductivity of deuterium gas was determined to be  $0.0137 \text{ W/m}\cdot\text{K}$ , which is 37% greater than the value of  $0.010 \text{ W/m}\cdot\text{K}$  quoted in Ref. 15. This fit was obtained with a specific heat of  $360 \text{ J/m}^3\cdot\text{K}$ , which is 7.5% greater than the original of  $335 \text{ J/m}^3\cdot\text{K}$ .<sup>15</sup> Despite being flawed at the low frequency range below 1 Hz, where the imaginary component goes negative, the data is fit well by the model.

The radial distance of the platinum wire to the wall heat bath in the experiment ranged

from 1 mm to 3 mm. Deuterium gas shows a significantly better fit with the wall heat bath at 3 mm (Figure 4.5). The effects of the wall heat bath can be isolated by examining the 1D solution in R, disallowing heat flow to the side heat baths. Heat is deposited in the platinum, flows across the platinum-deuterium boundary into the deuterium, and finally flows into the wall heat bath.



In Figure 4.6, the solid red and blue curves show 10 Hz temperature amplitudes along R with the wall heat bath at 3 mm and 1 mm, respectively. Since the penetration depth is much less than 1 mm, there is only a small difference in the temperature profiles between the two cases. The dashed curves are the same except that the frequency is 0.1 Hz. The large penetration depth at the lower frequency is disrupted by the wall heat bath, causing the maximum in-phase temperature in the 1 mm case [69 mK] to be significantly lower than that of the 3 mm case [84 mK]. The decrease in temperature amplitude that results from decreasing the radial distance of the wall heat bath is also seen in Figure 4.5. Only the parts of the curves less than a certain frequency threshold ( $\sim 10$  Hz) are affected, since the smaller penetration depths at frequencies above the threshold do not confront the wall heat bath. Thus the wall heat bath is sufficiently far from the wire to not affect the value of thermal conductivity obtained from Figure 4.5.

### 4.3 Liquid Deuterium

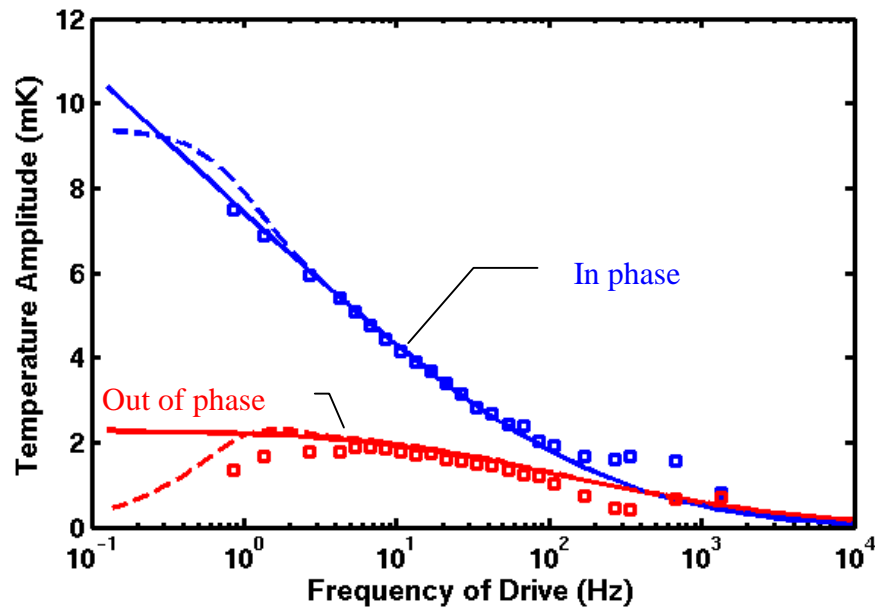


Figure 4.7 In-phase and out-of-phase temperature amplitudes as a function of drive frequency for a platinum wire in liquid deuterium at 24.3 K. The solid lines indicate that the wall heat bath is at 1 mm and the dashed lines indicate 0.2 mm.

A comparison of predictions and experimental data for liquid deuterium is shown in Figure 4.7. The agreement is generally good, but the out-of-phase data is suspect of premature falloff at 10 Hz and less. In an attempt to explain this behavior, the wall heat bath was moved closer in the simulation, to 0.2 mm (dashed curves). However, this fails to provide a convincing fit, and the closest heat bath in the experiment was at 1.0 mm. The distance of the wall heat bath only affects the low frequency range. The structure seen between 100 Hz and 1000 Hz is also questionable and may be due to a thin layer of frozen air between the platinum and the deuterium. The range of good data between 10 Hz and 100 Hz is insufficient to determine both thermal conductivity and specific heat. Yet a good fit was obtained using the standard specific heat,  $1.29 \times 10^6 \text{ J/m}^3 \cdot \text{K}$ , and the standard thermal conductivity,  $0.135 \text{ W/m} \cdot \text{K}$ .<sup>15</sup>

### 4.4 Solid Deuterium

From Figure 4.8, the thermal conductivity of solid deuterium was determined to be  $0.40 \text{ W/m} \cdot \text{K}$ , which is 46% greater than the original  $0.274 \text{ W/m} \cdot \text{K}$ .<sup>15</sup> This fit was obtained with the standard specific heat of  $5.68 \times 10^5 \text{ J/m}^3 \cdot \text{K}$ .<sup>15</sup> The data is very good in the limited range, but this

also contributes to uncertainty. Without a distinguishing shape such as seen in Figures 4.3 and 4.5, the conductivity and specific heat cannot both be absolutely determined, as different combinations of conductivity and specific heat can produce the same fit.

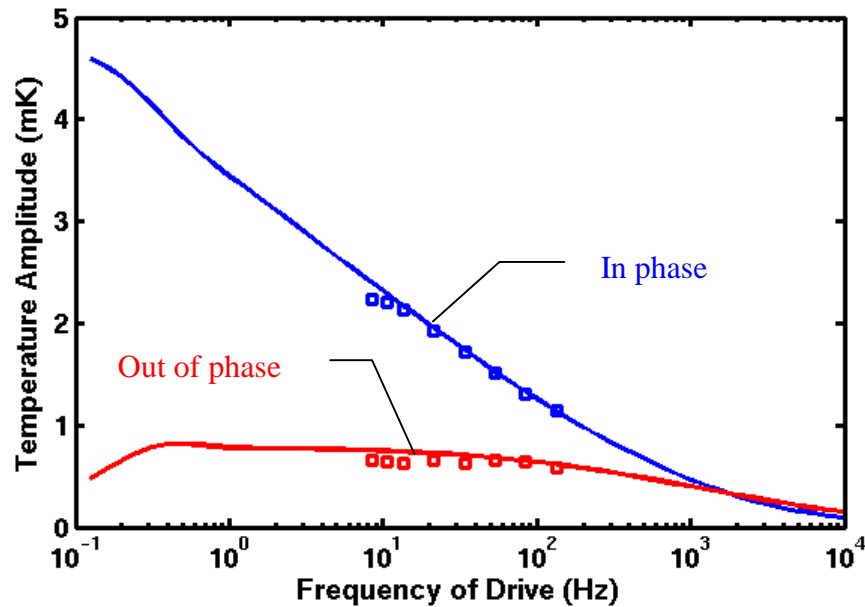


Figure 4.8 In-phase and out-of-phase temperature amplitudes as a function of drive frequency for a platinum wire in deuterium solid at 18.6 K.

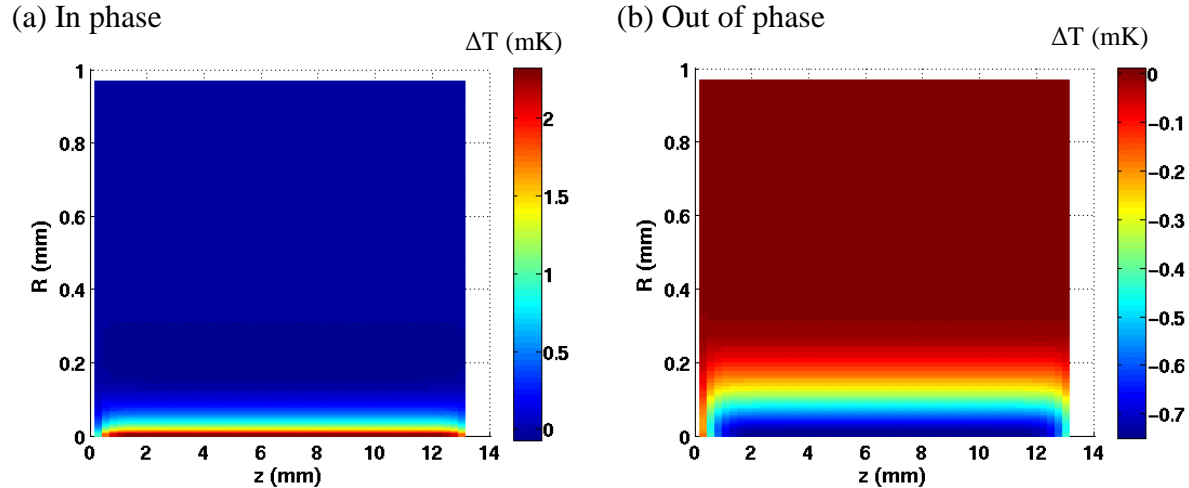


Figure 4.9 Temperature amplitudes of solid deuterium at 10 Hz split into (a) in-phase and (b) out-of-phase components, showing the relative uniformity of temperature amplitudes in Z.

In solid deuterium, temperature amplitudes are more uniform in Z (Figure 4.9) compared with gaseous deuterium (Figure 4.4) because the relatively high specific heat of solid deuterium results in smaller temperature amplitudes; thus the heat flow along Z (proportional to  $\partial T / \partial z$ ) is much smaller.

## 5. Summary

Improved values of thermal conductivity and specific heat of cryogenic deuterium have been obtained by a new 2D computer program and are summarized in Table 5.1. The program is able to fit data sets for gaseous, liquid, and solid deuterium. The program has confirmed the published values of thermal conductivity and specific heat for platinum. The 2D model provides a more accurate representation than conventional 1D solutions, and has demonstrated that the 3 $\omega$  method can be applied to cryogenic deuterium. The adaptation of the Incomplete Cholesky Conjugate Gradient<sup>13</sup> method to use complex coefficients is believed to be new.

*Table 5.1. Determined values of thermal conductivity and specific heat of deuterium, where values in parentheses are previous best values obtained from Ref. 15.*

	<b>Thermal Conductivity (W/m·K)</b>	<b>Specific Heat (J/m<sup>3</sup>·K)</b>
<b>D<sub>2</sub> Gas 20.9 K</b>	0.0137 (0.010)	360 (335)
<b>D<sub>2</sub> Liquid 24.3 K</b>	0.135 (0.135)	1.29×10 <sup>6</sup> (1.29×10 <sup>6</sup> )
<b>D<sub>2</sub> Solid 18.6 K</b>	0.400 (0.274)	5.68×10 <sup>5</sup> (5.68×10 <sup>5</sup> )

Future work should include the acquisition and analysis of improved experimental data. There are some obvious problems with the data: in the case of gaseous deuterium, there is a drop to negative out-of-phase temperature amplitudes below 1 Hz, and in the case of liquid deuterium, there is an unpredicted falloff below 10 Hz and structure between 100 Hz and 1000 Hz. Possible experimental improvements may be to increase the spectral range of the data and improve the measurement of the wire diameter.

In spite of the problems with some of the data, most of the data was found to be of good quality allowing improved values of the thermal conductivity of deuterium to be obtained. These values will be used to model cryogenic target behavior and to improve target quality.

## Acknowledgements

I would especially like to thank Dr. Craxton for his time and inspirational guidance throughout this project, and for providing me with the opportunity to work at the Laboratory for Laser Energetics. I would also like to thank Mr. Roger Gram for making this project possible. Finally, I thank everyone in the 2007 High School Summer Program for being an excellent friend.

## References

- <sup>1</sup>D. R. Harding *et al.*, Phys. Plasmas **13**, 056316 (2006).
- <sup>2</sup>R. W. Powers *et al.*, J. Am. Chem. Soc. **76**, 5974 (1954).
- <sup>3</sup>D. G. Cahill and R. O. Pohl, Phys. Rev. B **35**, 4067 (1986).
- <sup>4</sup>N. O. Birge and S. R. Nagel, Rev. Sci. Instrum. **58**, 1464 (1987).
- <sup>5</sup>L. Lu, W. Yi, and D. L. Zhang, Rev. Sci. Instrum. **72**, 2996 (2001).
- <sup>6</sup>A. Jacquot *et al.*, J. Appl. Phys. **91**, 4733 (2002).
- <sup>7</sup>F. Chen, *et al.*, Rev. Sci. Instrum. **75**, 4578 (2004).
- <sup>8</sup>C. Dames and G. Chen, Rev. Sci. Instrum. **76**, 124902 (2005).
- <sup>9</sup>R. Gram, unpublished results (2007).
- <sup>10</sup>D. G. Cahill, Rev. Sci. Instrum. **61**, 802 (1990).
- <sup>11</sup>D. G. Cahill, Rev. Sci. Instrum. **73**, 3701 (2002).
- <sup>12</sup>W. H. Press *et al.*, *Numerical Recipes: The Art of Scientific Computing*, Cambridge University Press, Cambridge, 1986, p. 635.
- <sup>13</sup>D. S. Kershaw, J. Comput. Phys. **26**, 43-65 (1978).
- <sup>14</sup>V. J. Johnson (ed.), *Properties of Materials at Low Temperature (Phase I) A Compendium*, New York, Pergamon Press, 1961 p4.182.
- <sup>15</sup>P. C. Souers, *Hydrogen Properties for Fusion Energy*, University of California Press, Berkeley, 1986, pp. 67 and 69.

## Appendix

This section details the numerical “steady state” solution of (3-1) and the calculation of the quindagonal matrix coefficients of (3-4). Integrating the heat equation (3-1) over the volume of cell  $i$  (see Figure A.1) gives

$$C_{mi}\Delta V_i \frac{\partial T_i}{\partial t} + [\Delta S_i^{(N)} Q_i^{(N)} - \Delta S_i^{(S)} Q_i^{(S)} + \Delta S_i^{(E)} Q_i^{(E)} - \Delta S_i^{(W)} Q_i^{(W)}] = W_i \Delta V_i \quad (\text{A-2})$$

where  $C_{mi}$  is the specific heat of cell  $i$ ,  $\Delta S_i$  are the cell interface areas, and  $\Delta V_i$  is the cell volume.

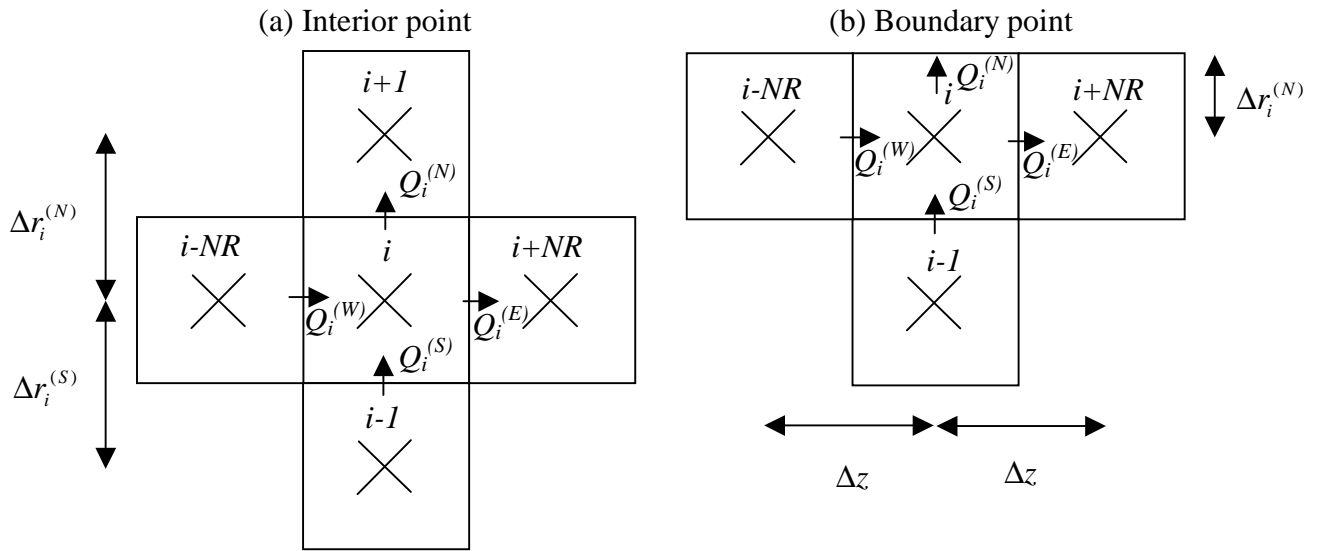


Figure A.1 (a) A typical interior cell with the heat flow  $Q$  into its four adjacent cells. (b) A depiction of a point on the wall heat bath.  $NR$  is the number of cells in the  $R$  direction.

Using  $T(r, z, t) = \tilde{T}(r, z)e^{2i\omega t}$  which differentiates to  $\frac{\partial T}{\partial t} = 2i\omega\tilde{T}e^{2i\omega t}$  (A-3)

$$Q_i^{(N)} = \frac{-\kappa_i^{(N)}(\tilde{T}_{i+1} - \tilde{T}_i)}{\Delta r_i^{(N)}}, \text{ etc. for interior points} \quad (\text{A-4})$$

$$Q_i^{(N)} = \frac{-\kappa_i^{(N)}(0 - \tilde{T}_i)}{\Delta r_i^{(N)}}, \text{ etc. for boundary points,} \quad (\text{A-5})$$

one finds

$$2i\omega \cdot C_{mi}\Delta V_i - \left[ \delta_i^{(N)}(\tilde{T}_{i+1} - \tilde{T}_i) - \delta_i^{(S)}(\tilde{T}_i - \tilde{T}_{i-1}) + \delta_i^{(E)}(\tilde{T}_{i+NR} - \tilde{T}_i) - \delta_i^{(W)}(\tilde{T}_i - \tilde{T}_{i-NR}) \right] - \left[ \beta_i^{(N)}(\tilde{T}_0 - \tilde{T}_i) - \beta_i^{(S)}(\tilde{T}_i - \tilde{T}_0) + \beta_i^{(E)}(\tilde{T}_0 - \tilde{T}_i) - \beta_i^{(W)}(\tilde{T}_i - \tilde{T}_0) \right] = W_i \Delta V_i \quad (\text{A-6})$$

where

$$\delta_i^{(N)} = \frac{\Delta S_i^{(N)} \kappa_i^{(N)}}{\Delta r_i^{(N)}}, \quad \delta_i^{(S)} = \frac{\Delta S_i^{(S)} \kappa_i^{(S)}}{\Delta r_i^{(S)}}, \quad \delta_i^{(E)} = \frac{\Delta S_i^{(E)} \kappa_i^{(E)}}{\Delta z}, \quad \delta_i^{(W)} = \frac{\Delta S_i^{(W)} \kappa_i^{(W)}}{\Delta z} \quad (\text{A-7})$$

$$\beta_i^{(N)} = \frac{\Delta S_i^{(N)} \kappa_i^{(N)}}{\Delta r_i^{(N)}}, \quad \beta_i^{(S)} = 0, \quad \beta_i^{(E)} = \frac{\Delta S_i^{(E)} \kappa_i^{(E)}}{\Delta z/2}, \quad \beta_i^{(W)} = \frac{\Delta S_i^{(W)} \kappa_i^{(W)}}{\Delta z/2} \quad (\text{A-8})$$

Here  $\Delta S_i^{(N)}$  is the surface area of the interface,  $\kappa_i^{(N)}$  is the thermal conductivity,  $\tilde{T}_0 = 0$ , and  $\Delta r_i$  and  $\Delta z$  are the distances between cell centers in R and Z, respectively.

The terms  $\delta_i$  represent the heat flow across interfaces between typical (interior) cells while  $\beta_i$  represents the heat flow across boundaries. The terms  $\delta_i$  and  $\beta_i$  for each interface are exclusively chosen, i.e., one must be zero. There is no heat flow across the lower boundary, since it is the exact center of the symmetric cylinder of the 3D depiction of the model (Figure 2.1b). The fluxes across the east and west side heat baths are represented similarly to the wall heat bath, except that  $\Delta z/2$  is the distance in Z from the cell center to the side heat bath.

Equation (A-6) can be expressed as

$$E_i \tilde{T}_{i-NR} + A_i \tilde{T}_{i-1} + B_i \tilde{T}_i + C_i \tilde{T}_{i+1} + F_i \tilde{T}_{i+NR} = D_i, \quad (\text{A-9})$$

$$\text{where } E_i = -\delta_i^{(W)} \quad (\text{A-9.1})$$

$$A_i = -\delta_i^{(S)} \quad (\text{A-9.2})$$

$$B_i = 2i\omega \cdot C_{mi} \Delta V_i + \delta_i^{(N)} + \delta_i^{(S)} + \delta_i^{(E)} + \delta_i^{(W)} + \beta_i^{(N)} + \beta_i^{(S)} + \beta_i^{(E)} + \beta_i^{(W)} \quad (\text{A-9.3})$$

$$C_i = -\delta_i^{(N)} \quad (\text{A-9.4})$$

$$F_i = -\delta_i^{(E)} \quad (\text{A-9.5})$$

$$D_i = W_i \Delta V_i \quad (\text{A-9.6})$$

The system of simultaneous equations forms a quindagonal matrix equation (3-4) that

can be solved by Kershaw's iterative ICCG<sup>13</sup> method, adapted to provide complex solutions for  $\tilde{T}_i$ . In 1D cases, a pair of diagonals becomes zero, and the matrix equation simplifies to a tridiagonal matrix that can be solved easily. With minor modifications to (A-9.1) to (A-9.6), the initial value equation (3-3) can also be solved.

# **Expansion of Search Capabilities for the Target Fabrication Database**

**Benjamin Smith**

# **Expansion of Search Capabilities for the Target Fabrication Database**

Benjamin S. Smith

**Webster Schroeder High School**  
Webster, NY

Advisor: Luke Elasky

**Laboratory for Laser Energetics**  
University of Rochester  
Rochester, NY

August, 2007

## **Abstract**

In order to develop more perfect cryogenic fusion targets, the Laboratory for Laser Energetics (LLE) maintains a database with information on the quality of past targets and the process details used to manufacture them. The database contains three tables, for file information, image information, and analysis information. These tables are organized in the same way and contain an identification number unique to each specific target image. Though access to this information is relatively simple on an image-by-image basis, there is no routine in place to access the same information on a large scale. This project entailed the creation and development of an application to fit that need, called DBsearch. The application, implemented in MATLAB (a data processing environment), allows a user to compile a list of files according to the user's parameters – for example, only files whose comments contain the word “rotation” – and then request a return of any value from those files across the three tables. Once the data is retrieved, it can be viewed as text, plotted to a graph using MATLAB's plotting utility, or exported to the MATLAB workspace for further processing. Selecting data according to parameters allows a user to view a large segment of data without unwanted variables.

### **1. Introduction**

One of the primary goals for the LLE is to research Inertial Confinement Fusion. For this research, cryogenic targets filled with isotopes of hydrogen are imploded by the laser in order to create the environment necessary for a fusion reaction. The creation of these targets is a complicated process with many variables to account for. The targets are created and processed in Moving Cryostat Transfer Carts (MCTCs). The target shells, pre-manufactured hollow plastic spheres, are filled with fuel by diffusion when the surrounding pressure is slowly increased to up to one thousand atmospheres. Once the fuel is inside the shell, the targets are cooled to cryogenic temperature and then transferred into MCTCs. The entire cart is then moved to a separate station used to monitor the target during the

processes used to smooth the frozen hydrogen. While at this station, and usually after the target has been frozen and the hydrogen ice smoothed, a program called CryoView, developed at the LLE, takes images of the target and stores them in a database (for an example, see appendix 1). Different types of information are stored in different tables of the database, TFAB. Background information about the image-- such as the target's ID, or the cart the target is in-- is entered into a table called cryo\_vdp\_file. Information about the circumstances of the image-- such as the camera type, the illumination level, or the relative position of the target-- is entered into the table called cyro\_vdp\_dataset. After the image is analyzed, that data-- including the ice thickness, the layer quality of the target (smoothness of the ice), and other measured values-- is entered into cryo\_vdp\_analysis. Between the three tables, much of the relevant information about the target's fabrication and quality are stored.

In the past, the information stored in those tables has been accessed using a direct Structured Query Language (SQL) query to TFAB. The central problem with this was that it required the user to build extremely complex queries in order to receive the appropriate results for relatively simple requests. The tables are structured on a three-column system: the first holds an identification number for each record, the second holds a description of the data in that particular row, and the third the actual value of the data (Figure 1).

So for each image generated by CryoView, a unique ID is given to the file and used across all three tables. Each image has a series of values input into each table, each with a description and a value set into an

individual row. In order to access the information in a particular row, the user only has to know the file

Target ID	Descrip	Value
2Y19354	MCTC	1
2Y19354	Shell Mat.	StrongCD
2Y19354	WallThick.	2.1
2Y19354	Fill ID	171
2Y19354	Ice Thick	94.6
2Y19354	Station	1X
1X22320	MCTC	2

Figure 1: an example of the three column database format.

ID and the description to get the value. The user can also find the appropriate file ID by using SQL to compare values, using a statement like “SELECT cvf\_file\_id FROM cryo\_vdp\_file WHERE cvf\_descrip = 'MCTC' AND cvf\_value = '1'”, selecting all files that originated in MCTC #1. The disadvantage of SQL is that developing more useful searches almost always leads to much more complicated queries. In order to simplify the process of obtaining useful information from the database, a utility needed to be written.

## 2. Functionality

DBsearch has two focuses for functionality: to simplify the process of finding the appropriate files, and to simplify the process of analyzing the resulting data. The entire process is broken up into three steps, the first two of which are concerned with locating the data, the third with presenting the data.

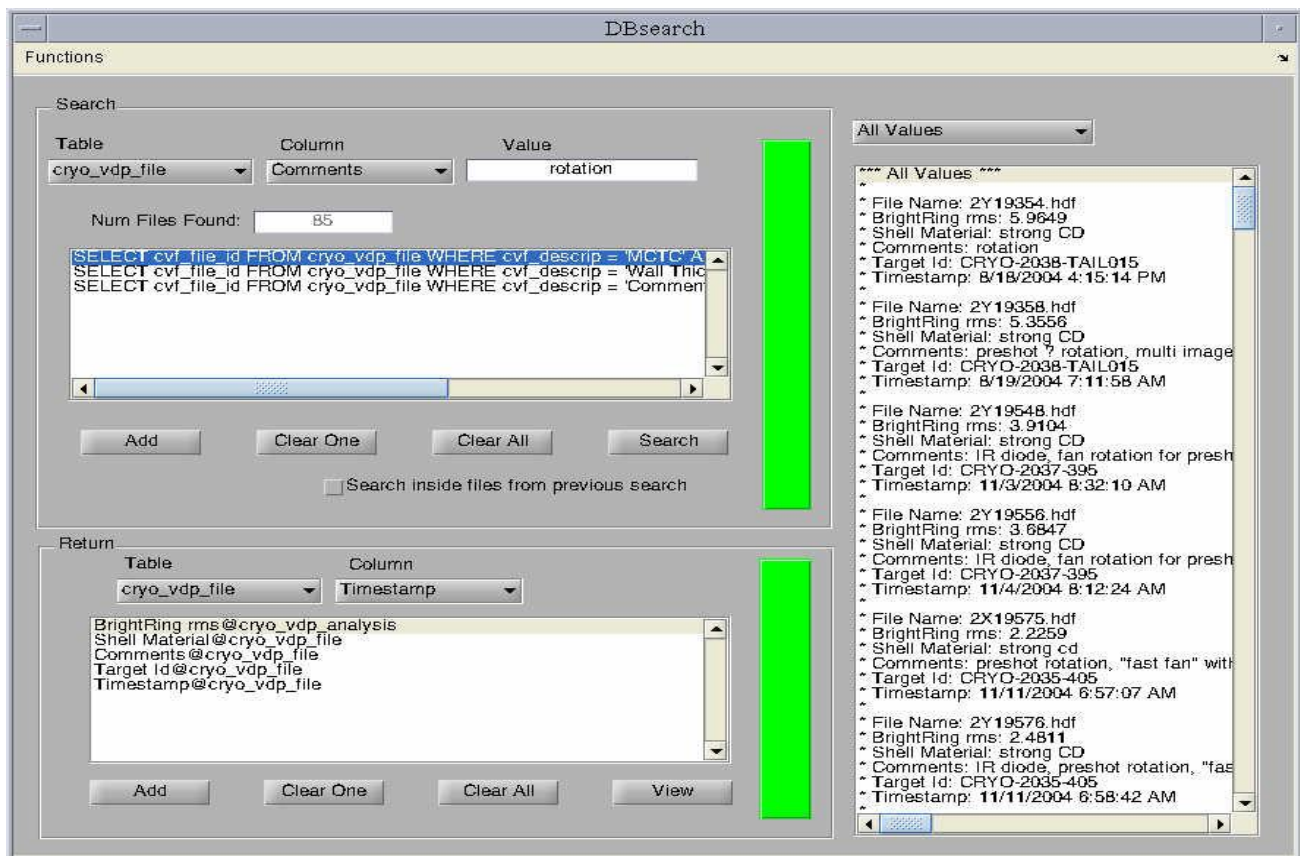


Figure 2: Main Window of DBsearch

## 2.1. Locating Data

Because DBsearch locates files through search parameters, the first step in accessing the desired output data is to find which files meet search criteria. DBsearch uses a menu and text box system to read the user's input into the program (Figure 2). The first menu contains a list of the three tables that DBsearch can access; the second contains the list of values contained in that table for each file. The third input is variable, depending on what type of parameter has been selected in the second menu. If the parameter has a limited number of different values, for example which MCTC the target was processed in, the third input field is a menu from which the user selects the appropriate value from the list. If the parameter is a string-- a combination of numbers and letters-- then the input is a simple text field. Finally, if the parameter is a numeric value, then the input is a text field with an additional field for a tolerance, allowing the user to input a value such as "37 +/- 2" using both parts of the input. Once the desired values are represented by the inputs, the criteria are added to the stack with three additional controls. The first control adds the criteria currently in the input fields to the stack, the second removes the selected criteria from the stack, and the third clears the entire stack. Once the stack accurately represents the search the user wishes to perform, the search control begins the process of searching the database with those criteria to compile a list of the fitting files. The colored status bar in association with this part of the interface will turn red while the program is busy; once the routine has finished, the bar will return to the original green color. In addition, the user has the option of only searching through the files in the list from the last search, in order to reduce the time taken to finish the search.

The second step involves selecting the data which the user would like returned. This uses a second part of the interface with similar controls to the first (see Figure 2, above). The first menu again selects the table which the user is accessing, the second the data within that table to be returned. These menus show the same information as the first two menus in the first step part of the interface. Also, the

three controls to manipulate the stack are similar: one to add, one to clear a specific row of the stack, and a final one to clear the entire stack. The view control in this section initiates a routine that proceeds through the list compiled in the first step, storing the data in local memory. Another status bar behaves in the same way as the first, red when busy and green when done.

## 2.2. Presenting Data

The main interface displays the first option for presenting data: a simple text output (Figure 3). The display consists of another drop-down menu and a scrolling text box. The menu allows the user to select either “All Values”-- to display each file with all returned values shown-- or select from the list any one of the values returned to display the files with only that value shown. The text box shows in the first line which display is being shown, and then the following lines show the file name followed by each value, followed by a blank line, then another file in the same format, and so on.

The remaining display and output options are accessible from the functions menu: extract and plot. The extract function displays a separate window with a menu, check box and button. The menu allows the user to select any of the returned values, the check box selects either numeric or not numeric, and the button initiates the

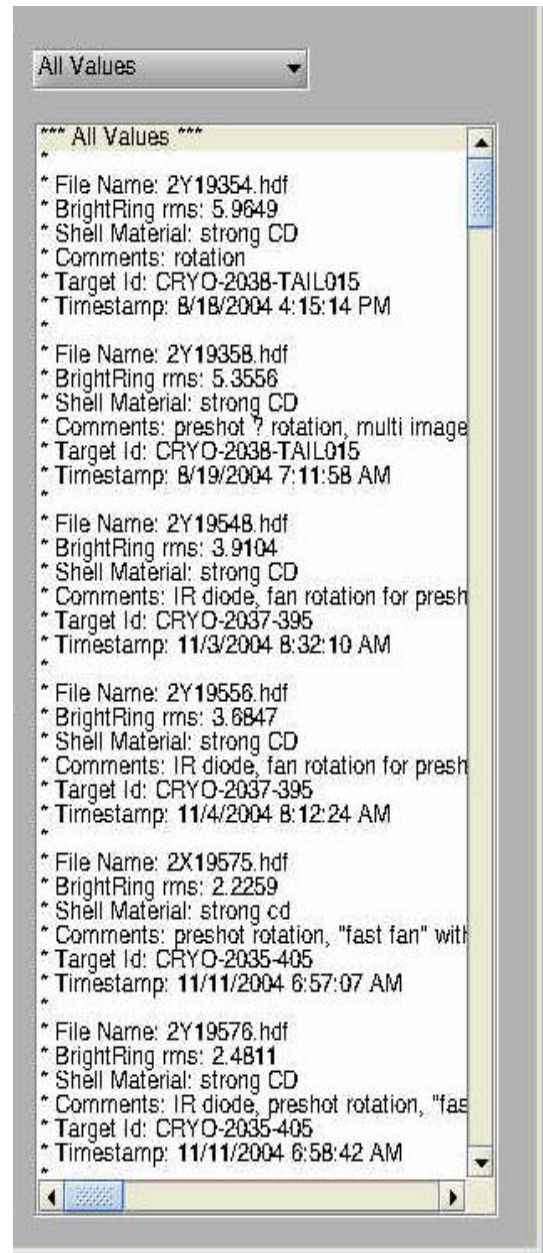


Figure 3: Example of simple text output

routine. The result is that the function DBoutput, used in the MATLAB workspace, can be used as a variable to access the data. If the data was numeric, then the variable is an array of doubles (datatype in MATLAB used to store numeric values); if the data was not, then the variable is a cell array of strings (a datatype in MATLAB used to store a list of different length character combinations-- words). The plotting function also displays a separate window. The interface allows the user a variety of options: what type of axis to plot on, which variables to plot, and which files of those variables to plot. The selectable types of axes are two dimensional rectangular, three dimensional rectangular, and two dimensional polar. Both the two dimensional plots allow two values to be selected, and the three dimensional allows three values. Also, a single variable can be plotted against index (the number representing the values position in the list of all values). Any value returned by the previous search can be plotted, assuming that the value is numeric. A text box displays the last value selected from one of the menus, and a combination of that text box and two text fields allow the user to select a range of files from the entire set that they wish to plot. Finally, the plot can be shown in the interface window, or it can be plotted to another window to allow access to MATLAB's plotting tools.

### **3. Implementation**

The code written for DBsearch uses event-initiated routines-- meaning that everything done by the program is begun by the user activating a control. Some controls are value controls, which do not activate an event but instead represent a value to be read by the program, some controls are event controls, meaning they begin a routine inside the program, and some include features of both types. Each time a new step is initiated, that step proceeds in a different workspace than all previous steps, so none of the stored values for the previous steps are available to the current step without using a different type of storage. In order to pass important values from step to step, those values either need to be stored by the interface, by a value control, or stored in a MATLAB global variable-- these variables

can be accessed from any part of MATLAB once they have been declared.

### **3.1. Compiling a List of Files**

The first step includes two sets of value controls and a main event control to initiate the search. The first set of controls includes the input fields. All of these are value controls, but the first and second menus also have event components. The first menu, where the user selects one of three tables, queries the database for all possible descriptions in that table, so as to have a complete and current list for the user to use. The second menu checks the value against a series of lists; if the value is in one of those lists, the input field changes type (for example, if the value is on the list of menu types, the input will be a menu). The second set of value controls are the stack display box and its event controls. The add event will generate a simple SQL query from the first set of value controls, and then add it to the display stack. The other two controls either clear one item from the stack, or all of the items. The last control is the main event control for the first step of the process-- the search control. When activated, the program begins to go through the stack and narrow down a list of viable files. The first query in the stack is executed as written, returning a list of files from the database that meets those criteria. If there are more files in the stack, the program modifies them before execution, adding a tag to the end of the statement. The tag contains a second criterion for the search that the files must be inside the list from the previous query. Because SQL only supports a certain length of lists in criteria and the number of files often exceeds that limit, DBsearch breaks up the list into 900 file long segments, executes them separately, and adds the segmented list back together after the most recent criteria is met. Once all of the queries in the stack have been run, the length of the list is displayed in the interface and the list itself is stored in a global variable for access by other event routines.

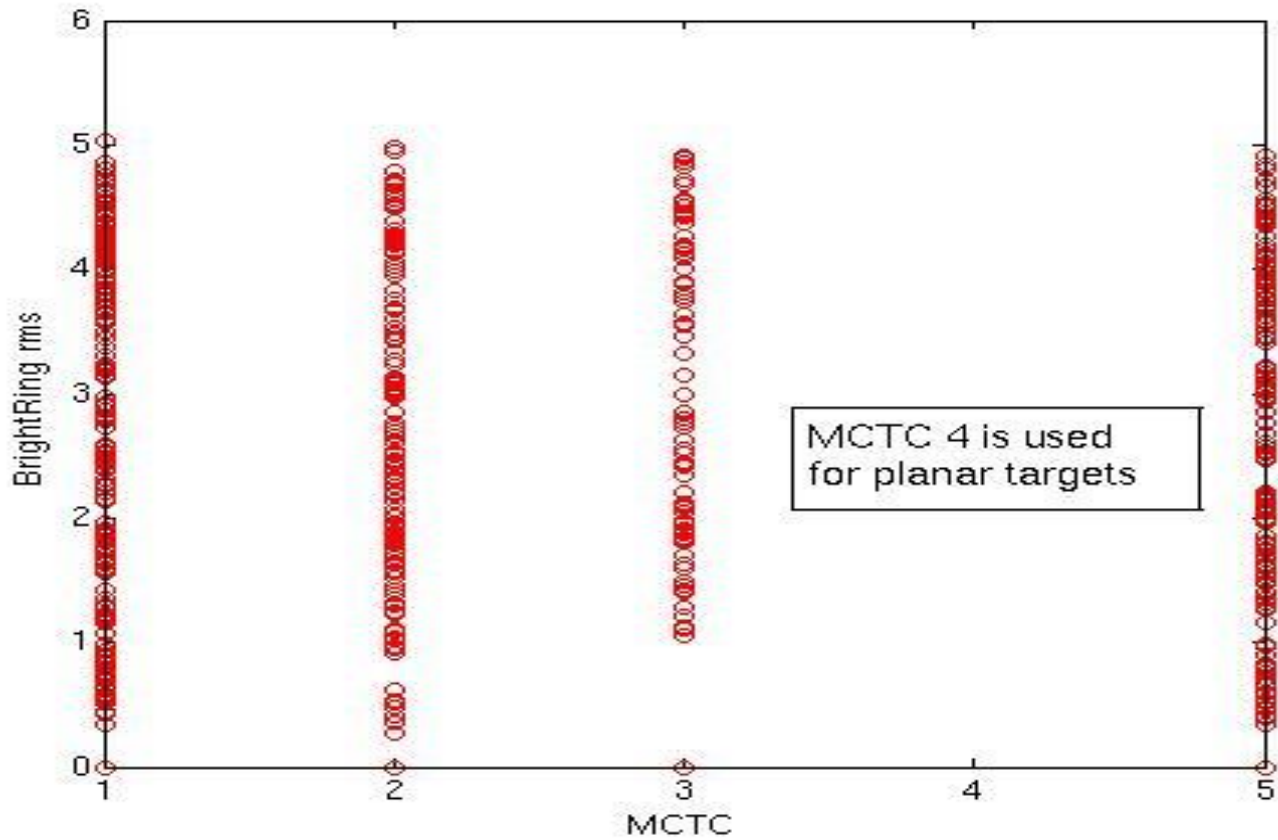
### **3.2. Locating the Desired Data**

The second segment of the interface also has two sets of value controls and one main event

control. The first set works exactly like the first two menus used to locate the files. The second set works similarly to its counterpart as well, with a minor difference in the add control. Instead of creating an SQL query, it merely prints the description and the table to the display. When the view control, the main event control for the second segment, is activated the actual database interaction for the second segment begins. DBsearch runs through the list of files compiled for the first segment, and for each file goes through the stack of desired data in the second stack display. Each individual value, once retrieved from the database, is stored in another global variable-- this one a structure organizing the data by file. Once all of the data is stored locally, the routine then generates the strings to be shown in the main output display. These are created by accessing the data stored locally, as opposed to querying the database again.

### **3.3. Presenting the Data**

The main interface has one control and a display for showing the data. The display shows in text form the strings compiled by the main event control in the second segment. While this is not necessarily the easiest way to read and compare data, it is simply a way for the user to ensure that the program has retrieved the correct data. The output reads the data from the local storage, and prints a text display. The control allows the user to choose which data are being displayed at that particular time; the user can choose to have either all returned data displayed or only one field of data (each of these are displayed by database file identification number). The display then shows a label for each ID number, a tree of the fields beneath that label, and a value for each field.



The most basic way to present the data in useful fashion is to use the plotting routine. This presents a new window, with several controls and a main display for showing the data. The controls are mainly value controls to interpret what the user would like to be displayed, with a single event control to initiate the actual plotting. The routine then puts the desired variables into arrays readable by MATLAB, according to the input by the user. Depending on the type of plot desired (two or three dimensional), either two or three arrays are generated. In the case of an indexed plot, only one of those arrays contains data from the database, while the other contains a simple incremental list to plot said data against. In the case of any other plot, both arrays are generated from the database. The routine then calls MATLAB's native plotting routine with parameters to place the resulting plot into the display on the window (Figure 4).

Figure 4: Sample Plot created using DBsearch

In cases where the plotting tool written into DBsearch cannot produce the desired plot, a separate tool can be used to output the data to the general MATLAB workspace. From there, a

MATLAB user can use the more powerful tools available to produce the intended result. The exporting tool from DBsearch's menu allows the general workspace to access either the entire structure used to locally store the data accessed by DBsearch, or an array generated by DBsearch that contains only a segment of that structure. While the structure cannot be read directly into the MATLAB's plotting routine, the array segments can be.

#### **4. Notes for Improvement**

This section details a few of the concepts that could prove useful in the future when implemented into DBsearch.

##### **4.1. Movie/Slide Show Generator**

This addition would require two additions to DBsearch: a routine for creating and storing slides, and a routine for displaying the slides. The first could be added to the plotting function, as that already produces images that are the primary sources for any slide. All that would then be required is for a button to add the slide to a list that is stored, either in a permanent file or temporarily (to be made permanent later). The second could be made fairly easily out of the code existing for the plot function window. The display can be modified to show images in sequence, and the inputs can be modified to choose the particular slide show to be displayed.

A third addition which could prove useful would be another window for displaying and ordering specific slides, in order to create the desired show. This would allow users to tailor the show more easily, as they would not have to generate the slides in order and they would not have to re-generate slides used in the past (if those slides themselves were stored separately).

##### **4.2. Additional Data Tables and Databases**

The tables currently accessed were chosen because they all held data for the same files. There are other tables in the database, and many more databases. The code used in DBsearch could be fairly

easily made to fit almost any table set up using the three-column system. The higher functions, such as plotting, may or may not prove useful in the new context, but the searching and returning code, the bulk of the code written for DBsearch, could be re-used.

The new tables would not necessarily be linked to the same application currently called DBsearch. This would make little sense, as the other tables hold very few related data. These would be run by other teams working with databases on projects not always associated with the manufacture of cryogenic targets.

### **4.3. Code Efficiency**

One of the basic tenets of software coding is that the code can always be made more efficient. For example, the code for DBsearch makes almost no use of MATLAB's number-crunching ability. As a language, MATLAB was designed to perform calculations on a large amount of data. DBsearch, on the other hand, uses an algorithm which processes tasks in sequence. The code could be made more efficient if the algorithm was better suited to the language's structure.

This is only one example of the many ways any piece of code could be improved. As an application, DBsearch runs fairly slowly—mostly because of the database interface and the time it requires retrieving data. Any improvement in processing time is an improvement that could be very helpful when processing large queries.

### **5. Acknowledgements**

Dr. R. Stephen Craxton, who accepted my application to the Laboratory's summer internship program;

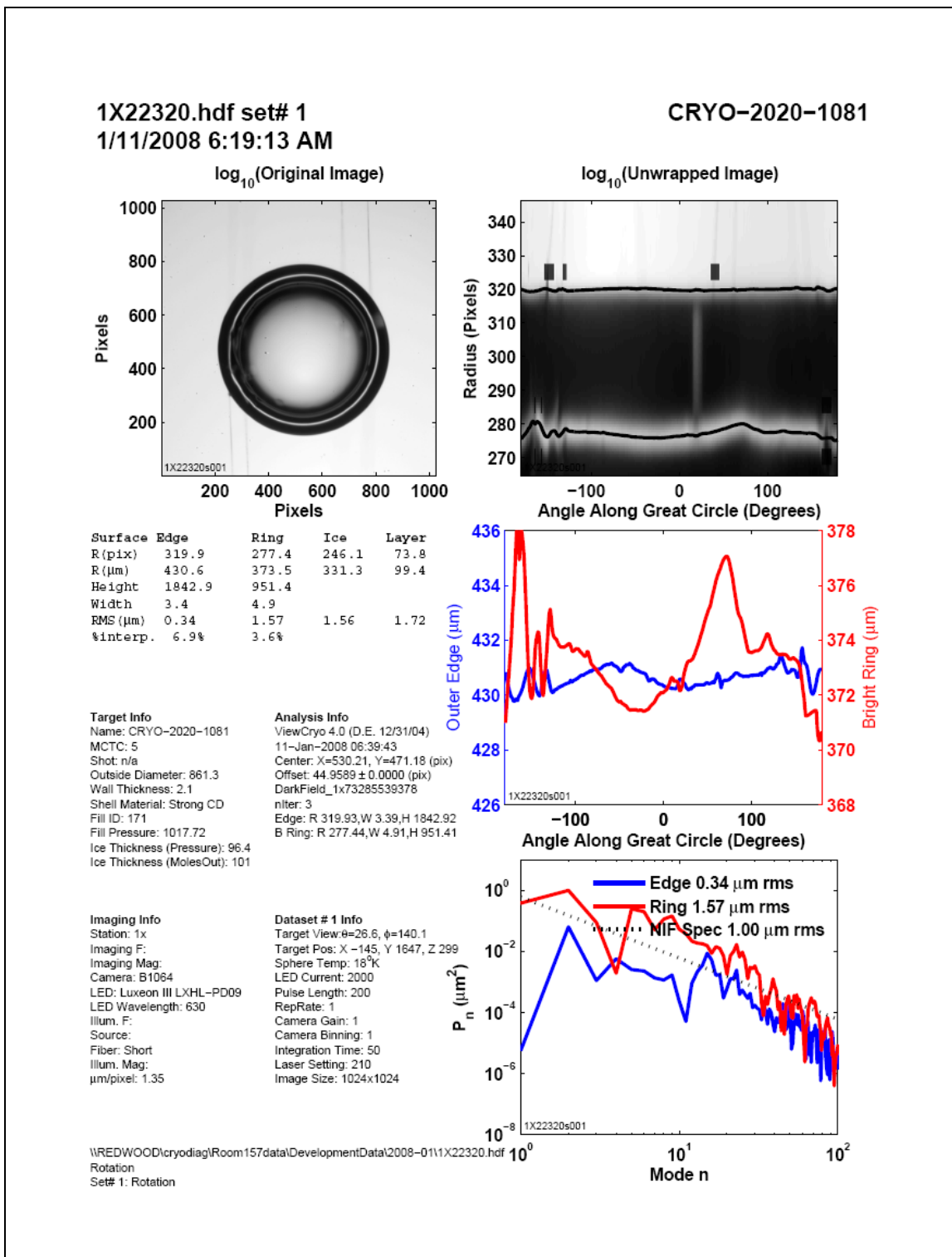
Luke Elasky, for mentoring me through the creation of DBsearch;

The LLE ITT staff, for providing assistance in a huge variety of ways;

The Laboratory for Laser Energetics, which hosted an amazing internship program and which provided

support to each and every one of its interns on every project.

Appendix 1: Example CryoView Output



# **Data Analysis for Electro-Magnetic Pulse (EMP) Measurements**

**Alexander Tait**

*Data Analysis for Electro-Magnetic Pulse (EMP) Measurements*

**Alexander N. Tait**

Allendale Columbia School

Rochester, New York

Advisor: Wade Bittle

**Laboratory for Laser Energetics**

University of Rochester

Rochester, New York

September 2007

**Abstract**

An electro-magnetic pulse (EMP) is produced when a high intensity laser strikes an inertial confinement fusion target and free electrons are displaced.<sup>1</sup> Electric and magnetic fields produced can disrupt or damage nearby electronic diagnostics and controls.<sup>2</sup> Electric ( $\dot{D}$ ) and magnetic ( $\dot{B}$ ) field probes are used to measure the EMP. This project developed a MATLAB™ routine and a graphical user interface to analyze data from the field probes. The routine converts time domain, raw-voltage data into the frequency domain and then to absolute magnetic and electric field strength. Plots of field strength versus frequency are valuable in assessing the EMP mitigation effects of shielding and filtering since their effectiveness is frequency dependent. The project also entailed calculating important EMP metrics as well as verifying theoretical predictions of EMP behavior. Predictions were verified relating to laser beam tubes connected to the target chamber acting as cylindrical wave guides and the electro-magnetic resonance of the spherical OMEGA target chamber. Several experiments were conducted to measure the propagation cut-off frequency of the beam tubes, to test the responsivity of the field probes, and to verify calculations within the MATLAB routine.

**1. Introduction**

The Laboratory for Laser Energetics (LLE) is a facility devoted to the study of the interaction of intense radiation with matter utilizing high powered laser systems. Currently, the primary experimental system at LLE is the OMEGA laser. OMEGA consists of 60 beams distributed spherically around a target chamber capable of delivering 30 kilo-Joules to a fusion target. The four-beam OMEGA EP (enhanced performance) laser system, which will come online in 2008, will support ultra short, ultra high intensity laser experiments for a variety of

millimeter-scale targets. The Multi TeraWatt Laser (MTW) is a moderately-sized laser system employing a single beam. The MTW laser is used primarily to study laser pulses similar to those that will be generated by the OMEGA EP.

When high-powered lasers strike the experimental targets on these laser systems, electrons are displaced. These electrons generate an electro-magnetic pulse (EMP), a powerful burst of broadband radio waves. It is vital to study and understand EMP because it can induce currents within conductors and electronic circuits. Induced current can interfere with, disrupt, or damage electronic diagnostics and controls. Interference causes noise which can reduce the accuracy and reliability of electric signals both for control and measurement purposes. Disruptions cause temporary functionality failures, which may render the affected equipment useless for at least the duration of the pulse. Damage can occur when the EMP power coupled into an electronic component exceeds its maximum rating. It is possible to protect equipment against EMP by electro-magnetic shielding and filtering. Completely enclosing equipment in metallic structures provides shielding against all electro-magnetic waves; however, EMP can still couple to external wires and be conducted into this housing. One way to attenuate EMP-induced electrical signals while leaving desired signals unaffected is by use of frequency selective electronic filters. Electronic filters present different impedances for different frequencies. If the spectral attributes of desired and interference signals are known, filters can effectively isolate and pass the desired signal. The purpose of this project was to develop a tool to analyze spectral aspects of the EMP event.

## 2. EMP Data Collection and Reduction

EMP is measured by electric or magnetic field antenna's called field probes. These field probes, which can be mounted wherever a field measurement is desired, produce a voltage output directly proportional to the change in the field strength.<sup>3</sup> This voltage is applied to an oscilloscope which digitizes the signal and stores the data. The raw data from the oscilloscope is of voltage versus time. Two file formats are utilized to store the raw data. The comma separated variable (CSV) format is a spreadsheet format. It contains numeric data as ASCII text with rows and columns delimited by commas. This format is the standard used by the oscilloscope. To archive data in a more memory efficient form, the hierarchal data format (HDF) file format is used. Unlike CSV files, HDF files contain metadata with important field probe and shot information.

A data series in the time domain can be converted to the frequency domain. This process, called the Fourier transform, can represent time domain data as a sum of sinusoids of scaled amplitude and phase with different frequencies. Plotting the amplitude of each sinusoid against its frequency reveals which frequencies are present and their magnitudes within the time sampled data. Every signal has a unique Fourier transform, and every Fourier transform has a corresponding time domain signal. Equation 1 presents the Fourier transform pair of a continuous signal.<sup>5</sup>

$$F(\omega) = \int_{-\infty}^{\infty} f(t) e^{-i\omega t} dt \quad (1a)$$

$$f(t) = \frac{1}{2\pi} \int_{-\infty}^{\infty} F(\omega) e^{i\omega t} d\omega \quad (1b)$$

where  $F(\omega)$  is the Fourier transform of  $f(t)$  and  $\omega$  is defined as the radian frequency,  $2\pi f$ . Since a sampled data waveform provides a finite number of discrete data points, the discrete Fourier transform pair (Equation 2) is used.<sup>6</sup>

$$X_n = \sum_{k=0}^{N-1} x_k e^{-i\omega_n t_k} \quad n = 0, 1, 2, \dots, N-1 \quad (2a)$$

$$x_k = \frac{1}{N} \sum_{n=0}^{N-1} X_n e^{i\omega_n t_k} \quad k = 0, 1, 2, \dots, N-1 \quad (2b)$$

$$\omega_n t_k = \left(\frac{2\pi}{N}\right)nk \quad (2c)$$

Here,  $N$  is the number of sample points,  $x_k$  is the time domain function,  $k$  is a discrete time counting variable,  $X_n$  is the frequency domain function, and  $n$  is a discrete frequency counting variable. The discrete Fourier transform is similar to a continuous Fourier transform, but it has some additional interesting properties, which will be discussed in section 3.3.

Using voltage versus frequency data, absolute electric or magnetic (depending on the type of field probe) field strength versus frequency can be calculated. This data is stored and saved for later assessment of EMP mitigation techniques.

### 3. The MATLAB EMP Analysis Routine

MATLAB™ is a high-level mathematical programming language, provided by The MathWorks, Inc., that uses matrices as fundamental objects. It offers sufficient user and system compatibility to facilitate the development of a self-contained program with a graphical user

interface (GUI). This project developed an EMP Measurement Analysis Routine using the MATLAB language.

### **3.1 Importing Field Probe Measurement Files**

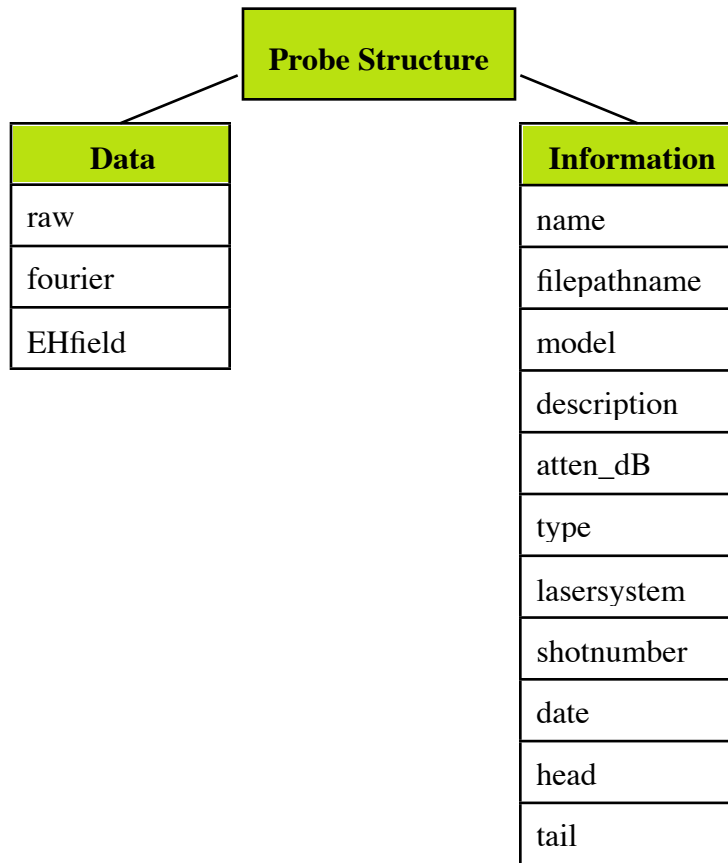
The first function of the EMP Analysis Routine is to read and import probe files stored by an oscilloscope. Voltage versus time data is stored in one of two formats.

The CSV format is stored directly by the oscilloscope. Different oscilloscope models create variations in the header information placement within the file. Some contain header information in the same two columns as the data values. In this case, the file has a total of two columns, and data starts in the first row without alphabetic characters. Other CSV files contain header information next to the data values. In this form, the file has five columns, and data starts at row 1, column 4. The final CSV storage convention encountered does not include header information. The MATLAB routine constructs a map of empty cells and cells with alphabetic characters to indicate where actual numeric values are located in each particular CSV.

The HDF format is specifically designed for scientific data set storage. Raw scope data sets to be archived are converted by a separate software task to an HDF file for efficient archival memory utilization. MATLAB has two built-in functions for importing HDFs. The function “`hdfread(filename)`” returns a vector of integers that are proportional to the y-values measured by an oscilloscope. Another function “`hdfinfo(filename)`” returns a structure that contains the scale factor for y-values, the time interval between samples, and experiment type. At this point, voltage versus time data has been imported into the MATLAB routine from either supported format. It is necessary to associate data with information about the particular experiment and probe so the analysis routine can produce correctly scaled and well-labeled results.

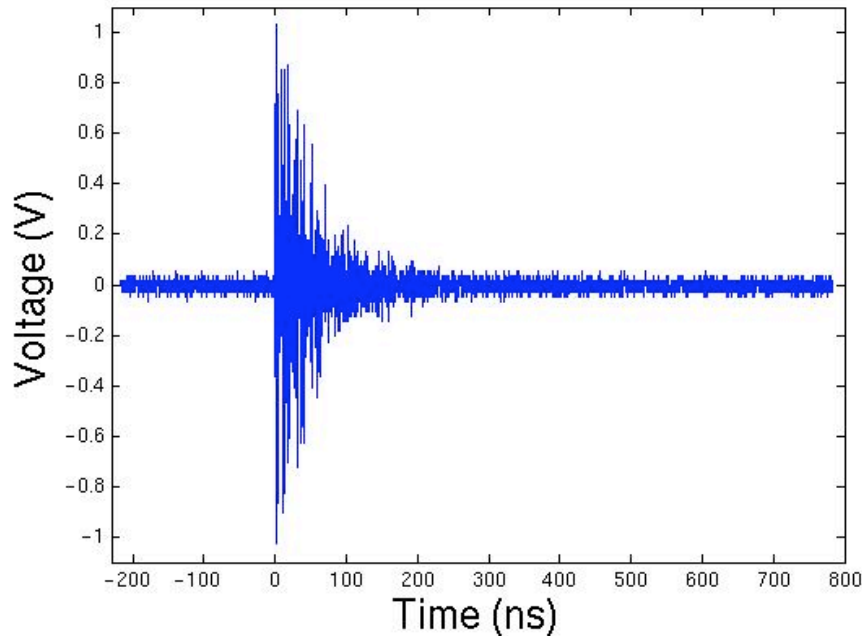
The probe structure, shown expanded in Figure 1, is defined and used throughout the EMP Analysis Routine to keep track of all of the aspects of each probe data set. Information fields are found using different methods, depending on the imported file format. HDF files specify most of the necessary information in their own information structure; however, CSV files

*Figure 1. An expansion of the probe structure convention*



have no useful metadata. Probe structure information from CSV files relies on the diligence of the experimentalist in placing that information in the filename. For example, if the string 'dB' is located in the filename, the program infers that the signal attenuation is equal to the number preceding 'dB.' Using the GUI, the user can manually enter or change a probe's information fields. Once data is imported and the probe structure identified, the program can analyze the raw voltage waveform.

Figure 2. A sample plot of a raw voltage versus time waveform



### 3.2 Analysis of the Time Domain

Although the primary purpose of the routine is to analyze the frequency spectrum of EMP, other important measurements, such as the peak voltages, attack time, pulse duration, and energy, are made in the time domain. For these metrics to be determined accurately, it is useful to know the peak voltages and the pulse start and end time. The peak voltages are found to be the maximum and minimum values of the data. EMP pulses from the OMEGA laser experiments generally take the form of a fast rising and exponentially decaying complex combination of sinusoids as illustrated in Figure 2. To find the start of the pulse or the head, a sample of pre-shot noise is taken. The head is defined as the point where the voltage exceeds twice the noise level. The attack time or the rise time is useful in assessing how abruptly EMP reaches its maximum voltage  $V_{\max}$ . To find the end of the pulse or tail, it is assumed that voltage decays exponentially with time. The program makes a moving average envelope of the waveform and fits an exponentially decaying function to it. The tail is defined to be where the envelope decays to less than 1% of the maximum voltage or approximately  $V_{\max} * e^{-5}$ . Once the head and tail are known,

the pulse duration is defined as the difference between these times. The EMP energy that the probe intercepts is one of the most useful tools for assessing the magnitude of EMP effects.

Energy is calculated with the equation:

$$W = \int \frac{V(t)^2}{R} dt \quad (3)$$

where W is energy and R is 50 ohms ( $\Omega$ ), the standard termination resistance presented to the probe by the data digitizing oscilloscope.

### 3.3 Transformation into Field Versus Frequency Data

The principal function of the EMP analysis routine is to convert field probes' measured voltage versus time data into a spectrum of electric or magnetic field strength versus frequency. Since the data consists of a sampled data set of a finite number of points, the discrete Fourier transform is used. When computing this transform for large data sets, the fast Fourier transform algorithm is used to save some computational repetition. MATLAB contains a built-in function "fft" (Fast Fourier Transform) which does most of the rigorous mathematics for the EMP routine.

The properties of discrete Fourier transforms have several characteristics. Because new information is neither gained nor lost in the transform, discrete Fourier transformed time domain data results in the same number of data points as the raw data. However, since the time domain data is real but the frequency domain data is complex, N discrete sample points yield N/2 discrete frequencies, each with a unique real and imaginary component. This means that the frequency domain result of a discrete Fourier transform is between 0 Hertz (Hz) and one-half of the inverse of the sample interval at which the raw data was collected, or half of the original Fourier transform data set. The routine therefore only keeps the first half of the transform result.

The inverse of the sampling interval divided the number of data points yields the frequency interval between Fourier data points. When setting oscilloscope sampling properties, the inter-relationship between the maximum measurable frequency, the resolution between points, and the size of the resulting data file must be kept in mind.

Once data is in the form of voltage versus frequency, the conversion to electric or magnetic field strength versus frequency is a linear algebraic operation. Determining which field to find depends on the type of probe (D-dot or B-dot) that made the initial measurements. Every field probe has an effective area that dictates the sensitivity of the probe to the field. The effective area of a probe, which is specified by the manufacturer, is important for determining the absolute field strength. Equations 4 and 5 present the linear relations used to calculate electric and magnetic field strengths versus frequency from voltage output as a function of frequency. Equation 4 is the relation between the D-dot probe response and the electric field strength.<sup>4</sup>

$$E(f) = \frac{V(f)}{2\pi \cdot f \cdot A_{eq} \cdot R \cdot \epsilon_0} \quad (4)$$

where E is the electric field strength, f is frequency,  $A_{eq}$  is the effective area, R is the resistance of the probe loading (100  $\Omega$ ), and  $\epsilon_0$  is the permittivity of free space. Equation 5 is the equivalent relation for the B-dot probe and the magnetic field strength.<sup>4</sup>

$$H(f) = \frac{V(f)}{2\pi \cdot f \cdot A_{eq} \cdot \mu_0} \quad (5)$$

where H is the magnetic field strength and  $\mu_0$  is the permeability of free space. The inverse frequency term in each equation results in the field strength appearing to approach infinity as f

approaches zero. The  $1/f$  issue at low frequencies presents certain problems for automated field strength versus frequency analysis. This issue is discussed further in section 3.4.

### **3.4 Frequency-Dependent Analysis**

Voltage and field versus frequency data is mainly interpreted visually. The EMP analysis routine can, however, automatically locate multiple spectral peaks. This peak picker function encounters two main difficulties. The first is where to differentiate between  $1/f$  noise and real field peaks. The second is how to define the difference between one and two discrete peaks. A self-iterative function picks peaks based on the specified number of peaks and buffer interval. The buffer interval defines the minimum allowable interval between adjacent peaks, so the user has a level of control over what constitutes a distinct peak. Currently, the only solution to filtering off  $1/f$  noise is through manual truncation of spectral data below a selected frequency.

At this stage in the study of laser generated EMP, it is unclear as to which aspects of the frequency domain are the most important. The EMP analysis routine provides a basic foundation for the application of further analytical methods.

### **3.5 User Oriented Interface and Output**

Apart from efficient spectral analysis of EMP data, the analysis routine gives the user control over how data is analyzed and how results are saved. A front end GUI gives the user this control, and serves to bundle the entire routine into an intuitive, user-friendly program. Data can be opened and imported in the GUI one probe at a time. The GUI itself (Figure 11) is divided into two areas. The top half displays probe structure information associated with the current probe, such as name, model, and effective area, and allows this information to be modified. The

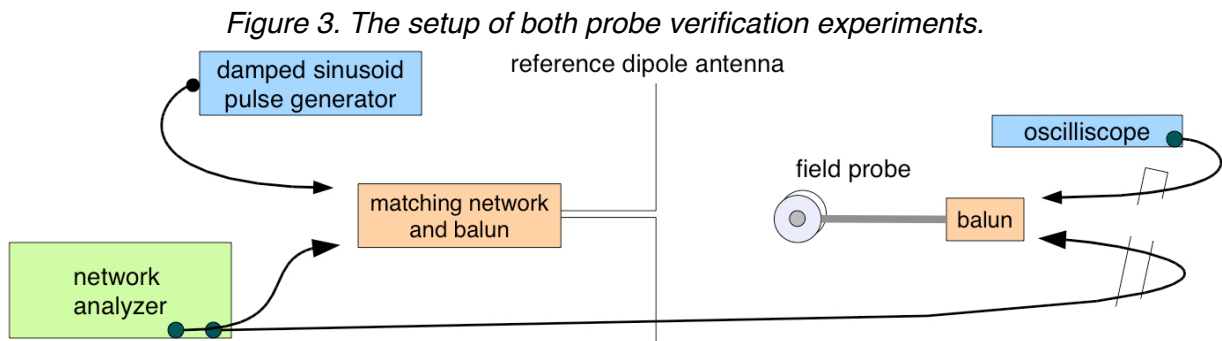
bottom half displays a plot of the raw digitized voltage, the Fourier transform, or the field magnitude with certain important points highlighted as specified by the user. The panel below the plot controls which plot is shown, and the panel to the right of the plot controls which parts of the analysis are displayed on the plot. For example, the option to highlight the peaks of a raw voltage versus time waveform is available when the “Raw Data” option is selected. When a spectral plot is displayed (as in Figure 11), the user can set parameters for a peak picker method(Section 3.4) and immediately see the result of changing each parameter. The GUI not only simplifies the operation of the routine, but it also adds to the routine’s overall capability.

By pressing a button in the lower right corner of the GUI, the analysis can be previewed, saved, or directly printed in the form of a standard, two-page output report (Figure 12). The first page of a report is headed by all the information associated with the given probe. It also shows the calculated scalar metrics of the time domain (Section 3.2) and the coordinates of the top “n” peaks of both the Fourier and field data. The parameters needed for picking peaks, which are specified by the user of the GUI, are used in determining these coordinates. The second page of a typical report exhibits three plots: raw, Fourier, and field plots. Analysis reports are initialized as MATLAB figures. If “preview” is selected, the figure representing the analysis report is displayed on the screen. If “print” is selected, that figure is exported to a postscript file and sent to the selected printer. If “save” is selected, the figure is exported to a postscript file and converted, using a system distiller, to a portable document file (PDF).

A final option for saving the results of an analysis is configured to save probe information and scalar metrics in a spreadsheet format along with point-by-point field data versus frequency. This format will facilitate the future study of EMP events.

### 3.6 Preliminary Work with Multiple Data Set Analysis

The analysis routine was primarily developed to work with individual probe data sets. Because of this limitation the original EMP analysis program can not automatically be used to efficiently examine data from many shots in order to spot trends or gather statistical information. The same tools used for analyzing individual probe files can be intuitively expanded to deal with multiple probe files. Since MATLAB relies on the use of matrices, a data structure that holds an arbitrary number of probes is identical to one that holds a single probe. Thus, the functions “import\_multiple” and “spreadsheet\_of\_all” were developed to import a vector of probe structures and to make a MATLAB workspace spreadsheet respectively. The spreadsheet function, “spreadsheet\_of\_all” also takes the names of which fields are of interest. For example, if the user only wants to know the shot number and EMP energy, the resultant spreadsheet will consist of a shot number column and the corresponding EMP energy column. Although these two functions are unrefined on their own, they can form the building blocks of future multiple field probe data analysis development.



### 4. Field Probe Verification Experiments

Two experiments were performed during the course of this project to verify the responsivity of the field probes and the accuracy of the EMP analysis routine. The premise of the

experiments was to place the field probes in a field of known amplitude and frequency and to compare the resultant measurements with a calculated, theoretical result. The experimental setup is shown in Figure 3.

A known field was created using various fixed frequency, half-wavelength vertical dipole antennas.<sup>7</sup> The particular antennas used were 1.88, 1.00, 0.6, and 0.3 meters long corresponding to frequencies of 80, 150, 250, and 500 MHz, respectively. At their half wavelength frequency, the dipoles generate the electric and magnetic fields along their horizontal axis given theoretically by Equations 6 and 7.<sup>7</sup>

$$E = \frac{\sqrt{\frac{\mu_0}{\epsilon_0}} \cdot I_0}{2\pi r} \quad (6)$$

$$H_\phi = \frac{I_0}{2\pi r} \quad (7)$$

where  $r$  is the distance between the dipole antenna and probe and  $I_0$  is the amplitude of the current applied to the dipole.

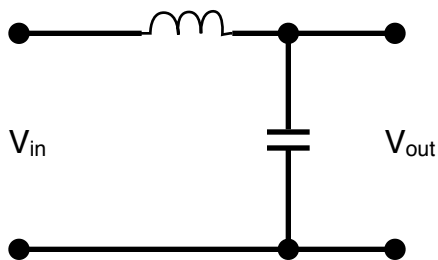


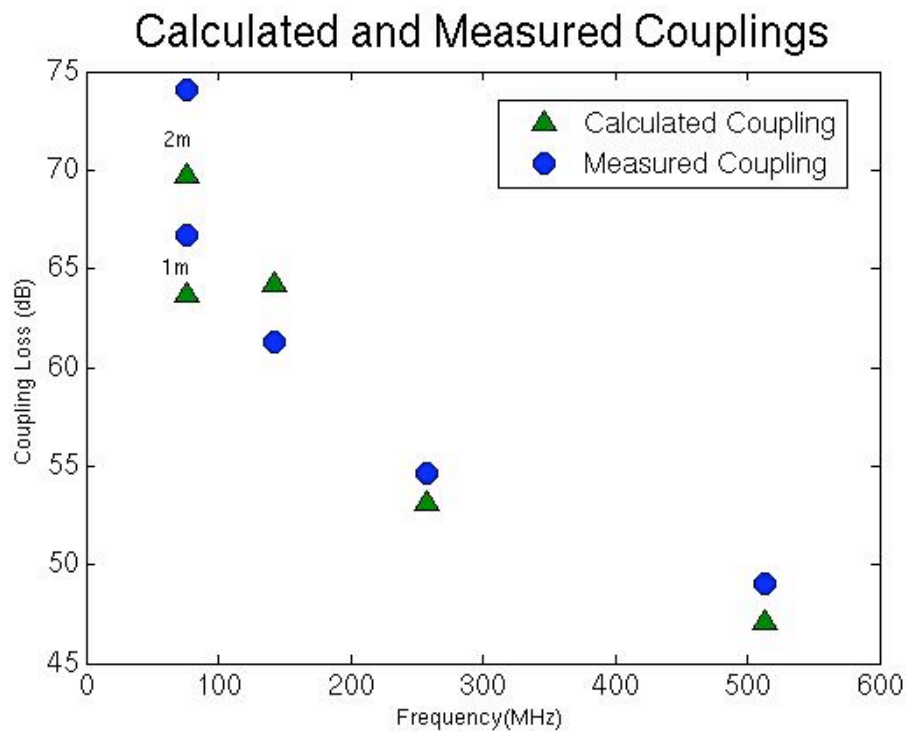
*Figure 4. The circuit diagram for a matching network. The input signal comes from the left and the dipole signal exits to the right. For the matching requirements of the 80 MHz dipole the series component is an inductor and the shunt component is a capacitor.*

The current source for each experiment was provided by a voltage generator of  $50 \Omega$  source impedance. However, the impedance of the dipole antennas differs from  $50 \Omega$  at the half wavelength frequency. This impedance mismatch causes the signal current to be reduced slightly

due to signal reflection. It was calculated that this attenuation effect was negligible (less than one decibel or 10%) for all of the antennas except the 80 MHz dipole. Therefore, a matching network circuit (Figure 4) was built to interface between the source and 80 MHz dipole. The matching network is designed by proper analytic selection of components to reactively match the dipole impedance to  $50 \Omega$  at the half wavelength frequency.

The first experiment was to measure the coupling between dipole and probe. This was performed with a two-port network analyzer, which compares a signal sent out to the dipole to a received signal from the field probe. Coupling is measured in decibels or dB, which is a scaled logarithmic ratio of the two signals. It can be calculated theoretically at a certain separation distance by determination of the field strength at the field probe location produced by the dipole driven by the network analyzer source using Equations 6 and 7. The probe response to this field is calculated using Equation 4 or 5, depending on the probe type.

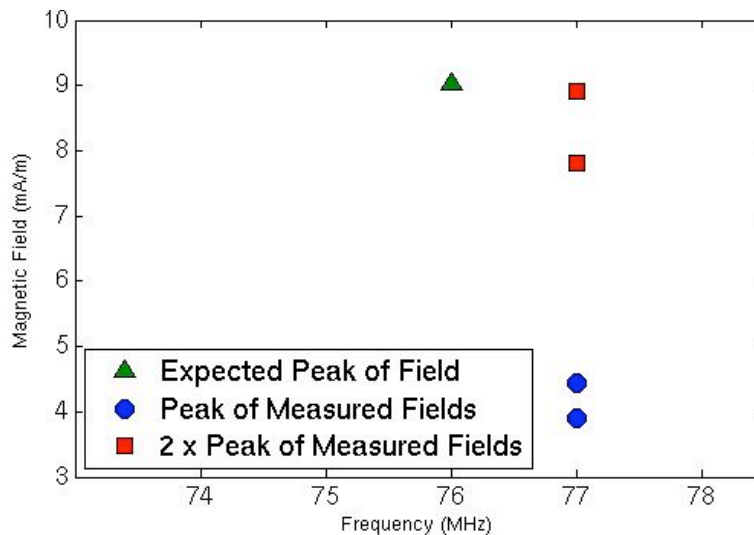
*Figure 5. A plot of theoretical and measured couplings versus frequency. There were two pairs of data at 80 MHz because distances of both 1 and 2 meters were used.*



Upon comparing the calculated and measured couplings in Figure 5, it is apparent by the close correlation of corresponding data points that the experimental setup was free of significant sources of error.

A second experiment was performed with the same dipole and field probe configuration as the first, except that an oscilloscope was connected to the probe output and an EMP pulse simulator was connected to the dipole input. The EMP pulse simulator uses a resistor-inductor-capacitor (RLC) resonator circuit to create an exponentially decaying 80 MHz sinusoidal signal when triggered, so it was only used with the 80 MHz dipole antenna. Initially, the pulse simulator was connected directly to the oscilloscope, and a dipole source drive waveform was recorded and saved. This waveform was converted into the frequency domain via the EMP analysis routine and then converted into electric (Equation 7) or magnetic (Equation 8) field strength versus frequency at the field probe location utilizing the dipole field equations.

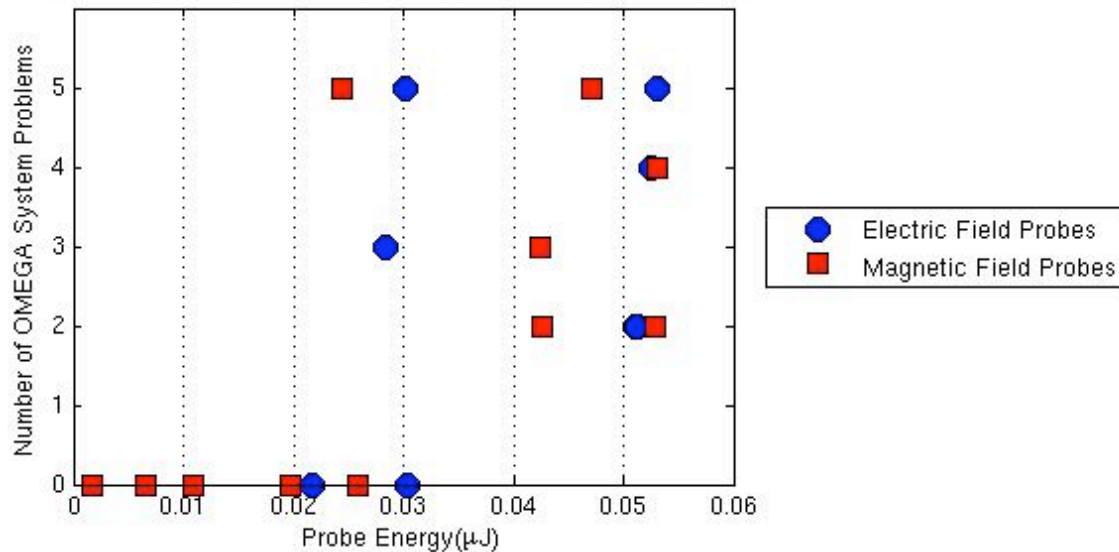
*Figure 6. Peaks of theoretical and measured magnetic field magnitude versus frequency. The measured field multiplied by two is also shown.*



The EMP source was reconnected to the dipole and a field probe was positioned to measure actual electric or magnetic fields a specific distance from the dipole. The MATLAB

routine was utilized to convert the scope data to field plots. The peaks of the theoretical magnetic field and measured magnetic fields are plotted in Figure 6. The frequency shift of 1 MHz is most likely produced by a slight shift in the RLC resonator characteristics when connected to the dipole antenna. Also, the measured field magnitude was roughly a factor of two less than the expected field magnitude. Similar results were obtained with the electric fields. This factor of two discrepancy has not been isolated yet. More work must be done to fully understand the source of this disparity.

*Figure 7. A plot of the number of EMP related OMEGA system problems versus the external field probe energy for shots 47713-47723.*

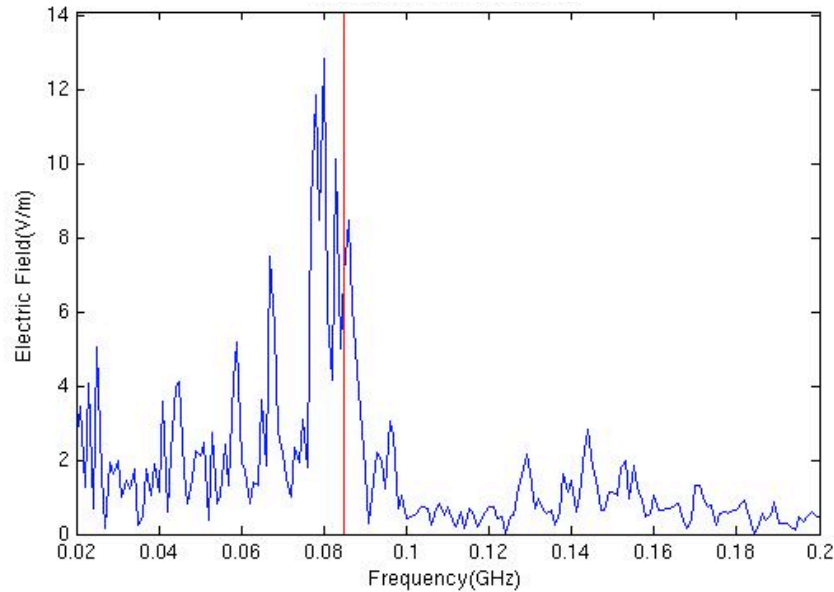


## 5. Verified EMP Event Effects

The EMP analysis routine has already been used to verify several hypotheses about EMP event effects for gathered field probe data sets. Based on work done previously at the LLE, it is suspected that the numbers of EMP generated control and diagnostic electronics system problems are related to EMP energy. This project was one of the first to analyze the measured EMP energy on the OMEGA laser. Figure 7 confirms the hypothesis that system failures are

related to EMP energy. As the measured EMP energy increases, the number of failures also increases.

*Figure 8. A plot of electric field strength versus frequency of a probe inside the target chamber. The theoretical resonant frequency of the chamber (~85 MHz) is shown in red.*



Another expectation is that the OMEGA target chamber acts as a resonator that ‘rings’ at a specific frequency related to the chamber geometry when excited by an EMP impulse. The chamber is a hollow metal structure and will therefore tend to support a specific wavelength of electro-magnetic waves. Of the waves bouncing back and forth in the chamber, one frequency, called the resonant frequency, and its harmonics will constructively interfere and sustain until being diminished by losses. The OMEGA target chamber is approximately a spherical cavity with a radius of 1.54 meters. The equation for the lowest order resonant frequency of a sphere is:

$$f_R = \frac{1}{2.29 a \sqrt{\mu_0 \epsilon_0}} \quad (9)$$

where  $f_R$  is the resonant frequency in Hz,  $a$  is the radius of the structure,  $\mu_0$  is the permeability of free space, and  $\epsilon_0$  is the permittivity of free space. Consequently, the OMEGA target chamber

has a resonant frequency of about 85 MHz. Figure 8 illustrates the close proximity between this theoretical resonant frequency (indicated by the vertical line) and the largest peak of a typical intra-chamber field plot. A slight difference in frequency can be accounted for by the fact that the OMEGA chamber is not a perfect sphere. A great number of metallic diagnostic and control structures reside within the chamber, each one producing some modifying effect to the overall resonant frequency.

The EMP analysis routine has also confirmed the prediction that metal cylindrical beam tube structures intended to guide laser beams into the target chamber act as electro-magnetic waveguide structures for EMP energy. Laser beam tubes, which are connected to the OMEGA, MTW, and OMEGA EP target chambers, have circular cross sections and, therefore, should act as waveguides with a defined low frequency cut-off for any electro-magnetic wave propagation through them. That means that an EMP event that is coupled through these beam tubes should exhibit a frequency below which the magnitude of the field will drop off. This cutoff frequency is related to the specific beam tube cross sectional dimensions by Equation 10 which provides the cut-off frequency in Hz for the lowest order mode of propagation.

$$f_c = \frac{1.841}{2\pi a \sqrt{\mu_0 \epsilon_0}} \quad (10)$$

where  $f_c$  is the high-pass cutoff frequency in Hz and  $a$  is the radius of the cylindrical waveguide structure. Utilizing equation 10, the OMEGA focus lens assemblies of radius 0.1715 meters have a cutoff frequency of 513 MHz, the OMEGA EP beam tubes of radius 0.298 meters have a cutoff frequency of 294 MHz, and the MTW beam tube has a cutoff frequency of 1.38 GHz. When these particular frequencies are highlighted on field versus frequency plots for the MTW (Figure 9) and OMEGA (Figure 10), a correlation is noted. Above the particular cutoff frequency, field

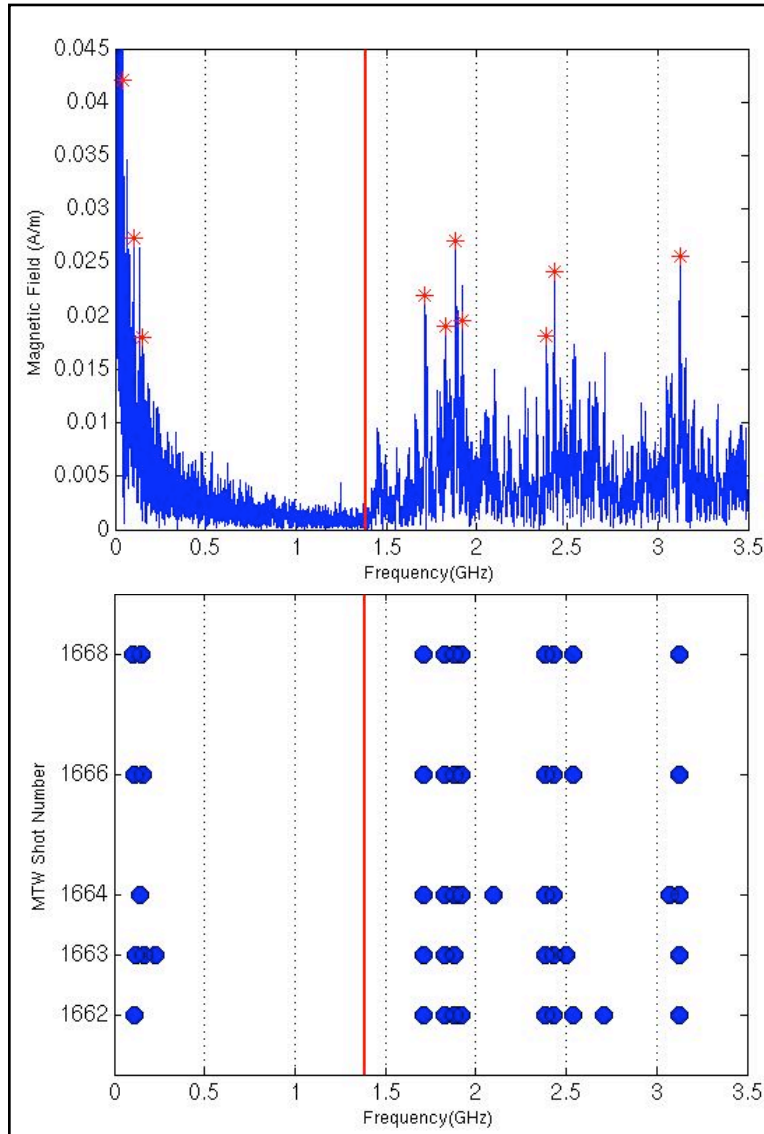


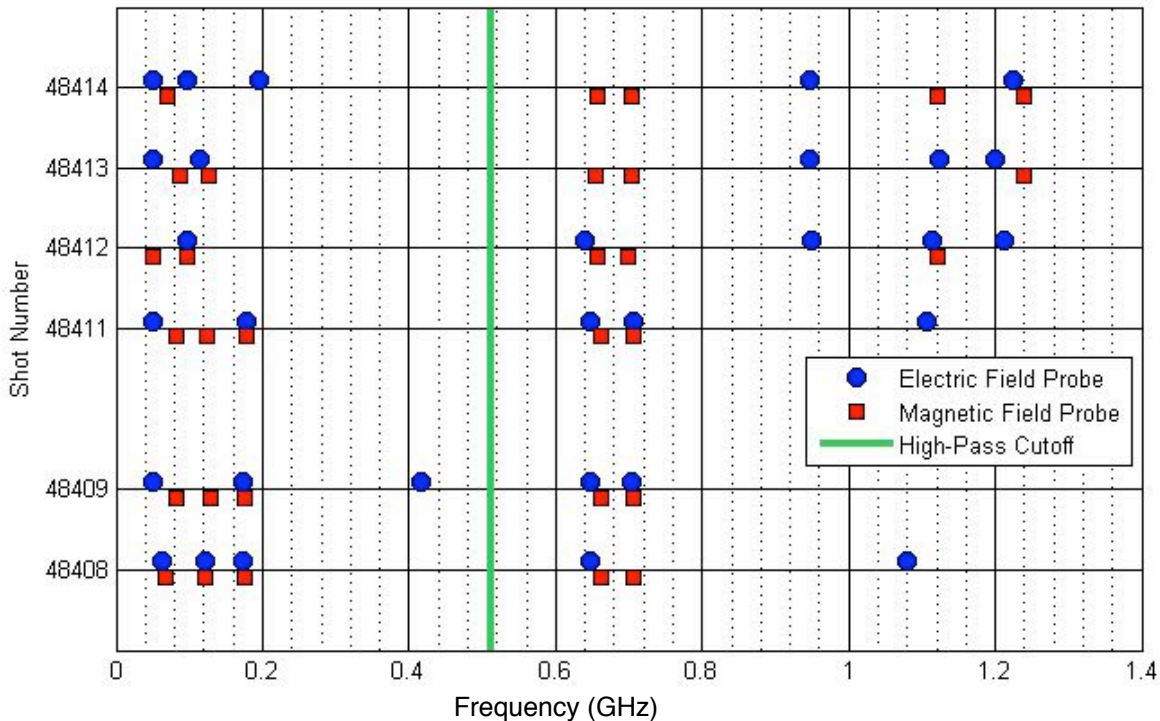
Figure 9. Field peak data for a field probe inside the MTW Grating Compression Chamber and outside the target chamber. The theoretical high-pass cutoff frequency of the MTW beam tube ( $\sim 1.38$  GHz) is shown as a vertical red line.

Figure 9a. A typical plot of magnetic field strength versus frequency illustrating the top ten peaks.

Figure 9b. A plot of the top ten peaks over multiple shot numbers with the same probe. Apparent peaks at low frequency should be ignored as  $1/f$  noise.

strength increases abruptly. Figure 9b is a plot of the top ten peaks for multiple MTW shots. Figure 10 shows a similar high-pass characteristic for OMEGA external field probes. The fact that most spectral peaks for the external OMEGA probes exist above the focus lens assembly tube cut-off indicates that these 60 ports may provide a major source for the internal to external chamber EMP coupling.

Figure 10. A plot of the top ten peaks frequencies over OMEGA shots 48408 - 48414 obtained automatically by the MATLAB analysis routine. The theoretical cutoff frequency of the OMEGA focus lens structures ( $\sim 513$  MHz) is shown as a vertical green line.



## 6. Conclusion

The EMP measurement analysis routine will continue to be a powerful tool for studying EMP events caused by high-intensity lasers. It greatly streamlines and simplifies analysis in the time and frequency domains by employing the technical efficiency of the MATLAB programming language. The analysis routine has already been used to verify several EMP event effects. Future utilization of this routine in the study of EMP events at the Laboratory for Laser Energetics will lead to a better understanding of EMP and how to mitigate electronic disruptions associated with it.

Figure 11. A snapshot of the Analysis GUI

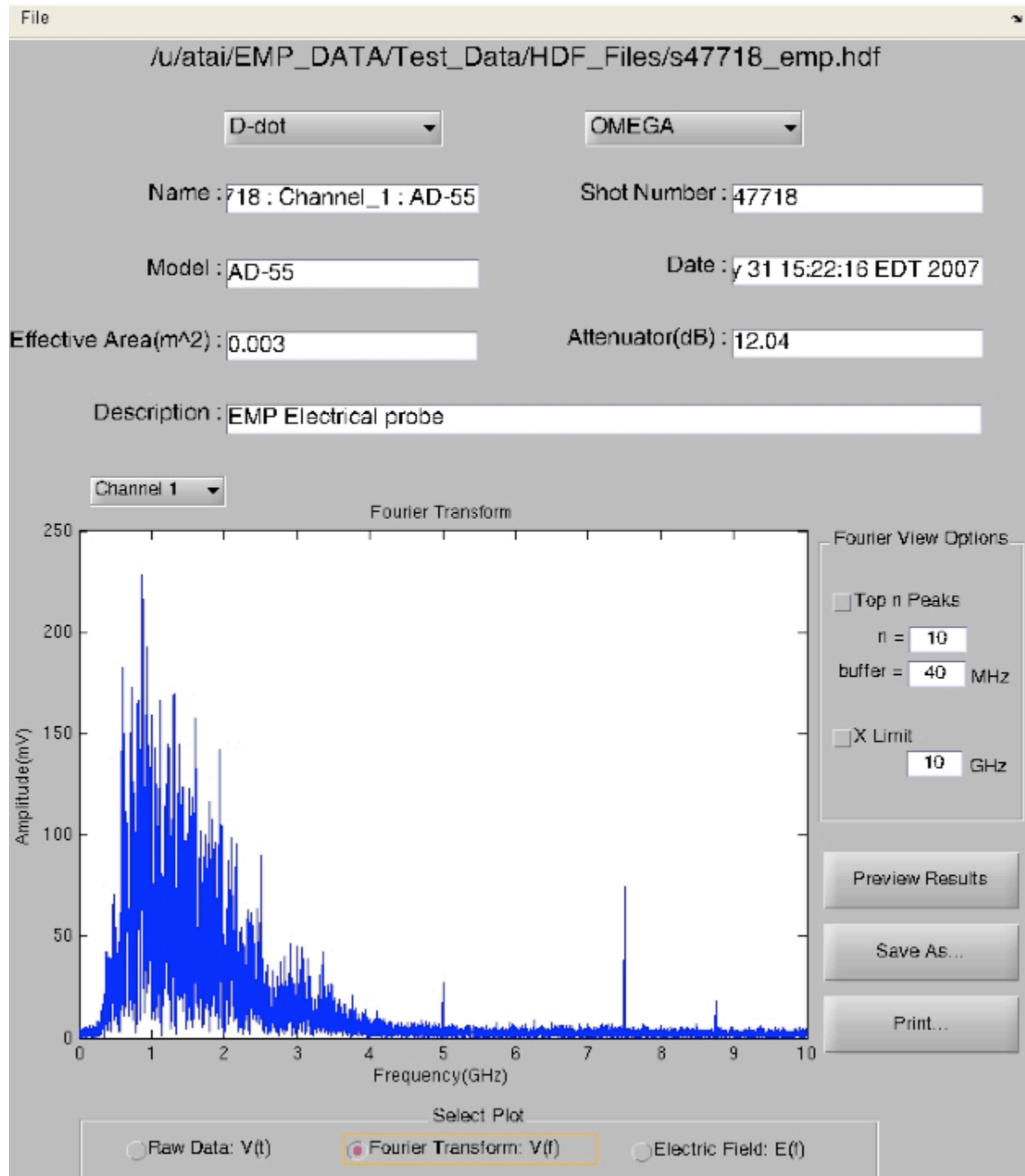
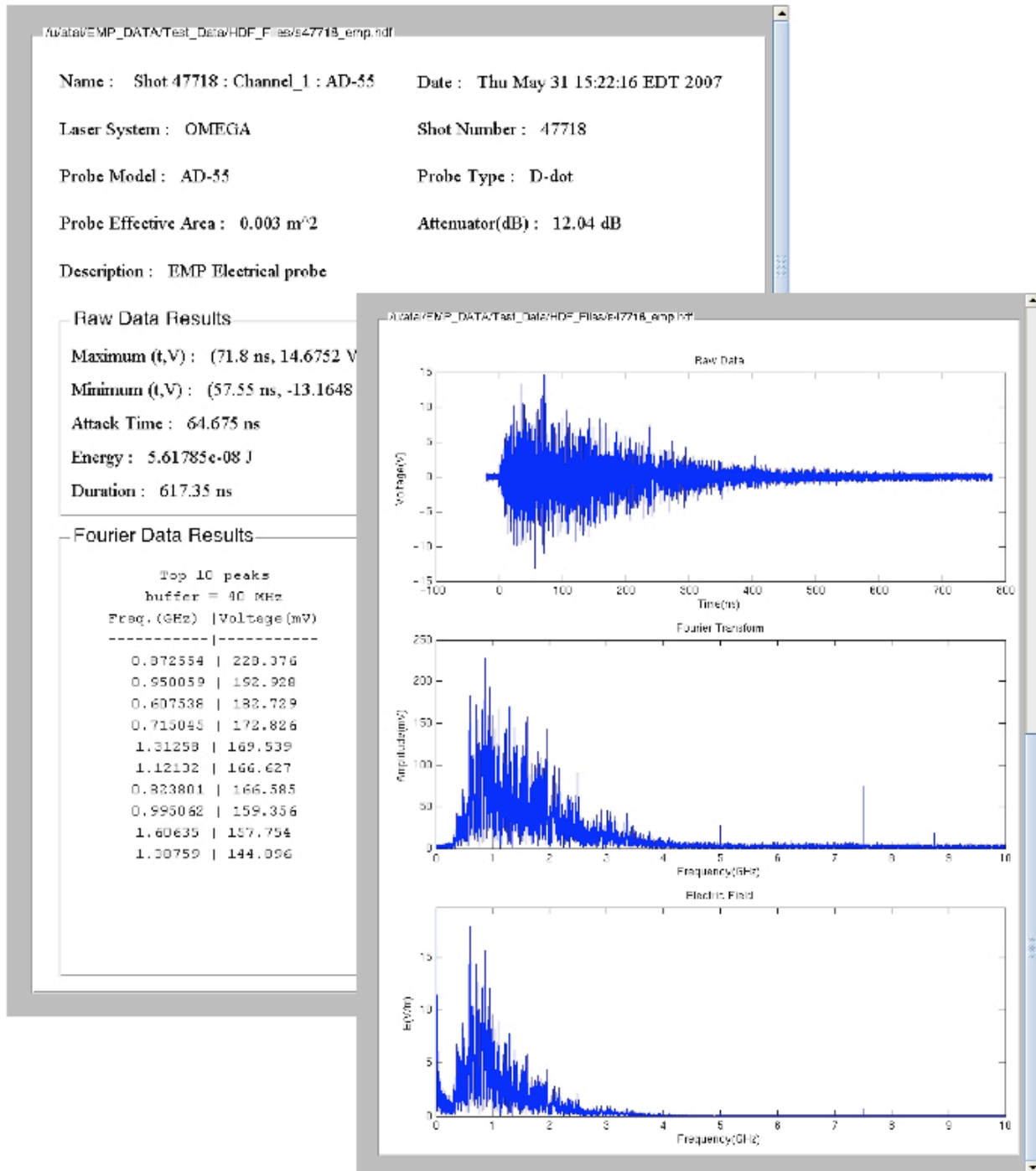


Figure 12. An example output report PDF. The first page contains numerical results, and the second page displays graphical results.



## References

### Electromagnetic Pulse Theory:

1. Mead, M.J., Neely, D., Gauoin, J., Heathcote, R., Patel, P., "Electromagnetic Pulse Generation within a Petawatt Laser Target Chamber", Review of Sci. Inst., Vol 75, No.10, Oct 2004, pp 4225 - 4227.
2. Electromagnetic Pulse (EMP) and Tempest Protection for Facilities, US Army Corp. of Engineers, Engineer Pamphlet, EP 1110-3-2, 31 Dec. 1990.

### EMP Probe Theory:

3. "Electric and Magnetic Field Sensor Application", Prodyn, Inc., Application Note No. 192
4. "Primer on Electromagnetic Field Measurements", Prodyn, Inc., Application Note No. 895

### Fourier Transform:

#### Continuous Fourier transform:

5. Schwartz, Mischa, Information Transmission, Modulation and Noise, McGraw - Hill Co., 4th Ed., 1990

#### Discrete Fourier transform:

6. Jong, M. T., Methods of Discrete Signal and System Analysis, McGraw - Hill, 1981

### Hertzian Dipole Theory:

7. Elliott, Robert S., Antenna Theory and Design, IEEE Press on Electromagnetic Wave Theory, John Wiley and Sons, Inc, 2003

# **Computational Modeling of Spectral Properties of Azobenzene Derivatives**

**Ernest Wang**

**Computational Modeling of Spectral Properties of Azobenzene Derivatives**

Ernest Wang

**Pittsford Mendon High School**  
Pittsford, NY

Advisor: Kenneth L. Marshall

**Laboratory for Laser Energetics**  
University of Rochester  
Rochester, NY

October 2007

## Abstract

Azobenzenes have been noted for their ability to undergo isomerization between the straight *trans* isomer and the bent *cis* isomer with visible light and UV irradiation, respectively. Their photochemically induced isomerization make them highly useful in optical switching devices. Time-dependent density functional theory (TDDFT) can model highly complex molecules like azobenzenes accurately, efficiently, and cost-effectively. In this study, TDDFT was used for the first time to model the absorption spectra of several azobenzene derivatives. The results show a reasonably good association between the theoretical and experimental values for the absorbance spectra of the azobenzenes. The ultimate goal is to use azobenzenes as terminal functional groups attached to nickel dithiolene metal complexes (which are well known to have an intense near IR absorbance band) to create photoswitchable absorbers with high sensitivity in the near IR region. Such systems are of special interest for liquid crystal device applications for near IR optical switching, modulation, and sensor protection applications.

## 1. Introduction

Azobenzenes are noted for the ease in which they undergo reversible photochemically induced isomerization. When the more thermodynamically stable, rod-like *trans* state is exposed to UV irradiation, it transforms into the bent *cis* state (Fig 1). Upon exposure to either visible light irradiation or elevated temperature, the less stable *cis* state is converted back into the *trans* state. This rapid and reversible isomerization makes azobenzenes useful as dopants for liquid crystal systems because of their ability to change the optical properties, such as birefringence and selective reflection, of the liquid crystal host[1].

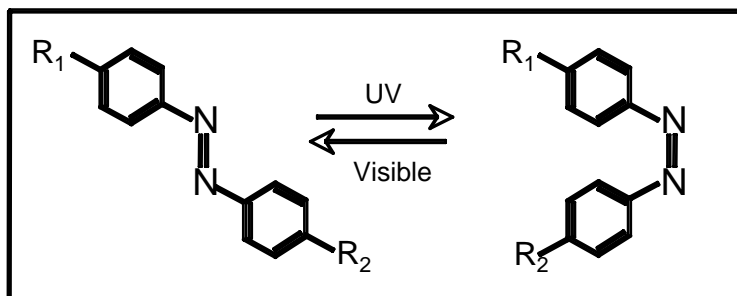


Fig. 1: Photochemically induced isomerization of azobenzenes. The terminal groups  $R_1$  and  $R_2$  can be any aliphatic, aromatic, or halogen substituent.

Nickel dithiolenes (Fig 2) are noted for properties that make them useful as liquid crystal dyes. They have intense long-wavelength absorption (600 nm to 1600 nm), a zerovalent core structure, high solubility in nonpolar solvents, and high thermal and optical stability. These properties make nickel dithiolenes good photodetectors. They are also capable of absorbing IR laser radiation and releasing short pulses upon saturation. Lastly, they are useful in IR sensor protection, tunable to absorb wavelengths from 600 nm to 1600 nm. There are several applications in photonics, telecommunications, military sensor protection, and laser systems [5].

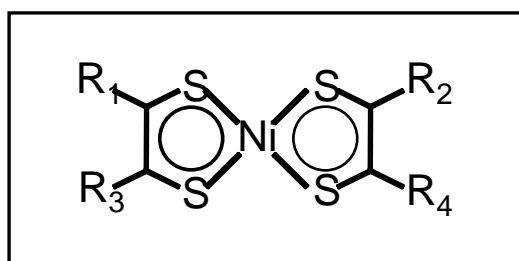


Fig. 2: Structure of nickel dithiolenes dye molecules. Different dyes are formed by substitutions of the R groups. The R groups are typically hydrogens, alkyl or alkoxy substituted phenyl groups, or alkylthio ether groups.

Nickel dithiolenes with azobenzene terminal groups, or azobenzene substituted nickel dithiolenes, have the potential to be rapid and reversible photoswitchable absorbers with high absorption in the near IR region. The nickel dithiolene core would be attached to the terminal azobenzene groups with linkage groups that promoted the extensive electron delocalization of the entire molecule. However, nickel dithiolenes are synthesized through a costly and time consuming, multi-step synthesis process. Conventional trial-and-error synthesis would be extremely inefficient considering that synthesis of azobenzene substituted nickel dithiolenes would require even greater resources and effort. Furthermore, large quantities would need to be synthesized in order to establish physical properties. Using computational chemistry, physical properties of only the most promising complexes would be predicted prior to synthesis. Rather than wasting resources through trial-and-error synthesis, computers can calculate complex structures and properties such as the absorbance spectra of molecules in hours or days.

In this study, a new computational method, time-dependent density functional theory (TDDFT) was applied to several azobenzene derivatives to successfully predict their spectral properties. Then TDDFT was applied to nickel dithiolene dyes substituted with the above-mentioned azobenzene derivatives. However, free energy convergence problems impeded with the modeling of the complex. Improper basis function selections caused the free energy to cycle in loops. The computers had trouble mapping the electron sharing between the nickel dithiolene cores and azobenzene terminal groups. Since larger molecules have diminished success and accuracy in convergence, and take a substantially longer time to compute, the azobenzene substituted nickel dithiolene dyes could not be modeled.

## 2. Previous Research

Previous attempts at modeling nickel dithiolenes have employed different computational methods for excited state calculations. Semiempirical methods use existing experimental data with approximations to fit the calculations according to known parameters. These semiempirical methods provide rapid computational time, but with reduced accuracy[2]. The Hartree-Fock method uses approximations of the electron wave function derived directly from theoretical principles. This method has better accuracy, but a longer computational time and is generally only successful in smaller molecules to which the theoretical principles better apply[3]. Lastly, the density functional theory (DFT) method bases calculations on a 3-D electron density function rather than numerous electron wave functions[4]. Though it does hold the advantage of being able to model highly complex molecules accurately, the computational time increases rapidly with structural complexity.

Time-dependent density functional theory (TDDFT) computations follow the evolution of electron density in a perturbed system as a function of time[1]. An impulse potential containing all frequencies is applied to “disturb” the molecular system while in the ground state. Frequency-dependent time evolution of the electron density is used to calculate the electronic absorbance spectra. This method provides both high computational accuracy and reduced computational times.

TDDFT has previously been employed in the modeling of the absorbance spectra of an extensive set of nickel dithiolenes for the first time by Marshall *et al* [5]. In this work, the density function was evaluated using Gaussian 03, an electronic structure program that predicts the energies, molecular structures, and vibrational frequencies of molecular systems,

along with numerous molecular properties derived from these basic computation types [6]. The theoretical values were in excellent agreement with the experimental results with a mean absolute error of only 0.034 eV, when a mean absolute error of less than 0.2 eV is considered accurate [5]. This study builds upon the modeling of nickel dithiolene dyes with TDDFT. Once the absorbance spectra of azobenzenes were modeled, TDDFT could be applied to azobenzene substituted nickel dithiolene dyes.

### 3. Methodology

The methodology of this study is shown in Fig 3. The first step involved the use of Spartan (Wavefunction Inc.), a computational chemistry software package used for generation of the molecular structure of the candidate molecules [7].

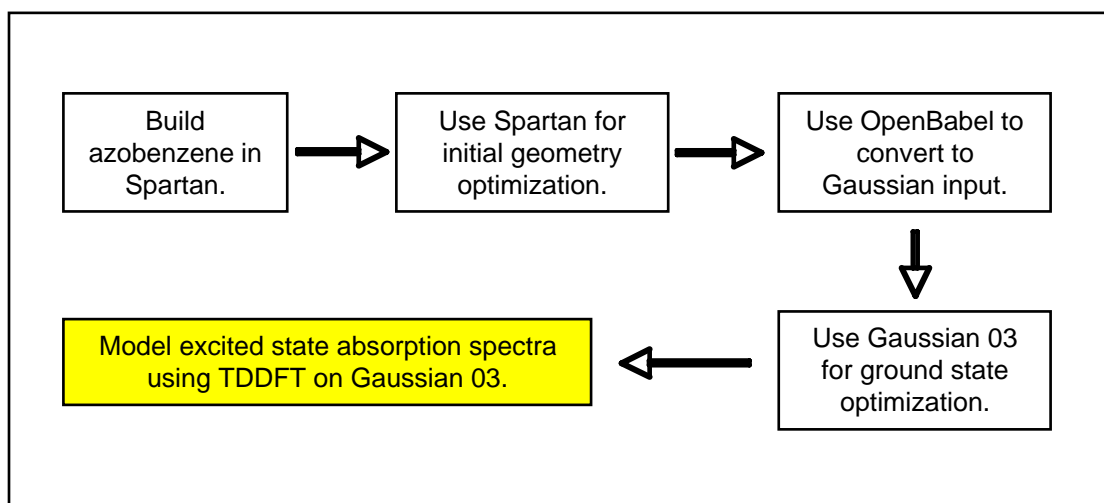


Fig. 3: Overview of the computational methodology used for the TDDFT calculations.

Spartan was also used for the initial geometry optimization, which is an important step for mapping the general structure. Spartan provides Cartesian coordinates for the approximate structures based on the bond lengths and angles of existing molecules. OpenBabel, a

chemical language translator, converted the Cartesian coordinates generated by Spartan into a Gaussian 03 input file. Using Gaussian 03, the ground states were first optimized by DFT. DFT optimizes the geometry by varying the coefficients of a selected basis set and the atom coordinates until a minimum energy is reached. Then the excited state absorption spectra were modeled using TDDFT. With TDDFT, an impulse potential containing all frequencies disturbs the molecular ground state so the absorption spectrum can be generated.

In order to accurately model the ground state and excited state absorption spectra, appropriate basis sets needed to be chosen. Basis sets determine the linear combination of spatially dependent elemental functions. In previous work it was established that out of the eighty-one Gaussian03 basis sets 6-311G(3d, 2p) was the most appropriate for the ground state geometry optimization of nickel dithiolenes [8]. This same basis set was applied to the azobenzene derivatives in hopes that it would later model azobenzene substituted nickel dithiolenes. For the excited state absorption spectra, the 6-311+G(d, 2p) basis set was chosen. Both the DFT and TDDFT calculations modeled the azobenzenes in cyclohexane solutions.

#### **4. Maximum Absorbance Wavelengths**

This study tested the accuracy to which TDDFT predicts the spectral properties of azobenzene derivatives. Five derivatives were chosen based on the experimental study conducted by Rau, Iacobescu and Meltzer [9]. The maximum absorbance wavelengths calculated by TDDFT were compared against experimental values (see Table 1). Each azobenzene derivative provided three maximum absorbance wavelengths. A reasonably good correlation was obtained between the theoretical and experimental values.

No.	Name	Experimental [9]	Theory
1	6"-methyl-4'-nitro-4-(N-phenylacetamidoxy)-azobenzene	249	336
		369	383
		422	494
2	6"-methyl-4'-cyano-4-(N-phenylacetamidoxy)-azobenzene	249	316
		353	368
		414	483
3	6"-methyl-4'-trifluoromethyl-4-(N-phenylacetamidoxy)-azobenzene	286	303
		349	356
		406	475
4	6"-methyl-4'-chloro-4-(N-phenylacetamidoxy)-azobenzene	247	294
		348	358
		402	465
5	4-(o-methyl-N-phenylacetamidoxy)-4'-[p-methyl-phenylazo] biphenyl	262	312
		332	388
		412	476

*All absorptions calculated using 6-311G(d,2p)*

Table 1: The maximum absorbance wavelengths calculated by TDDFT compared against experimental values from the literature (Ref 9).

When plotted against one another (Fig. 4), a Pearson correlation coefficient of  $R^2 = 0.95$  was found. When the wavelengths were converted into eV, there was a mean absolute error of 0.48 eV. An error of 0.4 eV is generally acceptable for azobenzene derivatives.

### 5. Free Energy Convergence Problems

Several azobenzene substituted nickel dithiolenes were also tested using the above-mentioned basis sets. However, the attempts to model the molecules using TDDFT were unsuccessful. The free energy of the molecules began to loop infinitely. This was attributed to the incorrect choice of basis sets. A large combination of spatially dependent elementary

functions substantially increases the computation time, and often leads no energy convergence. But too few functions would lead to poor accuracy.

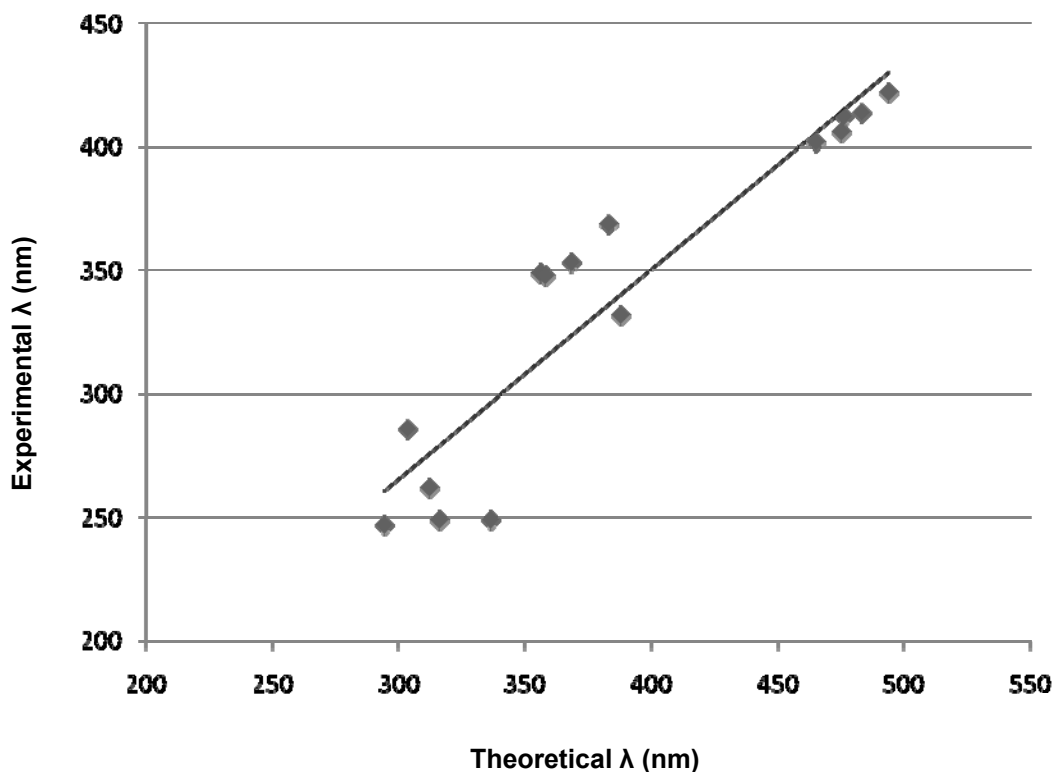


Fig. 4: Theoretical absorbance wavelengths calculated by TDDFT for the five substituted azobenzenes plotted against the experimental data for the same compounds. A Pearson correlation coefficient of  $R^2 = 0.95$  was found for this data.

Rather than discard basis sets marked as having the least convergence error, the azobenzene substituted nickel dithiolenes were modeled in a gaseous phase rather than in cyclohexane. This also resulted in free energy convergence problems that were attributed to the complexity of the azobenzene terminal groups. Computations ran between three to five days for each molecule. Although this is the typical computation time for nickel dithiolenes, it proved extremely inefficient considering that all molecules failed.

## 6. Discussion/Conclusions

The spectral properties of photochemically switchable azobenzene derivatives have been accurately modeled [9]. TDDFT was applied to the design of near IR photoswitchable nickel dithiolene dyes with terminal azobenzene groups. TDDFT can model highly complex molecules accurately, efficiently, and cost-effectively. Free energy convergence problems prevented modeling of both the core and the terminal groups at the same time. The absorbance spectra of the azobenzene derivatives were modeled independently of the dithiolene core. A reasonably good correlation was obtained between absorbance values calculated by TDDFT and experimental data for five azobenzene derivatives. Further research would entail finding appropriate basis sets to model the excited states for azobenzene substituted nickel dithiolene dyes.

## 7. Acknowledgements

I would like to thank the Laboratory for Laser Energetics for providing the resources that allowed me to do this research, Mr. Kenneth L. Marshall, my advisor, for guiding me along, Dr. Stephen Craxton for providing me this research opportunity, and my mentors Mary Coan and Rui Wang. I would also like to thank Tanya Kosc, Anthony Brancato, Violeta Kotarova-Gotcheva, Gaussian Inc., Wavefunction Inc, and all others in the Materials Lab at the Laboratory for Laser Energetics for giving me support.

## References

1. Mr. Kenneth L. Marshall, private communication.
2. M.C. Zerner; "ZINDO: A Semiempirical Quantum Chemistry Program", Quantum Theory Project; University of Florida, Gainesville, FL, 1996.

3. Stanton, J. F.; Gauss, J.; Ishikawa, N.; Head-Gordon, M. *J Chem. Phys.* 1995, 103, 4160-4174.
4. Runge, E.; Gross, E. K. U. *Phys. Rev. Lett.* 1984,52,997-1000.
5. Marshall, K. L. *et al*; “Using Time-Dependent Density Functional Theory (TDDFT) in the Design and Development of Near-IR Dopants for Liquid Crystal Device Applications”; Proc. of SPIE 2007 Vol. 6554, pp 65540F1-65540F13.
6. Frisch, M.J. *et al.*, Gaussian 03, Gaussian, Inc., Pittsburgh, PA, 2004.
7. SPARTAN '04, Wavefunction, Inc., 18401 Von Karman Ave., #370, Irvine, CA 92715, 2003.
8. Wang, Rui, “Computational Modeling of Spectral Properties of Nickel Dithiolene Dyes” ; LLE Summer High School Research Program, 2006.
9. Rau, Gabriela; Iacobescu, Gabriela; Meltzer, Viorica. *Revue Roumaine de Chimie.* 2005, 50(2), 119-124.

# **Design of an X-Ray Photoconductive Device Spectrometer**

**Eric Welch**

# **Design of an X-ray Photoconductive Device Spectrometer**

*Eric Welch*

*University of Rochester, Laboratory for Laser Energetics*

*2007 Summer High School Program*

When a target is imploded by the OMEGA laser, the plasma generated emits x rays. Cryogenic targets are affected by x rays that may preheat the fuel layer and make it harder to compress the fuel. Through the use of an x-ray spectrometer these x rays can be separated into their different wavelengths and measured, providing information important for understanding the implosion dynamics. An x-ray spectrometer was designed. It consists of a modified pinhole camera, a transmission grating, a diamond photoconductive detector (PCD) array, and a beryllium filter. The pinhole camera is used as the basic holder for the grating and diodes. The transmission grating separates the x rays into their individual wavelengths. The PCD's are used to determine the intensity of the diffracted x rays. The x-ray wavelength is calculated from the location of the PCD's. The beryllium filter is used to decrease the intensity of the x rays so that the grating will not be damaged.

## **Introduction**

The OMEGA laser at the Laboratory for Laser Energetics is attempting to obtain nuclear fusion through thermonuclear ignition of deuterium-tritium cryogenic targets. Thermonuclear ignition requires a temperature above 10 keV and density above 100 g/cm<sup>3</sup>. When the target is shot by the laser, it is transformed into plasma. The plasma implodes and briefly reaches the temperature and density requirements for thermonuclear ignition. After 100 picoseconds at these conditions, the target rapidly expands. X rays are emitted during the entire implosion process.

A model of the expected x-ray intensities integrated over time as a function of their energies has been calculated (Fig. 1). Preheating a cryogenic deuterium-tritium target involves heating the cold fuel layer prior to the target's implosion. When a target is preheated the core is much harder to compress and less neutrons are produced when compared to a non-preheated implosion. Fig. 1 shows the x-ray spectra expected for models with and without preheat.

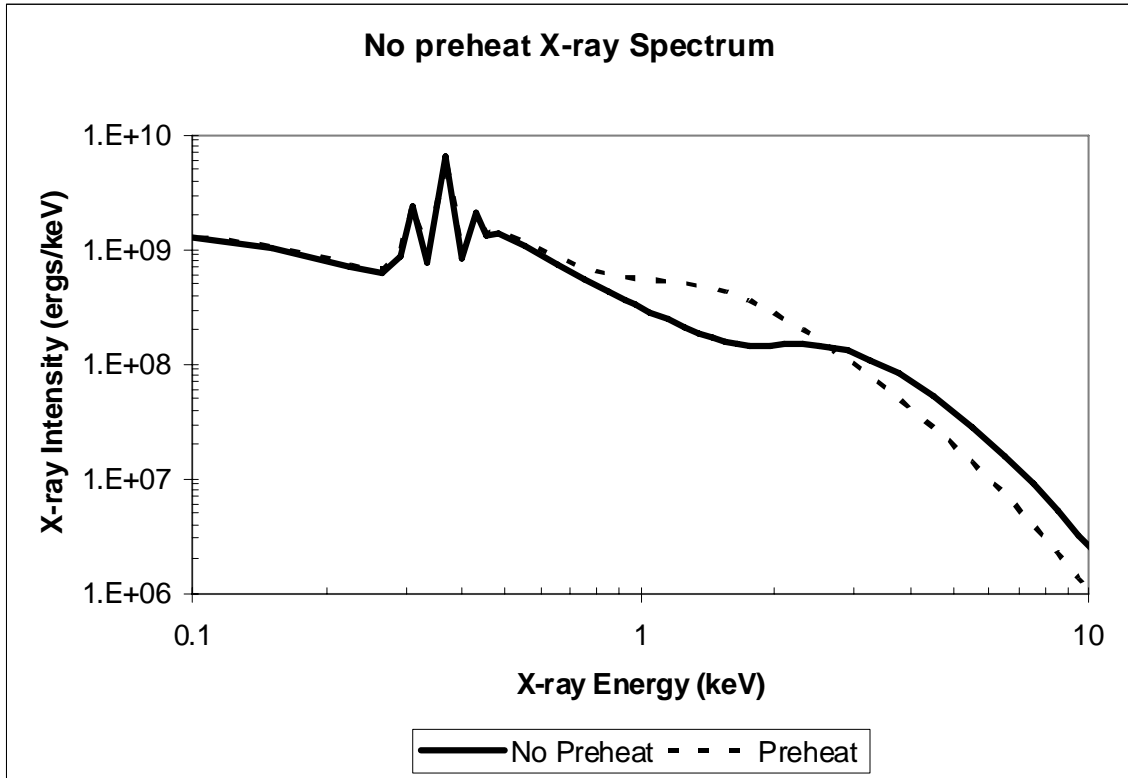


Fig. 1. The expected x-ray intensity as a function of its relative energy. The preheat and no-preheat models show a difference in intensity starting at about 0.5 keV.

The use of a spectrometer can provide valuable information about the implosion. The spectrometer provides information on how many volts each PCD emits. The voltage can be converted to intensity using a response function for each PCD. The position of the PCDs from the center can be used to calculate what wavelength range was detected. The equations will be able to provide the x-ray spectrum to determine dynamics of the implosion.

Diffraction is a property of light which makes the spectrometer possible. When light is passed through a small enough aperture, the waves will spread as if they came from the source. If many of these small openings are placed together interference occurs. Interference is when two waves of light combine either constructively or destructively. Constructive interference occurs when the two waves are in phase when combined and form anti-nodes (bright spot). Destructive interference is the opposite and instead of being in phase, the two waves are out of phase by  $180^\circ$  and form nodes (dark spots). A transmission grating has the same principle. Instead of many small apertures, a transmission grating is made up of a ruled light transmitting material. The grating used is

made of gold and has a period, or the distance from one slit to another, of 2000 Å. The longer wavelengths are diffracted much more than short wavelengths and therefore the spectrum is dispersed by the x-ray wavelength.

PCDs are used to detect light energy. These detectors consist of a semiconductor material, usually silicon, between two metal contacts. The PCD used for detecting x rays consists of a 1mm x 3mm x 1mm diamond semiconductor. Diamond is used because it has a higher band gap and a larger energy per electron-hole pair than silicon which makes it much less sensitive to UV energy. Electron and hole mobility, density, and resistivity help to increase the sensitivity to x ray energy.<sup>1</sup> When light energy is absorbed by the PCD, the valence electrons of the carbon atoms move to the conduction band. The electrons in the conduction band move to the anode and contribute to the electric current. The holes left by the electrons move to the cathode and also contribute to the current. This lowers the resistance of the diamond and the voltage increases. When too much x-ray energy is absorbed, many electrons move to the conduction band. This causes the carrier density to become too high and the resultant voltage will be less than what is predicted.<sup>2</sup>

The beryllium filter is used to protect the transmission grating and to prevent visible light from entering. The high intensity of the x rays will damage the grating and it may have to be replaced after every shot. The x rays are able to pass with only minor energy loss. The beryllium used for the spectrometer will be 25 µm thick and will be placed before the pinhole.

### **Transmission Grating and Photoconductive Detectors**

The experimental configuration is shown in Fig. 2. A transmission grating is placed 600 mm from the target and 1076 mm from the PCDs. The PCDs must be at least 1.5 mm and not more than 42 mm from the image, or 0<sup>th</sup> order. The image of the implosion will have a radius of 1.5 mm from the center and the diameter of where the PCDs will be placed is 85 mm, leaving a maximum distance of 42 mm. Based on this, the wavelength of the x rays can be calculated using

$$\lambda = \frac{d \sin \theta}{n} \quad (1)$$

where  $\lambda$  is the wavelength,  $d$  is the grating period,  $\theta$  is the diffraction angle, and  $n$  is the diffraction order.<sup>3</sup> Using this, the maximum energy that can be viewed by this spectrometer is 4446 eV at order 1 and 824 eV at order 5.

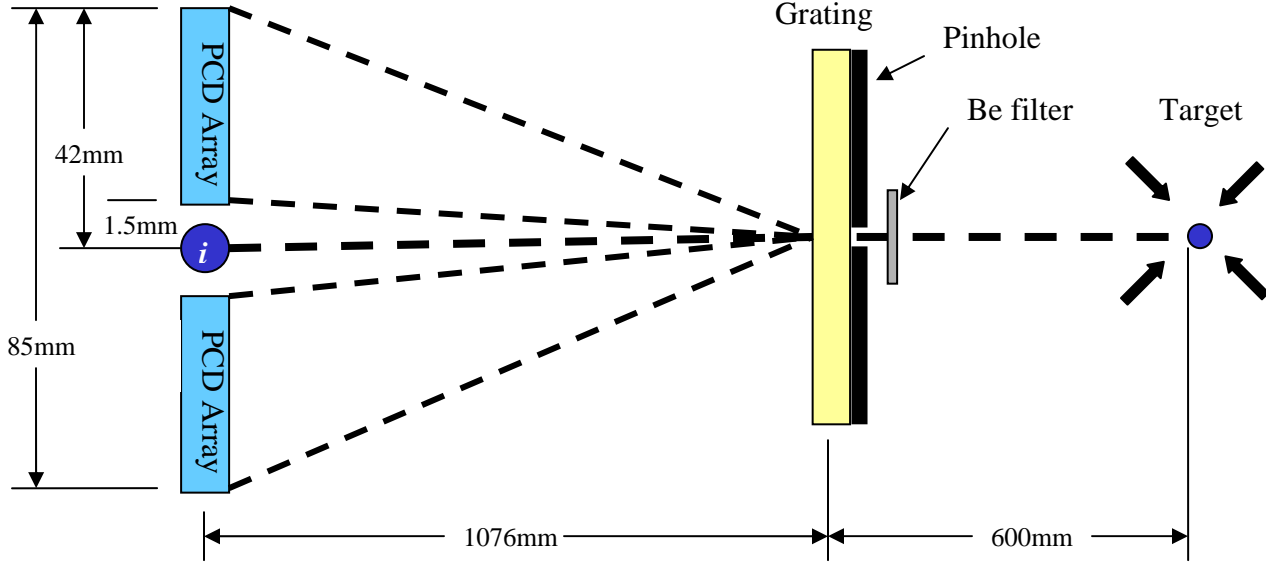


Fig. 2. Experimental configuration. The image (*i*) does not interfere with the PCD array. The image has a 1mm radius and the closest PCD is 1.5mm away from the center of the image.

When the x-ray energy passes through the beryllium filter, pinhole, grating, and PCDs, much of the energy is lost. The total intensity ( $E_x$ ) reaching the detectors can be calculated by

$$E_x = E_{rad} \cdot \varepsilon_g \cdot \varepsilon_\tau \cdot \left( \frac{\pi r^2}{l^2} \right) \cdot \left( \frac{1}{4\pi} \right) \cdot \left( 1 - e^{-t/\lambda_x} \right) \quad (2)$$

where  $E_{rad}$  is the initial intensity of the x rays,  $\varepsilon_g$  is the grating efficiency,  $\varepsilon_\tau$  is the transmission of the beryllium,  $r$  is the radius of the pinhole,  $l$  is the length from the source to the pinhole,  $t$  is the thickness of the PCD, and  $\lambda_x$  is the x-ray mean free path in diamond. The x-ray efficiencies and mean free path do not have to be calculated and are available at Lawrence Berkeley National Laboratory.<sup>4</sup> So much energy is lost that at the distances above, order one has an intensity nearly zero at low x-ray energy. Different orders have to be used to counteract this problem. By calculating the total efficiency and

determining which order has the least energy loss at each distance, the ideal order can be used. Based on these calculations, order 1 will be used between 1.5 mm and 6.5 mm, order 3 will be used between 6.5 mm and 16 mm, and order 5 will be used between 16 mm and 42 mm (Fig. 3).

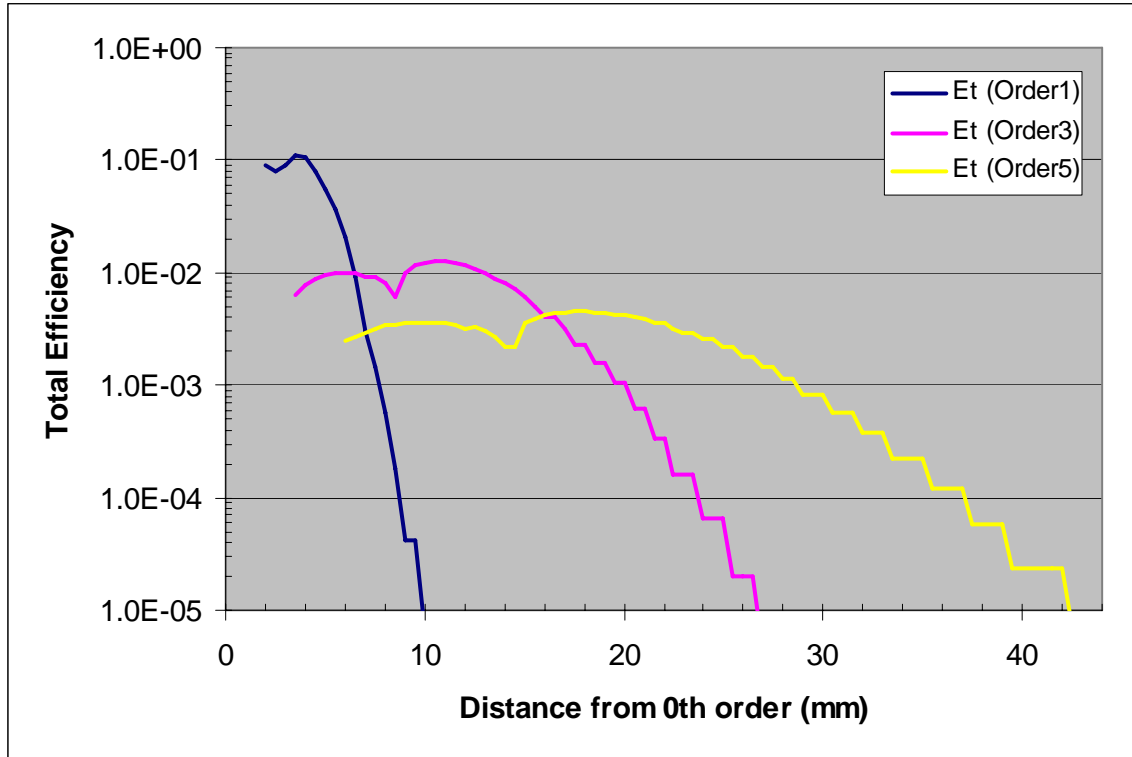


Fig. 3. The total efficiency at distances from 0<sup>th</sup> order. This shows that 3 orders must be used to ensure the total 42 mm distance can be detected.

The placement of the PCDs can now be determined (Fig. 4). The PCD array used for this experiment is expected to have a 1 mm distance between the diodes and have connectors on three sides. The desired energy range for each diode is 300 eV. To achieve this, the PCDs must be placed horizontal in the first and third orders and placed vertical in fifth order.

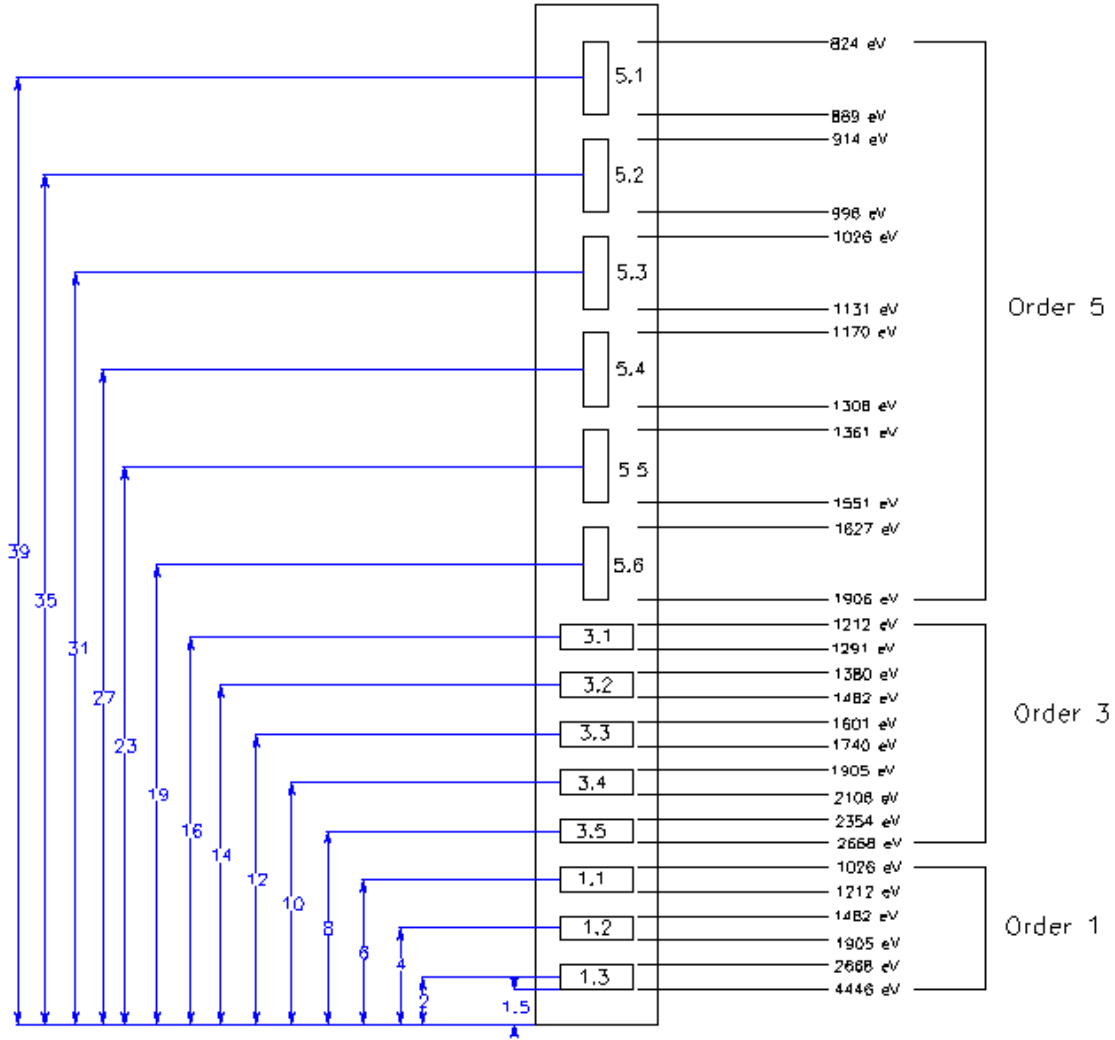


Fig. 4. The placement of the PCDs. Based on the distances the diodes are placed the energy range each diode will capture can be calculated.

Using equation 1, the energy range for each diode can be calculated. These energies can be graphed with the expected x-ray spectrum (Fig. 5). The combined coverage covers most of the x-ray energies between about 800 eV and 4500 eV. The inconsistency between the preheat and no-preheat spectrum which occurs in this region makes the placement ideal.

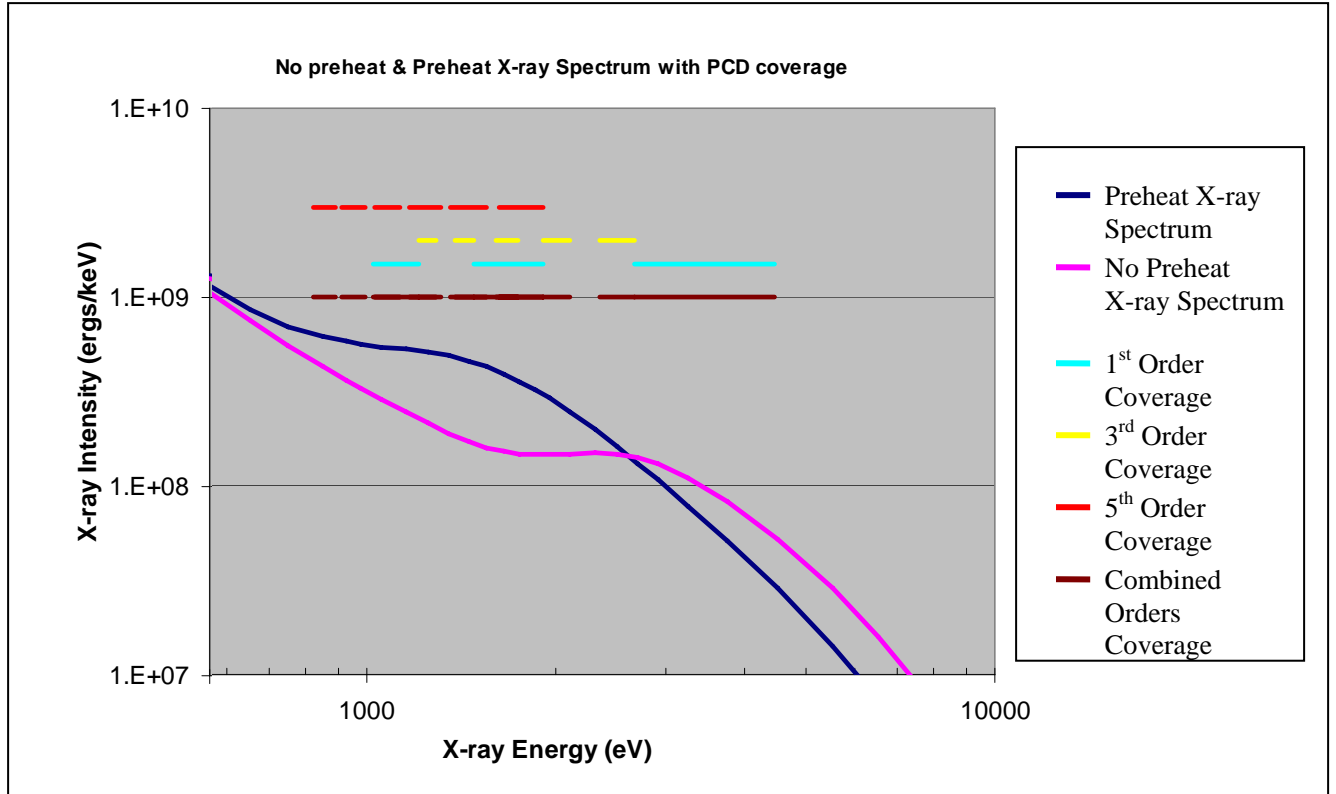


Fig. 5. PCD coverage and x-ray spectrum. The coverage by the PCDs is consistent with the difference between the preheat and no-preheat spectrum in the 800 to 4500eV range.

### Expected Data

The expected voltage output of the PCDs can be calculated. This data can be compared to what the actual voltage is. The equation used for determining the voltage out ( $V_{out}$ ) is

$$V_{out} = (qE)ARn_0(\mu e^{-t/\tau}) \quad (3)$$

where  $q$  is the electron charge,  $E$  is the applied field,  $A$  is the cross-sectional area,  $R$  is the impedance,  $n_0$  is the carrier density,  $\mu$  is the carrier mobility,  $t$  is time, and  $\tau$  is the carrier lifetime.<sup>5</sup> For these calculations  $q$  is  $1.6 \times 10^{-19}$  Coulombs,  $E$  is  $10^4$  V  $\text{cm}^{-1}$ ,  $A$  is  $0.03$   $\text{cm}^2$ ,  $R$  is  $50$   $\Omega$ ,  $\mu$  is  $4000$   $\text{cm}^2$   $\text{V}^{-1}$   $\text{s}^{-1}$ ,  $t$  is  $0$  seconds, and  $\tau$  is  $180$  ps.<sup>6</sup> To calculate  $n_0$ , two equations are used:

$$n_0 = \frac{E_x \cdot (1 - e^{-z/\lambda_x})}{\gamma \cdot A_{xy} \cdot \lambda_x} \quad (4.1)$$

$$n_0 = \frac{E_x \cdot z}{\gamma \cdot A_{xy} \cdot \lambda_x^2} \quad (4.2)$$

where  $E_x$  is the energy reaching the detector,  $t$  is time,  $\lambda_x$  is the x-ray attenuation length,  $\gamma$  is the energy per electron-hole pair,  $A_{xy}$  is the cross-sectional area, and  $z$  is the diode's thickness. For this equation  $t$  is 0 seconds,  $\gamma$  is 13,  $A_{xy}$  is  $0.03 \text{ cm}^2$ , and  $z$  is 0.01 cm. The value for  $\lambda_x$  can be found from Ref. 4. Equation 4.1 is used to calculate the peak carrier density and equation 4.2 for the average carrier density throughout the diamond.

Using equation 3 with the energy values for each PCD, the expected voltage can be calculated (Table 1). There is a direct relationship between the voltage and the x-ray intensity. The high no preheat voltage at the energy levels between 2604 eV and 4339 eV shows a high temperature implosion. Between 1142 eV and 1698 eV the preheat voltage is double the voltage of the no preheat. At the lower energies, between 804 eV and 1104 eV, the voltages with and without preheat are nearly equal.

Table 1. Expected voltages at specific distances.  $V_{out}$  calculated with equation 3 using equation 4.2 to calculate  $n_0$  can be used to predict the voltage the PCD will release.

Distance from 0 Order	X-ray energy (eV)	No Preheat Voltage	Preheat Voltage
1.5 – 2.5 mm	4339 – 2604	$1.7 \times 10^0$	$2.2 \times 10^{-1}$
3.5 – 4.5 mm	1860 – 1447	$8.8 \times 10^{-1}$	$1.1 \times 10^0$
5.5 – 6.5 mm	1184 – 1001	$1.4 \times 10^{-1}$	$1.4 \times 10^{-1}$
7.5 – 8.5 mm	2604 – 2297	$4.8 \times 10^{-2}$	$3.8 \times 10^{-2}$
9.5 – 10.5 mm	2056 – 1860	$4.7 \times 10^{-2}$	$6.4 \times 10^{-2}$
11.5 – 12.5 mm	1698 – 1562	$3.2 \times 10^{-2}$	$6.7 \times 10^{-2}$
13.5 – 14.5 mm	1447 – 1347	$1.9 \times 10^{-2}$	$2.8 \times 10^{-2}$
15.5 – 16.5 mm	1260 – 1184	$1.0 \times 10^{-2}$	$2.8 \times 10^{-2}$
17.5 – 20.5 mm	1860 – 1588	$3.2 \times 10^{-2}$	$4.8 \times 10^{-2}$
21.5 – 24.5 mm	1514 – 1329	$1.3 \times 10^{-2}$	$1.7 \times 10^{-2}$
25.5 – 28.5 mm	1277 – 1142	$6.3 \times 10^{-3}$	$1.0 \times 10^{-2}$
29.5 – 32.5 mm	1104 – 1002	$2.4 \times 10^{-3}$	$2.3 \times 10^{-3}$
33.5 – 36.5 mm	972 – 892	$7.3 \times 10^{-4}$	$1.0 \times 10^{-3}$
37.5 – 40.5 mm	868 – 804	$3.4 \times 10^{-4}$	$2.3 \times 10^{-4}$

## The Design

The x-ray spectrometer is based on a pinhole camera body (Fig. 6). Custom parts are created and added to the body to create the specific distances necessary. The transmission grating is placed between two parts in a 0.1” gap. The two parts are fastened together and then fastened to the camera body. The pinhole part is also attached to these parts. The pinhole part is tantalum with an outer diameter of 0.5” and a thickness of 0.01”. The pinhole assembly also contains a place for the 25  $\mu\text{m}$  beryllium filter. The back of the camera contains the PCD array. The back plate contains the array which will be adjustable.

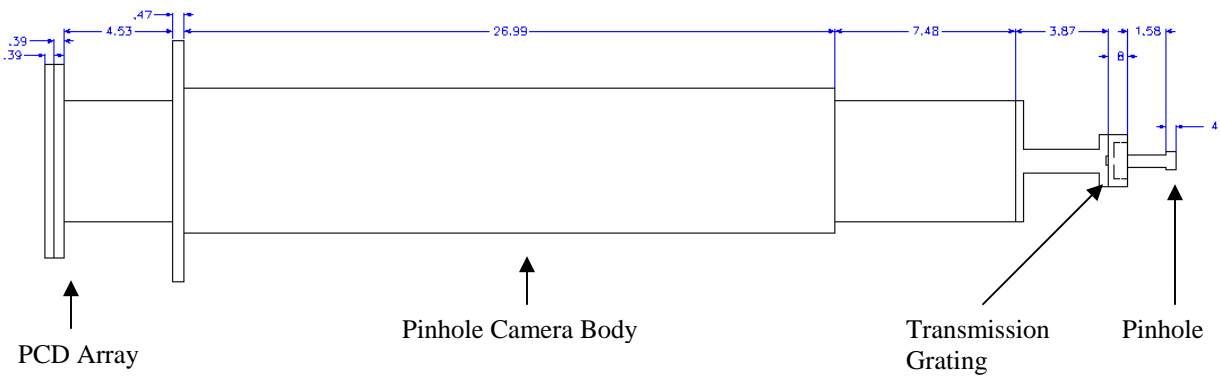


Fig. 6. The X-ray spectrometer design. The spectrometer uses a pinhole camera body with some custom parts. The pinhole is 525 mm from the center of the target chamber, the transmission grating is 600 mm from the target, and the PCD array is 1814 mm away from the target.

The camera must also be able to be centered. The exact way still has to be determined. One possible solution is to use the array and adjust it so one of the detectors is in the center. The spectrometer can be adjusted until the detector detects the image. Another solution is to use film and adjust the camera based on where the image appears on the film. The disadvantage of using film is that the vacuum will have to be broken to develop the film. The ideal solution is to move the detectors but accomplishing this may prove to be difficult.

## Conclusion

The x-ray spectrometer design will be able to detect the region where the preheat and no-preheat spectra models differ. The intensities found with the spectrometer can be used to determine the dynamics of the implosion. Based on the voltage output of the

PCDs, the intensity of the x rays can be calculated. The energy of the x rays can also be calculated based on how far the PCDs are away from the center of the image. The x-ray energies and intensities can be combined to produce a chart which can be compared to the expected data for the preheat and no preheat models. This design of an x-ray spectrometer will be very useful in the effort to obtain thermonuclear ignition.

### **Acknowledgements**

I would like to thank my advisor, Dr. James Knauer, for his guidance throughout this project. I would also like to thank Dr. Stephen Craxton for allowing me to participate in this program and for an unforgettable experience.

### **References**

1. D. R. Kania *et al.*, ‘Diamond radiation detectors,’ *Diamond and Related Materials* **2**, 1012 (1993).
2. L. S. Pan, D. R. Kania, and O. L. Landen, ‘Carrier density dependent photoconductivity in diamond,’ *Appl. Phys. Lett.* **57** (6), 623 (1990).
3. J. L. Weaver *et al.*, ‘The determination of absolutely calibrated spectra from laser produced plasmas using a transmission grating spectrometer at the Nike laser facility,’ *Rev. Sci. Instrum.* **72** (1), 108 (2001).
4. B.L. Henke, E.M. Gullikson, and J.C. Davis, ‘X-ray interactions: photoabsorption, scattering, transmission, and reflection at E=50-30000 eV, Z=1-92,’ *Atomic Data and Nuclear Data Tables.* **54** (2), 181-342 (July 1993).
5. L. S. Pan *et al.*, ‘Particle- and photoinduced conductivity in type-IIa diamonds,’ *J. Appl. Phys.* **74** (2), 1086 (15 July 1993).
6. M. A. Plano *et al.*, ‘Polycrystalline CVD Diamond Films with High Electrical Mobility,’ *Science* **260**, 1310 (28 May 1993)

# **Unfolding X-Ray Spectra from a Multichannel Spectrometer**

**Andrew Yang**

**Unfolding x-ray Spectra from a Multichannel Spectrometer**

Andrew Yang

Fairport High School

LLE Advisor: Reuben Epstein

**Laboratory for Laser Energetics**

University of Rochester

Summer High School Research Program

August 15, 2007

**Abstract:**

Limitations exist on the amount of spectral detail that can be unfolded from multichannel spectrometer readings and their known filter response functions. These limitations exist because during the process of converting (“folding”) x ray spectra into channel voltage readings, a lot of spectral detail and information is inevitably lost. Thus the process of “unfolding,” inferring a spectrum from a set of channel readings and their known response functions, can only recover a limited amount of spectral information. The goal of this project was to find out what parameterized spectrum model, when used with weighted least squares fitting, recovers the most spectral information. Weighted least squares, the method used to unfold the spectra, is a parameter estimation technique that finds the model spectrum parameters that are most consistent with the readings of the multichannel spectrometer. The multigroup model spectrum, with bin widths based on filter function edges, is the most reliable parameterized spectrum model.

**1.1 Introduction:**

During a direct drive fusion experiment conducted at the Laboratory for Laser Energetics, multiple high power laser beams strike a very small deuterium/tritium target. As a result, this target implodes at an exceedingly high velocity and emits x rays of various wavelengths. It is very important to study the entire spectrum of x rays emitted. Currently, at the Laboratory, a multi-channel spectrometer called Dante is used to analyze the x ray spectrum emitted by the imploding target. Dante is able to accurately interpret spectral power. However, Dante provides only a limited amount of spectral information. In this report, various “unfolding” algorithms for converting Dante measurements into the x ray spectrum emitted by the imploding target will be analyzed.

Dante is an x ray spectrometer currently used at the Laboratory for Laser Energetics to measure the spectra emitted by imploding targets. Dante is comprised of 19 distinct channels. Each channel covers different spectral regions spanning from 50 eV to 20 keV with 20-ps resolution. Only 15 channels are used in the following models because these channels have

spectral regions pertaining to the photon energies in the simulated LILAC spectra. In each channel, x ray radiation passes through a spectrally distinct filter which is opaque to certain photons. The remaining photons pass through the filter into an x ray diode, which registers the total power of the x ray radiation incident on it as a voltage reading.<sup>1</sup> These voltage readings can be expressed with the equation:  $V_i = \int_0^{\infty} k_i S(h\nu) f_i(h\nu) d h\nu$  [ $i = 1, 2, \dots, M$ ], where the spectrum,  $S(h\nu)$ , is folded into the filter response function,  $f_i(h\nu)$ , to give  $V_i$ , the voltage reading. Here,  $k_i$  is the fraction of the total spectrum captured by the channel, and  $M$  is the number of channels on the spectrometer,  $h$  is Planck's constant, and  $\nu$  is the frequency of a certain photon in the spectrum. A channel's sensitivity to certain photons can be characterized by its filter response function  $f_i(h\nu)$ .

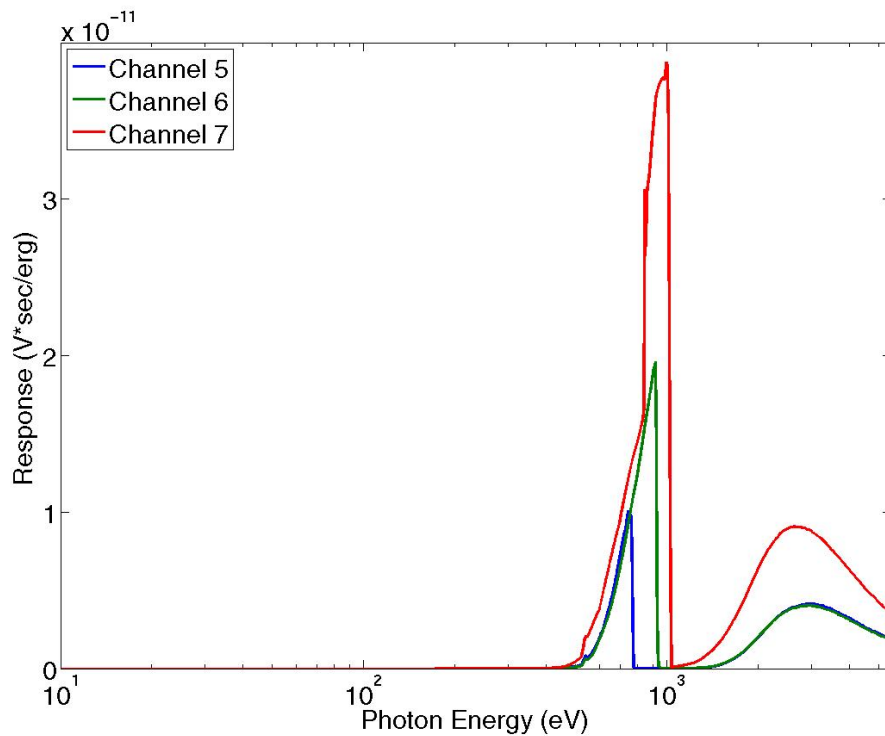


Fig. 1. Dante filter functions 5, 6, and 7 are plotted vs. photon energy. Each channel is sensitive to a specific range of photon energies. The location where the filter function turns suddenly opaque to certain photons corresponds to a photo-ionization “edge” of the filter material.

LILAC is a program used at the Laboratory for Laser Energetics that simulates an entire target implosion, including the x ray emission, at a series of time steps. The x ray emission is

divided into 48 spectral groups. The LILAC simulated x ray spectrum is then folded into the Dante channel response functions to obtain the voltage readings. These voltages are then unfolded into a spectrum that is compared with the original LILAC spectrum. Various algorithms are compared to see which one recovers the most spectral detail with the most accuracy.

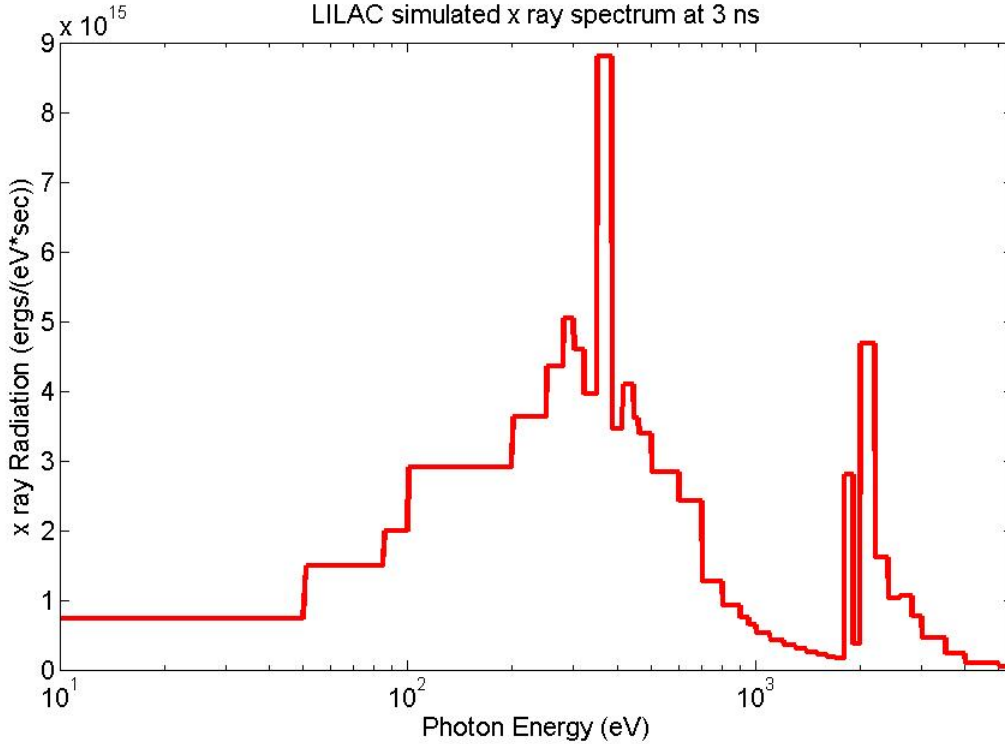


Fig. 2. A LILAC simulated spectrum of a target implosion at 3 ns is chosen as an example of hypothetical data. This simulated spectrum will be folded into Dante response functions and then unfolded as a fitted spectrum in order to illustrate the unfolding algorithm used.

## 2.1 Methodology:

The x ray spectra were unfolded using the weighted least squares method.<sup>3</sup> In this method, the set of parameter estimates  $x_j$ , that minimizes  $\chi^2 = \sum_{i=1}^M \frac{(V_i - Z_i)^2}{\sigma_i^2}$  is found, where  $V_i$  are measured voltage values,  $Z_i$  are the theoretical voltage values obtained from the model spectrum defined by the parameter estimates, and  $\sigma_i$  are the unavoidable random measurement errors in each channel associated with the experiment. The minimum of  $\chi^2$  is obtained when

$\frac{\partial \chi^2}{\partial x_j} = 0$  for all the parameters. This condition is satisfied by the solution to the set of M

equations and M unknowns,

$$\sum_{i=1}^M -\frac{2Z_i}{\sigma_i^2} \frac{\partial f(x_k; t_i)}{\partial x_j} + \frac{2f(x_k; t_i)}{\sigma_i^2} \frac{\partial f(x_k; t_i)}{\partial x_j} = 0.$$

Here, one assumes that the spectrum can be modeled as a function of the parameters  $x_k$  and  $t_i$ , where  $t_i$  is time. Time is a variable because a spectrum is time dependent, but it is not one of the fitting parameters. In other words,  $f(x_k; t_i)$  is the function which models the spectrum. One can use Newton's method to solve the equations described by the equation above. In this method, one iteratively uses nominal parameter values as guesses, in order to obtain corrections to these guesses. This iterative process converges to the actual solution. When applying this methodology to solve for the zero, one will come up with a system of equations written in matrix notation as  $\mathbf{J} * \Delta \mathbf{x} = \mathbf{r}$ . Here,  $\mathbf{J}$  is a square matrix, also known as the coefficient matrix, with length and width equal to the number of parameters, and  $\Delta \mathbf{x}$  and  $\mathbf{r}$  are both column vectors with lengths equal to the number of parameters. The quantities  $\mathbf{J}$  and  $\mathbf{r}$  are given by:

$$\mathbf{J}_{jk} = \sum_{i=1}^M \frac{1}{\sigma_i^2} \frac{\partial Z_i^0}{\partial x_j} \frac{\partial Z_i^0}{\partial x_k}, \text{ and}$$

$$\mathbf{r}_j = \sum_{i=1}^M \frac{1}{\sigma_i^2} \frac{\partial Z_i^0}{\partial x_j} (V_i - Z_i^0).$$

The superscript 0 in  $Z_i^0$  is used to denote the fact that nominal parameter values were used to obtain the voltage values. The elements of  $\Delta \mathbf{x}$  contain are the set of corrections that, when added to the set of parameter estimates, create a better set of parameter estimates. The set of corrections are obtained by multiplying each side of the equation by the matrix inverse of the coefficient matrix,  $\Delta \mathbf{x} = \mathbf{J}^{-1} * \mathbf{r}$ . The coefficient matrix is inverted using singular value decomposition as described by Press *et al.*<sup>4</sup> This particular method is used in order to minimize the deleterious effect of the near singularity of the coefficient matrix. After  $\Delta \mathbf{x}$  is found, new estimates for  $Z_i^0$  are calculated, which are closer to the actual solution. These corrections become smaller with each iteration. This process is repeated until the corrections become negligible. At this

point,  $\frac{\partial \chi^2}{\partial x_j} = 0$ , and the parameter values are considered to have been solved for all practical purposes. This entire process is programmed in Matlab.

## 2.2 Formal Errors Estimates:

One of the benefits of using the weighted least squares method is that formal error estimates of the parameter estimates, based on the random errors of the experiment, can be found.<sup>3</sup> The  $J^{-1}$  matrix is also known as the covariance matrix. Its elements are the covariances of the parameter estimates between parameter estimates  $x_j$  and  $x_i$ ;  $J_{ij}^{-1} = \langle \delta x_j \delta x_i \rangle$ . The angle brackets indicate the statistically expected value. The expected error is based on the assumption that the voltage errors,  $V_i$ , are normally distributed about 0. When  $j=i$ ,  $J_{ii}^{-1} = \langle \delta x_i^2 \rangle$ . Thus, one can take the square root of the elements on the major diagonal of the covariance matrix to see the errors associated with all of the parameter estimates. This is the method used to place error bars on the parameter estimates.

Total spectral power,  $P$ , and error,  $\delta P$ , can also be calculated, as  $P = \int_0^\infty S(h\nu) d h\nu$ . Total spectral power error,  $\delta P$ , can be found with the equation:

$$\delta P = \sqrt{\sum_{k=1}^M \sum_{j=1}^M \frac{\partial P}{\partial x_k} \frac{\partial P}{\partial x_j} \langle \delta x_k \delta x_j \rangle}$$

where once again,  $M$  is the number of parameters, and  $\langle \delta x_k \delta x_j \rangle$  is the variance of parameters  $k$  and  $j$ .

## 3.1 The Fits:

The weighted least squares method finds the set of parameter values that minimizes  $\chi^2$  for a particular spectral model. However, this method places no restrictions on the spectral model and its parameterization. Well-chosen models will give a more accurate representation of a spectrum than other models.

### 3.2 The Polynomial Fit:

A very popular fit used in many applications of curve fitting is the polynomial fit. In this fit, the spectrum is modeled with the equation

$$S(x) = a_1x^n + a_2x^{n-1} + a_3x^{n-2} + \dots + a_n,$$

where the fitting parameters are  $a_n$ .

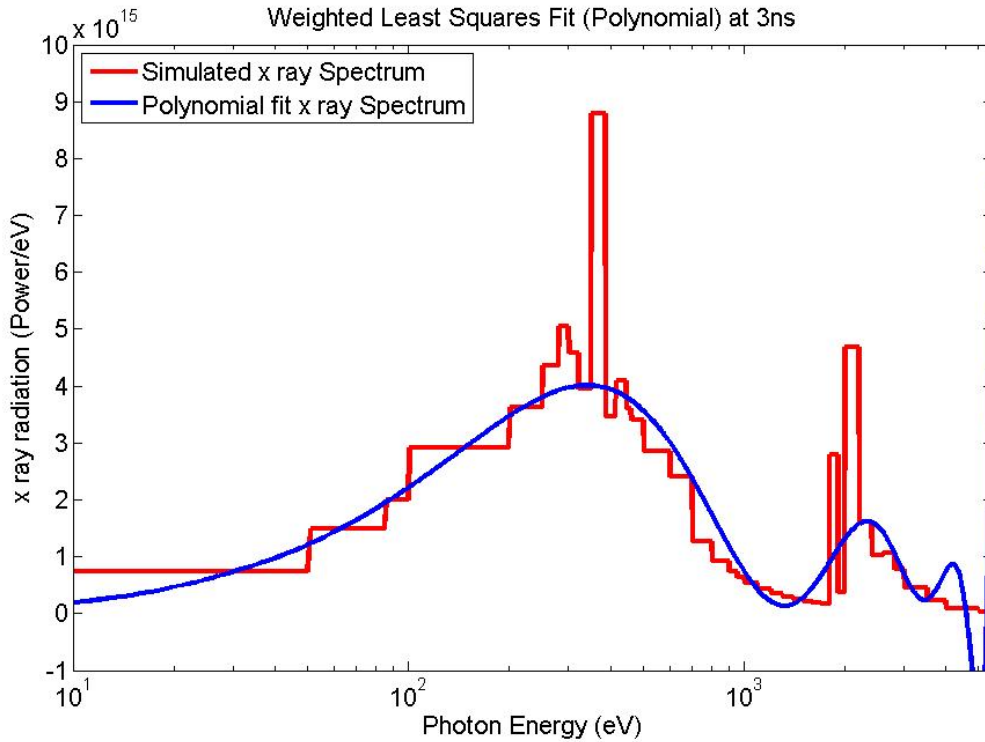


Fig. 3. The polynomial fit of the hypothetical spectrum obtained with a 10-parameter fit is shown. Fifteen Dante channels were used to unfold the spectrum.

A polynomial does not fit this spectrum well. The narrow spectral lines emitted by an imploding target are represented poorly by a smooth polynomial curve. In an attempt to match the peaks of the spectrum, artificial curves on the right side of the spectrum were generated. Furthermore, one of the major faults of a polynomial fit is the correlation between parameters. Correlation occurs when one parameter affects the value of another parameter. In this example, the adjustments in any one parameter (any one coefficient  $a_n$ ) will strongly affect the fitted

values of some of the other parameter values. This correlation was evident in the resulting near-singular  $\mathbf{J}$  matrix. The condition number, a number which gives evidence of a near-singular matrix,<sup>4</sup> was:  $2.05 \times 10^{-70}$ . A completely singular matrix has a condition number of 0. Therefore, the coefficient matrix in this example was very close to singular. The inverse was only approximated, the true solution could not be obtained, and the fit is not as unambiguous as it should be. A polynomial is obviously not a viable fit for this spectrum.

### 3.3 Spectral Point Fit:

In the spectral point method, the fitting parameters are the spectral points. Each point can move up and down to best fit the voltage readings. Neighboring spectral points are then connected with straight lines.

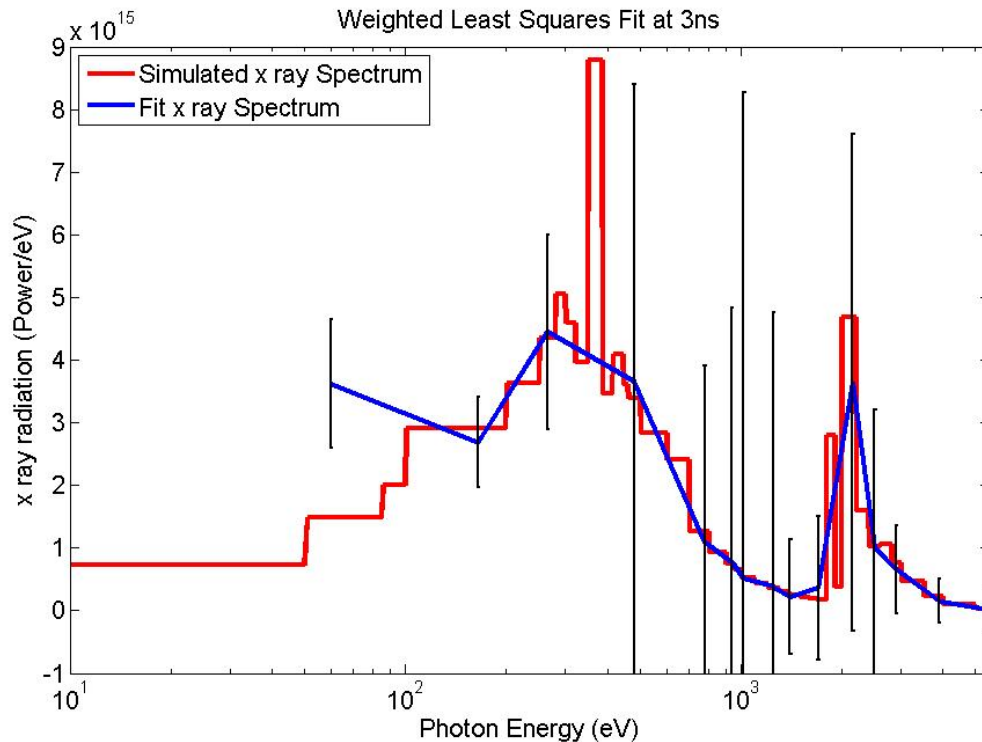


Fig. 4. A spectral point fit of the hypothetical spectrum is shown. Spectral points were placed in the middle of each filter function sensitivity range. Error bars were generated based on a 10% accuracy in Dante voltage readings.

Although the model spectrum is quite accurate, the error bars are very large. This is caused by the anti-correlation between the estimates of adjacent spectral points. If one point moves upward, re-optimizing the fit of the model spectrum to the voltage readings will push surrounding spectral points downward to maintain the quality of the fit of the model spectrum to the voltage reading data. Thus, the parameter estimates have some room to move, which translates into large error bars.

Despite the high relative uncertainties in the parameter estimates, the relative uncertainty in the power is still quite low. The total spectral power was  $5.30 \cdot 10^{18}$  ergs/sec, with an estimated error of  $6.18 \cdot 10^{17}$  ergs/sec. This is a relative uncertainty of 11.67%, which is much smaller than the error bars in Fig. 4 would suggest. This reflects the strong anti-correlation between the parameters. Although not much confidence can be placed on each parameter estimate individually, a lot of confidence can be placed on the total spectral power estimate.

### **3.4 Correlations:**

The largest problem that exists in both the spectral point fit and the polynomial fit is the large correlations between the parameter estimates for both models. A large correlation implies that a change in any one parameter estimate will drastically affect a different parameter estimate. Strong correlations generally impair the quality of the fit by creating a near-singular  $\mathbf{J}$  matrix, which reduces the accuracy of the parameter estimates, which can be seen in the large error bars of the spectral point fit. The errors associated with the parameter estimates in this model were unacceptable. Finding a set of parameters which are not correlated with one another is vital.

### **3.5 The multigroup model spectrum:**

One way to reduce the deleterious correlation between parameter estimates is to use a multigroup model spectrum, where one divides the entire spectrum into a number of intervals. A set of numbers  $n_k$  are the average spectrum values within each interval  $k$ . The different  $n_k$  numbers are the fitting parameters. The edges of the interval will be placed at the edges of the

filter functions.<sup>2</sup> It is very important to use filter function edges because if a filter has strong sensitivity in more than one parameter range, correlation will again present a problem. For example, when a filter function has sensitivity in two spectral intervals, the spectral values of the two intervals will be strongly anti-correlated with one another. If one parameter estimate increases, the other is able to decrease without affecting the overall voltage reading of the channel. By using filter function edges as interval boundaries, this anti-correlation will be minimized.

### 3.6 The “flat-top” multigroup model spectrum:

A “flat-top” multigroup model spectrum is the simplest multigroup spectrum. In each interval, there is only one spectrum value. Thus, each interval will have a “flat-top”.

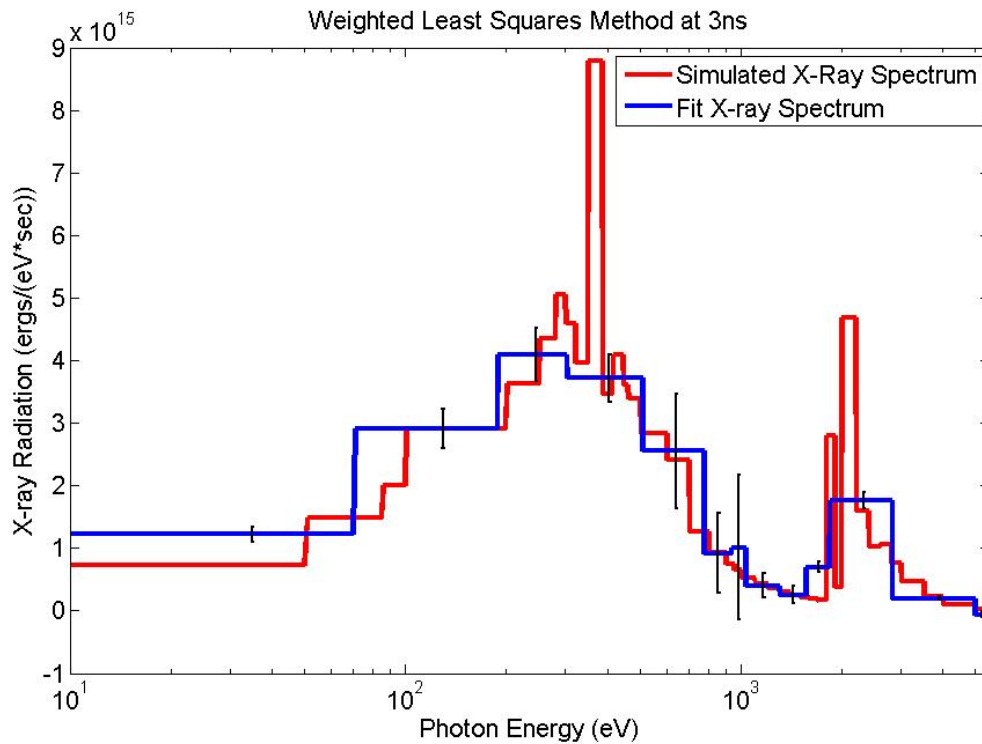


Fig. 5. A sample of the flat-top multigroup model spectrum with 13 intervals is shown. Error bars were generated based on a 10% accuracy in the voltage readings. Intervals were determined by the Dante filter function edges.

The “flat-top” multigroup model spectrum consistently models the general shape of the

actual spectrum. The error bars are also much smaller. However, almost no spectral detail is apparent in the model.

This model also minimizes spectral power uncertainty, which is estimated to be  $5.07 \cdot 10^{18}$  ergs/sec, with a relative uncertainty in the spectral power of only 4.13%.

### **3.7 The “spectrum-top” multigroup model spectrum:**

It is possible to use an expected spectrum as a guide when trying to fit Dante voltage readings. In this case, apparent detail in the fitted model spectrum that was not contained in the individual voltage readings is shown. This fit is an extension of the flat top model. Here, instead of using one average spectrum value in each interval as in the flat-top model, the form of the anticipated spectrum is retained within each interval. For this fit, an initial nominal guess of what the spectrum might possibly look like is needed. This nominal guess could be obtained from a LILAC simulation, for example, which has been done here. This nominal spectrum is broken up into several intervals and a multiplying factor  $n_k$  is added to the spectrum value in interval  $k$  as the adjustable model parameter.

This model spectrum fit shown in Fig. 6 is a very accurate representation of the spectrum. Almost all of the spectral detail has been artificially restored. This is not surprising, given that the shape of the model spectrum within each interval and the hypothetical voltage readings are obtained from the same LILAC-simulated spectrum. However, the relative uncertainties on each parameter are still quite large. This shows that errors are independent of how well the model spectrum fits the simulated spectrum.

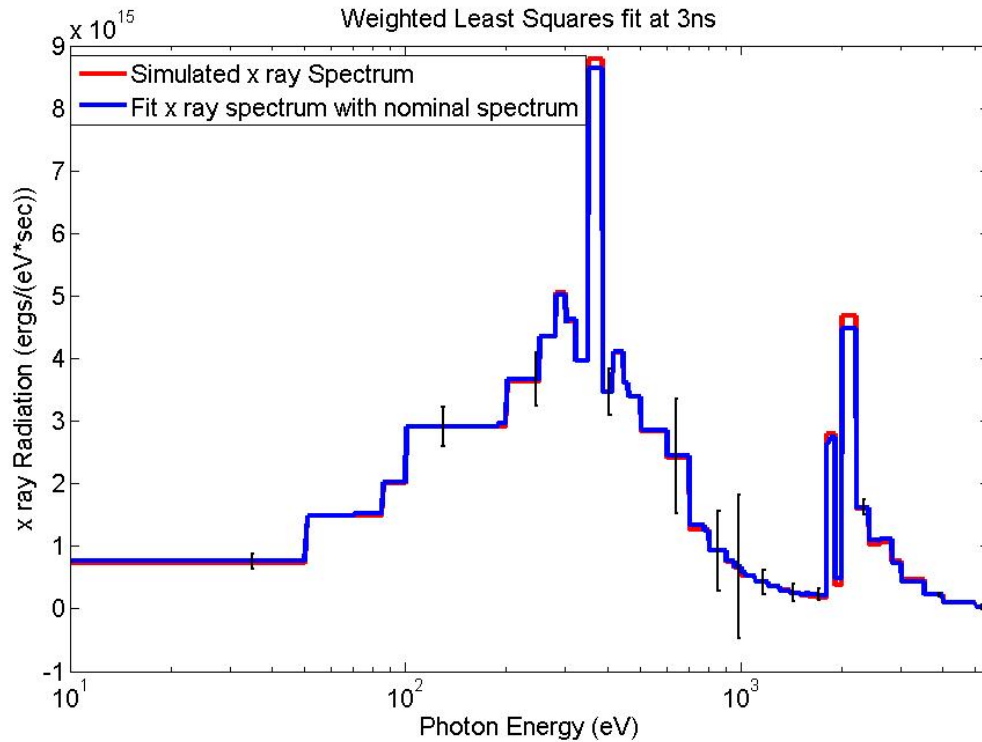


Fig. 6. A sample of a fit using the spectrum-top multigroup model spectrum with 13 intervals. Error bars were generated based on a 10% accuracy in the voltage readings. The LILAC simulation at 3 ns was folded into voltage readings and the simulated x ray spectrum at 2.98 ns was used as the nominal spectrum. Together, the voltages and the nominal spectrum were used to create the model.

The total model spectral power in this example was  $5.42 \cdot 10^{18}$  ergs/sec and the relative error was 3.87%. This small uncertainty in the estimate of the total power results from a 10% uncertainty in all of the voltage readings. Fifteen channels were used to estimate the total spectral power. According to the central limit theorem, one would expect  $\sigma_y = \frac{\sigma_x}{\sqrt{n}}$  for  $n$  uncorrelated parameter estimates. Thus, the error in the total spectral power should approach  $\frac{10\%}{\sqrt{15}}$  or 2.58% if the spectral model minimizes correlations, which it does. This verifies the methodology behind calculating the spectral power uncertainty.

#### 4.1 Discussion

In the previous example of the spectrum-top multigroup model, the nominal spectrum happened to be very accurate. However, if the nominal spectrum is not accurate, it could force

the model spectrum to take a shape that does not resemble the actual spectrum. In this case, the “flat-top” multigroup model spectrum may be a better fit.

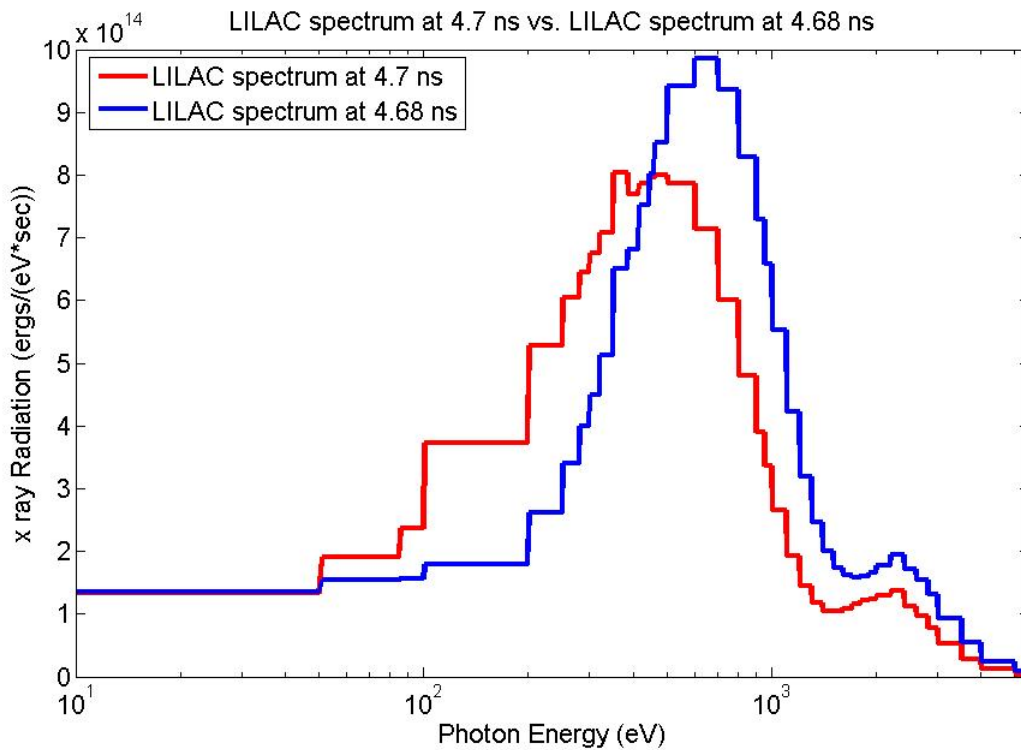


Fig. 7. LILAC spectra at 4.68 ns and 4.7 ns are shown. The spectrum at 4.7 ns is used as hypothetical data, and the spectrum at 4.68 ns is used to assign the shape of the fitting model spectrum within each spectral segment.

The spectrum at 4.68 ns is similar to the spectrum at 4.7 ns, but the peaks are shifted with respect to each other, as is shown in Fig. 7. The multigroup fitting process can only shift the model spectral values within their respective fixed spectral intervals, and the interval widths and positions are fixed. Thus, this model has a very difficult time predicting the shape of the spectrum.

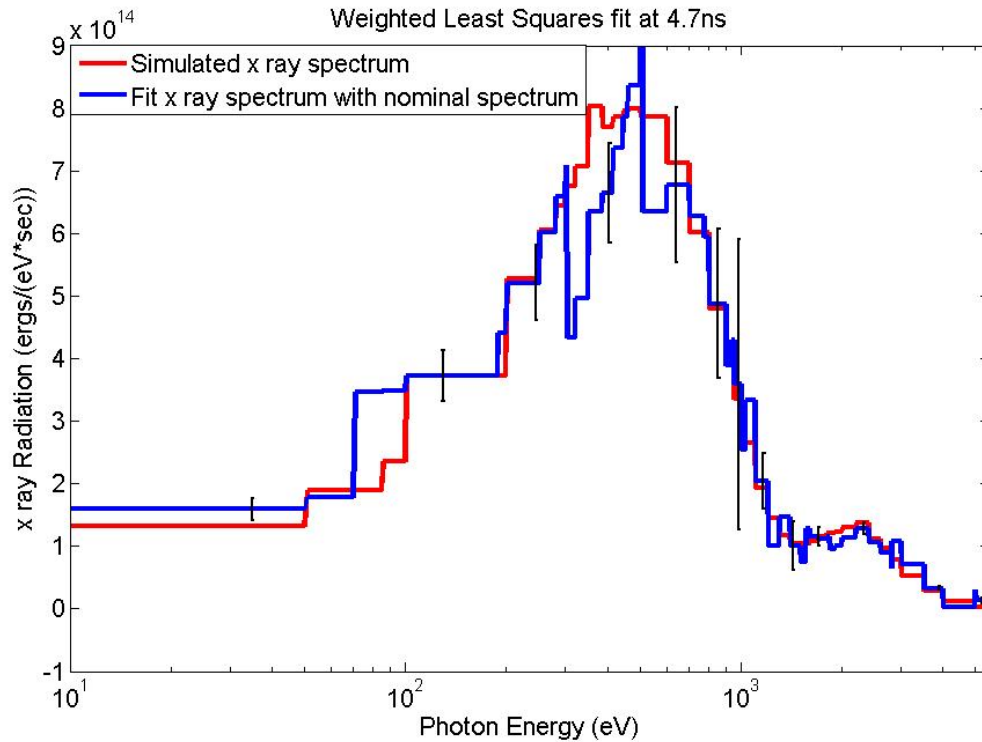


Fig. 8. A sample of the spectrum-top multigroup model spectrum fit with 13 intervals is shown. Error bars were generated based on a 10% accuracy in the voltage readings. The nominal spectrum was a LILAC simulated x-ray spectrum at 4.68 ns. Intervals were determined by Dante filter function edges.

In an attempt to fit the spectrum at 4.7 ns with the nominal spectrum at 4.68 ns, spurious spectral detail was created, as can be seen in Fig. 8. The program attempted to fit the behavior of the spectrum at higher photon energies with the nominal spectrum. As a result, the spectral peak at around 300 eV is mangled. In this example, the attempt to recover more spectral detail by anticipating it has reduced the reliability of the fit. A “flat top” model fit shown in Fig. 9 appears to recover less spectral detail, but is less vulnerable to the hazard of making poor nominal guesses. The “flat top” model is more reliable, in the sense that it does not create spectral information that does not exist in the first place. In addition, it still creates a fairly good representation of the spectrum.

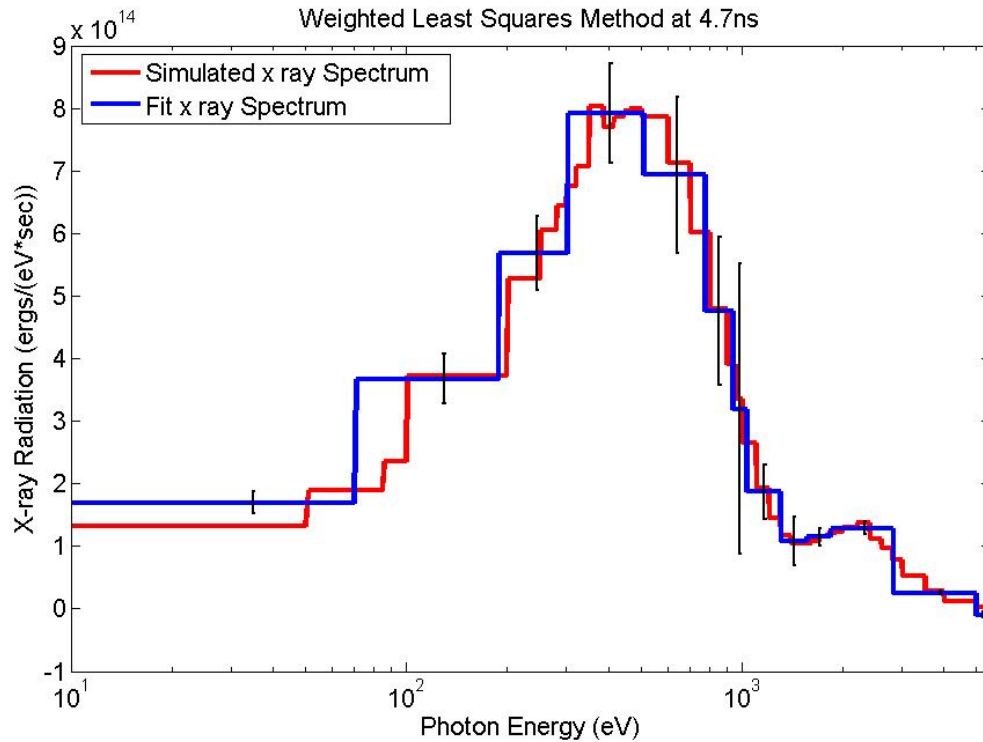


Fig. 9. A sample of the flat-top multigroup model spectrum fit with 13 intervals is shown. Error bars were generated based on a 10% accuracy in the voltage readings. Intervals were determined by Dante filter function edges.

When little confidence can be placed in the nominal spectrum, the “flat top” spectrum should be used because it is more reliable and will not create irrelevant spectral detail. However, if a lot of confidence can be placed in the “spectrum top” model, then the “spectrum top” model should be used because the spectral detail will be maintained.

### 5.1 Conclusion:

The weighted least squares method has been used to unfold x ray spectra obtained from simulated multi-channel spectrometer data using LILAC simulated spectra from laser-irradiated targets. The spectra emitted from these targets have been modeled with 15 parameters within 4 distinct modeling methods: the polynomial fit, the spectral point fit, the “flat top” multigroup model spectrum fit, and the “spectrum top” multigroup model spectrum fit. Each model utilizes the weighted least squares method to fit its parameters. The polynomial fit is able to capture the

basic curvature of the spectrum. However, this fit is crippled by correlation between parameter estimates. Furthermore, the shapes of polynomial functions are not characteristic of spectra. The spectral point model also introduces correlations that deleteriously affect the reliability of this fit. Formal estimates of the parameter variances reveal unreliability in the parameter estimates. The last two fits used multigroup models. This multigroup model divides the spectrum into groups based on filter function edges. These fits eliminate much of the correlation between parameter estimates. The “flat top” multigroup model is able to consistently capture the essential shape of the spectrum. The “spectrum top” multigroup model allows the user to enter a nominal spectrum and produces a good fit if the spectral detail can be anticipated with confidence. This model introduces artificial spectral detail if the first guess is not good enough. Only when confidence can be placed in the nominal spectrum can confidence be also placed in the “spectrum top” multigroup model. Otherwise, the more modest flat top multigroup model should be used.

### **Acknowledgements:**

I would like to thank Dr. Reuben Epstein for all of his guidance and help on this project. I would also like to thank Dr. Stephen Craxton and the Laboratory for Laser Energetics for allowing me to participate in this exciting high school summer research program.

1. Sorce, C, *et al.*, "Soft x-ray power diagnostic improvements at the Omega Laser Facility," *Rev. Sci. Instrum.* **77**, 10E518-1-4 (2006).
2. James Knauer, private communication, 2007.
3. Reuben Epstein, personal notes, private communication, 2007.
4. William H. Press, Brian P. Flannery, Saul A. Teukolsky, and William T. Vetterling, Numerical Recipes, Cambridge University Press, 1986.